Probing the Evolution of Galaxies Since $z \sim 1$ with the Tully-Fisher Relation

Alfred L. Tiley
St. Cross College
University of Oxford

A thesis submitted for the degree of
Doctor of Philosophy

Trinity 2016

Abstract

In this thesis we use the Tully-Fisher relation (TFR), the correlation between a galaxy's luminosity and its rotation velocity, to probe the luminous and dark matter in galaxies over the last ≈ 8 Gyr. First, we use samples of galaxies spatially resolved in Hα emission with integral field unit observations from the K-band Multi-Object Spectrograph (KMOS) Redshift One Spectroscopic Survey (KROSS) at $z \approx 1$ and the Sydney-Australian-Astronomical-Observatory Multi-object Integral-Field Spectrograph (SAMI) Galaxy Survey at $z \approx 0$. We match the data quality, analysis methods and sample selection between the two surveys to conduct a direct comparison of the absolute K-band magnitude (M_K) and stellar mass (M_*) TFRs at $z \approx 1$ and $z \approx 0$, free of any difference in biases between them. We measure no evolution of the M_K TFR zero-point for star-forming disk-like galaxies since $z \approx 1$, but an increase by 0.2 ± 0.2 dex of the M_* TFR zero-point for the same galaxies over the same period. This implies the total mass-to-stellar mass ratio of those galaxies has decreased by a factor of ≈ 0.4 since $z \approx 1$ at fixed rotation velocity, whilst their K-band stellar mass-to-light ratio has increased by a factor of ≈ 1.6. Moderate rates of star formation in galaxies and continued gas accretion since $z \approx 1$ can explain these changes. Second, we take a step toward an independent measure of the TFR evolution over the same period using carbon monoxide (CO) emission from galaxies as an alternative kinematic tracer. We present the M_* and *Wide-Field Infrared Survey Explorer* absolute Band 1 magnitude (M_{W1}) TFRs for galaxies from the CO Legacy Database for the *Galex* Arecibo SDSS Survey (COLD GASS) as $z \approx 0$ benchmarks that are pre-requisites to extend the CO TFR to $z \gtrsim 1$. We find no significant offsets between the COLD GASS TFR zero-points and those of similar $z \approx 0$ studies. The slope of the M_* COLD GASS TFR agrees with those of similar $z \approx 0$ studies, but the M_{W1} TFR slope is slightly shallower than previous studies at a similar redshift. We attribute this to the fact that the COLD GASS sample comprises galaxies of various (late-type) morphologies. Nevertheless, our work provides a robust reference point with which to compare future CO TFR studies.

Declaration

The work presented in this thesis is based on research carried out by me at the Sub-department of Astrophysics, University of Oxford between September 2013 and September 2016, under the supervision of Prof. Martin Bureau. It was funded by a Science and Technology Facilities Council Studentship. I hereby declare that no part of this thesis has been accepted or submitted for any degree, diploma, certificate or any other qualification at the University of Oxford or elsewhere. Except where it is explicitly stated or where explicit reference is made to the work of others, the work contained in this thesis is entirely my own.

The work presented in Chapter 2 is based on a peer-reviewed, published paper, Tiley A. L., et al., 2016, MNRAS, 460, 103, of which I am the lead author. Similarly, the work of Chapter 4 is based on a peer-reviewed, published paper, Tiley, A. L., et al., 2016, MNRAS, 461, 3494, of which I am the lead author.

In Chapter 2, the raw data cubes were reduced by Dr. John Stott (University of Oxford). However, the data reduction process was devised individually by both John and myself, with each of us independently arriving at the same final reduction method. The velocity fields and their best fit models, and the Hα flux maps used in that chapter were constructed by Dr. John Stott. Also in that chapter, the fits to the KROSS SEDs that used HyperZ were performed by Dr. Mark Swinbank (Durham University).

In Chapter 3, the KROSS velocity fields and Hα maps are those of Chapter 2 (constructed by Dr. John Stott). However, all other analysis products (including the best fit models to the KROSS velocity fields) and measurements are my own.

In Chapter 4, the generation of a library of noiseless integrated spectra using KinMS was helped by an IDL wrapper provided by Dr. Tim Davis (Cardiff University).

Alfred L. Tiley

(*September 2016*)

Acknowledgements

First and foremost I would like to thank my supervisor, Prof. Martin Bureau for his support and guidance, and for the time and red ink he has invested in me over the past three years. Without it I would not have reached this point. Thank you to John Stott for being a friend, colleague and mentor to me during my DPhil. I also extend my thanks to my collaborators in KROSS, and to Amélie Saintonge and Tim Davis for providing me with invaluable feedback on my work. To Laura, I could not have done this without your unending love and support. Thank you for spending the last two years with me and my laptop. To my parents, who have always been there for me. Helen, Russell, John and Ali thank you for believing in me and for your constant love and advice. And to my siblings Willum, Quin, Rosie, Lily and George thank you for helping me to get through the last three years. Thank you to Ciaran for your continuous encouragement and for keeping the Chatty Palace lights on. I am forever grateful. I extend my gratitudes to the Triangle for providing me with strength, and to the $\alpha\lambda\pi$ for the last year of domestic bliss and academic excellence. To Ashling, thank you for always offering the best advice and guidance. Lastly, a big thanks to Danielle for being a good friend and office mate.

To Helen, for your faith in me.

Contents

List of Figures

List of Tables

Chapter 1

Introduction

The work within this thesis explores the evolution of galaxies in our Universe over the last ≈8 Gyr. In this chapter we introduce this work by giving an overview of galaxy evolution over time, highlighting some key studies that have contributed to our current understanding of galaxies and their formation and evolution. In subsequent chapters we include separate introductions, more specific to the content of each.

1.1 An Overview of Our Universe

Galaxies - massive, gravitationally bound systems composed of dark matter, billions of stars, gas and dust - are the fundamental building blocks of our Universe. They populate the night sky, seemingly side-by-side with the stars in our own Galaxy, and have been the subject of fascination for over a thousand years - in the year 964, the persian astronomer Abd-al-Rahman Al Sufi described the Andromeda galaxy as a “Little Cloud” in his *Book of Fixed Stars* (al Rahman Al Sufi, 1965) - and intense scientific study in the past century. The modern study of galaxy evolution seeks to understand the nature and origin of galaxies. More broadly, it is the pursuit of a complete and evidenced description of how an initially smooth and homogenous Universe transformed into the complex, structured one that we observe today. From the very first galaxies to emerge in the young, dark Universe, to the plethora of galaxies of different morphologies in the present-day, the field seeks not only to describe and quantify this abundance of diversity, but also to determine and explain its causes.

It is now widely accepted that we reside in a Λ cold dark matter (ΛCDM) Universe, dominated by dark energy (Λ), an as yet unexplained agency that permeates the Universe, making up ≈67% of its energy budget and acting in opposition to gravity. The majority of the remainder of the Universe, ≈29% of the energy budget, is composed of dark matter - matter of an unkown nature that interacts under gravity but not electromagnetism. Suprisingly (at least to the naive observer), the baryonic matter that constitutes all visible structures in the Universe only accounts for ≈4% of its energy budget (e.g. Freedman & Turner, 2003). Yet without it, galaxies would not exist as we know them, remaining dark throughout time.

In the ΛCDM framework, our Universe originated in a “Big Bang” in which all of the Universe expanded from an infinitely hot and dense singularity. Immediately following the Big Bang, the temperature of the Universe was such that all baryonic matter was completely ionised and coupled with radiation. As the Universe expanded and cooled, the ionised baryonic matter condensed into neutral matter, mostly in the form of Hydrogen, and matter and radiation decoupled.

The seeds of galaxies were sown in the form of primordial density perturbations in the distribution of this matter, caused by quantum fluctuations and amplified by gravity in the ≈13.9 billion years since. As the perturbations grew, dark and luminous matter flowed into denser regions, and left ever-growing voids in the underdense regions. The disippative nature of baryonic matter allowed it to coalesce into large clouds that eventually collapsed and fragmented under their own gravity to form the first stars and then galaxies. Since their initial genesis, galaxies have continued to form and grow over time through hierarchical merging (e.g. Cole et al., 2000), and other complex processes such as continuous gas accretion (e.g. Katz et al., 2003; Kereš et al., 2005; Sancisi et al., 2008), and secular growth via clumpy star formation induced by gravitational instabilities (e.g. Noguchi, 1999; Elmegreen et al., 2008; Genzel et al., 2008, 2011; Forbes et al., 2014).

1.2 Galaxies in the Present Day

The existence of galaxies outside of our own Milky Way was definitively established when Hubble (1925) observed Cepheid variable stars in Messier Object 31 (M31), well known today as the Andromeda nebula, our largest neighbouring galaxy. Hubble used the relation between the period of the luminosity variations of the Cepheids and their luminosity to infer their distance, thus deducing that M31 was far outside of our own Galaxy. This resolved the ongoing debate over whether the multitude of "nebulae", as they were then referred to, that astronomers had observed throughout the night sky were objects within our own Galaxy or outside it. Given the angular diameters of the nebulae on the sky, which betrayed their huge spatial extents, it was now readily apparent that there existed galaxies beyond our own.

Since confirmation of their existence outside the Milky Way in the 1920s, astronomy has taken several great leaps in understanding the nature and evolution of galaxies; galaxies in the nearby Universe are now very well understood. Broadly they can be divided in two categories: early-types and late-types. The former appear red in colour, elliptical in shape and have little, if any, ongoing star formation. The latter are blue and actively star-forming, have a disk-like morphology, and often exhibit complex internal structures such as spiral arms and central bars and bulges (e.g. Toomre, 1964; Lin & Shu, 1964; Kennicutt, 1983; Sellwood & Carlberg, 1984; Kennicutt, 1998; Strateva et al., 2001; Baldry et al., 2004, 2006).

An important early example of a descriptive framework with which to explain these different galaxy morphologies is the classification scheme of Hubble (1926, 1936). Based on the appearance of galaxies on photographic plates, and well known today as the 'Hubble Tuning Fork', it is the origin of the paradoxical Hubble type (early-type and late-type) denominations of galaxies (paradoxical in the sense that late-types are understood to be the progenitors to early-types). Subsequently de Vaucouleurs (1953), again using photographic plates, discovered that the light distribution of early-type galaxies obeys a power law with respect to radius (today known as a de Vaucouleurs profile). Later still, Sérsic (1963) published a more general description of galaxies' light profiles, the *Sérsic profile* (of which the de Vaucouleurs profile is a special case), determining in the process that the light distribution of late-type galaxies follows an exponential profile, thus highlighting an important physical difference between the two types of galaxies.

The invention of digital imaging allowed to expand on these classification schemes with easily quantifiable descriptions of galaxies' light. This allowed to rapidly survey large numbers of galaxies across vast areas of the night sky and, combined with the digitisation of exisiting photographic observations, facilitated the construction of large multi-wavelength atlases of nearby galaxies. The Sloan Digital Sky Survey (SDSS; e.g. Stoughton et al., 2002; Abazajian et al., 2003) is arguably the most well known of such atlases. An important early result from the SDSS was the work of Strateva et al. (2001), that showed that early- and late-types occupied distinct and separate regions on a colour-magnitude diagram; early-types (compromising older, redder stars) fell along the now well-known "red sequence" on the diagram, whilst late-types (comprising a combination of both older, redder stars and younger, bluer stars) lay apart from early-types within a "blue cloud". As with the work of de Vaucouleurs (1953) and Sérsic (1963), this bimodality highlights a fundamental difference between early- and late-types.

Some galaxies reside in the "green valley", the intervening region on the colour-magnitude diagram between the red sequence and blue cloud, providing evidence of a transitionary phase (e.g. Bell et al., 2004; Faber et al., 2007; Martin et al., 2007; Mendez et al., 2011; Smethurst et al., 2015) between red and blue (early- and late-type) galaxies. The fact that this region is comparatively underpopulated in the local galaxy population also implies that any such transitionary phase is rapid (see § 1.2.1 for further discussion on the morphological evolution of galaxies).

Aside from differences in their visual appearance, early- and late-types also differ kinematically. Some early-type galaxies are dominated by complex (if not truly random) motions of their constituent stars, whilst others do display organised rotation (e.g. de Zeeuw et al., 2002; Cappellari et al., 2011a,b). Late-types are dominated by circular motion in the plane of their disk (see Sofue & Rubin, 2001, for a review).

1.2.1 Probing Galaxy Evolution at $z \approx 0$

The distinct differences between early-types and late-types provide clues as to their evolutionary pathways. The fact that late-types are apparently much more rotationally dominated, and have increased star formation rates compared to early-types, implies the former are the precursor to the latter (despite their names). One can envisage many more scenarios whereby a galaxy slows its rotation (e.g. Emsellem et al., 2008; Bois et al., 2011; Khochfar et al., 2011; Naab et al., 2014) than ones in which an already slowly-rotating galaxy increases its rotation. The ongoing star formation in spiral galaxies also suggests that these are systems that are still growing; they are still assembling stellar mass. Comparing this to the more quiescent elliptical systems, in which the most recent generation of stars is seemingly slowly fading into darkness, one is presented with a powerful sense of the direction of evolution of galaxies, seemingly from late-type to early-type morphologies.

To gain further insight into the origin and evolutionary history of present day galaxies, there are two main approaches. Firstly, one may study the morphologies, internal structures, and environments of galaxies in the present day, to deduce information about their pasts. Conversely, one may look at distant galaxies at higher redshifts to directly observe galaxies as they were in the past. Here we highlight some key studies that have applied the former approach, whilst the latter approach is discussed in § 1.3.

Any successful theory of galaxies must explain two key aspects of their evolution. Firstly, it must provide mechanisms for galaxy growth (e.g. in both size and mass). Secondly, it must explain how the morphologies of galaxies change over time. Both are intricately linked. Indeed, the same processes by which a galaxy grows could also turn an actively star-forming, blue spiral galaxy in to a quiescent, red elliptical one. Our current understanding champions two broad channels by which galaxies grow and evolve, namely major mergers (within the framework of hierarchical growth), and secular evolution whereby galaxies grow via minor-mergers and/or constant accretion of gas from their surroundings.

Considering either scenario, the mechanisms that may induce star formation in galaxies are easily envisaged. When galaxies undergo a major merger their gas collides, inducing its collapse and subsequent star formation (e.g. Joseph et al., 1984; Hernquist, 1989; Barnes &

Hernquist, 1991; Teyssier et al., 2010). For galaxies undergoing secular evolution, cosmological simulations predict that the accretion of metal poor gas from a galaxy's surroundings can fuel star formation (e.g. Dekel et al., 2009a,b). This could induce star formation in two ways. Firstly, the gas accretion itself could trigger star formation locally (e.g. Turner et al., 2015), perhaps via cold streams inducing local instabilities in the galaxy gas disk. Alternatively, the generally increased abundance of gas as a result of continued accretion may result in gravitational instabilities in the disk that trigger star formation (e.g. Sellwood & Carlberg, 1984; Wang & Silk, 1994).

The relative importance of merger-driven versus secular star formation remains an open area of research. A directly related topic is how the star formation in galaxies may be suppressed, or "quenched". Faber et al. (2007) used the DEEP2 and COMBO-17 surveys to measure the evolution of the luminosity functions of both red and blue galaxies since $z \approx 1$. They found that the number density of red galaxies has at least doubled (≈ 0.5 dex) over the last ≈ 8 Gyr, whilst the number density of blue galaxies has remained roughly constant. This implies that blue star forming galaxies are quenched and become red over this period. Simultaneously, additional blue galaxies are created. The question of how galaxies are quenched is therefore intimately linked with the broader question of how blue galaxies become red.

Given that star formation is fueled by cold gas in galaxies, it follows that quenching mechanisms act to reduce the amounts of cold gas available for star formation, either via heating it, making it more turbulent, or removing it from the galaxy entirely. Examples of the former two categories include "strangulation" whereby galaxies are prevented from accreting further cold gas as they enter a cluster (e.g. Kawata & Mulchaey, 2008; Peng et al., 2015; Maier et al., 2016), virial-shock-heating (e.g Birnboim & Dekel, 2003; Dekel & Birnboim, 2006; Kereš et al., 2009) via acrretion of gas on to a massive galaxy halo, and morphological quenching whereby a galaxy's cold gas reservoir is stabilised against star formation as a result of the galaxy's morphological transition from disk-like to spheroidal, and the associated increased shear in the disk as a result (Martig et al., 2009). Examples of the latter include supernovae winds (e.g. Efstathiou, 2000; Strickland et al., 2004; Hopkins et al., 2012), or active galactic nuclei (AGN) heating (e.g. Silk & Rees, 1998; Haehnelt et al., 1998; Dubois et al., 2012; Cicone et al., 2014; Harrison et al., 2014). The exact mechanisms by which AGN suppress star formation, if indeed they actually do, are still the subject of much debate.

1.2.1.1 Kinematics at $z \approx 0$

It is clear that categorising galaxies' visual appearance, and even quantifying the distribution of light within them, can provide valuable insights into the differences between galaxy types. However, to progress beyond the suspicion that late-types are the evolutionary precursors to early-types, what is really required is information on galaxies' dynamics as well as their appearance. Of course, the ultimate view of galaxies (or at least of their constituent stars), is a full six-dimensional description spanning the three dimensions of space (r_x,r_y,r_z) and velocity (v_x,v_y,v_z). Whilst measuring the transverse motions of distant galaxies (v_x,v_y), or their spatial extent along the line-of-sight (LOS) (i.e. r_z) is beyond our current capability, we may now easily add information on the LOS *velocity* to our descriptions of galaxies, using various gas emission lines or stellar absorption lines in galaxies. Here we discuss observations of galaxy kinematics, that use a variety of tracers to add this third dimension to the two-dimensional description of galaxies afforded from imaging along.

Before considering spatially-resolved observations of galaxy kinematics, it is worth noting that globally-integrated measures of the motions of a galaxy's stars and gas, be they circular or random, can be useful tools with which to probe the intrinsic properties of galaxies. For example, the size and bulk rotation speed of a galaxy say something about the total galaxy mass. Coupled with independent measurements of the galaxy's stellar mass and gas mass, one may then look for variations of the relative amounts of baryonic and dark matter between different galaxy populations (separated, for example, by time or environment or the intrinsic properties of the galaxies). One of the most famous illustrations of this approach is the Tully-Fisher relation (TFR; Tully & Fisher, 1977), that links a measure of a galaxy's circular motion to the luminosity of its stars. The TFR, and its evolution over time, is the main focus of this thesis. The relation is introduced and discussed in more detail in § 1.4. Here it is sufficent to note that studies of galaxies' global motions in the local Universe have traditionally been confined to the use of HI (e.g. Tully & Fisher, 1977; Mathewson et al., 1992; McGaugh et al., 2000; Tully & Pierce, 2000; Rhee & Broeils, 2005; Springob et al., 2005; Lagattuta et al., 2013) and Hα emission (e.g. Courteau, 1997; Catinella et al., 2005; Pizagno et al., 2007; Saintonge & Spekkens, 2011), and, for early-types in particular, various stellar absorption lines (e.g. Williams et al., 2010). A limited number of studies have also explored, with success, the viability of CO(1-0) emission from cold molecular gas in galaxies as an alternative kinematic tracer (e.g. Lavezzi & Dickey, 1998, 1999; Davis et al., 2011, 2013, 2016) (see § 1.5 for a more detailed discussion).

In the last two decades, the study of galaxies has benefited greatly from the advent of integral-field spectroscopy (IFS) and integral field units (IFUs), and with them the ability to study the *spatially-resolved* kinematics of galaxies to further probe their internal structures while avoiding any concerns over centering inaccuracies inherent in slit or fibre observations. As with the invention of digital imaging, IFS has opened a new window on the Universe. Before its invention, studies of galaxies were constrained to taking images and spectra of galaxies with separate exposures. In allowing the simultaneous extraction of a multitude of images over a large range of wavelengths in a single exposure (this can also be understood as a spectrum at every pixel of a conventional image), IFUs provide spatially-resolved information on both the physical properties (e.g. star formation rate, metallicity, stellar mass or gas mass) and kinematics (e.g. mean velocity, velocity dispersion, and shape of the LOS velocity distribution) of galaxies on timescales that were previously impossibly short.

A key application of IFS to the study of galaxies in the local Universe was conducted by the ATLAS^{3D} Project (Cappellari et al., 2011a), a multi-wavelength survey using the Spectrographic Areal Unit for Research on Optical Nebulae (SAURON; Bacon et al., 2001) to study the kinematics and stellar populations of early-type galaxies in the local Universe. The survey identified two distinct categories of galaxies based on the two-dimensional velocity maps of the surveyed galaxies: ‘fast-rotators’ and ‘slow-rotators’. Critically, the boundary between fast- and slow-rotators did not coincide with the traditional boundary between late- and early-types - many galaxies classified as early-type based on their visual appearance were found to be rapidly rotating. Only the most massive early-type galaxies were found to be true slow-rotators. This discovery raised as many questions as it answered with regards to the evolutionary pathways of galaxies. It is still an open area of research whether fast- and slow-rotators are just different points along the same evolutionary pathway of galaxies, or whether they are fundamentally different populations of galaxies with entirely separate formation mechanisms.

Of course, the implicit assumption in the work of ATLAS$^{\rm 3D}$ is that late-types, which are not probed by the survey but are known to rapidly rotate, continue the trend from early-type fast-rotators. Surveys such as the Calar Alto Legacy Integral Field spectroscopy Area (CALIFA; Sánchez et al., 2012) survey, the Mapping Nearby Galaxies at Apach Point Observatory (MaNGA; Bundy et al., 2015) survey, and the Sydney-Australian-Astronomical-Observatory Multi-object Integral-Field Spectrograph (SAMI; Croom et al., 2012) Galaxy Survey (e.g. Bryant et al., 2015) are all now conducting IFS observations of thousands of galaxies in the local Universe, across a range of galaxy properties, morphologies and evironments. They are in a position to confirm (or challenge) such an assumption, each providing the opportunity to expand on the work of ATLAS$^{\rm 3D}$ whilst also establishing $z \approx 0$ benchmark samples of IFU observations of galaxies that allows direct comparisons with analagous surveys at higher redshifts (see § 1.3.1.1).

1.3 Galaxies at Higher Redshift

As discussed above, galaxies in the local Universe have been well studied over the past century, with progress first made using photographic plates, then with digital imaging, and more recently with the advent of IFS. Descriptions of galaxies in the local Universe, such as Hubble's morphological and the ATLAS$^{\rm 3D}$'s kinematic classification schemes, have proved invaluable lenses through which to study and explain the origin of galaxies. In addition, large surveys of the night sky, such as the SDSS, have allowed a robust census of nearby galaxies, providing a clear picture of the number and nature of galaxies at $z \approx 0$. Studies are thus increasingly turning to the higher-redshift Universe to further unveil the evolutionary pathways of galaxies. However, the aforementioned descriptions of galaxies, that have been so effective in their applications to the present day galaxy population, begin to breakdown at higher redshifts. For example, Abraham (1999) argue that the Hubble sequence is not an effective classification at $z \gtrsim 0.5$. As will be discussed later, IFS observations of the $z \gtrsim 1$

Universe also reveal a galaxy population quite unlike the local one, dominated by turbulent gas-rich disks that only partially reflect the morphologies of fast-rotators or late-types in the local Universe, or by galaxies with disturbed kinematics suggesting recent interactions or merging episodes (e.g. Förster Schreiber et al., 2009; Contini et al., 2012; Epinat et al., 2012; Stott et al., 2016).

Further, it is now well established that the global star formation rate of the Universe peaks at $z \approx 1$–3 (e.g. Lilly et al., 1996; Madau et al., 1996, 1998; Hopkins & Beacom, 2006), with ≈50% of the present day stellar mass assembled by $z \approx 1$ (e.g. Pérez-González et al., 2008), around 8 Gyr ago. Either side of this peak, with increasing or decreasing redshift, the star formation rate of the Universe declines. Thus galaxies today, even those that are actively forming stars, are considerably more quiescient compared to typical galaxies at the epoch of peak star formation. The primary causes of this increased star formation at $z \approx 1$–3 are the subject of much debate, as are the dominant mechanisms for mass growth.

1.3.1 Probing Galaxy Evolution at $z \approx 1$

By comparing galaxies in the local Universe to those at higher redshifts, one may hope to determine which are the dominant mechanisms for galaxy growth, and what role they play in the formation of the population of early- and late-types, or fast- and slow-rotators, in the present day. Historically, this has proved difficult due to the high spatial resolution and sensitivy required to resolve and study distant galaxies. The *Hubble Space Telescope* (*HST*) went some way to addressing this problem with the *Hubble* Deep Fields observations (e.g. Dickinson, 1998), along with subsequent very deep observations such as the Great Observatories Origins Deep Survey (GOODS, Dickinson et al., 2003), the *HST* Ultra Deep Field (UDF; Beckwith et al., 2006), and the Cosmic Evolution Survey (COSMOS; Scoville, 2007) field. As hinted at above, they revealed a $z \approx 1$ Universe populated by galaxies that only partially reflect those of the present day. Whilst there are galaxies at $z \gtrsim 1$ that appear to resemble early- and late-types, their numbers are greatly reduced in favour of 'peculiar' galaxies that resemble neither, and whose appearances are consistent with signs of recent merging events (Conselice et al., 2005a).

This difference in populations is established at higher redshifts still. For example, Buitrago et al. (2013) compiled a large sample of massive galaxies with redshifts $0 < z < 3$, comprising galaxies at $z \approx 0$ from the SDSS and galaxies observed with the *HST* at higher redshifts, selected from the Palomar Observatory Wide-field InfraRed/DEEP2 (POWIR; Conselice et al., 2008) survey and the GOODS Near Infrared Camera and Multi-Object Spectrometer (NICMOS) Survey (GNS; Conselice et al., 2011). They found that the fraction of galaxies with late-type or peculiar morphologies declines from early times ($z \gtrsim 1.5$) until the present day, whilst the fraction of early-types increases over the same period. This trend was even more pronounced when galaxies were divided by their Sérsic index into those that are disk-like and those that are spheroid-like, with the fraction of disks declining from its peak at high redshift to the present day, and the fraction of spheroids following an opposite trend.

1.3.1.1 Kinematics at $z \gtrsim 1$

As with studies of galaxies in the local Universe, the application of IFU observations to high-redshift galaxies provides further insights into their nature, and highlights additional differences between them and the present day population. In particular, IFUs that operate in the near-infrared (NIR) have been particularly beneficial to our understanding of high-z galaxies, allowing a comparison of the well understood restframe optical properties of galaxies at $z \approx 0$ with those at $1 \lesssim z \lesssim 2$.

One of the earliest surveys to apply NIR IFS to the high-redshift Universe was the Spectroscopic Imaging survey in the Near-infrared with the Spectrograph for INtegral Field Observations in the Near Infrared (SINFONI; Bonnet et al., 2004) (SINS; Förster Schreiber et al., 2006a), that played a key role in revealing the kinematic nature of disk-like galaxies at high redshift. Förster Schreiber et al. (2009) studied the two-dimensional mean LOS velocity fields of 62 SINS galaxies in the redshift range $1.3 < z < 2.6$, each with detected rest-frame optical emission lines (predominantly Hα) and stellar masses $M_* \gtrsim 10^{10} M_\odot$. In one of the first steps towards compiling a representative sample of massive star-forming galaxies at the epoch of peak star formation, they found their sample to be composed of around one third rotation-dominated turbulent disks, one third dispersion-dominated systems, and a final one third displaying characteristics of interacting or merging systems.

Similarly, the Mass Assembly Survey with SINFONI in VIMOS VLT Deep Survey (VVDS) (MASSIV; Contini et al., 2012) used SINFONI to observe a representative sample of 84 "normal" star-forming galaxies (as determined by their emission line strengths, colours, and ultra-violet (UV) absorptions) with redshifts $0.9 < z < 1.8$, including galaxies with lower stellar masses (10^9–$10^{11} M_\odot$) than those of the SINS survey. Epinat et al. (2012) analysed the kinematics of a subsample of 50 MASSIV galaxies. Similarly to SINS, they found that at least 35% of the sample was dispersion dominated, whilst 44% of the sample was composed of systems exhibiting ordered rotation, with the ratio of the maximum rotation velocity probed by the galaxy's Hα emission to its global velocity dispersion $V_{\max}/\sigma > 1$. A large fraction (29%) of the sample also showed signs of interaction or merging.

Both SINS and MASSIV strengthened the view that galaxies at the epoch of peak star formation (i.e. $1 \lesssim z \lesssim 3$) are predominantly rotation-dominated, turbulent, disk-like galaxies and galaxies with peculiar morphologies. Dispersion dominated galaxies, that resemble early-types in the local Universe, make up a much smaller fraction of the population than at $z \approx 0$. A picture thus begins to form whereby early galaxies principally form as disks, with much of their stellar mass assembled in the first 6–7 billion years of the Universe (i.e. by $z \approx 1$), while the formation of early-types as we recognise them today mostly takes place at $z \lesssim 1$. In this framework, the peak in stellar mass assembly and galaxy growth at $z \approx 1$ may be driven either by an increased merger rate (as evidenced by the greater fraction of peculiar systems compared to the local Universe) leading to a higher star formation rate, or by the efficient and constant accretion of gas from galaxies' surroundings and subsequent star formation (as evidenced by the large fraction of galaxies exhibiting a high star formation rate coupled with ordered rotation and no sign of recent mergers).

The benefits to our understanding of galaxy evolution that single IFUs such as SAURON and SINFONI have provided are significant. In the present day, however, a new era of surveys using multiplex IFU instruments (i.e. instruments consisting of multiple IFUs that can be simultaneously deployed) is allowing spatially-resolved observations of ever increasing numbers of galaxies in much shorter observing timescales than previously possible with single IFUs. The K-band Multi-Object Spectrograph (KMOS; Sharples et al., 2013) is one such instrument. Consisting of 24 deployable IFUs, each with a $2.''8 \times 2.''8$ field-of-view, and with full NIR wavelength coverage (rest-frame optical at $z \approx 1$), it allows to conduct IFS observations of 24 galaxies in a single exposure. It has so far proved a powerful new tool to assemble large numbers of IFS observations of galaxies at high redshifts.

The KMOS Redshift One Spectroscopic Survey (KROSS; Stott et al., 2016) used KMOS to target ≈ 800 star-forming galaxies at $z \approx 1$ in the YJ-band, detecting and resolving Hα emission in ≈ 700 and ≈ 600 objects, respectively. The KROSS sample is the largest of its kind at $z \approx 1$ and provides a definitive view of the nature of typical star-forming galaxies at the epoch of peak global star formation rate. Its first results somewhat confirm the paradigm constructed on the evidence of earlier IFU studies at similar redshifts. Stott et al. (2016) find that 83% of the KROSS galaxies with resolved Hα emission display kinematics dominated by rotation, with a ratio of rotation velocity (extracted at 2.2 times the effective radius of the galaxy) to intrinsic velocity dispersion $V_{2.2}/\sigma > 1$. They also measure much larger gas fractions ($\approx 35\%$) than observed in late-type galaxies in the present day, substantiating the image of a $z \approx 1$ Universe populated by turbulent disk-like galaxies, with much increased star-formation rates possibly fueled by accretion of surrounding gas (given their ordered, rotation-dominated kinematics).

As mentioned in § 1.2.1.1, several $z \approx 0$ programs that provide a benchmark with which to compare KROSS have already reached maturity, having constructed IFU observations of similarly large or even larger samples of galaxies in the nearby Universe over recent years. Specifically, the CALIFA, MaNGA and SAMI galaxy surveys each comprise suitably large samples of IFU-observed $z \approx 0$ galaxies to compare to KROSS.

In addition to NIR IFS, mm and cm interferometry provide well-established alternative methods to study the spatially-resolved kinematics of galaxies at $z \gtrsim 1$. As evidenced by Stott et al. (2016), star-forming galaxies at $z \gtrsim 1$ are very gas-rich. The abundance of *molecular* gas, in particular, means that galaxies at this epoch are very bright in the low-J lines of CO. Indeed, multiple transitions of CO are now regularly detected in star-forming galaxies at $z \approx 1$–3 (e.g. Daddi et al., 2010; Magdis et al., 2012; Magnelli et al., 2012; Combes, 2013; Freundlich et al., 2013; Genzel et al., 2015) and in starbusting galaxies at even greater distances (up to $z \approx 7$; e.g. Walter et al., 2004; Riechers et al., 2008a,b, 2009; Wang et al., 2011; Wagg et al., 2014). Of particular note is the work of Tacconi et al. (2010, 2013) as part of the Institut de Radioastronomie Millimétrique (IRAM) Plateau de Bure HIgh-z Blue Sequence Survey (PHIBSS). They used mm interferometry to study the spatially-resolved CO(3-2) emission of 52 galaxies at $z \approx 1.2$ and $z \approx 2.2$., finding them to be highly star-forming and rich in turbulent molecular gas - in accordance with the findings of IFU studies at similar redshifts. With the dawn of the Atacama Large Millimeter/sub-millimeter Array (ALMA; e.g. Wootten & Thompson, 2009), the number of CO studies conducted at higher redshifts will increase rapidly over the coming years, providing a readily accessible means to probe the evolution of galaxies since $z \gtrsim 3$ independent of NIR IFU studies.

1.4 The Tully-Fisher relation

The focus on galaxies' rotation and kinematics throughout the 20th century resulted in the discovery of the Tully-Fisher relation (TFR), when Tully & Fisher (1977) noticed a tight relation between a galaxy's absolute magnitude (or luminosity) and the line width of its integrated HI emission. The correlation between these two observed quantities reflects an underlying, fundamental link between two intrinsic properties of a galaxy - its stellar mass (probed via the light emitted from its stars) and its total mass (encompassing both baryonic and dark matter and probed via the galaxy rotation velocity).

The relation can be derived easily by considering circular motion under gravity from a spherical mass distribution: $M(r) \propto v^2(r)r$, where M is the mass of the body enclosed within a radial distance r from its centre and v is the circular velocity at r. Defining the dynamical mass-to-light ratio M/L and surface mass density $\Sigma = M/\pi r^2$ of the body, one then obtains the TFR:

$$L \propto \frac{v^4}{\Sigma(M/L)} \quad . \tag{1.1}$$

Following its observational discovery, the TFR was initially used as a galaxy distance indicator and, once coupled with the galaxy systemic velocity, as a tool to measure the Hubble constant (e.g. Aaronson, 1983; Bottinelli et al., 1988; Giovanelli et al., 1997; Sakai et al., 2000; Tutui et al., 2001). Indeed, measuring a characteristic rotation velocity and an apparent luminosity, the TFR-predicted absolute luminosity then yields a distance estimate (e.g. Sandage & Tammann, 1976; Bottinelli et al., 1980; Teerikorpi, 1987; Fouque et al., 1990; Bureau et al., 1996; Ekholm et al., 2000). This of course assumes that one knows the mass-to-light ratio and surface density of the object studied, or more commonly that one compares populations of galaxies assumed to have identical M/L and Σ (e.g. galaxies of a given morphological type at a given epoch).

The TFR implies a tight relationship between luminous mass (traced by L) and dynamical or total mass (traced by v), evidence that the growth over time of the luminous and dark matter present in galaxies is closely connected. Most importantly, given a reliable measure of distance, the TFR can be turned around and used to probe the mass-to-light ratio and surface density of galaxies. Indeed, many studies have used the zero-point, slope, and scatter of the TFR to constrain cosmological models and models of galaxy formation (e.g. Cole & Kaiser, 1989; Eisenstein & Loeb, 1996; Willick et al., 1997; Steinmetz & Navarro, 1999; van den Bosch, 2000; Yang et al., 2003; Gnedin et al., 2007; McGaugh, 2012). Further, since a galaxy's redshift is itself a good distance indicator beyond the local Universe, the TFR is a powerful tool to directly probe the evolution of M/L and Σ over cosmological distances.

The TFR of local (i.e. low-z) galaxies is well studied, with a natural concentration on rotationally-supported late-type galaxies and predominant use of the width of a galaxy's globally-integrated HI profile to probe its rotation velocity (e.g. Tully & Pierce, 2000; Bell & de Jong, 2001; Masters et al., 2008; Lagattuta et al., 2013). However, some studies have also measured the TFR of early-types and 'lenticulars', an intermediate class of galaxies that suggests a transition between late- and early-type morphology. For example, Davis et al. (2011) showed that CO single-dish observations easily yield robust and unbiased TFRs for early-type galaxies in the local Universe, whilst Williams et al. (2010) used stellar kinematics to show that late-type spiral galaxies share a common TFR with lenticulars at $z \approx 0$.

The Tully-Fisher relation at $1 \lesssim z \lesssim 3$ has been the subject of many recent studies, that use small numbers of galaxies at this epoch. These can be broadly divided into studies that measure galaxy rotation via long-slit spectroscopy and, increasingly, studies that utilise the two-dimensional kinematics of galaxies derived from IFU observations. A key example of the former is the work of Miller et al. (2011), who studied the stellar mass TFR of 129 galaxies out to $z \approx 1.3$ using slit spectroscopy. They found an intrinsic scatter comparable to that of low redshift studies and, most importantly, no evolution in the stellar mass TFR from $z \approx 1$ to $z \approx 0.3$. Similarly, Miller et al. (2012) used resolved spectra - taken with the Keck I Low Resolution Imaging Spectrograph (Oke et al., 1995) - of 42 morphologically-selected star-forming galaxies at $1 < z < 1.7$, and found no evidence for an evolution of the zero-point of the TFR compared with the local Universe. Considering only the work of Miller et al., it would seem that the TFR as measured in the local Universe is already in place by $z \approx 1$. Similarly, Conselice et al. (2005b) used Keck spectroscopy to measure the K-band and stellar mass TFRs of 101 galaxies at redshifts $0.2 < z < 1.2$, finding no evolution in either relation from $z = 1.2$ to the present day.

The results of Conselice et al. (2005b) and Miller et al. (2011, 2012) are seemingly in accordance with the previously discussed picture of the $z \approx 1$ Universe, populated by turbulent yet rotation-dominated disk galaxies, with over half of all the stellar mass in present day galaxies assembled by this time. However, it is apparently at odds with the necessity of further stellar mass growth between $z \approx 1$ and the present day, and with the results of several IFU surveys conducted at similar redshifts. Flores et al. (2006) and Puech et al. (2008) used the multi-integral field spectrograph FLAMES-GIRAFFE (e.g. Pasquini et al., 2002) to study the [OII]3727 emission line kinematics of galaxies at $z \approx 0.6$, identifying those displaying characteristics of rotating disks. Whilst Flores et al. (2006) report no evidence for an evolution of either the stellar mass or K-band TFR slope, scatter, or zero-point since $z \approx 0.6$, Puech et al. (2008) report an evolution of the zero-point of the K-band TFR over the same period, with no change in the slope or scatter.

At higher redshifts, Cresci et al. (2009) used SINFONI to study the Hα kinematics of 18 galaxies at $z \approx 2.2$. Constructing the stellar mass TFR of the galaxies, they found an offset of -0.41 dex in stellar mass at fixed rotation velocity with respect to the local Universe. At higher redshifts still, Gnerucci et al. (2011) constructed the stellar mass TFR of 33 galaxies at $z \approx 3$, taken from the Assessing the Mass-Abundances redshift [Z] Evolution (AMAZE; Maiolino et al., 2008a) and Lyman-break galaxies Stellar population and Dynamics (LSD; Mannucci et al., 2009) surveys. They measured a much increased scatter in the relation compared to the present day. Critically, they also measured a very large offset in the zero-point of the TFR (-0.97 dex in stellar mass at fixed rotation velocity), corresponding to galaxies having ≈ 10 times less stellar mass at $z \approx 3$ than today for a fixed dynamical (i.e. total, including dark matter) mass.

The studies of the TFR at high redshifts ($z \gtrsim 1$) discussed here, as well as others (e.g. Kassin et al., 2007a,b; Förster Schreiber et al., 2009; Swinbank et al., 2012b; Sobral et al., 2013) therefore offer little consensus on whether the relation has evolved or not over the last 8–9 billion years.

1.5 This Thesis

Given the uncertainty surrounding whether the TFR has evolved since $z \gtrsim 1$, and the important implications that any measured evolution would have for galaxy evolution, there is a clear need for more expansive studies of the TFR at $z \approx 1$. Any such studies would require significantly larger galaxy samples than those of previous work at similar redshifts, and should capitalise on the recent technological advancements in multi-object integral field spectroscopy, or the increasing sophistication of instruments at other wavelengths such as radio (e.g. the Australian Square Kilometre Array (SKA) Pathfinder (ASKAP; Johnston et al., 2008), MeerKAT (Booth et al., 2009) and SKA (e.g. Dewdney et al., 2009)) and mm/sub-mm, i.e. ALMA. New studies should also aim for a careful and unbiased comparison to the $z \approx 0$ TFR, preferably measuring the $z \approx 0$ TFR in the exact same manner as the $z \approx 1$ relation. The work contained within this thesis goes some way toward fulfilling these requirements, exploring two parallel approaches and two different wavelength regimes to compare the TFRs at $z \approx 0$ and 1.

Until now it has not been possible to observe enough galaxies at $z \gtrsim 1$ to construct statistically robust samples with which to compare local samples. However, with the completion of large IFU surveys such as KROSS at high redshifts, and parallel surveys such as SAMI, MaNGA, and CALIFA already underway in the local Universe, the march of technology is now providing solutions to this long-standing problem. The work we present in Chapters 2 and 3 uses the large IFU data sets of KROSS and the SAMI Galaxy Survey to cast a more definitive light on the evolution of the TFR over the last ≈ 8 Gyr. In Chapter 2, we present the TFR of star-forming KROSS galaxies at $z \approx 1$. We construct the relation using KMOS observations of Hα emission from warm gas to measure the galaxies' rotation velocities. Chapter 3 comprises a comparison of the KROSS TFR at $z \approx 1$ and the SAMI TFR at $z \approx 0$. The latter we also construct using Hα as a kinematic tracer, first degrading the quality of the data to that of typical KROSS observations.

There is a particular benefit to using IFU observations, as opposed to slit or fibre observations, in that it allows to trace the entire two-dimensional kinematics whilst avoiding susceptibility to centering inaccuracies. With the exception of cm and mm/sub-mm interferometry, which comes with its own sets of drawbacks, this spatially-resolved information is unique to IFU observations and allows to separate those galaxies that are rotationally supported, and therefore obey the assumption of circular motion that is implicit in the TFR, from those that are pressure supported and do not. This is particularly useful when considering galaxies at $z \approx 1$, since even the disk-like galaxies among that population tend to be much more turbulent, with much reduced ratios of rotation to dispersion support compared to late-types at $z \approx 0$. In this regime, it should therefore not be taken for granted that a disk-like galaxy obeys the assumption of circular motions.

Aside from NIR IFU studies, and as mentioned in § 1.3.1.1, another increasingly viable option to measure the evolution of the TFR since $z \approx 1$ is the use of CO emission from cold molecular gas as a kinematic tracer. The use of CO emission to study galaxies at $z \gtrsim 1$ is now well established (as discussed previously). And with the ongoing operations of ALMA, the field is set to grow in the coming years. There is therefore a readily available opportunity to measure the CO TFR of galaxies at ever increasing distances, tracing the evolution of the relation out to at least $z \approx 6$–7 and, in the process, probing the associated changes in the fraction of baryonic to dark matter.

Suprisingly, to date there has been little use of CO at low-z. The earliest exploration of its use in the TFR was by Dickey & Kazes (1992), who found CO and HI line widths to be in good agreement for high signal-to-noise observations. A subsequent examination of the CO TFR in the works of Lavezzi & Dickey (1998, 1999) showed good agreement between the TFR of 59 local cluster galaxies constructed using CO linewidths and TFRs from the literature constructed using HI or Hα as kinematic tracers. The caveats to this being necessary corrections to the CO measures for turbulence and noise broadening, and the exclusion from their analysis of galaxies with CO profiles without steep flanks. Very few studies followed these initial ones and those that did dealt with similarly small numbers of galaxies. For example, Tutui et al. (2001) used CO(1-0) observations of 51 galaxies in the redshift range $0.02 < z < 0.1$ to construct the TFR in the J and H bands but only went as far in their conclusions as to highlight the potential use for the tracer at higher redshifts given the abundance of HI observations of local galaxies. More recently Davis et al. (2011, 2013, 2016) have highlighted the viability of the CO TFR for local early-type galaxies.

These studies have demonstrated that CO is a viable kinematic tracer for use in the construction of the TFR of local galaxies. However, the literature still lacks a comprehensive study of the CO TFR of a significantly large sample of local late-type galaxies to serve as a $z \approx 0$ benchmark with which to compare the inevitably large number of similar studies we can expect at high-z with the recent advent of ALMA. In Chapter 4 we address this by constructing the CO(1-0) TFR of sub-sets of $z \approx 0$ galaxies selected from the CO Legacy Database for the *GALEX* Arecibo SDSS Survey (GASS; Catinella et al., 2010) (COLD GASS; Saintonge et al., 2011). COLD GASS comprises observations of the cold molecular gas in 500 galaxies from GASS in the redshift interval $0.01 < z < 0.02$, and with stellar mass spanning $10^9 < M_*/M_\odot < 10^{11.5}$. It thus provides the means for the first definitive look at the CO TFR of local late-types. The work presented in Chapter 4 is a vital and timely first step in providing a measure of the evolution of the TFR since $z \approx 1$–3, entirely independent of IFU studies and the use of Hα as a kinematic tracer at high redshifts.

Finally, in Chapter 5, we provide concluding remarks for this thesis. We also include an outline of future research that will build upon and extend the work presented here.

Chapter 2

KROSS: The TFR at $z \approx 1$

2.1 Motivation

As discussed in Chapter 1, with the dawn of integral field spectroscopy and integral field units (IFUs) it is now possible to gain both the imaging and spatially resolved spectral information of galaxies to study their morphological, chemical, and dynamical properties and evolution in just a single observation. IFUs reveal spatially resolved information on galaxies' internal dynamics, metallicities, star formation, and stellar mass among other things. Work by surveys such as the ATLAS^{3D} Project (Cappellari et al., 2011a) to kinematically classify galaxy morphology, have arguably transformed the paradigm with which we describe the formation and evolution of (early-type) galaxies (see e.g. Cappellari et al., 2011b). More beneficial still was the advent of IFUs that operated in the near-infrared (NIR) (see e.g. Cambridge IR PAnoramic Survey Spectrograph [CIRPASS]: Parry et al. 2000; Smith et al. 2004, SINFONI: Bonnet et al. 2004), allowing a comparison between the restframe optical properties of galaxies at $z \approx 0$ with those at the peak epoch of star formation ($z \approx$ 1–2).

The leaps in understanding that single IFUs such as the Spectrographic Areal Unit for Research on Optical Nebulae (SAURON; Bacon et al., 2001) and the Spectrograph for INtegral Field Observations in the Near Infrared (SINFONI; Bonnet et al., 2004) provided are invaluable. Today, however, the study of galaxies benefits from ongoing surveys that use multi-object IFU instruments to conduct spatially resolved observations of multiple galaxies in a single exposure, significantly reducing the exposure times needed to construct large samples of IFU-observed galaxies. The K-band Multi-Object Spectrograph (KMOS; Sharples et al., 2013) Redshift One Spectroscopic Survey (KROSS; Stott et al., 2016), a joint undertaking between the University of Oxford and Durham University, is one such survey. Using KMOS, KROSS has observed 795 star-forming galaxies at $z \approx 1$ in the YJ-band. Hα was detected in 719 of those galaxies observed. 585 of these detections were resolved. KROSS has studied the spatially-resolved dynamics, star formation properties, and metallicities of these 585 galaxies.

As mentioned in § 1.3, at $z \approx 1$ we begin to probe the epoch of peak star formation in the Universe (e.g. Lilly et al., 1996; Madau et al., 1996; Hopkins & Beacom, 2006), a key era for galaxy mass assembly. It has been thought that the increased star formation rates in galaxies at intermediate redshifts is due to a larger galaxy merger rate than in the present day Universe (see e.g. Bridge et al., 2007). However there are recent theoretical claims that suggest an alternative explanation. At the epoch in question, numerical simulations predict that galaxies are being fed by constant streams of cold gas from their surroundings (Dekel et al., 2009a). These streams then induce gas instabilities, triggering star formation. Thus gas accretion has a direct and significant effect on the star formation rates of galaxies at this redshift (for a recent review see Sánchez Almeida et al., 2014). With this debate as a backdrop it is essential to constrain how the relationship between the stellar, gaseous and dark mass in galaxies has varied over cosmic time, and determine whether this is related to the global fall in star formation activity with decreasing look-back time since $z \approx 1 - 3$ (e.g. Sobral et al., 2014). This chapter employs the TFR as a useful tool with which to explore this issue.

As detailed in § 1.4, the TFR is a fundamental scaling relation describing the interdependence of luminous and dark matter in galaxies. It provides a simple means of tracing the evolution of the mass-to-luminosity ratio of populations of galaxies at different epochs. Numerous studies have examined the TFR of local (i.e. low-z) late-types (e.g. Tully & Pierce, 2000; Bell & de Jong, 2001; Masters et al., 2008; Lagattuta et al., 2013). However, the TFR at higher redshifts is less studied, and has only been the subject of very recent works (see e.g. the works of Flores et al. 2006; Puech et al. 2008 at $0.4 < z < 0.75$, Sobral et al. 2013 at $z = 0.84$, Conselice et al. 2005b; Kassin et al. 2007a,b; Miller et al. 2011 at

$z \lesssim 1.2$, Miller et al. 2012 at $1 < z < 1.7$, Förster Schreiber et al. 2009; Cresci et al. 2009 at $1.3 < z < 2.6$, and Gnerucci et al. 2011 at $z \approx 3.3$). The main hinderance to further study of the $z \gtrsim 1$ TFR until now has been the technical difficulty in observing large enough numbers of galaxies at this epoch in order to compare to large samples of local galaxies. With the use of KMOS, the KROSS survey is in a position to address this problem. In this chapter we present the K-corrected absolute K-band (M_K) and stellar mass (M_*) TFRs for the KROSS galaxies - the largest sample of galaxies of its kind at $z \approx 1$.

Circular motion is one of the main assumptions of the TFR. Thus, to maintain the validity of this assumption, we must only consider those galaxies that are predominantly rotationally supported in any comparison of TFRs. Whilst this is true of late-type galaxies in the local Universe, it is not neccessarily true of all the hotter "disky" galaxies we see at $z \approx 1$ (see e.g. Genzel et al., 2006). In this respect KROSS has the following advantages; firstly, since KROSS is an IFU survey it allows for the selection of those galaxies that are rotationally supported (as opposed to pressure supported), and thus exhibit ordered circular motions (essential for inclusion in the TFR), with much greater ease and certainty than previously possible with slit studies, for example. Secondly, such a large sample as KROSS allows us to make a meaningful comparison between the TFRs at $z \approx 1$ and the local Universe by selecting for those rotationally supported galaxies whilst maintaining a reasonable sample size. These matters are discussed further in § 2.3.5, § 2.4.3, and § 2.5. However, it can be seen from the outset that, in comparison to previous studies, KROSS, with its large sample of IFU galaxy observations, is in a strong position from which to cast a more definitive light on the evolution of the TFR over the last ≈ 8 Gyr.

This chapter is structured as follows: In § 2.2 we describe the KROSS survey and detail our methods of data acquisition and reduction using KMOS. In § 2.3 we outline the methods used to construct and fit the KROSS TFRs. We describe the velocity field modelling and discuss the extraction of M_K and M_* values via model fits to the spectral energy distributions (SEDs) of the KROSS galaxies. We also outline the selection criteria for three samples drawn from KROSS, namely the *parent* sample and sub-samples *all* and *disky*. We present the TFRs for these sub-samples in § 2.4 and compare them to existing lower and higher redshift TFR studies. Section 2.5 comprises a discussion and interpretation of the relations. Finally, in § 2.6 we give our main conclusions and outline our intentions for future work that will build and expand upon the results presented here.

A cosmology of $\Omega_\Lambda = 0.73$, $\Omega_m = 0.27$, and $H_0 = 72$ kms^{-1} Mpc^{-1} is used throughout this chapter. All magnitudes are quoted in the Vega system. All stellar masses are calculated assuming a Chabrier initial mass function (IMF), as detailed in Chabrier (2003). Masses extracted from the literature were converted to a Chabrier IMF (based on offsets taken from Madau & Dickinson, 2014) as

$$\log M_{*,\mathrm{C}} = \log M_{*,\mathrm{K}} - 0.034 = \log M_{*,\mathrm{S}} - 0.215 = \log M_{*,\mathrm{dS}} - 0.065 \quad (2.1)$$

where $M_{*,\mathrm{C}}$, $M_{*,\mathrm{K}}$, $M_{*,\mathrm{S}}$, and $M_{*,\mathrm{dS}}$ are the galaxy stellar masses calculated assuming a Chabrier, Kroupa (Kroupa, 2001), Salpeter (Salpeter, 1955), and "diet-Salpeter" (Bell & de Jong, 2001; Bell et al., 2003) IMF respectively. There are a number of differing stellar mass conversion factors used in the literature (see e.g. Karim et al., 2011; Papovich et al., 2011; Zahid et al., 2012; Speagle et al., 2014). To account for this, in this chapter we incorporate an uncertainty of ±0.06 dex in stellar mass in any measured offset between M_* TFRs where masses were originally derived assuming an IMF other than Chabrier.

2.2 The KMOS Redshift One Spectroscopic Survey: Description of the Survey

2.2.1 KMOS

KMOS (Sharples et al., 2013) is mounted on UT1 of the VLT, Cerro Paranal, Chile. As discussed in § 1.3.1.1, it consists of 24 arms that are deployable in the focal plane of the telescope over a circular area of diameter $7.'2$. Each arm has a pick-off mirror that directs the incident light to an image slicer, forming an IFU. Each IFU has a field of view $2.''8 \times 2.''8$ and divides this area into 14 slices, each acting like a classical slit. Each slice is further divided into 14 spatial pixels (spaxels). The result is 14 × 14 spaxels within the field of view, each of size $0.''2 \times 0.''2$ and each with a full spectrum associated with it.

As mentioned above, KROSS galaxies were observed with KMOS in the YJ band, which covers a wavelength range of approximately 1.02–1.36μm. Resolving power across the YJ band ranges from $R \approx 3000$ at shorter wavelengths to $R \approx 4000$ at longer wavelengths. KMOS allows for simultaneous integral field spectroscopy of 24 targets in a given field of view, and thus proves a valuable tool in conducting large surveys of the kinematic properties of galaxies over a large range of redshifts. Importantly, its wavelength range is such that galaxies at intermediate redshifts may be observed in the optical restframe (in which $z \approx 0$ galaxies have been well studied). For a more detailed description of KMOS, see the KMOS User's Manual [1].

2.2.2 Survey Aims

Using KMOS, KROSS aimed to detect the Hα emission line (redshifted in to the YJ band at $z \approx 1$) from the warm ionised gas within galaxies at $z \approx 1$. Combined with other emission lines, such as the [NII] doublet ([NII]6548 and [NII]6583), the internal dynamics of the galaxies can be studied along with other properties such as their chemical abundances, star formation rates, and ionisation mechanisms.

Now complete, KROSS has observed 795 star-forming galaxies at $0.8 < z < 1$. For a detailed description of the sample selection and statistics see Stott et al. (2016). Here we give a brief summary. The sample of galaxies was selected using a magnitude cut $K < 22.5$, and a colour cut r-$z < 1.5$. These selections were made with the intention of selecting so-called "blue cloud" galaxies (see Bell et al., 2004), characterised by their blue colour and ongoing star-formation. Some fainter, redder, more passive (or dusty) galaxies were also included in the sample selection, but these were given a lower priority for observations. Target galaxies for KROSS are spread between several fields, namely the Extended *Chandra* Deep Field-South Survey (ECDFS) field, the Special Selected Area field (SA22), the COSMOlogical evolution Survey (COSMOS) field, and the UKIRT Infrared Deep Sky Survey (UKIDSS) Ultra Deep Survey (UDS) field. KROSS detected Hα in 719 galaxies. As mentioned, 585 of these detections were resolved.

---

[1] `https://www.eso.org/sci/facilities/paranal/instruments/kmos/doc.html`

2.2.3 Data Reduction

For a detailed description of the reduction process see Stott et al. (2016). Here we present a summary.

The ESO Recipe EXecution tool (ESOREX) and the Software Package for Astronomical Reduction with KMOS (SPARK) pipeline (Davies et al., 2013) were utilised in order to reconstruct the datacube from each IFU observation. The pipeline performs initial corrections to the data using dark, flat, and arc frames, as well as an additional illumination correction. A telluric correction to each observation was made using an observed standard star. Observations were taken in an ABAABA nod-to-sky pattern, where A represents time on source, and B time on sky. Upon reconstruction of the datacubes, each AB pair was then further reduced separately.

An initial A-B sky subtraction was made of the cubes, using the temporally closest sky. Following this an attempt was made to remove any remaining residual sky using a designated sky cube per spectrograph, constructed by median combining all of the (8) A-B cubes per spectrograph. This “sky” cube was further median-collapsed to a single spectrum, reducing the noise between sky emission lines, and subtracted from the spectrum of each spaxel in the A-B cube. The reduced cubes of the same object from several observations were then combined via a 3-sigma-clipped average, using the FITS file header information for alignment.

To determine the accuracy of the wavelength calibration, the positions of four bright sky emission lines (well-spaced along the KMOS YJ bandpass) were compared across 35 reconstructed sky (i.e. B) frames from three separate observing runs carried out over a three year duration. For each frame the position of the sky emission line in each spaxel of each of the reconstructed cubes was determined from the central position of the best fit Gaussian to the line emission (see § 2.3.1 for a description of the fitting process); measurements were performed on a total of 613872 spectra across 783 reconstructed data cubes. The accuracy of the wavelength calibration was then taken as the standard deviation of the distribution of the position measurements, calculated to be 6 km s^{-1}.

In the nod-to-sky pattern the sky (i.e. B) frames are temporally separated by two source (i.e. A) frames. It is thus difficult to *directly* measure the sky subtraction accuracy using the method described above. However, an estimate may be made by subtracting from one sky frame the (temporally) closest neighbouring sky frame in the observing pattern. The residual sky signal may then be removed in the manner described above, again constructing a designated "sky" cube, and then spectrum, per spectrograph (this time from B-B cubes). This method was applied to a sky frame from each mask observed over the three aforementioned observing runs. The median flux (excluding bright line emission) in each of the 268 sky-subtracted (sky) cubes across the 11 sky frames sampled was compared to the median flux in the corresponding original (un-subtracted) sky cube, and the fractional difference between the two calculated. The median sky subtraction accuracy across all the cubes was determined to be 1 ± 1 percent (taking the uncertainty as the median absolute deviation from the median itself). One would expect the accuracy to improve beyond this if the two initially subtracted sky frames were temporally closer, as is the case for the A-B subtractions described above.

2.3 Constructing the KROSS TFRs

2.3.1 Modelling Velocity Fields

The velocity fields of the KROSS galaxies in this chapter were constructed and modelled by Stott et al. (2016). Here we summarise the method. Essentially, after re-gridding the KROSS cube (to give 28 × 28 spaxels, each with an area $0\farcs1$ squared), we simultaneously fit the Hα, [NII]6548, and [NII]6583 emission lines in each spaxel with three Gaussians. The fit uses the Levenberg-Marquardt technique to perform an uncertainty weighted, least-squares minimisation between the data and model. The intensity, central velocity and width of each of the Gaussians are left as free parameters, however the central velocity and width of the Hα and [NII] lines are coupled. If the Hα signal-to-noise ratio, $S/N < 5$ in a given $0\farcs1 \times 0\farcs1$ spaxel, we consider a larger area of $0\farcs3 \times 0\farcs3$. If the S/N is still insufficient the area is enlarged again to $0\farcs5 \times 0\farcs5$ and finally $0\farcs7 \times 0\farcs7$. If there is still insufficient signal we then exclude the spaxel from the velocity field. We construct the velocity fields by plotting the mean line-of-sight velocity in each spaxel , as determined from the best Gaussian fit to the

Hα emission. We plot all velocities relative to the systemic recession velocity calculated from the known spectroscopic redshift (taken from various surveys, see Table 1 of Stott et al., 2016). We also construct Hα flux maps by integrating the line-of-sight velocity distribution in each spaxel.

We model the velocity fields using a two-dimensional modification of the well known Courteau (1997) arctangent disk model for galaxy rotation curves, given as

$$V(r) = \frac{2}{\pi} V_{\mathrm{max}} \arctan\left(\frac{r}{r_{\mathrm{dyn}}}\right) \ , \tag{2.2}$$

where $V(r)$ is the rotation velocity at radius r, V_{max} is the rotation velocity at infinite radius, and r_{dyn} is the characteristic radius associated with the arctangent turn over. In practice we fit a model with seven parameters to the velocity field. The parameters include (x_0,y_0) (the dynamical centre in x and y spaxel space), the position angle ϕ, inclination i, r_{dyn}, and V_{max}. We also include a systemic velocity parameter V_0, which allows for a best-fit systemic recession velocity that differs from that calculated from the known spectroscopic redshift. We constrain the dynamical centre to lie within $0\overset{''}{.}7$ (equivalent to the typical seeing of KROSS observations) of the peak of the Hα integrated flux. We define the line-of-sight velocity at each spaxel as

$$V = V_0 + (\sin i \cos\theta V(r)) \ , \tag{2.3}$$

where

$$\cos\theta = \frac{(\sin\phi(x_0 - x)) + (\cos\phi(y - y_0))}{r} \ , \tag{2.4}$$

and the radial distance from the dynamical centre for each spaxel is given as

$$r = \sqrt{(x - x_0)^2 + \left(\frac{y - y_0}{\cos i}\right)^2} \ . \tag{2.5}$$

We use a genetic algorithm (Charbonneau, 1995) to find the best fitting model.

As an example, Figure 2.1 shows three observed velocity fields that are well modelled

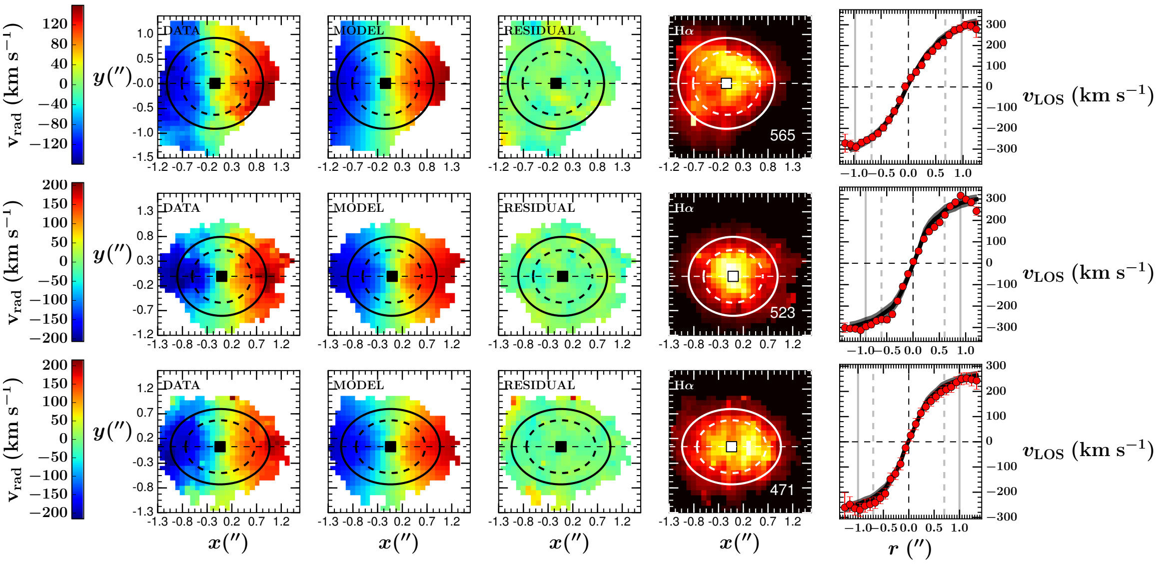

Figure 2.1: Three examples of KROSS galaxy velocity fields that are well modelled by the Courteau (1997) arctangent function. For each galaxy the observed ("DATA") and best fitting model ("MODEL") velocity fields are displayed (with $0''.1 \times 0''.1$ spaxels) along with the residual ("RESIDUAL") between the two. Also included is the associated integrated Hα flux map ("Hα"), constructed by integrating the line-of-sight velocity distribution in each spaxel. The dashed and solid ellipses, centred on the dynamical centre of the best fitting model velocity field, contain 50% and 80% of the total Hα flux respectively. The axial ratio of the ellipse is determined by initially fitting a two dimensional Gaussian to the entire flux map. On the far right, we display the extracted rotation curve (red points) from the inclination corrected observed velocity field. This is constructed by extracting velocities from each pixel along a $0''.7$ ($\approx$the typical seeing) wide strip, in $0''.1$ spaxel steps, along the position angle axis (horizontal in each map). Each spaxel's velocity is corrected for inclination. We also plot the rotation curve extracted from the corresponding model velocity field as a solid black line. We include the $\pm1\sigma$ bootstrap uncertainties from the model as a shaded grey region. These reflect the 1σ uncertainty in V_0, $V_{\rm max}$, and $r_{\rm dyn}$ of the model. Further, we include r_{50} and r_{80} as the vertical dashed and solid grey line respectively. It should be stressed that the black curve is not a fit to the extracted rotation curve but rather it is the curve extracted from the best fitting model field. Both the observed and model rotation curve are plotted only for reference. The KROSS galaxy ID is included at the bottom right of the Hα map. It should also be noted that the extracted rotation curve is more susceptible to noise within the data. In this respect, the residual map is a much clearer indicator of the quality of the arctangent model fit.

by the arctangent function, the corresponding model fields, as well as the associated Hα flux maps. For illustration purposes we also display rotation curves extracted from the corresponding observed and model fields along the position angle axis of the galaxy. The same plot for each of the 56 KROSS galaxies in a *disky* sub-sample (see § 2.3.5 for sub-sample selection) is shown in Figure A.2.

2.3.2 Extracting Rotation Velocities

To construct the KROSS TFRs we must first define and measure a characteristic velocity measure for each galaxy. Whilst the simple Courteau (1997) arctangent disk model used in this chapter is a satisfactory description of a disk-like galaxy's rotation curve, it is clear that the asymptotic velocity, $V_{\rm max}$ has little physical meaning; considering the finite spatial extent of the Hα emission (that constrains the model) it is obvious that, in all cases, a small change to the extrapolated velocity curve can lead to large changes in $V_{\rm max}$. It is therefore sensible to extract a velocity at a more physically motivated choice of radius. We note that the characteristic radius, $r_{\rm dyn}$ in the arctangent model defines only where the arctangent curve begins to turn over and has no direct relation to the mass distribution of the galaxy or the corresponding radius at which the rotation curve becomes flat. It is therefore not a suitable choice.

In choosing a better-suited radius we must consider two important factors. First, we must make our velocity measure at a radius that samples a galaxy's rotation curve at or beyond the turnover in order to probe the majority of its (dynamical) mass and avoid the rapidly changing inner parts of the curve. Second, we must take our velocity measure at a radius that the Hα emission in KROSS galaxies samples in a majority of cases. Previous studies have measured velocities at a circular radius containing 80% of the red (e.g. i-band) stellar light (see e.g. Pizagno et al., 2007). For an exponential disk, this radius corresponds to 3.03 times the disk scale radius and is thus a well motivated choice, physically. We would therefore proceed in extracting velocities from the KROSS velocity fields in a similar manner. However, the KROSS sample lacks a homogeneous set of high resolution near-infrared imaging for the stellar light of the galaxies. The signal-to-noise of continuum detections is also insufficient in the majority of KROSS cubes to reliably measure the galaxy size. These measurements are subject to improvement in Chapter 3, in which we make use of new measures of KROSS galaxy sizes (and photometric centres) from Harrison et al. (in preparation). In this chapter, we instead return to the Hα emission for which we have emission maps for all the KROSS galaxies.

We extract a rotation velocity, V_{80} for each galaxy from the best fitting arctangent model at a radius equal to the major axis of an ellipse containing 80% of the total integrated Hα flux, r_{80}. Naively, there is little reason to expect the spatial distribution of the Hα emission to correspond to the underyling mass distribution, as is true with the red stellar continuum light. However, previous studies have shown that the radial extent of Hα emission in galaxies at $z \approx 1$ is in agreement, or slightly more extended than the stellar light; Nelson et al. (2012) find $< r_e(\mathrm{H}\alpha)/\mathrm{r_e(R)} >= 1.3 \pm 0.1$ for a sample of 57 galaxies at $0.8 < z < 1.3$ selected from the 3D-*HST* grism survey (Brammer et al., 2012; van Dokkum et al., 2011), where $r_e(\mathrm{H}\alpha)$ and $r_e(R)$ are the Hα and R-band effective radius respectively. We determine r_{80} by growing ellipses (on the model integrated flux maps) outwardly from the best fitting dynamical centre. The ellipses from which we measure r_{80} are included in the plots of Figures 2.1 and A.2. For reference, for each galaxy we also include an additional ellipse with a semi-major axis r_{50}, that contains half of the integrated Hα flux. The axial ratio of the ellipse is determined by initially fitting a two dimensional Gaussian to the entire flux map, such that the ellipse reflects the overall spatial shape of the Hα emission.

2.3.3 Hα: Additional Tests

Despite the overall light distribution of Hα generally agreeing with the red stellar continuum, Hα emission traces the ongoing star formation in galaxies and thus tends to be more clumpy than the continuum light, particularly at $z \gtrsim 1$ as demonstrated from the model KROSS Hα maps (see Figures 2.1 and A.2). In some cases, the best fitting dynamical centre is displaced with respect to the peak of the integrated Hα flux. Here there is the potential for the value of r_{80} to be at odds with the radius containing 80% of the stellar continuum light. This will introduce scatter to the KROSS TFR.

To investigate this further, for those galaxies for which we are able to measure at least a continuum centre (i.e. the position of the peak of the continuum, extracted from the

KROSS cubes), we compare the difference between the dynamical centre as derived from the modelling of the velocity fields to the continuum centre. We find that in most cases the dynamical and continuum centres agree within $0.''3$. The typical seeing radius of any given KROSS observation is $\approx 0.''35$ (only 1.5 spaxels in the original KMOS spaxel scale of $0.''2$). We also measure no significant change in the scatter of the TFR for a sub-sample of KROSS galaxies (sub-sample *all*, see § 2.3.5) after excluding those galaxies with dynamical centres that differ from the continuum centre by more than $0.''3$. We are therefore satisfied that our measurements of the KROSS TFRs are not significantly improved by forcing the dynamical centres of the model velocity fields to be coincident with the continuum centres. In light of this, and since continuum centre values are not available for all 585 KROSS galaxies with resolved Hα, we thus proceed with the analysis using the best fitting model velocity fields.

In the same vein, in Appendix A.1 we also consider the effect those systems with asymmetric rotation curves (i.e. systems for which the Hα emission extends up to or beyond r_{80} on only one side of the rotation curve) have on the TFR scatter. One might expect the asymmetry in these systems to reduce the accuracy to which the dynamical centre may be determined. However, we show that exclusion of these systems from a sub-sample of KROSS galaxies (sub-sample *all*, see § 2.3.5) does not significantly change the scatter in the TFR. We therefore proceed with the analysis including all galaxies with Hα emission that extends up to or beyond r_{80} on at least one side.

2.3.4 SED fitting: Stellar Masses and Absolute Magnitudes

M_K and M_* were derived by finding comparing a suite of model spectral energy distributions (SEDs) to the observed SED of each of the KROSS galaxies using the HYPERZ (see Bolzonella et al., 2000) and LE PHARE (see Arnouts et al., 1999; Ilbert et al., 2006) fitting routines (the former is used to maintain homogeneity with Stott et al. 2016 but does not compute absolute magnitudes). As detailed in § 2.2.2, KROSS comprises targets from the fields of several large extragalactic surveys. As such there is extensive multi-wavelength photometry available for KROSS galaxies. We used images spanning (where available) the optical to mid-infared (U, g, B, V, R, I,z, J, H, K, and IRAC *ch*1–*ch*4; Cirasuolo et al., 2007; Lawrence et al., 2007; Hambly et al., 2008; Williams et al., 2009; Cardamone et al., 2010; Kim et al., 2011; Muzzin et al., 2013; Simpson et al., 2014; Sobral et al., 2015), comprising data taken predominantly from the Canada-France-Hawaii Telescope Legacy Survey (CFHTLS; Gwyn, 2011) and the Multiwavelength Survey by Yale-Chile (MUSYC; Gawiser & MUSYC Collaboration, 2003) in the optical, depending on the field. The near-infrared photometry comprises Wide-field InfraRed Camera (WIRCam; Puget et al., 2004) observations and data from UKIDSS, whilst the mid-infrared photometry is derived from imaging from the Infrared Array Camera (IRAC) for the *Spitzer* Space Telescope (Fazio et al., 2004). For a full description of the catalogs utilised for each field see Swinbank et al. (2016, in preparation.). Each fitting routine generates model SEDs from the Bruzual & Charlot (2003) stellar population synthesis models. We fit for extinction, metallicity, age, star formation, and stellar mass. Both routines allows for three main types of star formation history, namely a ‘single burst’, an exponential decline, or a constant/“boxy” star formation.

We note that we do not directly observe the rest-frame K-band for all of the KROSS galaxies; in such cases the K-band K-corrections may suffer from an added degree of uncertainty. Throughout this chapter we adopt a uniform stellar mass uncertainty of ±0.2 dex.

2.3.5 Defining Sub-Samples

Of the 585 KROSS galaxies with resolved Hα emission, we define a *parent* sample, for the purposes of this work, of 251 galaxies that were detected in Hα, have a non-zero rotation velocity (derived in the manner described in § 2.3.2), with a fractional uncertainty $\Delta_{V_{80}}$ / $V_{80} < 0.3$, and associated M_K and M_* values from SED fits. To ensure that those galaxies included in the *parent* sample are at least moderately well described by our simple arctangent model (i.e. have some disk-like rotation) we use an R^2 goodness of fit test (applied to the two-dimensional fit the velocity field), requiring for each galaxy that

$$R^2 \geq 85\% \ . \tag{2.6}$$

The choice of R^2 is subjective but was chosen to remove those galaxies for which the arctangent model is a “bad” fit whilst maintaining a reasonable sample size.

Of these 251 galaxies, 26 galaxies have Hα emission which does not extend out to, or beyond, r_{80}. Inclusion of these galaxies will introduce scatter in to the TFR as a result of extracting a velocity extrapolated from the model rotation curve, beyond the data. For this reason we exclude them, leaving 225 galaxies. Similarly, we also exclude a further 6 galaxies for which the best fitting dynamical centre is completely spatially offset from any Hα emission (i.e. the dynamical centre falls within a spaxel corresponding to a Hα $S/N < 5$ and that same spaxel is not contained within the largest contiguous region of Hα emission with $S/N \geq 5$ in the Hα flux map, this as judged by eye) as the best fitting models in these cases are obviously poorly constrained by the data. This leaves a total of 219 galaxies.

To avoid making large inclination corrections to the extracted galaxy rotation velocities, and in keeping with previous studies (see e.g. Meyer et al., 2008; Stark et al., 2009), we make a further cut such that the inclination $i > 25^o$, excluding an extra 4 galaxies – leaving 215.

Lastly, we employ KINEMETRY[2] (Krajnović et al., 2006) in order to exclude any major-merger candidate systems following the prescription of Shapiro et al. (2008). See Stott et al. (2014) for a previous application of KINEMETRY to KMOS data. Briefly, KINEMETRY describes the moment maps (e.g. surface brightness, velocity map, sigma map) of a given galaxy as a series of concentric ellipses of increasing radii, each with a common centre but with individual position angles and inclinations. The series of ellipses describing a moment, K can be expressed as

$$K(a,\psi) = A_0(a) + \sum_{n=1}^{N} k_n(a)\cos[n(\psi - \phi_n(r))] \ , \tag{2.7}$$

where a is the semi-major axis of each ellipse, ψ is the azimuthal angle in the plane of the galaxy, A_0 is the systemic velocity of each ellipse. The amplitude and phase coefficients are given as

$$k_n = \sqrt{A_n^2 + B_n^2} \quad \text{and} \quad \phi_n = \arctan(A_n/B_n) \ , \tag{2.8}$$

---

[2] KINEMETRY for IDL `http://davor.krajnovic.org/idl/`

where A_n, B_n are ("kinemetry") constants.

Each moment map can therefore be described by the values of A_n, B_n, and the orientations and semi-major axes of the ellipses. Further, different orders of each of the coefficients describe different characteristics of the map. Specifically for velocity maps, B_1 describes the bulk rotational motion of the galaxy i.e. for a perfect thin disk B_1 describes the entire motion of the map; any non-zero higher order coefficients (i.e. $A_1, A_2, B_2, A_3, B_3, ...$) represent non-circular motion. Similarly, the only non-zero kinemetry cofficient in the dispersion map of a perfect thin disk is A_0. Therefore, higher order (i.e. $n = 1, 2, 3, 4, 5, ...$) coefficients here also represent deviation from circular motion.

Shapiro et al. (2008) used these higher orders to quantify the assymetry of the Hα dynamics of high-redshift star-forming galaxies, in order to distinguish between major mergers and rotating disks. They excluded A_1 from their analysis since it can represent inflows/outflows into/from a galaxy, usually a result of stellar winds or AGN - not major mergers. They defined the asymmetry $v_{\rm asym}$, and $\sigma_{\rm asym}$ of a galaxy's velocity and sigma map respectively as

$$v_{\rm asym} = \left\langle \frac{k_2 + k_3 + k_4 + k_5}{B_{1,v}} \right\rangle_r \ , \tag{2.9}$$

and

$$\sigma_{\rm asym} = \left\langle \frac{k_1 + k_2 + k_3 + k_4 + k_5}{B_{1,v}} \right\rangle_r \ , \tag{2.10}$$

where $B_{1,v}$ is the B_1 kinemetry coefficent of the velocity map and the average is over all radii, r of the kinemetry ellipses. Using templates of high-redshift disks and mergers they defined an empirical delineation such that major mergers obeyed

$$K_{\rm asym} = \sqrt{v^2_{\rm asym} + \sigma^2_{\rm asym}} > 0.5 \ . \tag{2.11}$$

From our sample we exclude 5 systems with a kinemetry asymmetry parameter, $K_{\rm asym} > 0.5$. We hereon refer to the remaining 210 galaxies as sub-sample *all*.

Next, we define a further *disky* sub-sample that contains only those galaxies from sub-sample *all* that are primarily rotationally supported. The KROSS sample will contain a number of galaxies that can be deemed disk-like but that are much more turbulent and chaotic than the spiral galaxies we see in the local Universe (see e.g. Förster Schreiber et al., 2006b; Swinbank et al., 2012a; Stott et al., 2016). So whilst these galaxies may have disk-like structures and significant rotational support, they are also likely to have significant dispersion support as well. Since the TFR assumes circular motion and relies on the assumption that the galaxies in question are rotationally supported, we define a ratio of rotation to dispersion support, V_{80}/σ in order to exclude those galaxies that violate the assumption of circular motion. The intrinsic velocity dispersion σ is the flux weighted average value of the velocity dispersion map of each galaxy, after correcting for the instrumental resolution and local velocity gradient from beam smearing (see Stott et al. 2016 for more details).

A cut was made to sub-sample *all* such that $V_{80}/\sigma > 3$ in order to select galaxies that were predominantly rotationally supported (the choice of which value of V_{80}/σ to cut by is discussed in § 2.4.3.2). The resultant *disky* sub-sample contains 56 galaxies. This may seem a large reduction in the number of galaxies from the *parent* sub-sample to the *disky* sub-sample but the cut is vital in order to ensure validity in any measured evolution between the TFRs at $z \approx 1$ and $z \approx 0$ i.e. in order to compare $z \approx 1$ TFRs to $z \approx 0$ TFRs, we must select for the minority of galaxies within KROSS that are significantly rotation dominated. This is an issue that has not been sufficiently addressed in previous studies and is discussed further in § 2.4.3 and § 2.6.

A summary of the selection criteria for the samples and sub-samples defined in this chapter is given in Table 2.1, along with the number of galaxies in each.

The distributions of V_{80}, M_K, and M_* for the *parent* sample, sub-sample *all*, and the *disky* sub-sample can be seen in Figure 2.2. To quantify any biases between the distributions we conducted a Kolmogorov-Smirnov (K-S) two-sample test between the *parent* sample and sub-samples *disky* and *all*. We define a null hypothesis that the two samples in question are drawn from the same distribution. We reject the null hypothesis if the p-value, $p < 0.05$. The resultant p-values can be seen in Table 2.2.

It can be seen from Figure 2.2 that the width of the M_K and $\log(M_*/M_\odot)$ distributions,

Sample	$N_{\rm gal}$	Selection
parent	251	Detected in Hα, $V_{80} > 0$, $\Delta_{V_{80}}/V_{80} < 0.3$, $R^2 \geq 85\%$, M_K and M_* from SED fitting
all	210	Member of *parent*, sufficient Hα radial extent, dynamical centre coincident with Hα emission, $i > 25^o$, $K_{\rm asym} \leq 0.5$
disky	56	Member of *all*, $V_{80}/\sigma > 3$

Table 2.1: A summary of the selection criteria for samples and sub-samples defined in Chapter 2.

Distribution	*parent* vs. *all*	*parent* vs. *disky*
M_K	1.00	0.708
logM_*	1.00	0.618
V_{80}	0.999	1.99×10^{-6}

Table 2.2: p–values for Kolmogorov-Smirnov (K-S) two-sample tests between the *parent* sample and sub-samples *disky* and *all*. The null hypothesis is that the two samples in question are drawn from the same distribution. The null is rejected for $p < 0.05$.

and the positions of their peaks remain approximately constant between the *parent* sample and sub-samples *all* and *disky*, the only difference being the number of galaxies in each sample, and a moderate truncation in the range of stellar masses and absolute magnitudes for the *disky* sub-sample distributions compared to the corresponding distributions for the *parent* sample and sub-sample *all*. Correspondingly, Table 2.2 shows that for the M_K and log $(M_*/M_\odot)$ distributions, we do not reject the null hypothesis that both *parent* and *all*, and *parent* and *disky* are drawn from the same distribution. Considering the distribution of V_{80}, the average value remains roughly constant between the *parent* sample and sub-sample *all*. However there is an apparent increase in the average between sub-sample *all* and sub-sample *disky*. This is confirmed in Table 2.2, where it can be seen that we reject the null hypothesis that the V_{80} values of *parent* and *disky* are drawn from the same distribution. This is in line with expectation as the *disky* sub-sample comprises only those galaxies that are predominantly rotationally supported, with inevitably higher values of V_{80} on average than galaxies that are more dispersion dominated.

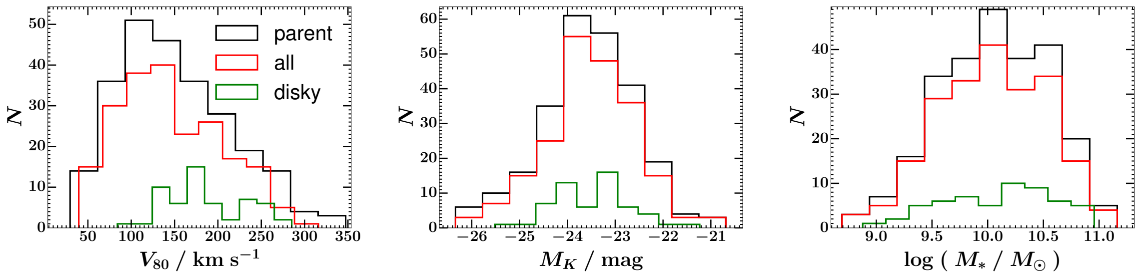

Figure 2.2: Distributions of V_{80}, M_K, and $\log(M_*/M_\odot)$ for the KROSS *parent* sample, and sub-samples *all* and *disky*. The width, and the position of the peak of all three distributions remain approximately constant between the *parent* sample and sub-sample *all*. Considering the *disky* sub-sample it can be seen that the peak position remains relatively constant in comparison to the *parent* sample and sub-sample *all* in both the M_K and $\log(M_*/M_\odot)$ distributions. However, the *disky* sub-sample is biased towards higher values of V_{80} than the *parent* sample and sub-sample *all*.

2.3.6 Fitting the TFR

We find the best forward and reverse straight line fits to each of the TFRs presented in this chapter using a Markov chain Monte Carlo (MCMC) minimisation technique, with EMCEE[3] (Foreman-Mackey et al., 2013) in PYTHON. The familiar forward fit minimises

$$\chi^2_{\rm for} \equiv \sum_i \left(\frac{1}{\sigma_i^2}\right) \{y_i - [m(x_i - x_0) + b]\}^{\ 2} \ , \tag{2.12}$$

where x_i and y_i are respectively the velocity and flux datum, x_0 is a “pivot” point chosen to minimise the uncertainty in the straight line intercept b (in practice we set x_0 to the median value of the x_i), m is the straight line gradient, and the sum is over all sample galaxies. σ_i is defined as

$$\sigma_i^2 \equiv \sigma_{y,i}^2 + m^2\sigma_{x,i}^2 + \sigma_{\rm int}^2 \ , \tag{2.13}$$

where $\sigma_{y,i}$ and $\sigma_{x,i}$ are respectively the uncertainty of an individual data point in y and x, and $\sigma_{\rm int}$ is a measure of the intrinsic scatter in the Tully-Fisher relation, determined by adjusting its value such that $\chi^2_{\rm for}/{\rm DOF} = 1$, where DOF is the number of degrees of freedom. It should be stressed that this measure is highly dependent on the accuracy of $\sigma_{x,i}$ and $\sigma_{y,i}$. As such, it is better thought of as the scatter unaccounted for by uncertainties.

---

[3] `http://dan.iel.fm/emcee/current/`

The total scatter in the relation is then

$$\sigma_{\mathrm{tot}}^2 = \frac{\chi_{\mathrm{for}}^2}{\sum\limits_i (1/\sigma_i^2)} \ . \tag{2.14}$$

For the reverse fit, the figure of merit to minimise is

$$\chi_{\mathrm{rev}}^2 = \sum_i \left(\frac{1}{\zeta_i^2}\right) \left[x_i - (My_i + B + x_0)\right]^2 , \tag{2.15}$$

where similarly M and B are respectively the gradient and intercept of the straight line and

$$\zeta_i^2 \equiv \sigma_{x,i}^2 + M^2 \sigma_{y,i}^2 + \zeta_{\mathrm{int}}^2 \ . \tag{2.16}$$

ζ_{int} is again the intrinsic scatter, determined such that $\chi_{\mathrm{rev}}^2/\mathrm{DOF} = 1$. The total scatter is then

$$\zeta_{\mathrm{tot}}^2 = \frac{\chi_{\mathrm{rev}}^2}{\sum\limits_i (1/\zeta_i^2)} \ . \tag{2.17}$$

The reverse fit parameters can be directly compared to the forward fit parameters by defining the equivalent slope, intercept, intrinsic scatter and total scatter as $m' \equiv 1/M$, $b' \equiv -B/M$, $\sigma'_{\mathrm{int}} \equiv M\zeta_{\mathrm{int}}$ and $\sigma'_{\mathrm{tot}} \equiv M\zeta_{\mathrm{tot}}$, respectively (Williams et al., 2010). Since the values of ζ_{tot} or ζ_{int} represent respectively the total and intrinsic scatter in $\log(V_{80})$, we do not tabulate the equivalent forward fit values but instead report them directly.

In all cases the best reverse fit slope was significantly (i.e. greater than three times the 1σ uncertainty) steeper than that of the forward fit. Given the comparable magnitude of uncertainty in both the abscissa ($\log V_{80}$) and ordinate (M_K and $\log(M_*)$) values of the TFRs presented in this chapter, we choose to favour neither the best forward fit nor the best reverse fit and instead take the bisector of the two as our best measurement of the TFR in each case.

2.4 Results

The M_K, and M_* TFRs for sub-sample *all* and the *disky* sub-sample can be seen in Figures 2.3 and 2.4 respectively. The corresponding free fit parameters are presented in Table 2.3, while Table 2.4 presents the best fit parameters for the case where the slope of the fit to each KROSS sub-sample (and several samples taken from the literature) is fixed to the local Universe value (see § 2.4.1 and § 2.4.3). Uncertainties are quoted at a 1σ level. Uncertainties in the TFR offsets between KROSS and the $z \approx 0$ comparison sample include the uncertainty in the $z \approx 0$ TFR zero-point and in converting between stellar masses calculated assuming different IMFs.

2.4.1 Comparing to the Local Universe

In each TFR plot a $z \approx 0$ relation is displayed for comparison, however it should be stressed that caution must be taken when directly comparing these with the KROSS relations. When comparing the TFR between any two samples of galaxies it is very important to consider the systematic bias that may be introduced as the result of the methods of measurement used. This is less of a problem when comparing absolute magnitudes and stellar masses as these are, by definition, corrected for redshift, extinction etc. However when considering the measure of a galaxy's rotation it can pose a problem. For example, the difference between a galaxy's rotation inferred from an IFU observation and a long slit observation may be significant (e.g. Förster Schreiber et al., 2006b); factors such as slit orientation, resolution, and sensitivity could all introduce bias to the measured rotation. Similarly, the choice of emission line used to trace the gas dynamics is also significant as different lines trace different phases of the gas, which may each extend out to different radii within a galaxy. Some lines suffer more absorption by dust in the line of sight than others (e.g. [O II] is more affected by dust than Hα, Aragón-Salamanca et al. 2003). As an attempt to account for their effect on the measured zero-point of the $z \approx 0$ comparison relations we combine the data from several studies from the literature, which use different measures of galaxy rotation and samples of galaxies from a range of different environment. We then compare the KROSS TFR to the best (free) fit relation of the combined $z \approx 0$ data.

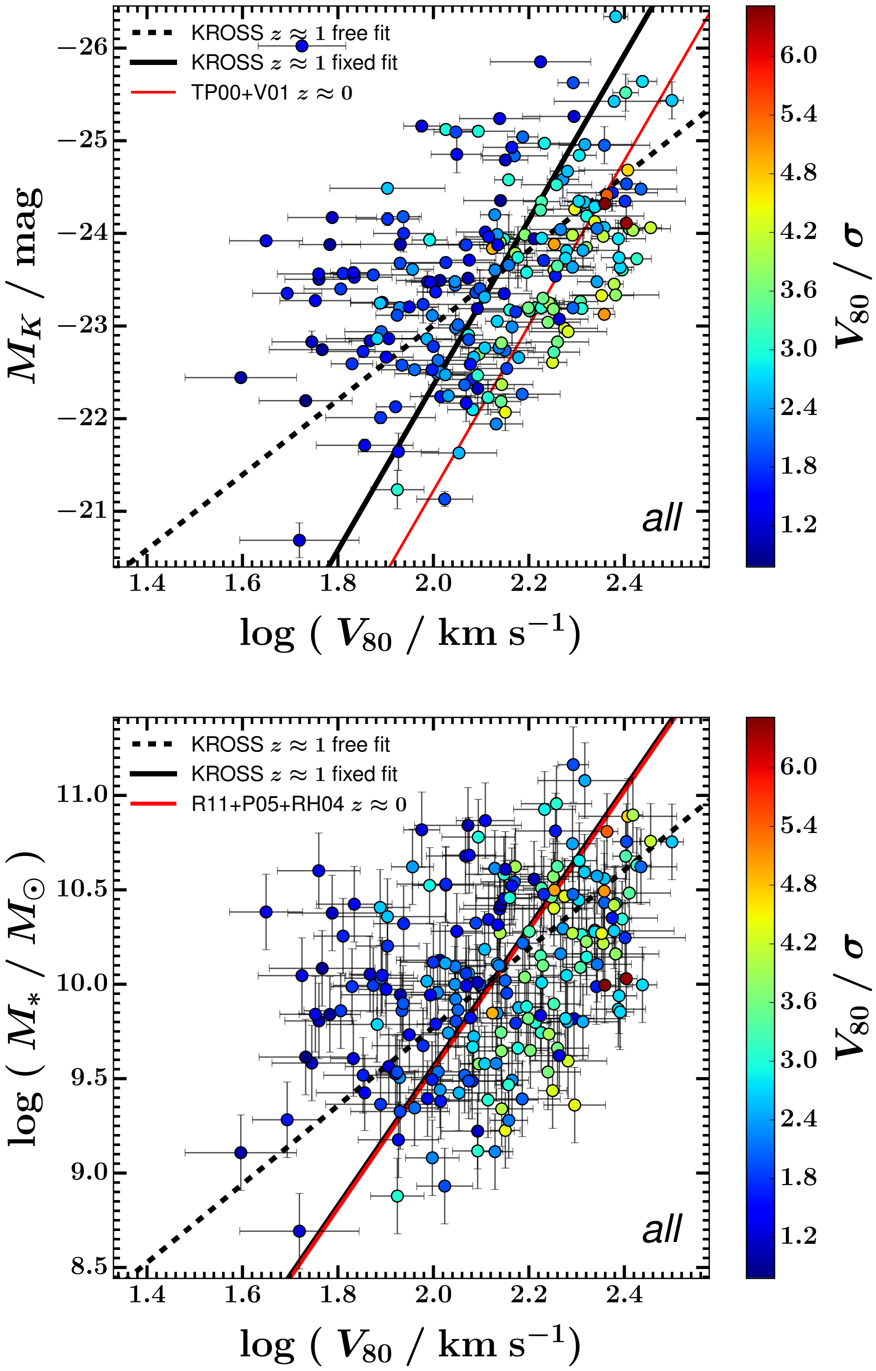

Figure 2.3: The M_K and M_* TFRs for sub-sample *all* as described in § 2.3.5. Displayed is the bisector of the best forward and reverse fits to the data, as well as the best fit when the slope is constrained to that of a $z \approx 0$ comparison sample (as described in § 2.4.1). The data points are colour-coded by their corresponding values of V_{80}/σ. Those data points with correspondingly high values of V_{80}/σ follow a tighter relation than those with lower values. The higher V_{80}/σ points are coincident with the $z \approx 0$ relation in the case of the M_K TFR. For the stellar mass TFR the same points are offset to lower values of $\log(M_*/M_\odot)$, for a given value of V_{80}, in comparison to the $z \approx 0$ relation. Those with lower V_{80}/σ tend to be scattered to lower values along the abscissa of the plot. These may correspond to systems with more dispersive motions and lower rotation velocities.

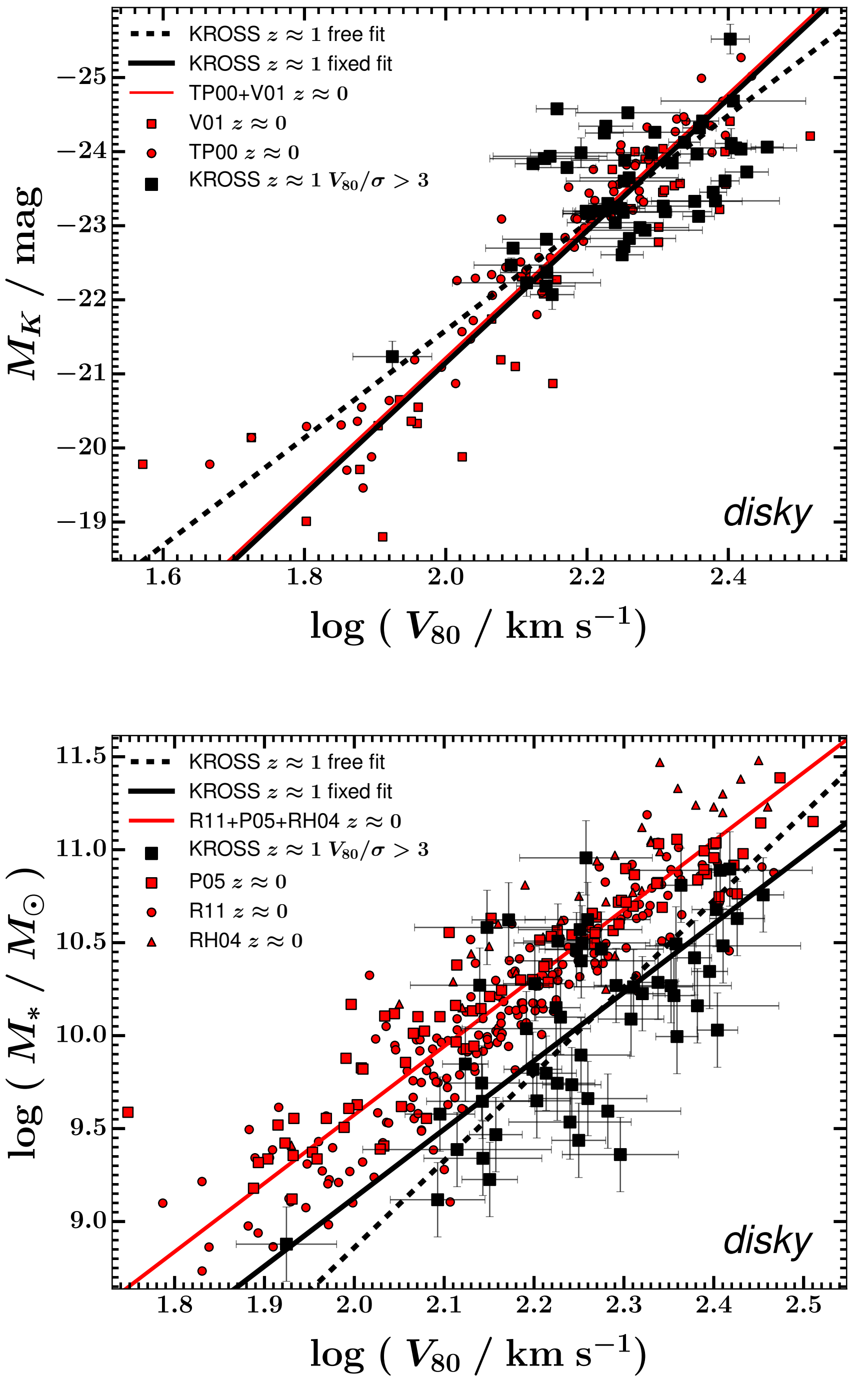

Figure 2.4: The M_K and M_* TFRs for the *disky* sub-sample as described in § 2.3.5. Displayed is the bisector of the best forward and reverse fits to the data, as well as the best fit when the slope is constrained to that of a $z \approx 0$ comparison sample (as described in § 2.4.1). There is a clear offset between the KROSS and the $z \approx 0$ M_* TFRs. Conversely, the zero-point of the KROSS M_K TFR is in agreement with that of the $z \approx 0$ comparison relation.

The M_K comparison relation comprises data from Tully & Pierce (2000, TP00), who use the linewidth of the integrated HI emission profile of galaxies from a range of cluster environments to derive their rotation velocity; and Verheijen (2001, V01), who use integrated HI profiles and HI rotation curves for a volume limited sample of late-type galaxies in the Ursa Major Cluster.

The M_* comparison relation comprises the data of Pizagno et al. (2005, P05), who use rotation velocities derived from long slit spectroscopy of Hα emission, Reyes et al. (2011, R11), who use long slit spectroscopy of Hα emission from a sub-sample of a large sample of disk galaxies selected from the Sloan Digital Sky Survey Data Release 7 and Rhee (2004, RH04), who re-analyse the optical emission line rotation curves of the Kent (1986) sample of Sb and Sc spiral galaxies.

Aside from using a composite $z \approx 0$ sample, the obvious solution is to use the same measurement of rotation for all galaxy samples considered for comparison. In this way, if there is systematic bias introduced as a result of the measurement method, the same bias will be present in both relations. Any measured relative offset between the TFRs of the two samples will then be the result of intrinsic differences between the two. With the advent of several large IFU surveys at $z \approx 0$ it is now possible to compare the observations of KROSS at $z \approx 1$ to a similarly observed sample in the local Universe. Such a comparison is the subject of Chapter 3. In this chapter we make do with the average of several different methods. This issue and work in relation to it are discussed further in § 2.6.

2.4.2 The TFRs

Figure 2.3 shows the M_K and M_* TFRs for sub-sample *all*. The parameters for the best bisector and fixed-slope fits are shown in Table 2.3 and Table 2.4, respectively. From the free fits to the KROSS TFRs we infer large intrinsic scatter in M_K and M_* compared to the corresponding $z \approx 0$ relations. For the M_K and M_* TFR we measure intrinsic scatters of respectively $\sigma_{\rm int} = 0.84 \pm 0.04$ mag and $\sigma_{\rm int} = 0.38 \pm 0.02$ dex. Considering the $z \approx 0$ TFRs we find an intrinsic scatter of $\sigma_{\rm int} = 0.36 \pm 0.04$ mag and $\sigma_{\rm int} = 0.16 \pm 0.01$ dex for the M_K and M_* relation respectively.

The free fit slope of each of the KROSS TFRs for the *all* sub-sample is much shallower

TFR	Sample	Slope	Intercept	Pivot	$\sigma_{\rm tot}$	$\sigma_{\rm int}$	$\zeta_{\rm tot}$	$\zeta_{\rm int}$
M_K	$z \approx 0$	-8.9 ± 0.3	-23.00 ± 0.04	2.2	0.41 mag	0.36 ± 0.04 mag	0.067 dex	0.045 ± 0.008 dex
	KROSS *all*	-4.0 ± 0.5	-23.57 ± 0.09	2.14	0.86 mag	0.84 ± 0.04 mag	0.169 dex	0.153 ± 0.009 dex
	KROSS *disky*	-7.3 ± 0.9	-23.4 ± 0.2	2.25	0.62 mag	0.57 ± 0.06 mag	0.086 dex	0.06 ± 0.01 dex
$\log M_*$	$z \approx 0$	3.68 ± 0.08	10.20 ± 0.01	2.17	0.21 dex	0.16 ± 0.01 dex	0.059 dex	0.054 ± 0.003 dex
	KROSS *all*	2.1 ± 0.2	10.06 ± 0.05	2.14	0.44 dex	0.38 ± 0.02 dex	0.171 dex	0.153 ± 0.009 dex
	KROSS *disky*	4.7 ± 0.4	10.0 ± 0.3	2.25	0.37 dex	0.25 ± 0.05 dex	0.08 dex	0.06 ± 0.01 dex

Table 2.3: Parameters of the bisector of the forward and reverse straight line fits to the M_K and M_* TFRs of the composite $z \approx 0$ comparison samples and KROSS sub-samples *all* and *disky*. Uncertainties are quoted at a 1σ level.

TFR	Sample	redshift	$N_{\rm gal}$	Slope	Intercept	Pivot	$\sigma_{\rm tot}$	$\sigma_{\rm int}$	Offset
M_K	KROSS all	0.8–1.0	210	−8.9	−23.6 ± 0.1	2.14	1.53 mag	1.43 ± 0.08 mag	−1.1 ± 0.1 mag
	KROSS disky	0.8–1.0	56	−8.9	−23.4 ± 0.1	2.25	0.79 mag	0.66 ± 0.08 mag	0.1 ± 0.1 mag
$\log M_*$	Miller et al. (2011)	0.2–0.5	129	3.68	9.83 ± 0.04	2.09	0.26 dex	0.20 ± 0.03 dex	−0.04 ± 0.07 dex
		0.5–0.8		3.68	9.74 ± 0.05	2.08	0.33 dex	0.26 ± 0.03 dex	−0.09 ± 0.08 dex
		0.8–1.3		3.68	10.34 ± 0.05	2.23	0.30 dex	0.21 ± 0.05 dex	−0.04 ± 0.08 dex
	Flores et al. (2006) all	0.41–0.71	30	3.68	10.48 ± 0.08	2.18	-	-	0.27 ± 0.09 dex
	Flores et al. (2006) RD	0.46–0.70	9	3.68	10.4 ± 0.1	2.29	-	-	−0.2 ± 0.2 dex
	Puech et al. (2008) all	0.42–0.74	54	3.68	10.34 ± 0.08	2.23	0.60 dex	0.43 ± 0.09 dex	0.0 ± 0.1 dex
	Puech et al. (2008) RD	0.42–0.70	12	3.68	10.52 ± 0.09	2.31	0.14 dex	0 dex	−0.2 ± 0.1 dex
	KROSS *all*	0.8–1.0	210	3.68	10.08 ± 0.04	2.14	0.66 dex	0.58 ± 0.03 dex	0.02 ± 0.08 dex
	KROSS *disky*	0.8–1.0	56	3.68	10.05 ± 0.05	2.25	0.37 dex	0.26 ± 0.05 dex	−0.41 ± 0.08 dex
	Miller et al. (2012)	1–1.7	42	3.68	9.88 ± 0.07	2.10	0.43 dex	0.26 ± 0.08 dex	−0.03 ± 0.09 dex
	Cresci et al. (2009)	1.5–2.5	16	3.68	10.57 ± 0.06	2.37	0.23 dex	0.1 ± 0.1 dex	−0.33 ± 0.09 dex
	Gnerucci et al. (2011)	3–3.6	11	3.68	9 ± 1	2.11	1.11 dex	0 dex	−0.6 ± 1.0 dex

Table 2.4: Parameters of the fixed slope linear fits to the M_K and $\log M_*$ TFRs of KROSS sub-samples *all* and *disky*, and samples of varying redshift from the literature. For each fit the slope was fixed to that of the respective $z \approx 0$ comparison relation and the pivot was set as the median value of V_{80}. The best fit to the data of Puech et al. (2008) RD, and Gnerucci et al. (2011) was consistent with zero intrinsic scatter. Since tabulated uncertainties were unavailable for the Flores et al. (2006) data, we make no attempt to determine the scatter of these samples. Uncertainties are quoted at a 1σ level. Uncertainties in the offsets include the uncertainty in the $z \approx 0$ TFR zero-point and an uncertainty of 0.06 dex in the conversion of stellar masses derived assuming an IMF other than Chabrier. We do not report $\zeta_{\rm tot}$ or $\zeta_{\rm int}$ since, in the case of fixed slope, m the forward and reverse total and intrinsic scatters are related as $\zeta_{\rm tot} = \sigma_{\rm tot}/m$ and $\zeta_{\rm int} = \sigma_{\rm int}/m$ respectively.

than that of the respective comparison relation, within uncertainties (-4.0 ± 0.5 and 2.1 ± 0.2 for the M_K and M_* KROSS relation, respectively compared to -8.9 ± 0.3 and 3.68 ± 0.08 for respectively the M_K and M_* $z \approx 0$ relation). Fixing the slopes to that of the $z \approx 0$ relations we find an increase in the inferred intrinsic scatter (1.43 ± 0.08 mag and 0.58 ± 0.03 dex for the M_K and M_* relation respectively) for both KROSS TFRs for the *all* sub-sample. Considering the fixed-slope fit to the KROSS M_* TFR for the *all* sub-sample, we find no evidence for a significant offset of the TFR zero-points between $z \approx 1$ and $z \approx 0$. Considering the M_K TFR for the same sample however, for a given rotation velocity we measure an offset of -1.1 ± 0.1 mag between the zero-points of the KROSS TFR and the corresponding $z \approx 0$ relation.

Importantly, the TFRs of sub-sample *all* exhibit large scatter in $\log V_{80}$ ($\zeta_{\rm int} = 0.153 \pm 0.009$ dex, or equivalently $\sigma'_{\rm int} = 1.9 \pm 0.1$ mag in M_K or $\sigma'_{\rm int} = 0.81 \pm 0.5$ dex in M_*). As is apparent from the colour-coding in Figure 2.3, this scatter dramatically reduces with increasing V_{80}/σ i.e. the scatter is reduced for the more rotation-dominated galaxies in the sample. Since the TFR assumes purely rotational motion, it is more informative to examine the TFR of galaxies with high V_{80}/σ. We thus look to the TFRs of the *disky* sub-sample displayed in Figure 2.4, that contain galaxies selected to have $V_{80}/\sigma > 3$ (as described in § 2.3.5). The fit parameters for the free and fixed-slope fits are shown in Table 2.3 and Table 2.4, respectively. We see a reduction of the intrinsic scatter compared to that of sub-sample *all* ($\sigma_{\rm int} = 0.57 \pm 0.06$ mag and $\sigma_{\rm int} = 0.25 \pm 0.05$ dex for the M_K and M_* relation, respectively for the *disky* sub-sample). However, this is still large compared to the corresponding $z \approx 0$ comparison relations. The bisector (free fit) slopes of both TFRs for the *disky* sub-sample (-7.3 ± 0.9 and 4.7 ± 0.4 for the M_K and M_* relation, respectively) are much steeper than the free fit slopes of the corresponding TFRs for sub-sample *all*, with the slope of the *disky* sub-sample M_* TFR steeper even than the $z \approx 0$ comparison relation, within uncertainties. The slope of the M_K KROSS TFR for the *disky* sub-sample remains slightly shallower than that of the corresponding $z \approx 0$ TFR, within uncertainties.

Fixing the slopes to match those of $z \approx 0$ TFRs we see a change in the zero-point offset, towards dimmer magnitudes or lower stellar masses at fixed rotation velocity, across both TFRs in comparison to sub-sample *all*. For the M_K TFRs, this brings the KROSS relation in line with the $z \approx 0$ M_K TFR (we measure a zero-point offset of 0.1 ± 0.1 mag). However, we measure a large offset (-0.41 ± 0.08 dex), towards lower stellar masses at fixed rotation velocity, between the KROSS M_* TFR and the corresponding $z \approx 0$ relation zero-points i.e. at fixed rotation velocity the KROSS galaxies have less stellar mass than their $z \approx 0$ counterparts. This offset is larger than the measured intrinsic scatter and greater than three times the 1σ uncertainty on the KROSS TFR zero-point. We note that the measured zero-points of both the M_* and M_K TFRs for the *disky* sub-sample are robust to changes in the radial position at which the velocity measure is extracted for each galaxy; extracting velocities V_{70} and V_{90} (i.e. at a radius containing respectively 70% and 90% of the Hα flux) changes the measured offset by only ± 0.08 dex and ± 0.2 mag for the M_* and M_K KROSS TFRs, respectively for the *disky* sub-sample. We thus find evidence for a significant evolution in the zero-point of the M_* TFR for rotation-dominated galaxies with an increase in stellar mass at fixed rotation velocity from $z \approx 1$ to $z \approx 0$. For the same galaxies we find no evolution in the zero-point of the M_K TFR over the same period. Again, the measured intrinsic scatters increase in comparison to the free fit, but are reduced in comparison to the fixed fit of sub-sample *all*.

If the zero-point of the M_* TFR has evolved as measured since $z \approx 1$ to the present day (and assuming a galaxy's rotation velocity is a reasonable proxy for its dynamical (i.e. total) mass $M_{\rm dyn}$), this implies a decrease by a factor of ≈ 0.6 in the *dynamical* mass-to-stellar mass ratio of disk-like galaxies over the last ≈8 Gyr i.e. $(M_{\rm dyn}/M_*)_{z=0} \approx 0.4 \times (M_{\rm dyn}/M_*)_{z=1}$. At fixed rotation velocity, rotation-dominated galaxies at $z \approx 1$ have less stellar mass than they do in the local Universe. Further, given that there is no apparent evolution in the zero-point of the M_K TFR, this also implies an increase in the K-band *stellar* mass-to-light ratio by a factor of ≈ 2.6 since $z \approx 1$. There is more K-band light emitted per stellar mass at $z \approx 1$ than at $z \approx 0$. This is not outside of reasonable expectation given the greater specific star formation rates of galaxies at $z \approx 1$ compared to those in the local Universe (see § 2.5 for further discussion on this point).

2.4.3 Evolution

The offset between the (KROSS) $z \approx 1$ M_* TFR and the corresponding $z \approx 0$ TFR is at odds with the findings of Miller et al. (2011) who (as discussed in § 1.4) used long-slit observations to construct the TFR for 129 disk-like galaxies at $z \lesssim 1.3$, finding both the intrinsic scatter and zero-point of the TFR to be constant in the range $0.3 \lesssim z \lesssim 1$. An extention of this work by Miller et al. (2012) used the Keck I Low Resolution Imaging Spectrograph (Oke et al., 1995) to observe 42 star-forming galaxies at $1 < z < 1.7$, selected on the basis of their morphologies, confirming the findings of Miller et al. (2011).

To investigate this further and put the results of this work in context, we use the data of Miller et al. (2011, 2012) and other intermediate redshift studies by Flores et al. (2006), Puech et al. (2008), Cresci et al. (2009), and Gnerucci et al. (2011) in order to directly measure and compare the zero-point of each study with our composite $z \approx 0$ comparison sample and with the predicted TFR zero-point evolution according to theory and simulations. We find the best fit to each of the studies' data, constraining the slope to that of our $z \approx 0$ M_* TFR comparison relation (detailed in § 2.4.1). We thus obtain a homogeneous measure of any difference between the zero-points of our $z \approx 0$ M_* TFR and the corresponding TFR for each sample. The resulting measurements are presented in Table 2.4 and displayed in the left panel of Figure 2.5. Each of the previous studies we use (in addition to the works of Miller et al. 2011, 2012) is discussed in § 1.4. However, we provide further descriptions of each in § 2.4.3.1. There we also describe the predictions from theory and simulation to which we compare our results. In § 2.4.3.2 we discuss the emergent picture of the evolution of the M_* TFR zero-point since $z \approx 3$.

2.4.3.1 Comparison Studies

Here we summarise the works of Flores et al. (2006), Puech et al. (2008), Cresci et al. (2009), and Gnerucci et al. (2011) (see also § 1.4). We also discuss the work of Dutton et al. (2011), who use semi-analytical modelling (SAM) to predict the TFR zero-point evolution as a function of redshift. Lastly we describe the process by which we derive similar predictions from the Evolution and Assembly of GaLaxies and their Environments (EAGLE) simulation

(Schaye et al., 2015; Crain et al., 2015; McAlpine et al., 2015).

Flores et al. (2006) and Puech et al. (2008) both used FLAMES-GIRAFFE (see e.g. Pasquini et al., 2002) to conduct spatially-resolved observations of [OII]3727 emission from galaxies at $z \approx 0.6$. Both studies apply the kinematic classification scheme devised by Flores et al. (2006) to their galaxy sample. The scheme uses optical images combined with the velocity and dispersion fields of each galaxy to place it in one of three kinematic categories:

- *rotating disks* (RD): the axis of rotation of the line-of-sight velocity field is aligned with the projected optical minor axis, and the peak of the velocity dispersion is close to the galaxy's dynamical centre,
- *perturbed rotation* (PR): the axis of rotation is aligned with the projected optical minor axis but the peak of the dispersion is misaligned with the dynamical centre,
- *complex kinematics* (CK): both the line-of-sight velocity and velocity dispersion fields differ greatly from that expected of a rotating disk.

In order to draw parallels with our own *all* and *disky* sub-samples, we examine the offset between our composite $z \approx 0$ M_* TFR and those of both Flores et al. (2006) and Puech et al. (2008), first including galaxies within all three of their kinematic categories, and second considering just RDs. We note that the authors of both studies focus mainly on the RD samples in their discussions.

Cresci et al. (2009) constructed the M_* TFR of 18 star-forming galaxies at $z \approx 2.2$, using spatially resolved Hα emission line kinematics as observed with the SINFONI (Eisenhauer et al., 2003) integral field spectrograph at the VLT. The galaxies were selected from the high-z galaxy Spectroscopic Imaging survey in the NIR with SINFONI (SINS; Förster Schreiber et al., 2009) based on the prominence of ordered rotation versus more complex dynamics in each system. Combining the empirical kinemetry methods of Shapiro et al. (2008) (see § 2.3.5) with visual inspection of the velocity maps of each galaxy, the authors deemed all 18 galaxies to exhibit ordered rotation. We include 16 of these 18 galaxies, for which there are definitive stellar mass values, in our comparison. 2 galaxies, for which the authors state only upper limits on the stellar mass, are excluded.

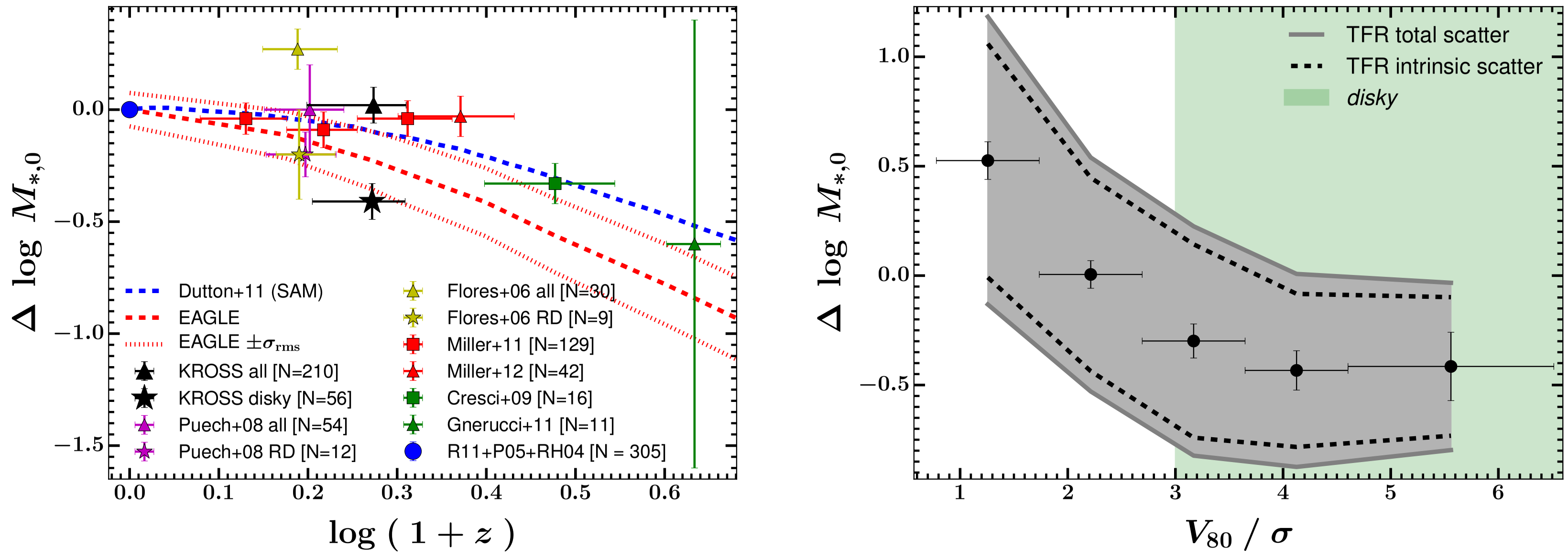

Figure 2.5: **Left:** The evolution of the stellar mass TFR zero-point with respect to the $z \approx 0$ comparison sample as described in § 2.4.1. The corresponding fit parameters are shown in Table 2.4. We use the best fit to KROSS sub-samples *all* and *disky* and several samples at various redshifts from the literature. The slope of the best fit is fixed to that of the best free fit to the $z \approx 0$ comparison sample. We include the evolution of the TFR zero-point (with respect to $z \approx 0$) with redshift, as predicted by the semi-analytical modelling (SAM) of Dutton et al. (2011) and the EAGLE simulation. For reference we also plot the rms scatter as measured from the EAGLE samples. We linearly interpolate between each point in order to better highlight the trend in predicted offset as a function of redshift from EAGLE and Dutton et al. (2011). The KROSS *disky* sub-sample, and the literature samples which comprise rotating disks, generally agree with the predictions of EAGLE or SAM. We measure little (or in some cases positive) evolution of the TFR zero-point for those samples that do not use IFU observations to differentiate between disk-like and non-disk-like galaxies; these tend to lie above the predictions of EAGLE and Dutton et al. (2011). **Right:** The evolution of the KROSS stellar mass TFR zero-point as a function of V_{80} / σ. As with the left panel we find the offset of the TFR zero-point with respect to the $z \approx 0$ comparison sample, but in this case for the best fit to the M_* TFR for KROSS galaxies within bins of varying V_{80}/σ. We again fix the slope of the fit to that of the $z \approx 0$ comparison sample. The points are plotted at the centre of each bin whilst the error bars in V_{80}/σ denote the width of the bin. The intrinsic and total scatter are interpolated between points. There is a general trend from positive zero-point offsets to negative offsets (with respect to the $z \approx 0$ relation) with increasing V_{80}/σ. This is consistent with a significantly offset TFR, with respect to $z \approx 0$ for *disky* galaxies (i.e. $V_{80}/\sigma > 3$, indicated by the green shaded area), whilst more positive zero-point offsets are associated with lower values of V_{80}/σ corresponding to a greater predominance of dispersive motions in galaxies.

Finally, Gnerucci et al. (2011) also used SINFONI to study the spatially resolved kinematics of 33 galaxies at $z \approx 3$ from the Assessing the Mass-Abundances redshift [Z] Evolution (AMAZE; Maiolino et al., 2008a,b) and Lyman-break galaxies Stellar population and Dynamics (LSD; Mannucci & Maiolino, 2008; Mannucci et al., 2009) projects. Of the 33 galaxies observed, they studied the TFR of 11 that displayed ordered rotation (as quantified by the goodness of fit of a plane to their velocity maps). We include these 11 in our comparison.

We also compare our measured offsets with predictions from the galaxy formation models of Dutton et al. (2011), that consist of N-body simulations of baryonic (stellar and gas) discs grown in Navarro-Frenk-White haloes (Navarro et al., 1997) that evolve with redshift. A further additional comparison is made to the M_* TFR zero-point evolution as predicted by the EAGLE simulation. EAGLE comprises a state-of-the-art suite of cosmological hydrodynamical galaxy formation simulations performed in volumes ranging from 25 to 100 comoving Mpc^3. It has been shown to pass a large range of observational tests in both the local and higher redshift Universe. We compute the predicted TFR zero-point evolution by drawing samples of galaxies from the EAGLE public data release[4] at redshifts, $z = 0, 0.5, 0.87, 1.0, 1.5, 2, 3, \text{and } 3.98$ respectively. To facilitate a reasonable comparison to observations, at each redshift we include only those galaxies with star formation rates $> 1 M_{\odot}\text{yr}^{-1}$. We first find the best (free) fit to the TFR of the extracted $z = 0$ EAGLE sample. We then perform fixed-slope fits to the TFRs of the successively higher redshift samples with the slope constrained to that of the best (free) fit to $z = 0$ EAGLE TFR.

2.4.3.2 Zero-Point Evolution

From the left panel of Figure 2.5 it can be seen that our analysis of the Miller et al. (2011) and Miller et al. (2012) samples agrees with their findings - we find no evidence for any significant (i.e. greater than 3 times the 1σ uncertainty) evolution of the stellar mass TFR offset for the $z \lesssim 1.7$ redshift range of their data. The maximum offset we find is -0.09 ± 0.08 dex in stellar mass for galaxies in the redshift range $0.5 < z < 0.8$. We find a significant negative offset in M_* with respect to the $z \approx 0$ TFR for the Cresci et al. (2009)

---

[4] `http://icc.dur.ac.uk/Eagle/database.php`

sample (-0.33 ± 0.09 dex). Similarly we measure a large offset (-0.6 ± 1.0 dex) between the Gnerucci et al. (2011) sample and our composite $z \approx 0$ M_* TFR, although the uncertainty is very large. The general trend is marginally consistent with that predicted by Dutton et al. (2011), and EAGLE. However, the zero offsets that we measure between the zero-points of the TFRs for the highest redshift sample of Miller et al. (2011) and the sample of Miller et al. (2012) and the zero-point of our $z \approx 0$ M_* TFR disagree with both predictions.

Next we consider the samples of Flores et al. (2006) and Puech et al. (2008), where we initially include galaxies within all three of their kinematic categories (samples Flores+06 all, and Puech+08 all). For the Flores et al. (2006) sample, we find a marginally significant offset (0.27 ± 0.09 dex) towards larger stellar masses at fixed rotation velocity in comparison to the $z \approx 0$ relation. Whilst the Puech et al. (2008) relation is consistent with no zero-point offset with respect to the $z \approx 0$ TFR, within three times the 1σ uncertainties. However, the measured zero-points are shifted towards much lower M_* values when considering RD galaxies only. Indeed, we find offsets between the zero-points of the TFRs for the RD sample of Flores et al. (2006) and Puech et al. (2008) and the zero-point of our $z \approx 0$ TFR of -0.2 ± 0.2 dex and -0.2 ± 0.1 dex, respectively. These measurements are at odds with the predicted zero-point evolution for this redshift according to the SAM of Dutton et al. (2011) but agree well with the prediction from EAGLE.

Similarly, considering the M_* KROSS TFR for the *all* sub-sample, we find a zero-point offset with respect to $z \approx 0$ consistent with that of Miller et al. (2011, 2012) and with little to no evolution of the zero-point of the M_* TFR since $z \approx 1$. This is at odds with the predictions of both Dutton et al. (2011) and EAGLE. However as discussed above, considering the M_* KROSS TFR for the *disky* sub-sample (that is composed of rotation-dominated galaxies), we see a significant offset of the zero-point (-0.41 ± 0.08 dex) to lower stellar masses with respect to our $z \approx M_*$ TFR, at fixed rotation velocity. This zero-point offset agrees with the prediction of EAGLE within uncertainties, but is perhaps larger than expected. The intepretation of such an offset is explored further in § 2.5.

These results suggest that previous studies such as Miller et al. (2011, 2012) detect no evolution in the TFR out to $z \approx 1$ due to the inclusion of galaxies with low ratios of rotational-to-dispersive motions. With the benefit of IFU observations, a more direct selection of galaxies displaying ordered rotation is possible. Despite the differing methods by which rotating disks or disk-like galaxies are selected in the IFU studies discussed here, in each of the cases where some distinction has been possible we find the zero-point of the M_* TFR for the rotation-dominated (disk-like) galaxies to be significantly offset to lower stellar masses at fixed rotation velocity compared to the TFR from the same study that includes more dispersion-dominated (non-disk-like) galaxies. Similarly, whilst the models of Dutton et al. (2011) describe the evolution of the baryonic discs of galaxies, they do not make any distinction between those that are dispersion-dominated or rotation-dominated. The same may be said of the predictions from EAGLE, in which we only select galaxies based on their star formation rates. This may explain the discrepancy between the predicted evolution of the TFR zero-point and that measured for the M_* TFR for the KROSS *disky* sub-sample in this work.

The offset of the M_* TFR for the KROSS *disky* sub-sample is representative of a more general dependence of the KROSS M_* TFR zero-point on V_{80}/σ, which can be seen in the right panel of Figure 2.5. There is a shift in the offset between the zero-point of the KROSS M_* TFR and that of our $z \approx 0$ M_* TFR from positive to negative with increasing V_{80}/σ. This can be interpreted as evidence for an offset of the M_* TFR for rotation-dominated galaxies at $z \approx 1$, with galaxies being scattered in the direction of lower velocities on the TFR plot depending on to what extent their motions are rotation- or dispersion-dominated. We note here that the flattening of the curve in the right panel of Figure 2.5 for galaxies $V_{80}/\sigma \gtrsim 3$, balanced with the need to maintain a reasonable sample size, lead to the chosen cut of $V_{80}/\sigma > 3$ for *disky* KROSS galaxies (see § 2.3.5). Thus the zero-point offset of -0.41 ± 0.08 dex with respect to our $z \approx 0$ M_* TFR we find for this sub-sample is (unsurprisingly) approximately the average of the zero-point offsets of the three highest bins in V_{80}/σ of the plot.

2.5 Discussion

For a *disky* sub-sample of KROSS galaxies, we found the best bisector fits to the rest-frame absolute K-band magnitude (M_K) and stellar mass (M_*) TFRs to be as follows

$$M_K/\mathrm{mag} \;=\; (-7.3 \;\pm\; 0.9) \;\times\; [(\log(\mathrm{V}_{80}/\mathrm{km\ s}^{-1}) \;-\; 2.25] \;-\; 23.4 \;\pm\; 0.2 \quad (2.18)$$

$$\log(M_*/M_\odot) \;=\; (4.7 \;\pm\; 0.4) \;\times\; [(\log(V_{80}/\mathrm{km\ s}^{-1}) \;-\; 2.25] \;+\; 10.0 \;\pm\; 0.3 \quad (2.19)$$

Considering the *all* sub-sample, we found the slope of both the M_K and M_* KROSS TFRs to be shallower than those of corresponding $z \approx 0$ relations. For the *disky* sub-sample, we found the slope of the M_K KROSS TFR to be slightly shallower, within 1σ uncertainties, than that of a comparison relation for $z \approx 0$ galaxies (see § 2.4.1). Conversely the slope of the M_* KROSS TFR for the *disky* sub-sample was slightly steeper, within 1σ uncertainties, than that of an M_* $z \approx 0$ comparison relation. We draw no conclusions from the free-fit slopes given the still comparatively large scatter, with respect to $z \approx 0$, for the $z \approx 1$ TFRs.

Fixing the slope of the KROSS TFRs to that of their respective comparison relations provided evidence to suggest an evolution of the M_* TFR zero-point between $z \approx 1$ and $z \approx 0$, for rotationally-supported (*disky*) galaxies. However, we found no evolution in the M_K TFR zero-point between $z \approx 1$ and $z \approx 0$ for the same galaxies. We note that both these measurements are robust to the choice of radius at which we extract a rotation velocity (see § 2.4.2).

These results imply that rotation-dominated (disk-like) galaxies of a given dynamical mass contain less stellar mass at $z \approx 1$ than at $z \approx 0$, yet emit the same amounts of K-band light. The latter implies an increase in the K-band stellar mass-to-light ratio by a factor of ≈ 2.6 since $z \approx 1$. Arnouts et al. (2007) analyse the evolution of the stellar mass-to-light ratio since $z \approx 1.5$ via SED fitting (with visible to mid-IR photometry) for a sample containing tens of thousands of galaxies. They find that the average K-band stellar mass-to-light ratio, M_*/L_K of actively star-forming galaxies increases by 0.27 dex, but with a root-mean-squared (rms) scatter of 0.21 dex over this period. Incorporating the rms scatter, this equates to a maximum increase of a factor of $\approx$ 1.1–3.0. Drory et al. (2004) measure the evolution of M_*/L_K since $z \approx 1.2$ by fitting a grid of stellar populations models of varying star formations histories, ages, and metallicities to the visible and near-IR photometry for a sample of over 500 galaxies selected in the K-band. They find an increase, by a factor of ≈ 1.4–3.4, in the M_*/L_K since $z \approx 1$. Thus, whilst the increase in the M_*/L_K inferred from this work is towards the higher ends of these ranges, it appears a feasible evolution.

The measured offset in the M_* TFR zero-point between $z \approx 1$ and $z \approx 0$ implies that stellar mass assembly continues despite the drop off in global star formation rate density in the Universe at redshifts $z \lesssim 1$ (see e.g. Hopkins & Beacom, 2006; Sobral et al., 2013). We did not compare the measured zero-point offset to that predicted from stellar population models as the latter will depend strongly on the assumed galaxy age and star formation history at $z \approx 1$. Instead we prefered to compare to the cosmological hydrodynamical galaxy formation simulations of EAGLE. The measured increase in stellar mass at fixed rotation velocity for rotation-dominated galaxies since $z \approx 1$ agrees, within uncertainties, with the predicted evolution of the M_* TFR zero-point derived from star-forming (star formation rates $> 1 M_\odot$ yr^{-1}) EAGLE galaxies. However, it is on the upper limit of the EAGLE prediction. We therefore consider whether such an evolution in the M_* TFR zero-point since $z \approx 1$ is physically feasible.

The relative increase in stellar mass is most easily reconciled with the conversion of gas mass in to stellar mass in galaxies over the last ≈8 Gyr in a secular evolution scenario. However, to determine the likelihood of this scenario, the gas mass fraction of the KROSS galaxies must first be considered. Stott et al. (2016) inverted the Kennicutt-Schmidt relation (Kennicutt, 1998) of KROSS galaxies in order to obtain an estimated gas mass-to-baryonic mass ratio of 35 ± 7 percent. Converting all of the gas mass within the KROSS galaxies in to stellar mass would therefore only account for, at most, 0.24 dex of the measured offset between the M_* TFR zero-point and that of our the $z \approx 0$ M_* comparison relation (i.e. an increase by a factor ≈ 1.7 in the stellar mass since $z \approx 1$). In fact, to reconcile the measured -0.41 dex offset in this manner would require a baryonic gas fraction of ≈ 72 percent for the KROSS *disky* sub-sample galaxies.

There is of course the possibility of galaxies accreting extra gas over the last ≈ 8 Gyr. Indeed, the observed specific baryon accretion rate at $z \approx 1$ ranges from ≈ 0.8–0.6 Gyr^{-1}

for galaxies with stellar mass $\log(M_*/M_\odot) = 9.3$–10.7, decreasing to ≈ 0.2–0.1 Gyr^{-1} for galaxies of the same stellar mass in the local Universe (Elbaz et al., 2007; Salim et al., 2007a; Dutton et al., 2010). Combining this with a measured depletion timescale for KROSS galaxies of ≈ 1 Gyr (Stott et al., 2016), it can be seen there is opportunity for star-forming galaxies to assemble significant amounts of stellar mass since $z \approx 1$ such as those inferred by the offset between the zero-points of the M_* KROSS TFR and the $z \approx 0$ M_* comparison relation measured in this work.

Our findings are at odds with the studies of Miller et al. (2011, 2012), which find no evolution of the TFR zero-point over a similar range in redshifts. Excluded from our analysis (due to a lack of tabulated data) is the work of Conselice et al. (2005b), who examined the the evolution of both the K-band and stellar mass TFR out to $z \approx 1.2$ using Keck spectroscopy and near-infrared photometry from the Keck Near-Infrared Camera, the UKIRT Fast-Track Imager, and the Cooled Infrared Spectrograph and Camera for OHS on the *Subaru* telescope. They found no significant evolution of the TFR zero-point with redshift, in agreement with the works of Miller et al. (2011, 2012). However the key point is that, unlike those studies, this work is able to select for only those galaxies at $z \approx 1$ that are rotation-dominated in their motions. Inclusion of galaxies that are more turbulent sees a decrease in the magnitude of the measured evolution of the TFR zero-point with redshift - in line with the findings of Miller et al. (2011) and Conselice et al. (2005b), but at odds with the IFU studies of Flores et al. (2006), Puech et al. (2008), Cresci et al. (2009), and Gnerucci et al. (2011), all of which predominantly agree with the predictions of the EAGLE simulation and, to a lesser degree, those of Dutton et al. (2011).

In a recent paper by Di Teodoro et al. (2016), the authors constructed the $z \approx 1$ M_* TFR using a sample of only 18 galaxies, each observed with KMOS, of which 14 are publicly available KROSS observations. They reported no evolution of the TFR since $z \approx 1$ and present this as evidence that disk-like galaxies at this epoch closely resemble their kinematically mature counterparts in the local Universe. However, there is an obvious danger to drawing conclusions on the nature of all disk-like galaxies at $z \approx 1$ from such a small sample. Furthermore, their sample was selected to include only those galaxies that lend themselves best to the modelling of their kinematics and is thus unlikely to be statistically representative of the bulk of the population of $z \approx 1$ galaxies. With the much larger sample presented in this work, we show that, infact, a minority of star-forming galaxies at $z \approx 1$ are strongly rotation dominated ($V_{80}/\sigma > 3$) and only with the full KROSS sample do we detect an evolution in the M_* TFR zero-point with redshift.

Both TFRs for the KROSS *all* sub-sample exhibit large scatter. This scatter is reduced in the relations of the *disky* sub-sample, but still large in comparison the $z \approx 0$ comparison TFRs. There are several potential sources contributing to the intrinsic scatter in the KROSS TFRs. The most obvious source of scatter in the TFRs for the *all* sub-sample is the inclusion of galaxies that have significant dispersive motions and thus violate the initial assumption of circular motion of the TFR. This source of scatter is confirmed as we see reductions in the intrinsic scatter of the M_K and M_* TFR, respectively between the *all* and *disky* sub-samples, where for the latter we select only those galaxies deemed to be rotation-dominated (and thus disk-like). The intrinsic scatters of the M_K and M_* KROSS TFRs for the *all* sub-sample are respectively ≈ 2.3 and ≈ 2.4 times larger than the corresponding $z \approx 0$ comparison relation. However, the intrinsic scatter in both the M_K and M_* KROSS TFR reduces to ≈ 1.6 times that of the corresponding $z \approx 0$ relation when only rotation-dominated galaxies are considered at $z \approx 1$ (i.e. the *disky* sub-sample). Conceptually, we may consider the rotation velocity as a rough proxy for the total (dynamical) mass. Assuming this is true it is clear then that an erroneously small total mass will be inferred for those galaxies with significant dispersive motions in comparison to rotational motions. As a result those galaxies will be scattered to lower values along the abscissa of the TFR.

KROSS galaxies with low Hα S/N will have noisier observed velocity fields. In these cases, the best fit arctangent model is less reliable. This may also increase the scatter in the TFR. More importantly, the arctangent model is an unsatisfactory description of the dynamics for those galaxies that, while having predominantly circular motions, have a rotation curve that peaks centrally ($r \lesssim 10$ kpc) before flattening out at lower velocity at greater radii. This is consistent with the (baryonic) disk component of the galaxy dominating dynamically over its (dark) halo component in its inner regions (see e.g. Casertano & van Gorkom, 1991). Thankfully, in the *disky* sub-sample at least, both types of system are rare with most systems adequately described by the arctangent model (see Appendix A.2).

The *disky* sub-sample contains galaxies determined to be predominantly rotationally supported as decided by a $V_{80}/\sigma > 3$ cut to the *all* sub-sample (see § 2.4.3.2). The specific limit was chosen in order to select galaxies that were rotation-dominated whilst also maintaining a reasonable sample size. However, importantly it is also the value above which the offset of theM_* TFR zero-point does not undergo further significant evolution (with respect to that of a $z \approx 0$ comparison relation). In this respect, the choice of limit is not a subjective one but is rather driven by the data. It is clear however that a change to the limiting value of V_{80}/σ will lead to a change in the measured intrinsic scatter, slope, and offset of the TFR as extra galaxies are included or excluded from the sub-sample. This is apparent in Figure 2.5 (Right). It is important also to view the choice of $V_{80}/\sigma > 3$ to select rotation-dominated galaxies in the context of galaxies at $z \approx 0$. Indeed, in the local Universe, we see typical ratios of galaxy rotation-to-dispersion $V/\sigma \gtrsim 10$ for the thin disk of spiral galaxies (Genzel et al., 2006). Thus it is clear that, despite the many different definitions of V/σ abound in the literature (see Stott et al. 2016 for a discussion), even in the upper limit of the range of V_{80}/σ values seen in the KROSS sample, these galaxies are far more turbulent in terms of their gas dynamics than galaxies in the present day. In this respect, we may still attribute some of the intrinsic scatter measured in the TFRs for the KROSS *disky* sub-sample to turbulence within the gaseous disk that provides some form of pressure support.

In addition to the assumption of circular motion inherent in the TFR, a second important assumption that must be considered is that the average surface mass density of the galaxies within a sample is constant. In the local Universe this means comparing galaxies of the same morphological type. Previous studies have shown that the TFRs for early-type and late-type galaxies have different slopes (see e.g. Williams et al., 2010; Davis et al., 2011). Even between late-type morphologies, studies have shown significantly different slopes (see e.g. Lagattuta et al., 2013). At $z \approx 1$, “disky” galaxies are just starting to emerge. In this regime it makes less sense to talk about morphological types in the same way as at $z \approx 0$. Abraham (1999) argues infact that the classic “Hubble Tuning Fork” description of galaxy morphology begins to break down from $z \approx 0.5$ onwards. Whilst the KROSS galaxies were selected to be “normal” star-forming galaxies at $z \approx 1$, there are no further morphological selection criteria. Thus it is likely that there will be variation in the surface mass density from galaxy to galaxy in the KROSS sample. In practice this will result in an increase in the inferred intrinsic scatter as this is effectively combining several different morphological types each with different slopes and scatter for the TFR, and then fitting them with one single slope and scatter.

One must also consider a further issue related to this. Although the KROSS sample and $z \approx 0$ comparison sample span similar ranges in rotation velocity and stellar mass (in fact, the comparison sample spans a slightly wider range than the KROSS sample in both respects), we cannot assume that we are "following" the same population of galaxies between $z \approx 1$ and the local Universe. Indeed, considering a window of stellar mass, galaxies will evolve in to and out of this window as time passes between $z \approx 1$ and $z \approx 0$. The implications of choosing to compare samples within the same (stellar) mass window between redshifts as opposed to, for example, galaxies within a similar range of star formation are complex and are left to future work. As discussed above, the evidence presented in this chapter is most easily reconciled with a secular evolution or minor-mergers scenario whereby galaxies continually accrete and convert gas mass to stellar mass between $z \approx 1$ and $z \approx 0$.

2.6 Conclusions & Future Work

In this chapter, we have presented the M_K and M_* TFRs for sub-samples drawn from the 585 galaxies observed by KROSS with resolved Hα emission. We examined the TFRs for a sub-sample of KROSS galaxies with well measured rotation velocities (the *all* sub-sample) and a further sub-set of those that were rotation-dominated (the *disky* sub-sample). The selection criteria for both *all* and *disky* sub-samples are described in § 2.3.5.

We found the intrinsic scatters in the M_K and M_* KROSS TFRs for the *all* sub-sample to be ≈ 2.3 times and ≈ 2.4 times larger than $z \approx 0$ comparison relations. However, the intrinsic scatters of both TFRs reduced to ≈ 1.6 times those of $z \approx 0$ comparison relations when only rotation-dominated galaxies were considered i.e. the *disky* sub-sample. We noted that compared to the local Universe, however, these *disky* galaxies still have much more turbulent gas dynamics. This turbulence is likely to contribute to the measured intrinsic scatter. We attributed the remaining intrinsic scatter to the fact that, even after selecting the *disky* sub-sample, we consider a single TFR for galaxies with (likely) various different morphologies, sizes and/or surface mass densities - effectively an average of several TFRs, all with differing slopes.

Contrary to some previous studies conducted at similar redshift (Miller et al., 2011, 2012; Di Teodoro et al., 2016), but in broad agreement with the predictions of the state-of-the-art hydrodynamical simulations of EAGLE, we measured a significant offset of the M_* TFR zero-point for rotation-dominated galaxies at $z \approx 1$ toward lower stellar mass values (-0.41 dex with respect to $z \approx 0$) at fixed rotation velocity. Yet we measured no significant offset in the M_K TFR zero-point over the same period. We concluded that the ability of KROSS to differentiate between those galaxies with high or low ratios of rotational-to-dispersive motions (V_{80}/σ) is why this work detected an evolution of the M_* TFR zero-point between $z \approx 1$ and $z \approx 0$, whilst some previous studies have not. We calculated that, assuming no evolution in the surface mass density of galaxies over this period, the detected zero-point evolution implies a decrease by a factor of ≈ 0.6 in the dynamical mass-to-stellar mass ratio of rotation-dominated galaxies since $z \approx 1$. It also implies an increase in the K-band stellar-mass-to light ratio, by a factor of ≈ 2.6 over the same period. We reasoned that this may be consistent with a secular evolution scenario whereby gas mass in (and accreted on to) galaxies is converted in to stellar mass over the last ≈ 8 Gyr. If galaxies have grown mostly via mergers since $z \approx 1$, then we would expect the M_* TFR at one epoch to be indistinguishable from the relation at the other. In this regime, we would still expect to see an offset, to brighter magnitudes with respect to $z \approx 0$, of the $z \approx 1$ M_K TFR, reflecting the comparitively larger specific star formation rates of the higher-z galaxies. However, as galaxies grow via mergers (ignoring any non-linear increase in star formation rate as a result of a merger) they would only evolve along the stellar mass TFR, with no evolution of the offset.

Whilst the results presented in this chapter have potentially significant consequences for galaxy evolution, as stressed previously in order to make a direct comparison between the TFRs at $z \approx 1$ and $z \approx 0$ it is essential to construct the TFRs at each epoch using the same observational and analytical methods to negate the possibility of different systematic biases introduced to each relation, confusing any comparison between the two. In practice, in order to directly compare the KROSS TFRs to those constructed with $z \approx 0$ galaxies we must take IFU observations of galaxies in the local Universe and degrade this data to the same quality as that of KROSS data e.g. the signal-to-noise ratio, spatial and spectral resolutions must all be matched. This degraded data must then be analysed in the same manner as the KROSS data, at which point a more direct comparison of the TFRs may be made.

There are a number of IFU surveys of galaxies at low redshift that are already online, or will be online in the near future, that will provide suitable samples of large numbers of galaxies in the local Universe that we may compare to KROSS. These include Mapping Nearby Galaxies at APO (MaNGA[5]; Bundy et al., 2015), the Calar Alto Legacy Integral Field spectroscopy Area survey (CALIFA[6]; see e.g. Sánchez et al., 2012), and the Sydney-Australian-Astronomical-Observatory Multi-object Integral-Field Spectrograph (SAMI) Galaxy Survey[7] (see e.g. Bryant et al., 2015). Chapter 3 uses data from the SAMI Galaxy Survey, in the manner described above, in order to gain a clearer understanding of how the TFR has evolved from the epoch of peak global star formation rate density in the Universe to the present day.

---

[5] `https://www.sdss3.org/future/manga.php`

[6] `http://www.caha.es/CALIFA/public_html/?q=node/1`

[7] `http://sami-survey.org/`

Chapter 3

KROSS vs SAMI: The Evolution of the TFR since $z \approx 1$

3.1 Motivation

In Chapter 2, we measured the evolution of the stellar mass (M_*) and absolute K-band magnitude (M_K) Tully-Fisher relations (TFRs) since $z \approx 1$ by constructing $z \approx 1$ TFRs using line-of-sight (LOS) velocities derived from spatially-resolved K-band Multi-Object Spectrograph (KMOS; Sharples et al., 2013) observations of Hα emission from KMOS Redshift One Spectroscopic Survey (KROSS) galaxies. We compared them to relations at $z \approx 0$, that we constructed using data from several previous studies using different measures of the galaxies' rotation. Using a carefully selected sub-sample of *disky* KROSS galaxies (with rotationally dominated kinematics $V_{80}/\sigma > 3$, where V_{80} is the LOS velocity of the galaxy at the semi-major axis of an ellipse containing 80% of the galaxy Hα flux and σ is the galaxy's intrinsic velocity dispersion), we found no evolution in the M_K TFR zero-point since $z \approx 1$, but a significant evolution in the M_* TFR zero-point (-0.41 dex). Assuming no evolution in surface mass density, this result implies a significant reduction (by a factor of ≈ 2.6) of the dynamical mass-to-stellar mass ratio of rotation-dominated galaxies over the last ~ 8 Gyr, and it suggests substantial stellar mass growth in galaxies since the epoch of peak star formation.

The implications for galaxy evolution theory of the result presented in Chapter 2 are potentially significant. However, as with any comparison between TFRs, one must carefully take account of potential systematic biases resulting from the methods used to construct the relations. The measurement of galaxy rotation is particularly important, so too is the radius at which this velocity is extracted. Additionally, the methods used to derive M_* and M_K are often indirect, particularly at high redshifts, and usually rely on fitting sets of predefined model spectral energy distributions (SEDs) to observations, the choice of which is based on implicit assumptions about the galaxies' stellar populations. Finally, the calculation of galaxy inclination can also have a pronounced effect on the resultant TFRs. Although removing highly inclined galaxies from the sample goes some way toward reducing this, given that the major-axis of the Hα emission is sometimes even at right angles to the maximum velocity gradient of the KROSS galaxies (albeit in only a few cases), as demonstrated in the plots of Appendix A, it is clear that galaxy inclinations derived from Hα axial ratios should only be used in the absence of an inclination measured from the galaxy star light.

As discussed in § 2.4.1, the obvious solution to producing an unbiased measure of the evolution of the TFR since $z \approx 1$ (or between any TFRs for that matter) is to examine, using a single methodology, data of the exact same quality at both $z \approx 1$ and $z \approx 0$, thus constructing TFRs at each redshift that are truly directly comparable. Until very recently, however, such an approach was not possible when comparing the $z \approx 1$ Universe to the local one. Whilst pioneering integral field unit (IFU) surveys in the near-infrared (NIR), such as the Spectroscopic Imaging survey in the Near-infrared with the Spectrograph for INtegral Field Observations in the Near Infrared (SINFONI; Bonnet et al., 2004) (SINS; Förster Schreiber et al., 2006a), the Mass Assembly Survey with SINFONI in VIMOS VLT Deep Survey (VVDS) (MASSIV; Contini et al., 2012), and the Assessing the Mass-Abundances redshift [Z] Evolution (AMAZE; Maiolino et al., 2008a) and Lyman-break galaxies Stellar population and Dynamics (LSD; Mannucci et al., 2009) surveys, have slowly opened a new window on the rest-frame optical Universe at $z \gtrsim 1$, only with the advent of multiplex IFU surveys such as KROSS have we been able to compile samples of galaxies large enough to construct robust censuses of galaxies at these epochs. And despite the gains provided by surveys such as KROSS, until now there had not been equally large numbers of IFU observations of $z \approx 0$ galaxies - the ATLAS$^{\rm 3D}$ (Cappellari et al., 2011a) survey is a notable early exception, but targeted only local early-type galaxies. Thankfully, the recent maturity of the the Mapping Nearby Galaxies at Apach Point Observatory (MaNGA; Bundy et al., 2015) survey, the Calar Alto Legacy Integral Field spectroscopy Area (CALIFA; Sánchez et al., 2012) survey, and the Sydney-Australian-Astronomical-Observatory Multi-object Integral-Field Spectrograph (SAMI; Croom et al., 2012) Galaxy Survey (e.g. Bryant et al., 2015) now make robust comparisons of the $z \approx 0$ and $z \approx 1$ Universe possible. Each of these surveys has now conducted many hundreds or thousands of IFU observations of galaxies in the local Universe, providing a unique data set with which to compare to KROSS.

This chapter uses data from SAMI to construct $z \approx 0$ TFRs that are directly comparable to the $z \approx 1$ KROSS TFRs presented in Chapter 2. The key difference between the work presented in this chapter and previous comparisons of $z \approx 1$ and $z \approx 0$ samples (including that presented in Chapter 2) is the degrading process that we apply to the SAMI data so that they exactly match the quality of KROSS observations. Degrading the SAMI data in this way provides two important benefits. First and foremost, it allows an unbiased measure of any evolution in the TFR between $z \approx 1$ and the present day. As any systematic bias will be present in equal measure in both relations, any difference between the relations can be attributed to intrinsic differences between the galaxy populations at the different epochs. Secondly, it allows to identify and quantify any biases that are introduced in to the $z \gtrsim 1$ IFU observations and their associated selection function, as a result of the lower signal-to-noise ratio (S/N), spatial and spectral resolution typical of observations at this epoch, similarly for any TFR constructed using such data. In light of this, in addition to the KROSS TFRs, in this chapter we construct TFRs using the SAMI data both in its original form and after they have been degraded to match the quality of the KROSS data (in terms of their spatial and spectral resolutions, and the Hα S/N). As the degraded SAMI data are of lower quality than the original SAMI data, we hereafter refer to them as the SAMI low quality (LQ) sample (or data). We analogously refer to the original, undegraded SAMI data as the SAMI high quality (HQ) sample (or data).

This chapter is divided in to several sections. Section 3.2 concerns the SAMI HQ data. In § 3.2.1, we describe the SAMI Galaxy Survey, and in § 3.2.2 the HQ data cubes. In § 3.2.3 we detail the methods used to construct the SAMI HQ TFR, including measures of galaxy stellar mass and absolute magnitude from SED fitting of associated SAMI photometry from the Galaxy And Mass Assembly project (GAMA; Driver et al., 2011), the extraction of both continuum maps and LOS velocity fields from the SAMI cubes, and subsequent modelling of the latter. Section 3.3 concerns the SAMI LQ data. In § 3.3.1 we describe the process by which we degrade the SAMI HQ data to match the quality of KROSS. In § 3.3.2 we discuss the construction of the SAMI LQ TFR. In § 3.4 we describe further steps taken to homogenise the TFRs of the SAMI HQ, SAMI LQ and KROSS samples; here we include details of improvements to the KROSS velocity field modelling, define a new measure of galaxy rotation, and lastly detail the uniform selection criteria applied to the SAMI (HQ and LQ) and KROSS samples. The SAMI HQ, SAMI LQ and KROSS TFRs are presented in § 3.5. In § 3.5.1 we compare the SAMI HQ and SAMI LQ TFRs, describing how the degradation of the SAMI data affects the resultant TFRs. Section 3.5.2 comprises a comparison of the SAMI LQ and KROSS TFRs. In § 3.6 we discuss the implications for galaxy evolution of the results presented in § 3.5. Concluding remarks and an outline of future work are provided in § 3.7.

3.2 SAMI HQ Data

3.2.1 SAMI Galaxy Survey

Using the SAMI spectrograph (Croom et al., 2012) on the 4-meter Anglo-Australian Telescope at Sidings Spring Observatory, Australia, the SAMI Galaxy Survey (Bryant et al., 2015) aims to observe the spatially-resolved stellar and gas kinematics of $\approx$ 3400 galaxies in the redshift range $0.004 < z < 0.095$, in blue ($\approx$ 3700–5700 Å) and red ($\approx$ 6300–7400 Å) optical bandpasses, over a large range of local environments. Having so far (at the time of submission of this thesis) mapped the kinematics of 824 galaxies out to, or beyond, one effective radius, the SAMI Galaxy Survey is well suited to provide a $z \approx 0$ comparison to KROSS. Indeed, it is well matched in its sample size, restframe optical bandpass, and the

IFU nature of its observations.

3.2.2 SAMI Data Cubes

The SAMI spectrograph comprises 12 separate bundles of optical fibres, known as "hexabundles" (Bland-Hawthorn et al., 2011; Bryant et al., 2014), $\approx 14\overset{''}{.}7$ in diameter and comprising 61 individual fibers (each with a diameter of $\approx 1\overset{''}{.}6$). Each bundle is deployable within a 1 degree field of view. Observations are carried out in typical seeing in the range $0\overset{''}{.}9$–$3\overset{''}{.}0$ Each observation is conducted in both a blue ($\approx$ 3700–5700Å) and a red ($\approx$ 6300–7400Å) optical bandpass, with resolving powers $R \sim 1750$ and $R \sim 4500$, respectively. The resulting data are reduced via the latest version (v0.8) of the SAMI reduction pipeline (Sharp et al., 2015; Allen et al., 2015) and undergo a flux calibration and a telluric correction. The resultant data cubes have $0\overset{''}{.}5 \times 0\overset{''}{.}5$ spaxels.

The work presented in this chapter draws upon the latest internal SAMI data release (v0.9, kindly provided by the SAMI team ahead of its public release), comprising 824 galaxies that were also observed as part of the GAMA project. It does not include those ≈ 600 SAMI galaxies specifically targeted as being members of clusters (see Bryant et al., 2015). Since our ultimate goal is to compare like-for-like with KROSS, we utilise here only those cubes observed in the red SAMI bandpass, giving a reasonable match to the restframe optical bandpass observed by the KMOS YJ filter at $z \approx 1$. Specifically, our goal is to compare the restframe ionised gas kinematics (Hα and [NII] lines) of both the KROSS and SAMI samples, which for the latter requires the red bandpass.

3.2.3 SAMI HQ TFR

As discussed in § 3.1 and Chapter 2 (see § 2.4.1 and 2.6) the most direct method to measure any intrinsic evolution in the TFR since $z \approx 1$ (i.e. to measure a difference between the TFRs at $z \approx 1$ and 0 that can be attributed purely to differences in the intrinsic properties of the two galaxy populations and is free of bias) is to analyse data of the exact same quality, with the exact same methods, at each epoch. That way, any bias that is introduced in the relation will hopefully be the same in nature and equal in magnitude at both epochs, so that it cancels out when measuring differences between the two. In practice this means degrading the HQ SAMI data set so that it matches typical KROSS observations. We discuss the process of degrading the SAMI data in § 3.3.1 and the construction of the resultant LQ TFR in § 3.3.2. However, before embarking on such an endeavour it is prudent to first construct the best quality TFR possible from the SAMI data. This way we can clearly quantify the biases that are introduced in the relation as a result of subsequently lowering the quality of the data to the quality of KROSS data.

We thus describe below the methods used to construct the HQ SAMI TFR, using the best SAMI photometry and IFU observations available.

3.2.3.1 SED Fits

As with the KROSS galaxies in Chapter 2 (see § 2.3.4), stellar masses and absolute rest-frame magnitudes were computed for each SAMI galaxy using the SED fitting routine Le Phare (Arnouts et al., 1999; Ilbert et al., 2006). Each of the SAMI SEDs comprised photometry ranging (where available) from the far-ultra-violet (*Galaxy Evolution Explorer* (*GALEX*; Martin et al., 2005) *FUV* and *NUV*), through the optical (SDSS u, g, r, i, and z), near-infrared (Visible and Infrared Survey Telescope for Astronomy (VISTA; Sutherland et al., 2015) Z, J, H, and K), mid-infrared (*Wide-Field Infrared Survey Explorer* (*WISE*; Wright et al., 2010) $W1$, $W2$, $W3$, and $W4$), to the far-infrared (*Herschel* (Pilbratt et al., 2010) Photoconductor Array Camera and Spectrometer (PACS) *green* (≈ 98 μm) and *red* (≈ 154 μm), and Spectral and Photometric Imaging Receiver (SPIRE) *PSW* (≈ 243 μm), *PMW* (≈ 341 μm), and *PLW* (≈ 482 μm)). The 21-band photometric data sets are taken from the GAMA Panchromatic Data Release (PDR; Driver et al., 2016). For each galaxy's photometry the Lambda Adaptive Multi-Band Deblending Algorithm in R (LAMBDAR; Wright et al., 2016) was applied. LAMBDAR is designed to calculate matched aperture photometry across a range of non-homogeneous images with differing PSFs and pixel scales, given prior aperture information from high resolution imaging in the visible regime - Wright et al. define an initial aperture for each SAMI galaxy using a combination of Source Extractor (SExtractor; Bertin & Arnouts, 1996) and visual inspection of its r-band images from SDSS and Z-band images from the VISTA Kilo-degree Infrared Galaxy Survey (VIKING; Edge et al., 2013) . The derived fluxes are aperture corrected and converted to magnitudes in the Vega system.

Each SAMI SED is compared to model SEDs generated using Bruzual & Charlot (2003) stellar population synthesis models. This allows for variation in extinction, metallicity, age, stellar mass, and star formation rate, as explained in § 2.3.4. Le Phare allows for a single burst, an exponential decline, or a constant/"boxy" star formation history.

In keeping with Chapter 2, we adopt a uniform stellar mass uncertainty of ±0.2 dex throughout this chapter.

3.2.3.2 Continuum Maps

Unlike the KROSS galaxies, the closer proximity of the SAMI galaxies allows for significant detections of the stellar continuum in many of the SAMI spaxels within typical exposure times. As such, before fitting the Hα and [NII] emission lines (see § 3.2.3.3), we first measure and subtract the continuum baseline in each spaxel by finding the best-fit 0^{th} order polynomial (i.e. a horizontal line). To perform this fit, we first mask regions of the spectrum containing line-emission from the source and from the sky. We then construct a continuum map for each HQ SAMI galaxy cube by calculating the magnitude of the best-fit 0^{th} order polynomial in its corresponding spaxel.

3.2.3.3 Velocity Field Extraction and Modelling

Following the continuum baseline subtraction, velocity fields were extracted from each of the HQ SAMI cubes using the methodology of Stott et al. (2016), as described in § 2.3.1. Recall that for each spectrum (i.e. each spaxel) we simultaneously fit the Hα, [NII]6548, and [NII]6583 emission lines, where the central velocity and width of the Hα and [NII] lines are coupled but left free to vary in unison. If the Hα $S/N < 5$ for a given $0.''5 \times 0''.5$ spaxel, we consider a larger area of $1.''5 \times 1''.5$. If the S/N is still insufficient, we consider areas of $2.''5 \times 2''.5$ and $3.''5 \times 3''.5$, as required. If at this point the S/N is still too low we exclude the spaxel from the resultant velocity field.

To maintain homogeneity and faciliate a direct comparison with respectively the LQ SAMI and KROSS velocity fields, we model the HQ SAMI velocity fields with the Courteau (1997) arctangent model given in Equation 2.3.1 and discussed in detail in § 2.3.1. Whilst this model is simplistic and does not account for the more complex, higher-order kinematics that may be resolved in the HQ SAMI velocity maps, it makes for the most straightforward comparison to the LQ SAMI cubes, allowing to quantify with confidence any biases introduced in the SAMI LQ sample selection (and indirectly the KROSS sample selection) as a result of the poorer data quality. Despite its simplicity, the arctangent function is sufficient to measure the rotation velocity of galaxies in the outer (i.e. flat) parts of their rotation curves and thus construct a TFR.

With the additional information available to us from SAMI galaxy continuum maps, extensive SAMI imaging, and from a careful re-analysis of the KROSS data cubes and photometry by Harrison et al. (in preparation), we can improve on the velocity measurement method presented in Chapter 2. First, we make several small changes to the model fitting process. Second, we make changes to the way we extract the rotation velocity from the subsequent modelling. The latter are discussed later in § 3.4.2. Here we focus on the former.

Previously, for the KROSS velocity fields, we could only constrain the best-fit dynamical centre to be within a certain radius of the integrated Hα flux peak, but for the SAMI velocity maps (HQ and LQ) we can instead use the peak of the continuum light distribution to constrain this parameter. The latter is clearly preferable given that the Hα distribution of galaxies tends to be more clumpy than the stellar light, particularly at higher-z (as can been seen in the maps of integrated Hα emission of the KROSS galaxies presented in Figure 2.1 and Appendix A). For each of the HQ SAMI velocity fields, we thus constrain the dynamical centre of the best-fit model field to fall within $1''$ of the peak in the continuum.

In addition to using the continuum maps, we can also improve the fitting procedure itself. To ensure a good fit of the arctangent model to the extracted velocity field, we employ an iterative *sigma-clipping* method to account for "bad" spaxels in the velocity field (i.e. spaxels with LOS velocities unphysically large or seemingly at great odds with those of neighbouring spaxels and the general trend of the velocity field). The method entails finding the initial-best-fit model to the velocity field, and then using the residuals to decide which spaxels are "bad" and remove them. Spaxels are removed via a two-sigma iterative clip with SIGMACLIP[1] from SciPy[2] (a collection of open-source mathematical and scientific software in Python). Starting with the full set of residuals, the routine removes all elements outside of the range $\mu \pm 2\sigma_{\rm s.d.}$, where μ is the mean of the residuals and $\sigma_{\rm s.d.}$ is the standard deviation. The mean and standard deviation are then recalculated for the remaining residuals and further elements are removed in the same manner. The routine iterates until no residual is outside of the critical range. For each spaxel of the residual map removed via this routine we also remove the corresponding spaxel from the observed velocity field. With the bad spaxels removed from the velocity field, we then repeat the entire process again, finding the new best-fit model and using the new set of residual values to identify and remove further bad spaxels. As a last step we carry out a third and last fit and thus identify the final best-fit model from the twice-"pruned" observed velocity field. Removing spaxels in this way provides a more robust best-fit, reducing the chances of a skewed result due to a small number of extremely outlying LOS velocity values.

Examples of observed velocity fields extracted from HQ SAMI data cubes that are well modelled by the arctangent function, and the corresponding best-fit model are shown in Figure 3.1. Each of the maps is also corrected for the best-fit systemic velocity (see Equation 2.3.1). The same plot for each galaxy in a *disky* sub-sample (see § 3.4.3) of SAMI HQ galaxies are displayed in Figure B.1 of Appendix B. The process of extracting a measure of galaxy rotation from the best-fit model for use in the TFR is discussed in § 3.4.2 in which we detail extracting LOS velocities from the SAMI and KROSS data in a homogeneous manner. For each HQ plot in Figure 3.1 we also include the SAMI LQ plot for the corresponding galaxy. The conversion of the SAMI data cubes from HQ to LQ is detailed in § 3.3.1. The extraction of the corresponding LQ velocity fields, and their subsequent modelling is described in § 3.3.2.1. For completeness, in Figure 3.2 we show examples of HQ velocity fields that are *not* well described by the arctangent function and that dropped out of our analysis during the degrading process (described in § 3.3.1). For each of these galaxies there is no corresponding LQ velocity field.

---

[1] `http://docs.scipy.org/doc/scipy-0.14.0/reference/generated/scipy.stats.sigmaclip.html`

[2] `http://www.scipy.org/`

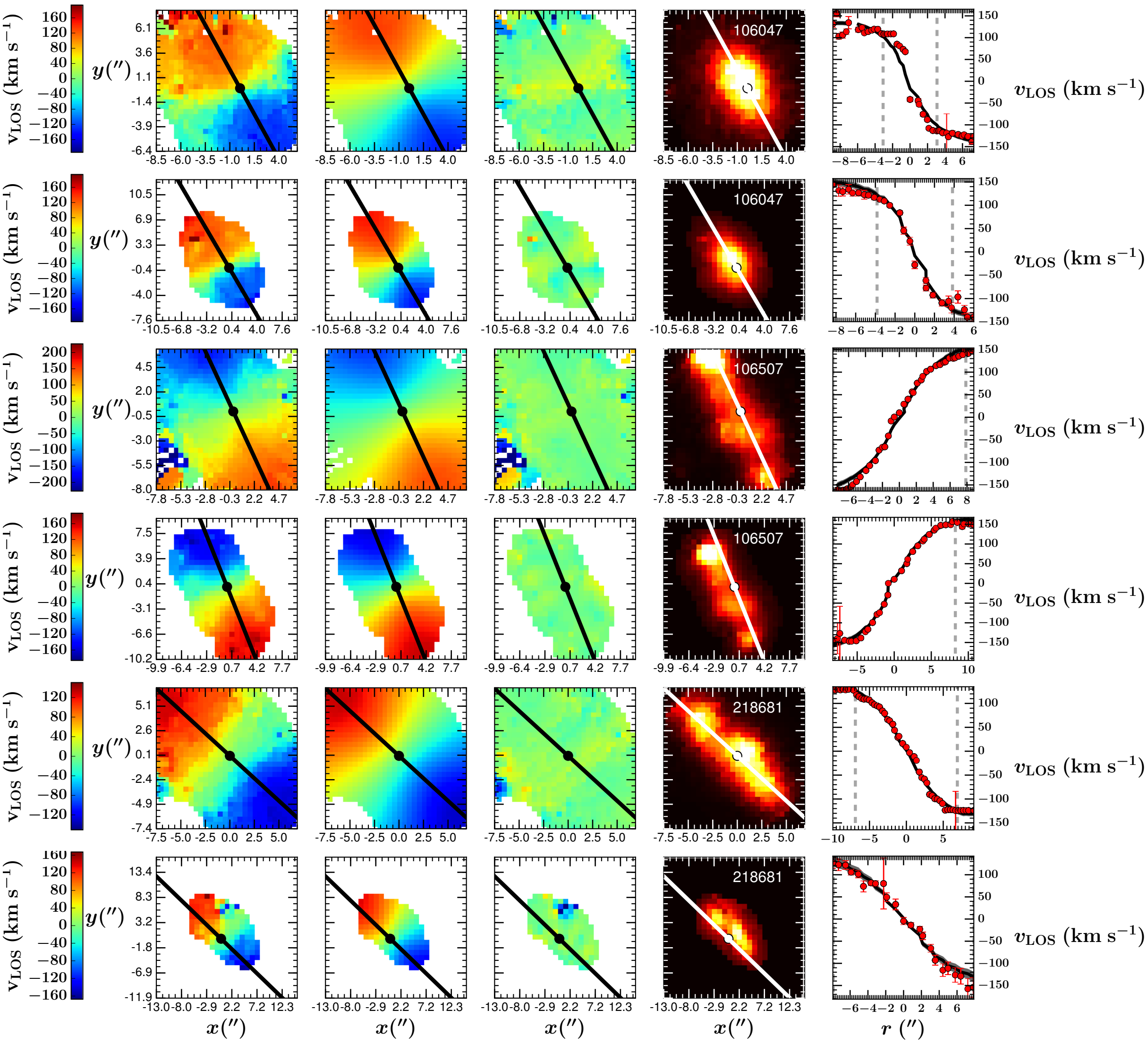

Figure 3.1: Three examples of SAMI HQ velocity fields that are well modelled by the arctangent function and the corresponding LQ velocity field. HQ and LQ galaxies are arranged in alternating rows, starting with HQ on the top row. For each galaxy the observed (far-left) and best-fit model (centre-left) velocity fields are displayed along with the residual (centre). The Hα flux map (centre-right) is constructed by integrating the best-fit LOS velocity distribution in each spaxel. The rotation curve from the observed velocity field is shown on the far-right (red points). This is constructed by extracting the mean velocity at each spaxel along the best-fit major axis (black line in the velocity field, best-fit model, and residual, and white line in the Hα map). The rotation curve is not corrected for inclination. We also plot the rotation curve extracted from the best-fit model as the black curve in the far-right panel. We include the $\pm1\sigma$ bootstrap uncertainties as a shaded grey region. The vertical dashed grey lines indicate radii of $\pm1.31r_e$. We include the SAMI galaxy ID at the top right of the Hα map. We stress the black curve is not a fit to the extracted rotation curve, but rather it is extracted from the best-fit model.

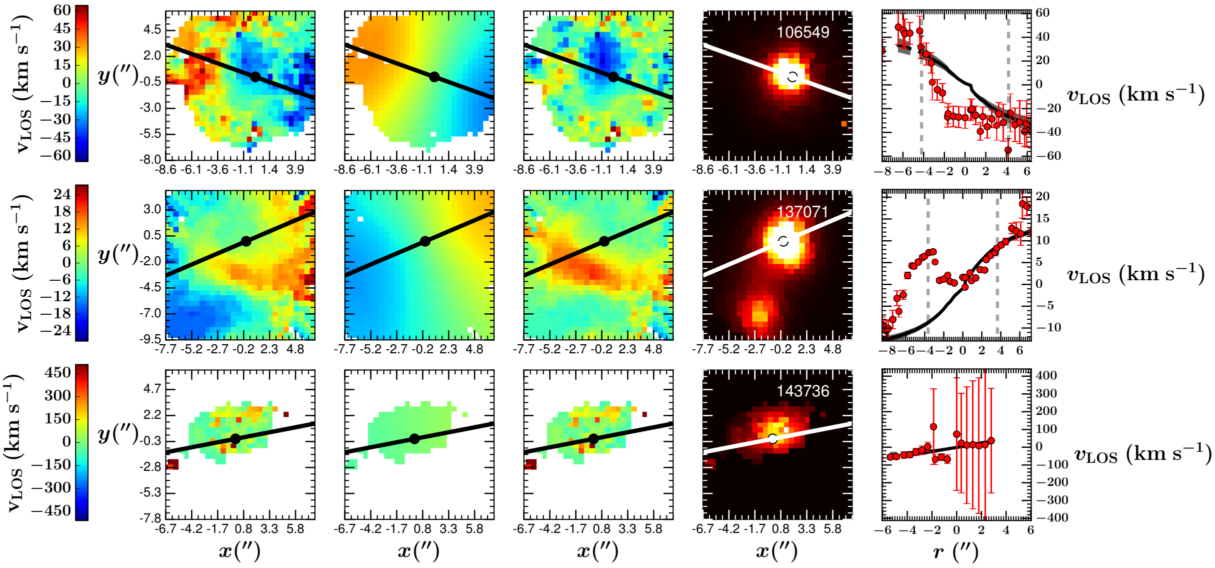

Figure 3.2: As Figure 3.1, but for three SAMI HQ velocity fields that are *not* well modelled by the arctangent function and that dropped out of our analysis after degrading.

3.3 SAMI LQ Data

3.3.1 SAMI to KROSS Match

As discussed at length above, to facilitate a direct and fair comparison between the TFR at $z \approx 1$ and $z \approx 0$, we must degrade the HQ SAMI data so that they match the typical quality of KROSS observations. Specifically, we must ensure that respectively the spatial (relative to the size of the galaxy, i.e. in physical rather than angular scale) and spectral resolution and sampling, and the Hα S/N of the SAMI cubes match those of KROSS observations of galaxies of similar stellar masses. We also require that the spatial extent of the data should be comparable to that of KROSS - more specifically we only require that the field-of-view (FOV) or spatial extent of the Hα emission (whichever is smallest) is enough to measure the LOS velocity in the outer (i.e. flat) parts of the galaxies' rotation curves, as for KROSS. The radius at which we take our velocity measure is a delicate choice and is justified and discussed in § 3.4.2.

It should be stressed that degrading the SAMI cubes to match the typical Hα S/N of KROSS observations does nothing to address the question of how the observed Hα S/N of SAMI galaxies would be affected were they observed with KMOS at similar distances as the KROSS galaxies and in the same manner as KROSS, i.e. in this work we do not adjust the flux to mimic the effects of "redshifting" a galaxy to $z \approx 1$. We focus only on how IFU observations of galaxies of differing qualities at any epoch bias the resultant galaxy sample and measurements. We thus degrade the SAMI data to match the quality of KROSS purely to negate any observational biases. We leave the subject of cosmological and evolutionary sample selection biases to future work. Each of the-fully reduced, flux-calibrated, telluric-corrected red data cubes from the SAMI internal data release v0.9 was thus degraded in the following manner, step by step.

3.3.1.1 Spatial Resolution and Sampling

First, the seeing of each SAMI HQ cube was calculated by fitting a two-dimensional, circular Gaussian to the median-collapsed image of the corresponding reference star (i.e. the median intensity value in each spaxel, that should trace the observed continuum light distribution of the star), extracted from the relevant star cube. This fit was performed using the MPFIT2DPEAK function in INTERACTIVE DATA LANGUAGE (IDL). The seeing was then taken as the full-width-at-half-maximum (FWHM) of the best-fit Gaussian, FWHM_0, in angular scale. The median FWHM seeing of KROSS observations is $\approx 0.7''$, corresponding to a size of ≈ 5.3 kpc at $z = 0.8$ (the median redshift of KROSS galaxies). To match the SAMI seeing in physical scale to KROSS we thus require a $\mathrm{FWHM}_1 = 5.3\ \mathrm{kpc}/S_\mathrm{D}$, where S_D is the co-moving distance at the redshift of the SAMI galaxy, calculated assuming a WMAP9 cosmology (Hinshaw et al., 2013).

To match the seeing of the SAMI data cubes to that of KROSS, we therefore simply convolved each spectral slice with a two-dimensional circular Gaussian (normalised so that its integral is unity) of width

$$\mathrm{FWHM}_\delta = \sqrt{\mathrm{FWHM}_1^2 - \mathrm{FWHM}_0^2}\ . \tag{3.1}$$

Next, using a third-degree bivariate spline approximation (the RECTBIVARIATESPLINE[3] routine in SCIPY module in PYTHON), we regrided each of the spatially-convolved slices

---

[3] `http://docs.scipy.org/doc/scipy/reference/generated/scipy.interpolate.RectBivariateSpline.html`

of the SAMI cube so that the physical size of the spaxels matches that of KROSS. We calculated the number of spaxels, N_1, required across the width of each square SAMI slice as

$$N_1 = 0\rlap{.}''5 S_{\rm D} N_0 / \ l_{\rm K} \ , \tag{3.2}$$

where N_0 is the original number of spaxels across the width of the SAMI slice and $l_{\rm K} =$ 1.6kpc is the physical width of a $0\rlap{.}''2$ wide KROSS spaxel at the median redshift of KROSS galaxies ($z = 0.8$).

3.3.1.2 Spectral Resolution and Sampling

We then require to match the SAMI resolving power to that of KROSS. We use a Gaussian filter in PYTHON to smooth the spectrum of each spaxel, using a Gaussian of width

$$\mathrm{FWHM_d} = \sqrt{\mathrm{FWHM_K^2} - \mathrm{FWHM_S^2}} \ , \tag{3.3}$$

where $\mathrm{FWHM_K} = \lambda_{\rm central}/(R_{\rm K})$ is the width of a Gaussian corresponding to the SAMI spectral resolution required to match the resolving power of KROSS ($R_{\rm K}$), $\lambda_{\rm central}$ is the central wavelength of the SAMI red filter and $\mathrm{FWHM_S}$ is the width of a Gaussian corresponding to the original spectral resolution of SAMI. To match the spectral sampling to that of KROSS we then binned up the smoothed spectra, using a linear interpolation to calculate the flux in each bin.

3.3.1.3 Hα S/N

Lastly, we match the distribution of Hα S/N in the spaxels of each SAMI cube to that of KROSS observations of galaxies of similar masses. As discussed in § 3.2.3.2, given that we typically do not detect spatially extended continuum emission in KROSS, and that we are primarily interested in a comparison of the gas kinematics of SAMI and KROSS galaxies, we first remove any continuum signal from the SAMI cubes by fitting a $0^{\rm th}$ order polynomial to the spectrum of each spaxel of each SAMI cube, excluding regions containing sky, Hα or [NII] emission, and then subtracting the best-fit from each spectrum. Using the baseline-subtracted cubes, we then simultaneously fit the Hα, [NII]6548, and [NII]6583 emission lines of each spectrum with three single Gaussians, in the exact same manner as described in § 2.3.1. Both the baseline fit and emission line fits are performed using the routine PySpecKit (Ginsburg & Mirocha, 2011), that uses MPFIT[4] (Markwardt 2009; translated into PYTHON by Mark River and updated by Sergey Koposov), that employs a Levenberg-Marquardt minimisation algorithm. We then take the S/N of the Hα emission in each spaxel as the square root of the difference between the χ^2 value of the best-fit Gaussian (to the Hα emission line) and that of the best-fit straight line (avoiding regions of sky emission). This approach relies on the assumption that the χ^2 of the noise in the spectrum is unity i.e. that the noise is Gaussian.

To ascertain the typical S/N of the Hα emission in KROSS observations of galaxies of a similar mass, for each SAMI galaxy we select galaxies from the KROSS survey within the stellar mass interval $\log(M_{\rm S}/M_{\odot}) \pm \Delta M$, where $M_{\rm S}$ is the stellar mass of the SAMI galaxy in question, and initially $\Delta M = 0.01$ dex. If necessary, ΔM is increased in increments of 0.01 dex such that there are at least 2 KROSS galaxies with which to compare each SAMI galaxy. For each KROSS galaxy selected, we then calculate the S/N of the Hα emission in each spaxel. To match the S/N of the SAMI galaxy to the KROSS galaxies, we require that the maximum S/N of the spaxels in the SAMI cube ($(S/N)_{\rm S,max}$) is equal to the maximum S/N measured across all spaxels of all the mass-matched KROSS cubes ($(S/N)_{\rm K,max}$). To achieve this, we must therefore increase the noise (and thus decrease the S/N) in all the SAMI spectra. We thus require a final noise value

$$N_{\rm f} = N_{\rm i}\ (S/N)_{\rm S,max}/\ (S/N)_{\rm K,max}\ . \tag{3.4}$$

for the spectrum in each SAMI spaxel, where the noise $N_{\rm i}$ is the root-mean-square value of the original spectrum in an wavelength range devoid of signal. To set the final noise to the required value, we add random Gaussian noise to the original spectrum where the width of the noise Gaussian is given by

---

[4] https://code.google.com/p/astrolibpy/source/browse/mpfit/mpfit.py

$$\sigma_{\mathrm{rms},\delta} = \sqrt{N_{\mathrm{f}}^2 - N_{\mathrm{i}}^2}\ . \tag{3.5}$$

3.3.2 SAMI LQ TFR

3.3.2.1 Velocity Field Models

Once the SAMI cubes are degraded to match the quality of KROSS observations, we extract velocity fields in the same manner as for the SAMI HQ and KROSS cubes, as described in § 2.3.1 and § 3.2.3.3. To model the resultant velocity fields we use the same iterative clipping method as described in § 3.2.3.3. However, given that the residuals between the observed and best-fit model velocity fields may not be as sharply peaked, we err on the side of caution and iteratively remove spaxels with residuals outside of a critical range of $\mu \pm 2.5\sigma_{\mathrm{s.d.}}$ only. The width of this critical range was a subjective choice but was determined as a compromise between maintaining a reasonable number of spaxels in the velocity field and ensuring the best-fit is not biased by clear outliers (as determined by visual inspection of a subset of SAMI LQ observed and best-fit velocity fields). The dynamical centres are again constrained to be spatially coincident with the peak of the continuum derived from the HQ SAMI cubes. Given the uncertainty in the HQ to LQ centering, however, we relax the constraint on the best-fit dynamical centre such that it now must fall within 1.5 spaxels of the peak continuum position. This matches the constraint applied when finding the best-fit model KROSS velocity fields (see § 3.4.1), where the position of the continuum peak is measured from maps with spaxels equal in size to the KROSS velocity maps and therefore with a much coarser spatial sampling than the SAMI HQ continuum maps. Examples of the LQ SAMI velocity fields and associated best-fit models are displayed in Figure 3.1. The same plot for each galaxy in a *disky* sub-sample (see § 3.4.3) of SAMI LQ galaxies are displayed in Figure B.2 of Appendix B.

3.3.2.2 SED Fits

Since the purpose of degrading the SAMI data cubes was to make a fair and direct comparison of the KROSS $z \approx 1$ TFR and the SAMI $z \approx 0$ TFR, we apply the same conditions to the SED fits as we applied to degrading the quality of the SAMI cubes. Specifically, we must restrict the available SAMI photometry to only include bandpasses that match those available in the restframe for the KROSS galaxies. In practice, this means truncating the full SAMI photometry range to only span the FUV to K band. Stellar masses and absolute K-band magnitudes are then derived from the truncated SEDs using Le Phare in the exact same manner as for the KROSS photometry in Chapter 2 (see § 2.3.4).

3.4 Homogenising the TFRs

After completing the velocity field modelling and SED fitting for the SAMI HQ and SAMI LQ samples, we may now begin to compare the TFRs of each sample to those of KROSS. However, to do this we must first ensure that the relations of each sample are constructed in the most homogeneous manner possible. This includes ensuring that we extract a LOS velocity for each galaxy at the same radius, despite the differences in the spatial resolution of the imaging between the various samples. It also entails selecting galaxies using uniform criteria to construct the TFRs of each sample. Since we wish to exclude galaxies from our analysis based on the ratio of rotation to dispersion support in each, we must extract intrinsic velocity dispersions from the SAMI HQ and LQ data cubes in the exact same manner as Stott et al. (2016) did from the KROSS cubes. Additionally, with the privilege of more accurate measures of the size and inclination for the KROSS galaxies, as derived by Harrison et al. (in preparation) in a careful analysis of composite KROSS imaging, we may now improve the modelling process of the KROSS velocity fields so that it matches the methods applied to the SAMI HQ and SAMI LQ fields.

In light of these requirements, in this section we detail steps taken to homogenise the SAMI HQ, SAMI LQ and KROSS TFRs presented in § 3.5. In particular we describe improvements to the measure of the KROSS TFR in § 3.4.1, consistent measurements (between the SAMI HQ, SAMI LQ, and KROSS samples) of galaxy rotation and intrinsic velocity dispersion in § 3.4.2 and § 3.4.2, respectively and the application of identical criteria to select sub-samples of galaxies (based on the selections presented in § 2.3.5) from both the KROSS and SAMI (HQ and LQ) data sets.

3.4.1 KROSS Measurements Improvements

As mentioned in § 3.2.3.3, as a result of a careful re-analysis of the KROSS data cubes and photometry by Harrison et al. (in preparation), we are now able to improve on the KROSS galaxy rotation velocities presented in Chapter 2. The improvements are made to both the velocity field fitting process and the methods of velocity extraction from the subsequent best-fit model velocity fields. The former stem from employing the improved iterative 2.5σ-clipping fitting routine (as detailed in § 3.2.3.3) to find the new best-fit arctangent model, and from the use of newly measured continuum peak positions to constrain the best-fit dynamical centre. Despite the difficulty of measuring continuum in the KROSS cubes, Harrison et al. found that many KROSS cubes have a number of spaxels with detectable continuum emission. In the majority of cases (84% of KROSS galaxies detected in Hα) this allows to measure the position of the continuum peak. Unfortunately the continuum is still insufficient to measure a radius. In a small number of additional cases (11% of Hα detected KROSS galaxies) for which the continuum emission is too faint (as judged by eye), the integrated Hα flux map is used to confirm the estimate of the galaxy centre from the continuum map. In the remaining cases (5% of Hα detected KROSS galaxies) neither of these methods are applicable, so the best centre position is determined by visual inspection of the observed velocity field. As with the LQ SAMI velocity field modelling, we constrain the best-fit dynamical centre to fall within $0.''3$ of the best centre position. The best-fit model velocity fields and corresponding observed velocity fields for a *disky* sub-sample (see § 3.4.3) of KROSS galaxies are displayed in Figure B.3 of Appendix B. There we also display rotation curves extracted from both, along with the integrated Hα maps for each galaxy.

Following the improved velocity field fitting, the improvements to the subsequent measure of the galaxy rotation velocity stem from the use of the newly measured characteristic radii and inclinations derived by Harrison et al. using the finest spatial resolution archival images available for the KROSS galaxies. The archival imaging comprises *HST* observations of the majority of the KROSS fields (the Extended *Chandra* Deep Field-South Survey (ECDFS) field, the COSMOlogical evolution Survey (COSMOS) field, and subsets of the

UK Infrared Telescope (UKIRT) Infrared Deep Sky Survey (UKIDSS; Lawrence et al., 2007) Ultra Deep Survey (UDS) field), and UKIRT images of those UDS targets without *HST* imaging and each Special Selected Area (SSA22) target.

Both the half-light radii and inclinations derived from the KROSS broad-band images are improvements over those derived from the integrated Hα maps in Chapter 2, as the broadband images trace primarily the stellar light, that is less prone to clumpiness than the Hα emission. Since it better traces the underlying stellar mass, the peak of the stellar light is also more likely to coincide with the true dynamical centre of the galaxy, particularly at high-z. For the same reasons, the inclinations derived from Hα less accurately constrain the true inclinations of the galaxy disks.

The improvements listed here mean that the resultant KROSS TFRs are directly comparable to the SAMI HQ and LQ relations with regard to their method of construction.

3.4.2 Rotation Velocity and Velocity Dispersion Measurement

Satisfied that the methods used to construct and model the velocity fields of each of the SAMI HQ, SAMI LQ, and KROSS galaxy samples are as homogeneous as possible, we must also ensure that we extract a LOS velocity from each galaxy at a uniform radius across each of the model fields, taking account of differences between both the spatial resolution of the broadband imaging of each survey and between the broadband imaging and the IFU observation of each.

As there are potential degeneracies between several parameters of the arctangent model (e.g. between the turnover radius, inclination and asymptotic rotation velocity), we do not assign any physical meaning to the best-fit model parameters (aside from the best-fit systemic velocity and the position angle, both of which seem to be robustly measured). The best-fit model is intended solely as a noiseless description of the observed velocity field. For the measure of the rotation velocity necessary in the TFR, we evaluate the best fit arctangent function at 1.31 times the effective (half-light) radius $r_{\rm e}$, as measured in the r- and (predominantly) H-band for respectively SAMI and KROSS (see § 3.4.1), corrected for the image's PSF, and then convolved to the "native" seeing of the velocity maps. This radius is equivalent to 2.2 times the scale length of an exponential disk, and is physically well motivated as it corresponds to the peak of the rotation for such a disk (Freeman, 1970; Courteau & Rix, 1997; Miller et al., 2011). It also allows to extract the velocity measure at the same radius across the large majority of galaxies in each of the SAMI HQ, SAMI LQ, and KROSS data sets. See Figure 3.4 for a comparison of the stellar half-light radii (panel a) and Hα radial extent (panel d) of the SAMI and KROSS galaxies, that shows that whilst the average r_e of KROSS galaxies is larger than the average SAMI HQ and SAMI LQ r_e, the fraction of galaxies with Hα emission that extends out to or beyond $1.31r_{\rm e}$ (2.2 times the disk scale length) is comparable between the KROSS, SAMI HQ and SAMI LQ samples. We note that this radius is smaller than r_{80} used in Chapter 2, that corresponds to $\approx 1.8r_{\rm e}$ ($\approx$ 3 times the disk scale length). If the Hα emission does not reach $1.31r_{\rm e}$, we extract the velocity measure at the maximum Hα extent along the galaxy's position angle axis.

Finally, the rotation velocity measure, which we refer to as $v_{2.2}$, is corrected for the effects of inclination i derived from the galaxy axial ratio q as

$$\cos(i) = \left(\frac{q^2 - q_0^2}{1 - q_0^2}\right)^{1/2} \quad , \tag{3.6}$$

where q is measured in the same band as $r_{\rm e}$. We adopt an intrinsic axial ratio of $q_0 = 0.2$, following the prescription adopted by Davis et al. (2011) for late-type galaxies in the local Universe.

The intrinsic velocity dispersion of each KROSS galaxy was measured by Stott et al. (2016). We measure the corresponding values for the SAMI HQ and LQ data sets in the exact same manner, summarised as follows. We first construct a map of the *observed* velocity dispersion $\sigma_{\rm obs}$, by plotting in each spaxel the width of the best-fit Gaussian to the Hα emission line in that spaxel. We then calculate the *intrinsic* velocity dispersion in each spaxel as

$$\sigma_i = \sqrt{(\sigma_{\rm obs} - {\rm d}v/{\rm d}r)^2 - \sigma_{\rm inst}^2} \ , \tag{3.7}$$

where ${\rm d}v/{\rm d}r$ is the local velocity gradient (calculated within the seeing radius and measured from the best-fit model velocity field), and $\sigma_{\rm inst}$ is the instrument spectral PSF. For a unique measure of the intrinsic velocity dispersion of each galaxy (σ), we then simply take the flux-weighted average of all the resultant intrinsic velocity dispersions within the map.

3.4.3 Sample Selection

The final step to construct the TFRs is to carefully and uniformly select those galaxies from each data set that are suitable for inclusion in the relations. Since the sample selection criteria are almost identical to those described in § 2.3.5, we retain the sample nomenclature, sorting the galaxies into three categories, namely the *parent*, *all*, and *disky* sub-samples.

As previously, we define the *parent* sub-samples as those galaxies that are detected in Hα, and for which we are able to measure a rotation velocity (even if the Hα emission does not extend out to $1.31r_{\rm e}$) with a fractional error less than 30% (for this step, we include an inspection by eye of the velocity field for each galaxy to ensure the velocity field extraction process has been successful i.e. the velocity field contains sufficient spaxels as to measure a velocity). The corresponding best-fit model to the observed velocity field must also have an associated goodness of fit parameter $R^2 > 85\%$ (see § 2.3.5). Lastly, each galaxy must have M_* and M_K values from SED fitting.

Considering the HQ SAMI data set, there are 805 galaxies detected in Hα. Each of these has an associated M_* and M_K. We were able to successfully measure a LOS velocity for 779 of these 805 galaxies. Of those, 715 galaxies had a fractional uncertainty in the measured LOS velocity less than 30%. Finally, R^2 of the associated best-fit to the observed velocity field was greater than 85% for 646 of those 715 galaxies, that thus comprise the HQ SAMI *parent* sample.

Of the 805 LQ SAMI data cubes, we were able to detect Hα in, and extract a velocity map from, 628 of them. Each of these again had an associated M_* and M_K. We successfully measured a LOS velocity for 578 of these 628 galaxies. 503 of these had a fractional error less than 30%. Finally, of these 503 galaxies, 434 had an $R^2 > 85\%$ from their best-fit model and constitute the LQ SAMI *parent* sample.

Given the improved KROSS best-fit models (see § 3.4.1), we reapply the selection criteria to the 585 KROSS galaxies with resolved Hα emission. Of these, 573 galaxies have associated M_* and M_K, each of which we were able to measure a LOS velocity for. 507 of those 573 measurements had a fractional uncertainty less than 30%. However, only 352 of those 507 galaxies had a best-fit to the velocity field with an associated $R^2 > 85\%$ and thus form the KROSS *parent* sample.

Similarly to Chapter 2, we define the *all* sub-samples as those galaxies that are a member of the *parent* sample, but also have a sufficient radial extent in Hα to emperically constrain the velocity measure adopted here (we thus require a maximum Hα radius $r_{\mathrm{H}\alpha,\mathrm{max}} \geq 1.31r_{\mathrm{e}}$). We apply kinemetry[5] (Krajnović et al., 2006) in order to exclude major-merger candidate systems from each of the SAMI HQ and LQ galaxies following the prescription of Shapiro et al. (2008) and in the exact same manner as for the KROSS galaxies, described in § 2.3.5. We exclude those galaxies with an associated KINEMETRY asymmetry parameter $K_{\mathrm{asym}} \geq 0.5$. We increase the severity of the cut in galaxy inclination from $i > 25°$ in Chapter 2 to $i > 35°$ in keeping with the findings presented in Chapter 4 (see § 4.3.2). Unlike in Chapter 2, we do not require that the best-fit dynamical centre be spatially coincident with Hα emission, as we are anyway now able to much better constrain the dynamical centre and galaxy size from the broadband images. In this chapter we add one further final criterion to the *all* sub-samples, that the ratio of rotation to intrinsic velocity dispersion $v_{2.2}/\sigma > 1$. Whilst this criterion was not explicitly applied in Chapter 2, the other selection criteria of the *all* sub-sample served to effectively impose it; all the galaxies in the Chapter 2 *all* sub-sample had $v_{80}/\sigma > 1$ (note the LOS velocity extracted at the radius containing 80% of the Hα flux, rather than $v_{2.2}$ used in this chapter).

Of the 646 SAMI HQ *parent* galaxies, 436 have $r_{\mathrm{H}\alpha,\mathrm{max}} \geq 1.31r_{\mathrm{e}}$. 382 of these have $i > 35°$ and a further 347 also have $K_{\mathrm{asym}} \leq 0.5$. A final 308 of these galaxies have $v_{2.2}/\sigma > 1$, thus comprising the HQ SAMI *all* sample.

Of the 434 SAMI LQ *parent* galaxies, 319 have $r_{\mathrm{H}\alpha,\mathrm{max}} \geq 1.31r_{\mathrm{e}}$, of which 284 have $i > 35°$, and 234 also have $K_{\mathrm{asym}} \leq 0.5$. A further 220 of these galaxies have $v_{2.2}/\sigma > 1$, thus constituting the LQ SAMI *all* sample.

Lastly, considering the KROSS *parent* sample of 352 galaxies, 283 of them have $r_{\mathrm{H}\alpha,\mathrm{max}} \geq 1.31r_{\mathrm{e}}$), of which 232 have $i > 35°$. All 232 of these galaxies have $K_{\mathrm{asym}} \leq 0.5$, and 212 of these have $v_{2.2}/\sigma > 1$, thus forming the KROSS *all* sample.

---

[5] KINEMETRY for IDL `http://davor.krajnovic.org/idl/`

Sub-sample	$N_{\rm HQ}$	$N_{\rm LQ}$	$N_{\rm KROSS}$	Selection
parent	646	434	352	Detected in Hα, $v_{2.2} > 0$, $\Delta_{v_{2.2}}/v_{2.2} < 0.3$, $R^2 \geq 85\%$, M_K and M_* from SED fitting
all	308	220	212	Member of *parent*, $r_{\rm H\alpha,max}/r_{\rm e} \geq 1.31$, $K_{\rm asym} \leq 0.5$, $v_{2.2}/\sigma > 1$, $i > 35°$
disky	162	162	50	Member of *all*, $v_{2.2}/\sigma > 3$

Table 3.1: Summary of the selection criteria and size for the sub-samples defined in § 3.4.3.

Finally, as in Chapter 2, for each data set we define a *disky* sub-sample comprising all those members of the *all* sub-sample for which the ratio of rotation velocity to intrinsic velocity dispersion $v_{2.2}/\sigma > 3$. This results in *disky* sub-samples of 162 HQ SAMI, 162 LQ SAMI, and 50 KROSS galaxies.

A summary of the selection criteria of each sample, along with the number of galaxies in each, is provided in Table 3.1 for each of the SAMI LQ, SAMI HQ, and KROSS data sets.

3.5 Results

In this section we present the M_* and M_K TFRs of the *all* and *disky* sub-samples of the SAMI HQ, SAMI LQ and KROSS data sets. In Figure 3.4 we present histograms of various derived quantities for the *parent*, *all* and *disky* sub-samples of each of the three data sets. These include the quantities used to construct the TFRs (i.e. $v_{2.2}$, σ, M_K, and M_*), but also quantities that inform our interpretation and discussion of the relations, namely the intrinsic half-light radius r_e and the scaled Hα radial extent relative to the stellar disk $r_{\rm H\alpha,max}/h$, where we calculate the disk scale length as $h = 0.6r_{\rm e}$ under the assumption that each galaxy is an exponential disk. In Figure 3.3 we further present the mass-size relations of the SAMI HQ, SAMI LQ, and KROSS *parent* samples, that show that the galaxies of all three data sets follow the same general trend of increasing size with increasing stellar mass (as is expected), although the KROSS sample is clearly biased to higher stellar masses.

The SAMI HQ and LQ TFRs are compared in § 3.5.1, where the biases introduced via the degrading process are explored. In § 3.5.2 we then compare the SAMI LQ and KROSS TFRs to measure the evolution of the relations since $z \approx 1$.

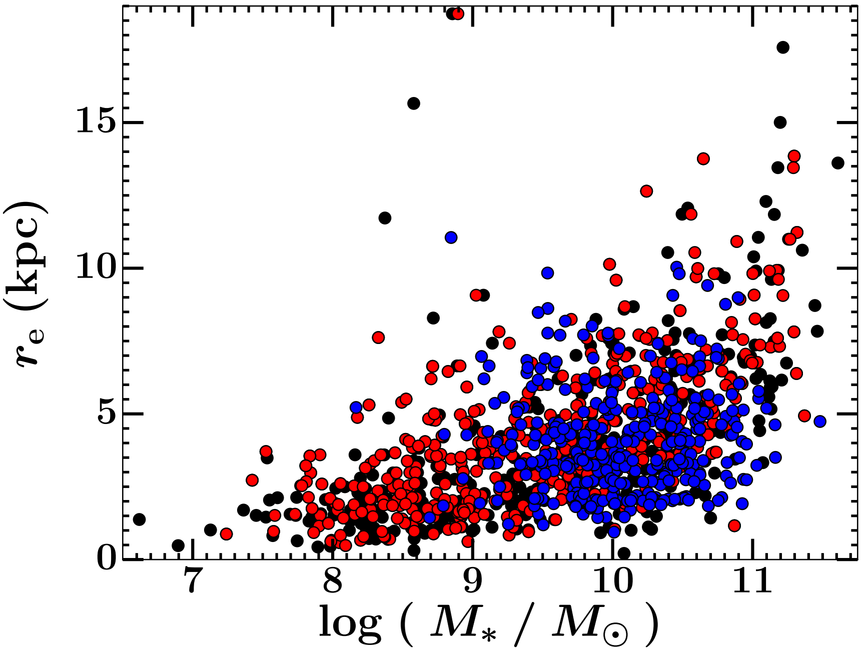

Figure 3.3: Mass-size relation (r_e-log$M_*/M_\odot$), for the SAMI HQ (black), SAMI LQ (red), and KROSS (blue) *parent* sub-sample, respectively. The three sub-samples generally follow the same trend, more massive galaxies tending to be larger (as expected Shen et al., 2003; Bernardi et al., 2011). The KROSS *parent* sub-sample is, however, limited to higher stellar masses than the SAMI HQ and LQ sub-samples.

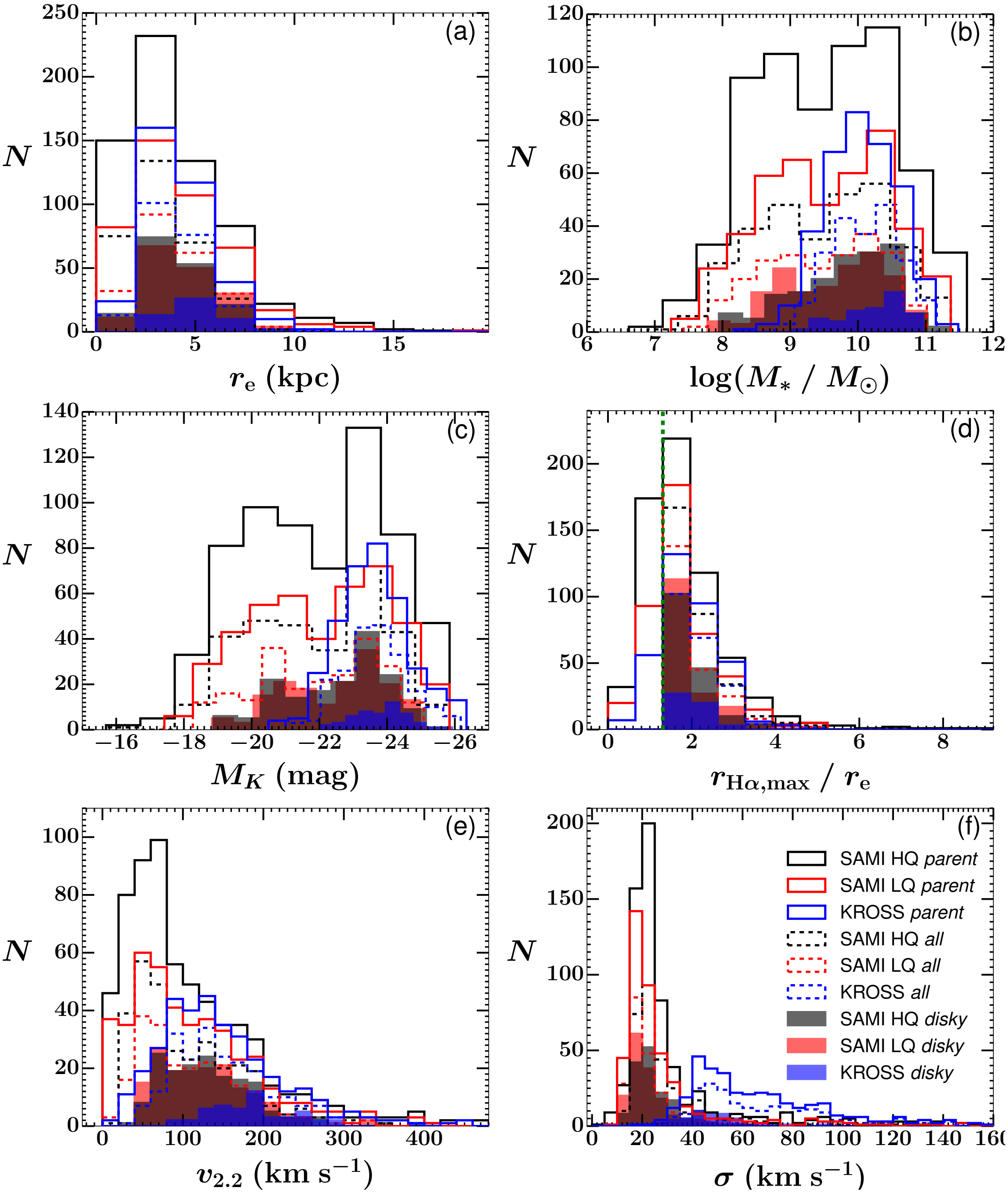

Figure 3.4: Distributions of the intrinsic (i.e. deconvolved) half-light radii (r_e), $\log(M_*/M_\odot)$, M_K, $v_{2.2}$ and σ, as defined in the text, for respectively the SAMI HQ, SAMI LQ, and KROSS *parent*, *all* and *disky* sub-samples (defined in § 3.4.3). For each of the three data sets, the width of the distribution, and the position of the peak in all of the distributions remain approximately constant between the *parent* sample and sub-sample *all* for each of the three data sets. Comparing the *disky* sub-sample to the *parent* and *all* sub-samples for all three data sets, however, the peak position is similar for M_K, $\log(M_*/M_\odot)$ and σ but is biased to higher values for $v_{2.2}$. The KROSS *disky* sub-sample is also biased towards galaxies with larger r_e. However, this is not the case for the SAMI HQ and LQ *disky* sub-samples. The green dashed line in panel (d) indicates the radius corresponding to $1.31r_e$ (2.2 disk scale lengths) at which we measure the LOS velocity for the TFRs shown in § 3.5.1 and § 3.5.2. It can be seen that the fraction of galaxies with $r_{H\alpha,\max} \geq 1.31r_e$ is comparable between the three *parent* samples. $r_{H\alpha,\max} \geq 1.31r_e$ for the *all* and *disky* sub-samples of all three data sets, by design.

Data Set	Sample	Fit	Slope	Intercept	Pivot	$\sigma_{\rm tot}$ (mag)	$\sigma_{\rm int}$ (mag)	$\zeta_{\rm tot}$ (dex)	$\zeta_{\rm int}$ (dex)
SAMI HQ	*all*	free	-6.6 ± 0.2	-21.9 ± 0.3	1.93	0.956 ± 0.004	0.83 ± 0.04	0.1426 ± 0.0008	0.125 ± 0.007
	disky	free	-7.6 ± 0.3	-22.8 ± 0.3	2.11	0.571 ± 0.005	0.45 ± 0.04	0.0748 ± 0.0007	0.059 ± 0.006
SAMI LQ	*all*	free	-6.4 ± 0.2	-22.0 ± 0.4	1.97	0.913 ± 0.005	0.79 ± 0.05	0.142 ± 0.001	0.123 ± 0.008
		fixed	-6.6 ± 0	-21.77 ± 0.06	1.93	0.949 ± 0.003	0.81 ± 0.05	0.1444 ± 0.0004	0.123 ± 0.008
	disky	free	-7.5 ± 0.2	-22.6 ± 0.6	2.08	0.631 ± 0.006	0.50 ± 0.05	0.084 ± 0.001	0.068 ± 0.007
		fixed	-7.6 ± 0	-22.8 ± 0.1	2.11	0.641 ± 0.003	0.50 ± 0.05	0.0848 ± 0.0003	0.066 ± 0.007
KROSS	*all*	free	-4.1 ± 0.5	-23.63 ± 0.09	2.13	0.891 ± 0.005	0.88 ± 0.04	0.1596 ± 0.0007	0.155 ± 0.008
		fixed	-6.4 ± 0	-22.60 ± 0.08	1.97	1.142 ± 0.004	1.13 ± 0.06	0.1785 ± 0.0006	0.176 ± 0.009
	disky	free	-6 ± 1	-23.9 ± 0.2	2.26	0.69 ± 0.01	0.68 ± 0.07	0.099 ± 0.002	0.10 ± 0.01
		fixed	-7.5 ± 0	-22.5 ± 0.1	2.08	0.81 ± 0.01	0.79 ± 0.08	0.108 ± 0.002	0.11 ± 0.01

Table 3.2: Parameters of the best M_K TFRs fits for the *all* and *disky* sub-samples. Uncertainties are quoted at a 1σ level (parameters are quoted at the corresponding precisions), and the intercept of each relation is calculated at the stated pivot.

Data Set	Sample	Fit	Slope	Intercept	Pivot	$\sigma_{\rm tot}$ (dex)	$\sigma_{\rm int}$ (dex)	$\zeta_{\rm tot}$ (dex)	$\zeta_{\rm int}$ (dex)
SAMI HQ	*all*	free	3.22 ± 0.08	9.4 ± 0.2	1.93	0.500 ± 0.002	0.44 ± 0.02	0.1520 ± 0.0009	0.139 ± 0.007
	disky	free	3.6 ± 0.1	9.9 ± 0.2	2.11	0.366 ± 0.003	0.29 ± 0.03	0.098 ± 0.001	0.079 ± 0.007
SAMI LQ	*all*	free	3.04 ± 0.09	9.5 ± 0.2	1.97	0.450 ± 0.003	0.39 ± 0.03	0.148 ± 0.001	0.132 ± 0.008
		fixed	3.22 ± 0	9.34 ± 0.03	1.93	0.476 ± 0.001	0.41 ± 0.03	0.1479 ± 0.0005	0.130 ± 0.008
	disky	free	3.6 ± 0.1	9.7 ± 0.2	2.08	0.381 ± 0.003	0.30 ± 0.03	0.102 ± 0.001	0.085 ± 0.008
		fixed	3.6 ± 0	9.84 ± 0.03	2.11	0.388 ± 0.002	0.31 ± 0.03	0.1069 ± 0.0004	0.085 ± 0.008
KROSS	*all*	free	2.4 ± 0.2	10.06 ± 0.06	2.13	0.421 ± 0.002	0.37 ± 0.02	0.148 ± 0.002	0.135 ± 0.008
		fixed	3.04 ± 0	9.58 ± 0.03	1.97	0.491 ± 0.002	0.45 ± 0.03	0.1618 ± 0.0005	0.147 ± 0.009
	disky	free	3.9 ± 0.5	10.2 ± 0.1	2.26	0.408 ± 0.009	0.35 ± 0.05	0.095 ± 0.003	0.09 ± 0.01
		fixed	3.6 ± 0	9.58 ± 0.06	2.08	0.429 ± 0.006	0.38 ± 0.05	0.118 ± 0.002	0.11 ± 0.01

Table 3.3: Parameters of the best M_* TFR fits for the *all* and *disky* sub-samples. Uncertainties are quoted at a 1σ level (parameters are quoted at the corresponding precisions), and the intercept of each relation is calculated at the stated pivot.

TFR	Sample	SAMI LQ-SAMI HQ	KROSS-SAMI LQ
M_K	*all*	0.1 ± 0.3 mag	-0.6 ± 0.4 mag
	disky	0.0 ± 0.6 mag	0.0 ± 0.6 mag
M_*	*all*	-0.1 ± 0.2 dex	0.1 ± 0.2 dex
	disky	0.0 ± 0.2 dex	-0.2 ± 0.2 dex

Table 3.4: Zero-point offsets between respectively the SAMI HQ and SAMI LQ TFRs and the SAMI LQ and KROSS TFRs, measured with a fixed slope at a given rotation velocity. Uncertainties are quoted at a 1σ level (parameters are quoted at the corresponding precisions).

3.5.1 SAMI: LQ vs. HQ

Considering only the SAMI HQ and LQ *parent* sub-samples, Figure 3.4 (b), (c), and (f) demonstrates that the degrading process described in § 3.3.1, and the subsequent velocity field modelling and extraction, do not significantly bias the resultant M_K, M_*, and σ distributions. However, panels (a), (d), and (e) reveal that compared to the SAMI HQ *parent* sub-sample, the SAMI LQ *parent* sub-sample is biased towards galaxies with larger r_e and $r_{\mathrm{H}\alpha,\mathrm{max}}/0.6r_{\mathrm{e}}$, with a large reduction in the number of galaxies with low $v_{2.2}$.

This can be understood by considering how the degrading process disproportionately affects those galaxies that are either intrinsically compact, or have compact Hα emission. In these cases, decreasing the spatial resolution and sampling make it harder to measure a velocity gradient across the Hα emission. Most importantly, we must consider how matching the Hα S/N of the LQ SAMI cubes to those of KROSS observations can also bias our measurements (and thus sample) toward more extended objects. Since we expect the Hα to be somewhat centrally peaked (James et al., 2009), adding noise so that the peak of the SAMI Hα S/N distribution matches that of the KROSS galaxies will disproportionately affect the spaxels in the outer regions of the SAMI cubes (corresponding to lower Hα S/N), away from the galaxy centres. This means that the size of the region in which we can succesfully detect and fit the Hα emission is considerably reduced as a result of the degrading process. Since in general a galaxy's size, mass, and rotation are coupled (e.g. Shen et al., 2003; Bernardi et al., 2011), it is unsurprising that the primary effect of the degrading process is to exclude those galaxies that are more compact and more slowly rotating.

It is also clear that, not only does the $R^2 > 85\%$ condition excludes more galaxies from our analysis than any other criterion used to select the *parent* sub-samples for each data set, but also that relatively more are excluded from the LQ than the HQ sample as a result of this cut. Considering the application of this criterion in the final step of the *parent* sub-sample selection for the HQ and LQ data sets (i.e. to those galaxies detected in Hα, with $v_{2.2} > 0$, $\Delta v_{2.2}/v_{2.2} < 0.3$, and M_* and M_K from SED fits), $\approx 10\%$ of HQ galaxies are excluded by the cut whereas $\approx 14\%$ of LQ galaxies are excluded. It is therefore apparent that the degrading process reduces the number of galaxy velocity fields that are well described by the arctangent model.

Although there is a clear reduction in the number of galaxies when considering the *all* and *disky* sub-samples (from 646 to 308 and 162 galaxies for the SAMI HQ data set and from 434 to 220 and 162 galaxies for the SAMI LQ data set, respectively; see Table 3.1), applying the selection criteria of the *all* and *disky* sub-samples to both *parent* sub-samples does not appear to introduce any further bias between the SAMI HQ and SAMI LQ data sets.

Before comparing the TFRs of the SAMI HQ and LQ data sets, however, it is informative to first compare the measurements used to construct both, i.e. assess how the measurements of $v_{2.2}$ and σ are affected by the degradation process and subsequent velocity field extraction and modelling. Similarly, we must quantify to what extent the truncation of the SAMI SEDs alters the derived M_* of each galaxy (M_K is nearly SED independent and thus unaffected). We thus compare the $v_{2.2}$, σ, and M_* measurement of those galaxies in the SAMI LQ *parent* sample to the corresponding measurements made using the SAMI HQ data.

Figure 3.5 shows comparisons between the LQ and HQ measurements of $v_{2.2}$ (top), σ (middle), and M_* (bottom). The parameters of the bisector of the best forward and best reverse straight line fit (with free slopes) to each comparison are listed in Table 3.5, along with measures of the total and intrinsic scatters. The LQ and HQ measurements generally agree with each other, being highly correlated with best fits consistent with 1:1 relations with varying total scatters (and no systematic offset between the HQ measurements and the corresponding LQ measurements). For each measure, we calculate total and intrinsic scatters that are consistent between the HQ and LQ measurements. For the $v_{2.2}$ measurements, we find a total scatter of 50.8 ± 0.2 and 51.2 ± 0.2 km s^{-1} for the LQ and HQ data, respectively and corresponding intrinsic scatters of 50.0 ± 0.2 and 50.00 ± 0.05 km s^{-1}. For the measurements of σ, we find a total scatter of 10 ± 6 and 8 ± 2 km s^{-1} for respectively the LQ and HQ measurements. We find both the corresponding intrinsic scatters to be consistent with zero, suggesting perhaps that the uncertainties in σ are over-estimated. The correlation between the LQ and HQ measurements of M_* gives a total and intrinsic scatter of 0.341 ± 0.002 and 0.20 ± 0.2 dex, respectively for both the HQ and LQ measurements. Both measures of scatter in M_* are therefore essentially equal between the HQ and LQ data set. This suggests that the truncation of the SAMI LQ SEDs to match the KROSS (restframe) wavelength range does little to alter the accuracy or precision in the subsequent M_* measure from SED fitting.

That the best fits between the SAMI HQ and LQ measurements are consistent with 1:1 relations is encouraging when anticipating the KROSS measurements, as it demonstrates that despite increased scatter, reduced quality data do not hamper our ability to recover general trends in $v_{2.2}$, σ, and M_* essential to accurately measure the TFR. We therefore proceed to compare the SAMI HQ and SAMI LQ *all* and *disky* TFRs, in the knowledge that any difference between the relations is primarily a result of the bias to the sample selection introduced by the degradation process, rather than any bias in the measurements themselves. We must however keep in mind that the *scatter* in the measurements will be affected by the reduced data quality from SAMI HQ to LQ.

Figures 3.6 and 3.7 show respectively the M_K and M_* TFRs of the SAMI HQ and LQ *all* (top panel) and *disky* (bottom panel) sub-samples. The parameters of the bisector of the best forward and best reverse straight line fit (with free slopes) to each relation are listed in Tables 3.2 and 3.3, along with measures of the total and intrinsic scatters. We see that within each data set (HQ and LQ), and for both the M_K and M_* TFRs, the total and intrinsic scatters in both axes are reduced in the *disky* relations compared to the *all* relations, as a result of the tighter cut in $v_{2.2}/\sigma$. We also note that the *all* TFRs of both samples have larger total scatters compared to those of previous work at similar redshifts (Tully & Pierce (2000) found a total scatter of 0.44 mag in the K'-band TFR of $z \approx 0$ spiral galaxies and Verheijen (2001) measured a total scatter of 0.32 mag in the same filter,

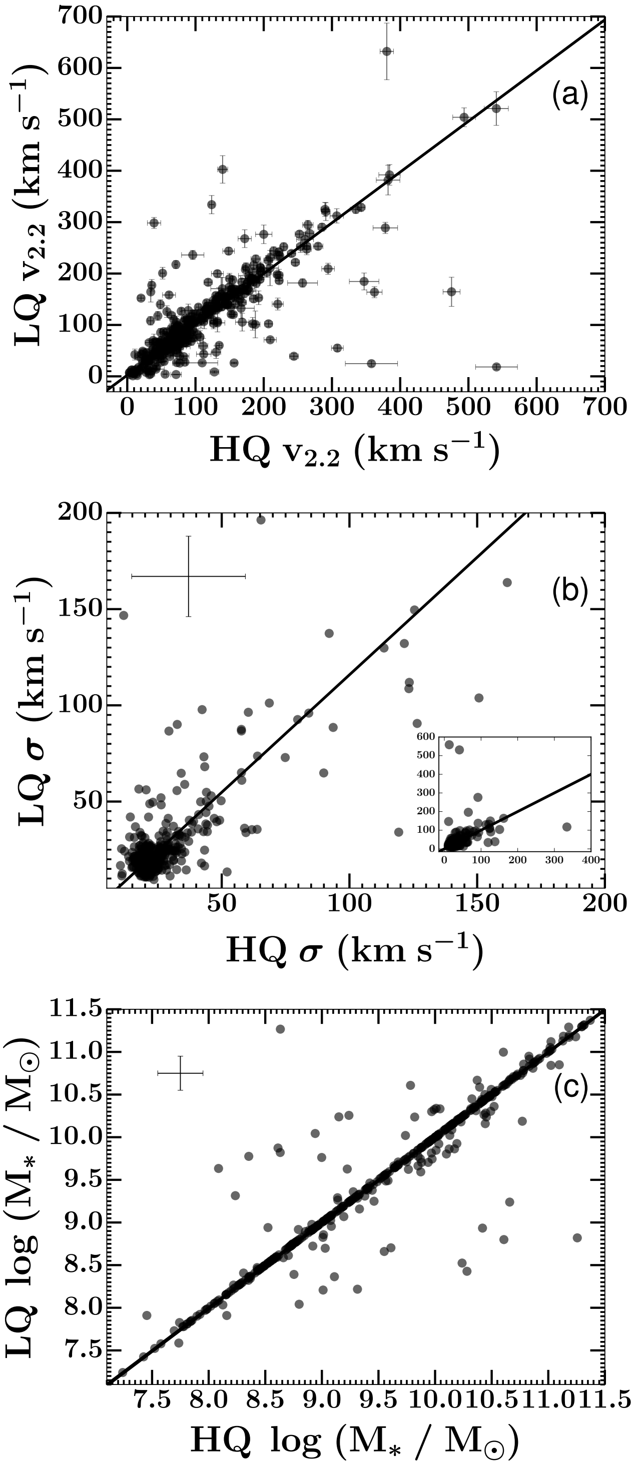

Figure 3.5: SAMI LQ *parent* sample measurements of $v_{2.2}$ (top), σ (middle) and M_* (bottom) versus the corresponding SAMI HQ measurements. The black solid line in each panel is the bisector of the best forward and best reverse fits (with free slopes) to the data. We include an inset panel with increased axis limits in panel (b) to show four outliers that would otherwise not be displayed in the main plot. In all cases, the LQ and HQ measurements generally agree, with the bisector fits consistent with one-to-one relations with varying scatters and no systematic offsets between the HQ measurements and the corresponding LQ measurements.

Measure	Slope	Intercept	Pivot	$\sigma_{\rm tot}$	$\sigma_{\rm int}$	$\zeta_{\rm tot}$	$\zeta_{\rm int}$
$v_{2.2}$	0.99 ± 0.02	89 ± 13	87.5	50.8 ± 0.2 km s^{-1}	50.0 ± 0.2 km s^{-1}	51.2 ± 0.2 km s^{-1}	50.00 ± 0.05 km s^{-1}
σ	1.2 ± 0.6	21 ± 21	22.3	10 ± 6 km s^{-1}	0 ± 0 km s^{-1}	8 ± 2 km s^{-1}	0 ± 0 km s^{-1}
M_*	1.00 ± 0.01	9.6 ± 0.6	9.6	0.341 ± 0.002 dex	0.20 ± 0.02 dex	0.341 ± 0.002 dex	0.20 ± 0.02 dex

Table 3.5: Parameters of the bisectors of the best forward and best reverse straight line fits (with free slopes) to the comparison between SAMI HQ and SAMI LQ measures of respectively $v_{2.2}$, σ, and M_*, as defined in the text. Uncertainties are quoted at a 1σ level (parameters are quoted at the corresponding precisions), and the intercept of each relation is calculated at the stated pivot.

whilst Bell & de Jong (2001) and Pizagno et al. (2005) measure a total scatter of 0.13 dex and an intrinsic scatter of 0.16 dex, respectively in stellar mass TFR of local late-type galaxies). Whilst these scatters may not be driven purely by the inclusion (or exclusion) of systems with small $v_{2.2}/\sigma$, it would seem that given the intrinsically low velocity dispersions of the SAMI galaxies (see Fig. 3.4 f) and indeed local late-type galaxies, a $v_{2.2}/\sigma > 1$ cut is not stringent enough to select truly rotation-dominated galaxies that obey the assumption of circular motions implicit in the TFR. One should thus bear this in mind when considering the results of studies at high redshifts that have applied such a cut to select galaxies suitable for comparison with $z \approx 0$ TFRs.

The slopes of the SAMI HQ and LQ M_K and M_* TFRs are consistent within uncertainties, for both the *all* and *disky* sub-samples.The slopes of the M_K *all* relations of both data sets are slightly shallower than those of previous similar studies (e.g. Tully & Pierce 2000 measure a slope of −8.78 for the local K'-band TFR, whilst Verheijen 2001 measure slopes varying from −8.0 to −10.6 for the TFR in the same passband for various galaxy samples), but this discrepancy disappears when considering the *disky* sub-sample TFRs, that have steeper slopes than those of the *all* sub-sample relations in every case. The slopes of the M_* *all* relations of both data sets are consistent within uncertainties with those of a similar study by Pizagno et al. (2005), who measure a slope of 3.05 ± 0.12 for the stellar mass TFR of local galaxies. However, the slopes of both *disky* TFRs are steeper than that of Pizagno et al. (but consistent with the composite stellar mass relation of Chapter 2 - see § 2.4.1 and Table 2.3).

To measure any offset between the zero-points of the SAMI HQ and LQ TFRs, we fix the slopes of the LQ relations to those of the corresponding HQ relations. The resulting SAMI HQ-SAMI LQ zero-point offsets are listed in Table 3.4. There is no significant offset of the zero-points of any of the TFRs for the *all* and *disky* sub-samples taken separately.

Comparing the scatters of the relations of the two data sets, somewhat surprisingly the SAMI HQ and LQ M_K and M_* relations of the *all* sub-samples display comparable total and intrinsic scatters in both axes. In fact, the scatter of the LQ relations are formally slightly *lower*. This is probably again testament to sample selection being the driving factor of the scatters in these relations. A key factor here is probably the inclusion of

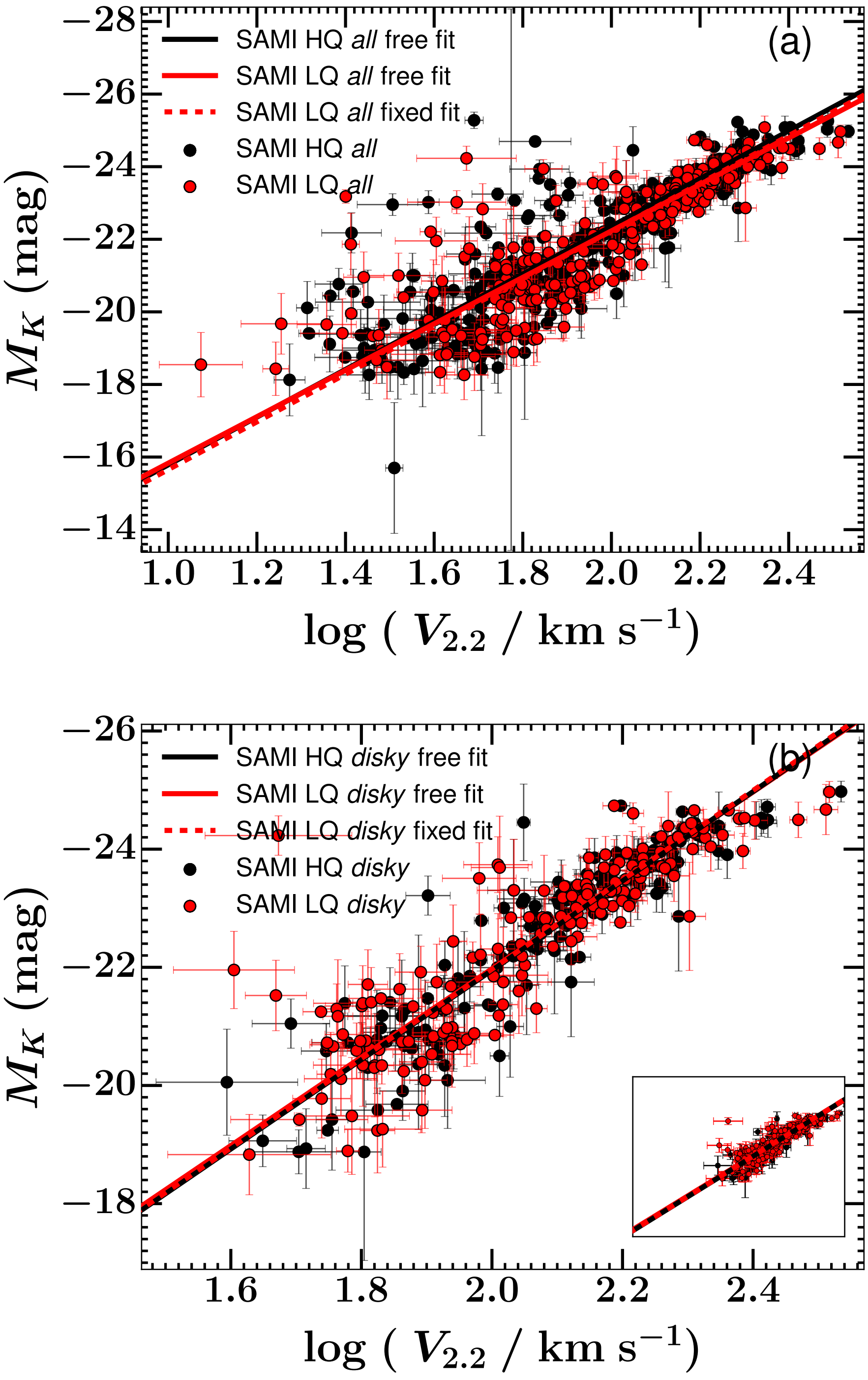

Figure 3.6: The M_K TFRs of the SAMI HQ and SAMI LQ *all* (top panel) and *disky* (bottom panel) sub-samples as described in § 3.4.3. The black and red solid lines are the bisectors of the best forward and best reverse fits (with free slopes) to the SAMI HQ and LQ data, respectively. In each panel, the red dotted line is the best straight line fit to the SAMI LQ data with the slope fixed to that of the best (free) fit to the corresponding HQ data. The embedded panel in (b) shows the *disky* TFRs but with the axes ranges of (a). For both *all* and *disky*, the slopes, offsets, and scatters of the SAMI HQ and LQ TFRs generally agree. The LQ TFR of the *all* sub-sample is however slightly truncated at its lower end compared to the HQ relation. This results in slightly decreased scatters in the LQ TFR compared to the HQ relation, as the scatters increase in both relations at low velocities. For the *disky* sub-sample, however, the scatters of the LQ TFRs are higher than those of the HQ relations, as expected.

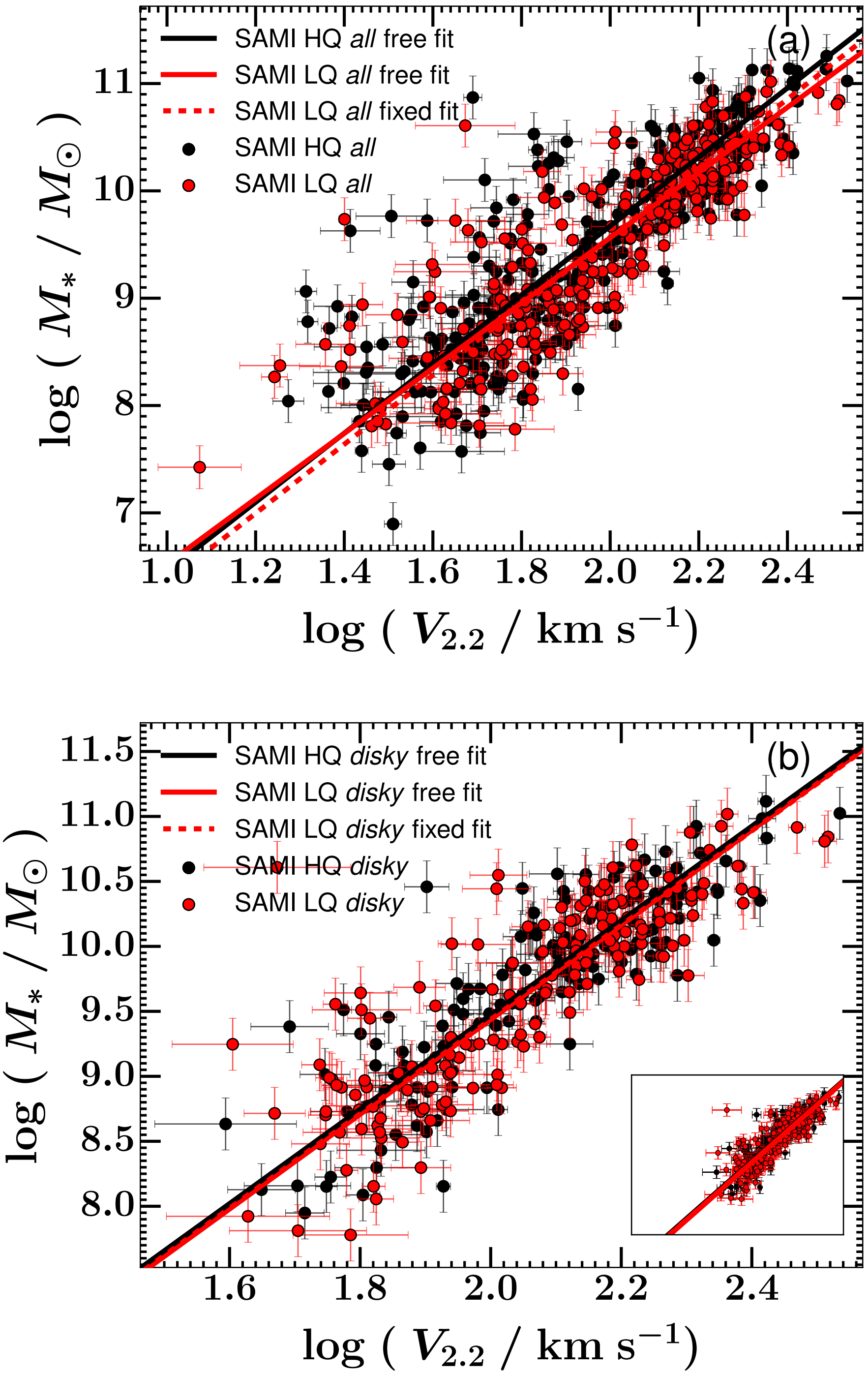

Figure 3.7: As Figure 3.6, but for the M_* TFRs of the SAMI HQ and SAMI LQ *all* and *disky* sub-samples, as described in § 3.4.3.

more galaxies at the low-velocity end of the TFR in the SAMI HQ relations. Indeed, the scatter in both axes visibly increases with decreasing velocity for each of the TFRs. We also know that the degrading process preferentially selects galaxies with more spatially extended Hα emission. It may thus be that our measurements of the rotation velocities of galaxies with compact Hα are inaccurate due to the compactness of the Hα emission and the finite spaxel size of the SAMI cubes, even for the HQ data. However, once those same cubes are degraded, we may then be entirely unable to detect the Hα emission and therefore unable to measure any rotation, excluding those galaxies from any subsequent LQ TFR. In this respect, and somewhat ironically, the process of degrading the SAMI data may actually act to preferentially select only those SAMI cubes of the highest quality (in terms of Hα emission stength and spatial extent), thus leading to lower scatter.

In this section we have thus shown that there are tangible differences between the SAMI HQ and LQ TFRs (primarily in the scatter), and that these are due to a combination of selection (primarily for the *all* sub-sample) and measurement (primarily for the *disky* sub-sample) effects. Therefore, to make a fair and unbiased comparison between the KROSS $z \approx 1$ TFRs and the SAMI $z \approx 0$ TFRs, we now proceed to compare the SAMI LQ TFRs to the KROSS TFRs and do not discuss further the SAMI HQ relations.

3.5.2 KROSS vs. SAMI LQ

Figures 3.8 and 3.9 show respectively the M_K and M_* TFRs of the SAMI LQ and KROSS *all* (top panel) and *disky* (bottom panel) sub-samples. The corresponding bisector best-fit parameters (with free slopes) are listed in Tables 3.2 and 3.3, along with the parameters of the best-fits to the KROSS TFRs when the slope is fixed to that of the corresponding SAMI LQ relation. For reference, we also show in Figures 3.8 and 3.9 the relevant composite $z \approx 0$ comparison relations used in Chapter 2 (and discussed in detail in § 2.4.1), as well as the corresponding Chapter 2 fits to the KROSS data where the slopes are fixed to those of the composite $z \approx 0$ relations. These relations will inform our interpretation of the main results presented in this chapter.

First, considering the TFRs of the SAMI LQ and KROSS *all* sub-samples, the slopes of the M_K and M_* KROSS TFRs are much shallower than those of the corresponding

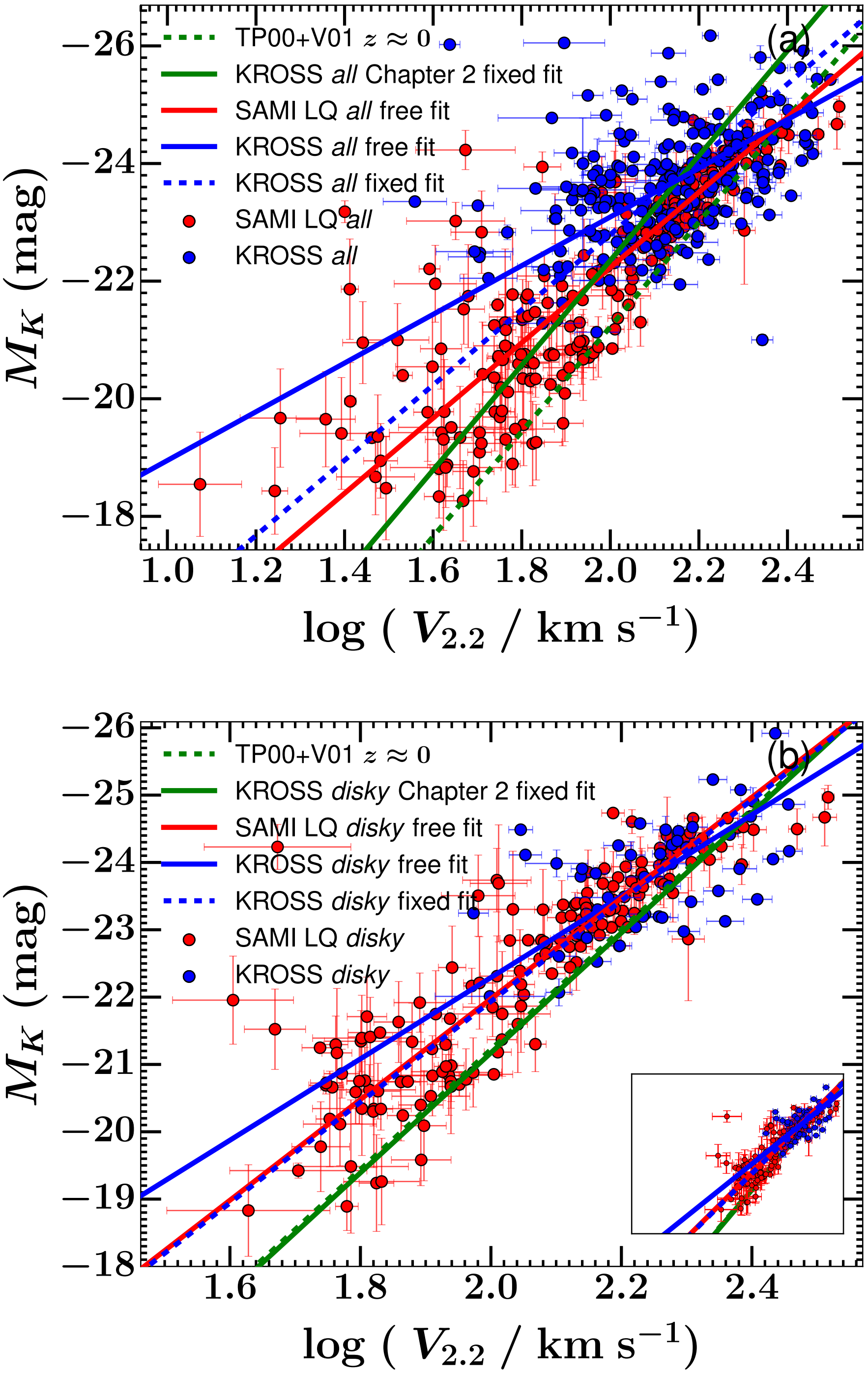

Figure 3.8: The M_K TFRs of the SAMI LQ and KROSS *all* and *disky* sub-samples, as described in § 3.4.3. The red and blue solid lines are the bisector of the best forward and reverse fits (with free slopes) to the SAMI LQ and KROSS data, respectively. The blue dashed line is the best fit the KROSS *disky* sub-sample TFR of the current chapter with the slope fixed to that of the best (free) fit the SAMI LQ *disky* sub-sample TFR. The green dashed line is the best fit the the $z \approx 0$ comparison M_K TFR of Chapter 2. The embedded panel in (b) shows the *disky* TFRs but with the axes ranges of (a).

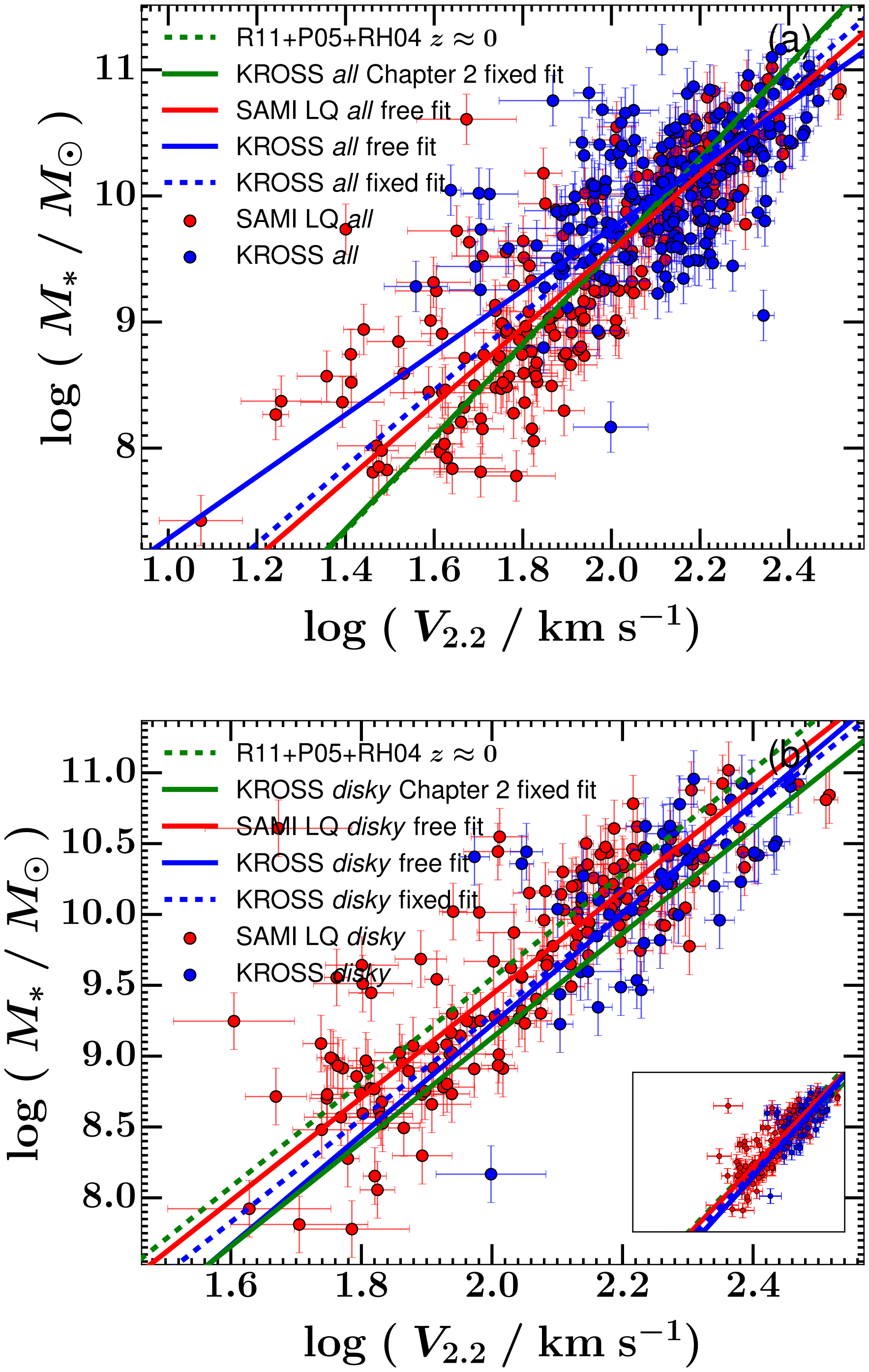

Figure 3.9: As Figure 3.8, but for the M_* TFRs of the SAMI LQ and KROSS *all* and *disky* sub-samples, as described in § 3.4.3. The green dashed line is the best fit the the $z \approx 0$ comparison M_* TFR of Chapter 2.

SAMI LQ relations. This may be the result of a combination of the increased scatter in the KROSS data and their artificial truncation at low luminosities or stellar masses (and thus velocities), due to the limiting magnitude (and thus roughly mass) of the KROSS sample. As the low-mass ends of the TFRs are not probed, the KROSS TFR slopes are also less well constrained. Now considering the SAMI LQ and KROSS TFRs of the *disky* sub-samples, we see that the slopes of both the M_K and M_* KROSS TFRs are much steeper than for the *all* sub-sample, while there is general agreement with the corresponding SAMI LQ TFRs within the uncertainties (although the slope of the M_K KROSS TFR of the *disky* sub-sample is still slightly shallower than that of the corresponding SAMI LQ relation).

Considering the scatters of the SAMI LQ and KROSS TFRs of the *all* sub-samples, the total scatters in the ordinate of the M_K and M_* KROSS TFRs are actually *smaller* than those of the corresponding SAMI LQ relations. However, the difference is reversed for the M_K relation when instead considering the intrinsic scatter, whilst for the M_* relation the intrinsic scatters are consistent within the uncertainties. Considering the scatters in the abscissa of the same relations, the total and intrinsic scatters of both KROSS TFRs for the *all* sub-sample are at least comparable to, and in most cases larger than, the corresponding SAMI LQ relations. Now comparing the SAMI LQ and KROSS TFRs of the *disky* sub-sample, the total and intrinsic scatters in M_K, M_*, and $v_{2.2}$ are larger for the KROSS data than for the SAMI LQ data in all cases, with the exception of the total scatter in $v_{2.2}$ for the M_* TFR.

To measure any offset between the zero-points of the SAMI LQ and KROSS TFRs, we fix the slopes of the KROSS relations to those of the corresponding SAMI relations. The resulting SAMI LQ-KROSS zero-point offsets are listed in Table 3.4.

Considering the offset between the SAMI LQ and KROSS M_K TFRs of the *all* sub-sample, the KROSS galaxies are 0.6 ± 0.4 mag brighter than the SAMI LQ galaxies at fixed rotation velocity. However, this zero-point offset disappears (0.0 ± 0.6 mag) when considering the *disky* sub-sample instead. Now considering the M_* TFRs of the *all* sub-sample, we measure a small zero-point offset (0.1 ± 0.2 dex) between the KROSS and SAMI LQ relations, in the sense that that the KROSS galaxies are slightly more massive than the SAMI LQ galaxies at fixed rotation velocity. For the *disky* sub-sample, this offset increases in magnitude and reverses in direction, as the KROSS galaxies are slightly less massive (-0.2 ± 0.2 dex) at fixed rotation velocity. Within the uncertainties, this is consistent with the zero-point offset we measured between the Chapter 2 KROSS relation of the *disky* sub-sample (as defined in § 2.3.5) and the composite $z \approx 0$ relation defined in that chapter (see § 2.4.1). However, we also note that, within the uncertainties, this offset is also consistent with zero evolution of the stellar mass TFR zero-point since $z \approx 1$.

It is clear that the magnitude of the measured zero-point evolution is significantly reduced with respect to the measurement made in Chapter 2. Consideration of the $z \approx 0$ composite comparison samples and the corresponding KROSS fixed slope best-fits from the same Chapter (see Figures 3.8 and 3.9) reveals two clear reasons for this. Firstly, there is a significant offset for the *disky* sub-sample between the (improved) KROSS TFR of this chapter and the fixed-slope best fit of Chapter 2 (0.1 ± 0.4 dex mean offset toward higher masses for the new measurements, where the uncertainty is the standard deviation of the offsets between the fixed-slope fit and the individual data points of this chapter). This offset may be the result of the use of inclinations and sizes derived from broadband imaging (rather than Hα emission) and improvements to the velocity field modelling in this chapter, but it is most likely the result of our now extracting the velocity measure at a smaller radius($1.31r_{\rm e}$ rather than $1.81r_{\rm e}$). Secondly, there is also a clear offset between the $z \approx 0$ composite relation of Chapter 2 (Reyes et al. 2011 [R11]+Pizagno et al. 2005 [P05]+Rhee 2004 [RH04]) and the M_* SAMI LQ TFR for the *disky* sub-sample presented in this chapter (the former being 0.1 ± 0.4 dex more massive, calculated as above). This offset may be due to the selection of galaxies via a minimum $v_{2.2}/\sigma$ value in KROSS, that is bound to preferentially select those galaxies with large $v_{2.2}$, and thus systematically bias the relation toward higher velocities (or equivalently higher masses). Since this and other potential biases are avoided through the application of homogeneous analysis methods to the SAMI and KROSS data in this chapter, we proceed with our discussion with the understanding that the measured M_* SAMI LQ-KROSS TFR offset of -0.2 ± 0.2 dex for the *disky* sub-sample presented in this chapter is the most accurate.

3.6 Discussion

The comparisons of the SAMI HQ and LQ data sets presented in § 3.5.1 are the first of their kind and constitute a direct measure of the observational biases that IFU studies of $z \approx 1$ galaxies must account for. Whilst we find the LQ sample biased toward those galaxies with more extended Hα emission and that more rapidly rotate, importantly for the comparison of TFRs at $z \approx 1$ and $z \approx 0$, not only does the degrading process not affect our ability to recover accurate measurements of key galaxy properties from the LQ data, but the selection bias introduced as the result of the lower data quality does not affect our measure of the TFRs. Indeed, we measure TFRs generally consistent in slope and zero-point between the HQ and LQ data sets. The key difference between them being the measures of total and intrinsic scatter.

That the measure of intrinsic scatter differs as the result of data quality alone is important. Accurately determining the intrinsic scatter in the TFRs at $z \approx 1$ and $z \approx 0$ is a vital step in understanding the physical processes in galaxies that underpin any difference between the relations at the two epochs. In this work, even if we cannot absolutely remove potential biases from our measures of the intrinsic scatter at each redshift, we can at least be sure that our careful matching of data quality and analysis methods allows an accurate measure of the *relative* differences between the two. Future IFU studies conducted at similar redshifts that wish to compare to the local Universe must therefore similarly nullify the potentially different biases in the TFRs at each epoch, either by matching the data quality and analysis methods between the two epochs as in this work or by otherwise addressing the potential for confused measures of the differences between the relations.

Whilst we have quantified the effects of degrading $z \approx 0$ IFU data to the quality of typical (KROSS) $z \approx 1$ observations, we must bear in mind this is not the same as asking what one might observe were the $z \approx 0$ galaxy population to be figuratively placed at $z \approx 1$ and observed in the same manner as the *actual* galaxy population at that epoch. Comparing the star formation rate in the local Universe to that at $z \approx 1$, one can imagine that the probable answer to that question is that we would see very little. Only the most rare systems at $z \approx 0$ have star formation rates comparable to typical galaxies at $z \approx 1$. We can therefore deduce that, given the sensitivity limits of current detectors and with similar exposure times as KROSS, we would detect many fewer galaxies with typical $z \approx 0$ star formation rates. Furthermore, those local galaxies with star formation rates comparable to $z \approx 1$ galaxies are generally unusual systems such as Ultra-Luminous InfraRed Galaxies (ULIRGs), galaxies with excess infrared luminosities that are now understood to be the result of gas rich mergers in the local Universe (ULIRGs; e.g. Lonsdale et al., 2006), that are quite unlike the typical star-forming galaxy at $z \approx 0$. Therefore, comparing these galaxies to typical $z \approx 1$ star-forming galaxies asks a very different question than comparing "main sequence" galaxies at each epoch (as in this work). Moreover, it requires very large numbers of IFU observations of $z \approx 0$ galaxies to then select from them a sub-sample with $z \approx 1$ rates of star formation that is comparable in size to KROSS. Therefore, whilst both are worthwhile comparisons, we have concentrated on the latter that is most directly measurable with the current sample sizes of $z \approx 0$ IFU surveys.

In partial agreement with the evolution of the TFR measured in Chapter 2 (respectively -0.41 ± 0.08 dex in stellar mass and 0.1 ± 0.1 mag at K-band from $z \approx 0$ to $z \approx 1$, at fixed galaxy rotation velocity), a careful and homogeneous comparison in this chapter between the $z \approx 1$ and $z \approx 0$ TFRs reveals that the M_K TFR is well established for *disky* galaxies by $z \approx 1$, with little or no difference in the relation slope or zero-point between the two epochs and only a moderately increased scatter at $z \approx 1$. Also similar to Chapter 2, we measure a small offset (0.1 ± 0.2 dex) toward higher stellar masses (at fixed rotation velocity) for the zero-point of the M_* KROSS TFR of the *all* sub-sample compared to a $z \approx 0$ comparison relation, in this case the corresponding SAMI LQ TFR carefully matched to the KROSS relation in its construction. However, considering only *disky* galaxies (both KROSS and SAMI), whilst the slope and scatter of the M_* KROSS TFR are comparable to those of the same relation measured at $z \approx 0$ with the SAMI LQ data, the zero-point of the M_* KROSS TFR is offset by -0.2 ± 0.2 dex with respect to the corresponding SAMI LQ relation (at a fixed rotation), i.e. *disky* KROSS galaxies have slightly less stellar mass than *disky* SAMI LQ galaxies. This offset is in the same direction as that measured in Chapter 2, but is lesser in magnitude. This reduction is likely the result of both an improved measure of the KROSS TFR that makes use of galaxy inclinations, photometric centres, and sizes carefully derived from composite KROSS photometry and continuum maps by Harrison et al., (in preparation), and the use of a $z \approx 0$ comparison TFR (SAMI LQ) constructed from data matched to the typical quality of KROSS observations and analysed in an identical manner (that nullifies any bias introduced as a result of the better SAMI data quality). Unlike Chapter 2, in this chapter we could also extract our velocity measure at a uniform radius within each galaxy across both samples.

In Figure 3.10, we add the newly measured stellar mass TFR zero-point offsets from the SAMI LQ and KROSS *all* and *disky* sub-sample comparisons to the plot of the TFR zero-point evolution as a function of redshift presented in Figure 2.5. As the comparison of the M_* SAMI and KROSS TFR zero-points of the *all* sub-sample is likely to be affected by increased scatter in the abscissas of the TFRs, as a result of the inclusion of galaxies with velocity dispersions comparable to their rotation velocities, we can safely ignore it in favour of the comparison between the M_* SAMI LQ and KROSS TFRs of the *disky* sub-sample. We thus see that our revised measurement of the TFR zero-point evolution is consistent with the predictions of the EAGLE simulation (Schaye et al., 2015; Crain et al., 2015; McAlpine et al., 2015), the semi-analytical modelling of Dutton et al. (2011) (see § 2.4.3.1), but also with zero evolution of the stellar mass TFR zero-point over the last ≈ 8 Gyr. Indeed, considering the $\pm 1\sigma$ uncertainty in the measurement (0.2 dex), the range of plausible offsets between the $z \approx 1$ and $z \approx 0$ M_* TFR zero-points of the *disky* sub-sample spans from zero to -0.4 dex. Unfortunately, the implications of the measured offset for galaxy evolution vary significantly when considering the two extremes of this uncertainty range.

First, the consequences of the uppermost plausible zero-point offset (-0.4 dex) were explored at length in Chapter 2 (see § 2.5). Briefly, such an offset paired with zero evolution in the M_K TFR zero-point over the same period (and assuming a constant galaxy surface mass density) implies an increase since $z \approx 1$ in the K-band stellar mass-to-light ratio by a factor of ≈ 2.5 and a decrease in the dynamical mass-to-stellar mass ratio by a factor of ≈ 0.6 for star-forming galaxies at fixed rotation velocity. Given that the gas fractions of KROSS galaxies at $z \approx 1$ can only account for a maximum offset of -0.24 dex in the M_* TFR (assuming all the gas is converted into stars), such a large zero-point evolution

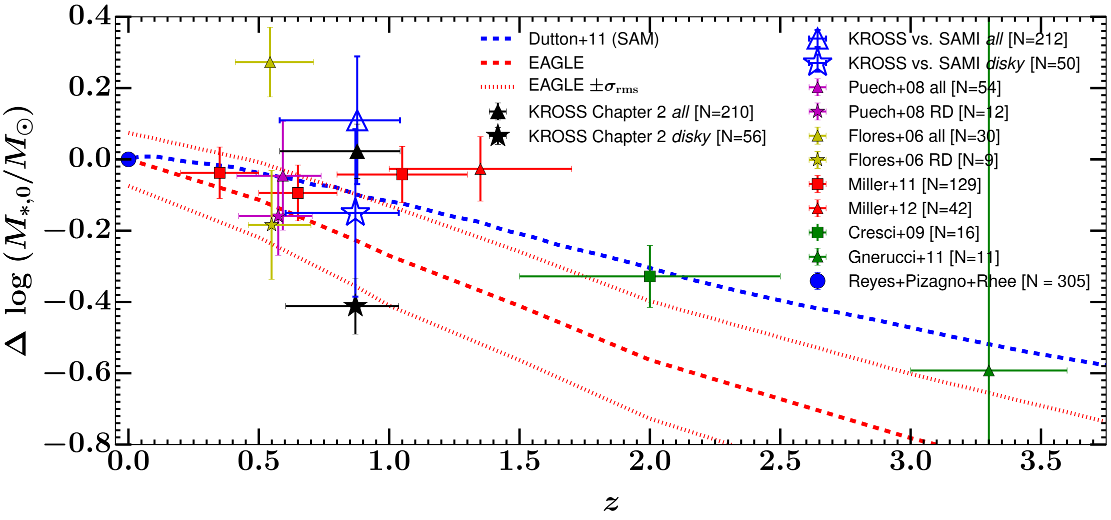

Figure 3.10: Evolution of the stellar mass TFR zero-point offset (with respect to the $z \approx 0$ relation) as a function of redshift. For each sample (each point on the plot), the slope of the best-fit TFR is constrained to that of the best free fit to the $z \approx 0$ comparison sample described in §2.4.1 (the corresponding fit parameters are shown in Table 2.4). The exceptions are the “KROSS vs. SAMI” points calculated in this chapter, for which we fix the slopes of the (improved) KROSS TFRs of this chapter to those of the corresponding best fits to the SAMI LQ TFRs. We include the evolution of the TFR zero-point (with respect to $z \approx 0$) with redshift, as predicted by the semi-analytical modelling (SAM) of Dutton et al. (2011) and the EAGLE simulation (Schaye et al., 2015; Crain et al., 2015; McAlpine et al., 2015). The latter is our own calculation and is described § 2.4.3.1. For reference we plot the rms scatter as measured from the EAGLE samples. We also linearly interpolate between each point to better highlight the predicted trend as a function of redshift from EAGLE and Dutton et al. (2011). The zero-point offsets of the KROSS *disky* TFR constructed in Chapter 2, the corresponding (improved) relation defined in this chapter, and the TFRs of the literature samples we measured in Chapter 2, that each comprise rotating disks, generally agree with the EAGLE or SAM predictions. We measure little (or in some cases positive) evolution of the TFR zero-point for those samples that do not use IFU observations to differentiate between disk-like and non-disk-like galaxies. Those tend to lie above the EAGLE and Dutton et al. (2011) predictions.

requires a significant amount of further gas accretion over the same period. As discussed in § 2.5, the accretion masses required are towards the upper end of the plausible range over this period with respect to the observed specific baryon accretion rates of high mass galaxies ($\log(M_*/M_\odot) = 9.3$–10.7) from $z \approx 1$ to $z \approx 0$ (Elbaz et al., 2007; Salim et al., 2007a; Dutton et al., 2010).

Second, no offset between the M_* KROSS and SAMI TFR zero-points of the *disky* sub-sample would imply that the M_* TFR is well established for disk-like star-forming galaxies by $z \approx 1$, despite them having only recently emerged at this epoch. The total stellar mass of the KROSS galaxies is toward the upper end of the range of late-type galaxies at $z \approx 0$. Whilst the KROSS sample selection was largely based on an absolute magnitude cut and is therefore bound to be biased towards the brighter, more massive star-forming systems at $z \approx 1$, no M_* TFR zero-point evolution would imply that the (secular) stellar mass assembly is nearly complete in at least the most massive disk-like star-forming galaxies at this epoch. This conclusion must be reconciled with the large gas fractions of KROSS galaxies (as measured by Stott et al. 2016 and discussed in § 2.5), their short gas depletion times, and the evidence for further accretion of large amounts of gas onto galaxies since $z \approx 1$ (Elbaz et al., 2007; Salim et al., 2007a; Dutton et al., 2010). These imply that significant stellar mass growth must have taken place since $z \approx 1$. At the very least, these apparently contradictory conclusions would require that dark and stellar mass growth have been intimately linked from the epoch of peak star formation to the present day, with matched levels of accretion of both dark and baryonic matter, subsequent star formation being fueled by the latter. Of course, a lack of evolution of the TFR would also lend credence to the postulate that disk-like galaxies have formed in a predominantly hierarchical manner since $z \approx 1$, maintaining a constant dynamical (total) mass-to-light ratio as they grow.

Considering the mostly likely result that, as measured from the KROSS and SAMI LQ relations, at a fixed galaxy rotation velocity the zero-point of the stellar mass TFR of disk-like galaxies has increased by 0.2 dex since $z \approx 1$, we infer a modest decrease (factor ≈ 0.37) of the dynamical mass-to-stellar mass ratio of disk-like star-forming galaxies since $z \approx 1$, and a corresponding increase (factor of ≈ 1.58) of the K-band stellar mass-to-light ratio over the same period. Such changes may be accounted for entirely by the large gas fractions of the KROSS galaxies, without the need for further accretion over the last ≈8 Gyrs. Of course, this assumes that 100% of the gas in disk-like star-forming galaxies at $z \approx 1$ is converted to stars and no further gas is accreted. More likely, we might expect such an offset to result from the conversion of gas into stars at a moderate (and gradually decreasing) rate over the last ≈8 Gyrs, with continued replenishment of the gas reservoir via accretion. Given that for a given galaxy stellar mass both the star formation rate *and* the gas accretion rate have decreased with time since $z \approx 1$ (see § 2.5), one may speculate that the gas accretion onto galaxies is closely linked to their star formation rate, regardless of whether it is the direct cause.

All of the conclusions drawn here assume that the total surface mass density Σ of star-forming galaxies has not evolved since $z \approx 1$ (recall from Equation 1.1 that evolution of the TFR zero-point probes evolution in both $\Sigma(M/L)$ and M/L). We must keep in mind that we are unlikely to be "following" a single population of star-forming galaxies and charting their evolution since $z \approx 1$. Rather, we are comparing the typical star-forming galaxy population at each epoch and how their mass-to-light ratios differ (or not). The fact that the KROSS and SAMI galaxies follow the same broad trend in size versus mass (see Fig 3.3) does however suggest that their mass surface densities are similar, at least for galaxies of similar masses.

3.7 Conclusions

We have presented a careful comparison of the M_K and M_* TFRs at $z \approx 1$ and $z \approx 0$, derived using IFU observations of Hα emission from respectively $z \approx 1$ star-forming galaxies from KROSS using KMOS and local galaxies from the SAMI Galaxy Survey with the SAMI spectrograph. To nullify potentially different biases in the relations resulting from differing data quality and analysis methods, we matched the spectral and spatial resolution and sampling of both sets of observations, degrading the quality of the SAMI data to that typical of KROSS. We also increased the noise in the SAMI cubes so that the maximum Hα S/N of each SAMI galaxy data cube matched that of KROSS galaxies of similar stellar masses. Lastly, we analysed the SAMI data in the exact same way as the KROSS data.

We found that degrading the SAMI data served to preferentially exclude from our analysis those galaxies that are more compact and rotate more slowly.

Despite this impact on the sample selection, the degrading process did not affect our ability to accurately measure key galaxy parameters. We found 1:1 relations (with varying scatter) between the measures of rotation velocity $v_{2.2}$, intrinsic velocity dispersion σ, stellar mass M_*, and absolute K-band magnitude M_K derived from the SAMI data before (HQ) and after (LQ) they were degraded.

We also compared the TFRs derived from the SAMI HQ and LQ data for carefully selected samples of galaxies with associated $v_{2.2}$, M_K, and M_* measurements reliable enough for inclusion in our TFR analysis, and referred to as the *all* sub-samples. We defined a further *disky* sub-sample for each data set, containing those galaxies within the *all* sub-sample that have a sufficiently high ratio of rotation velocity to velocity dispersion to suggest they are disk-like ($v_{2.2}/\sigma > 3$).

Somewhat surprisingly, for the *all* sub-sample we measured similar scatter in the abscissa and ordinate of the M_K and M_* LQ TFRs and the corresponding HQ relations. This can be understood when one considers that the degrading process preferentially selects those galaxies that have more extended Hα emission (and therefore more reliable velocity measures) and that are intrinsically larger in size as judged by their intrinsic effective radius r_e) (and therefore more massive and rotating more rapidly). The LQ SAMI TFRs are thus less populated toward the low velocity and mass (or luminosity) end of the relation, the region that appears to dominate the scatter in the relation, this both intrinsically (as $v_{2.2}/\sigma$ decreases with decreasing $v_{2.2}$) and observationally (as it is more difficult to reliably spatially resolve the Hα emission in these smaller galaxies, thus reducing the probability of extracting an accurate velocity field and subsequently measuring a robust rotation velocity). It is therefore arguably unsurprising that we measure similar scatter in the HQ and LQ TFRs of the *all* sub-sample. This explanation is confirmed when we consider the TFRs derived from the HQ and LQ SAMI *disky* sub-samples from which we exclude galaxies with $v_{2.2}/\sigma \leq 3$. The *disky* sub-samples thus comprise those galaxies with larger $v_{2.2}$ and therefore M_* and r_e. Correspondingly, the scatter of the LQ relation is then larger than that of the HQ relations along both axes.

After exploring the effects of degrading the SAMI data, we compared the $z \approx 0$ SAMI LQ TFRs to the $z \approx 1$ KROSS relations. As in Chapter 2, considering the *all* sub-samples, we found shallower slopes for both the M_K and M_* KROSS TFRs compared to the corresponding $z \approx 0$ relations. These differences disappeared when considering the *disky* sub-samples, with the slopes of the KROSS relations now much steeper than for the *all* sub-samples and consistent with the corresponding SAMI LQ relations.

In partial agreement with the result presented in Chapter 2, for a fixed TFR slope we found no evidence for any evolution in the zero-point of the M_K TFRs between $z \approx 1$ (KROSS *disky* sub-sample) and $z \approx 0$ (SAMI LQ *disky* sub-sample), and a marginally significant offset of -0.2 ± 0.2 dex in stellar mass between the M_* KROSS TFR and the corresponding SAMI LQ relation. This zero-point offset is in the same direction as that measured in Chapter 2 but reduced in magnitude. We attribute this reduction to a combination of the difference between the improved measure of the KROSS TFRs presented in this chapter those of Chapter 2, and the careful construction of our own $z \approx 0$ comparison relations. In other words, the previously measured offset was too large due to systematic biases introduced by the differing sample selection and analysis methods of the $z \approx 1$ and $z \approx 0$ data. In particular, we were unable in Chapter 2 to apply a v/σ cut to the $z \approx 0$ comparison sample. The measured zero-point evolution is halved when these biases are nullified by the careful comparison presented here.

We further conclude that whilst the M_K TFR is already well established for disk-like star-forming galaxies at $z \approx 1$, and that the slope and scatter of the M_* TFR are similar at $z \approx 1$ and the present day, there is some evidence for an increase in the zero-point of the latter since $z \approx 1$ (by 0.2 dex in stellar mass). This implies that the total mass-to-stellar mass ratio of *disky* star-forming galaxies has decreased by a factor of ≈ 0.37 over the last ≈ 8 Gyr, and their K-band stellar mass-to-light ratio has increased by a factor of ≈ 1.58.

Two main conclusions can be drawn from this result. Firstly, considering the inferred decrease in the total mass-to-stellar mass ratio since $z \approx 1$, the large gas fractions of $z \approx 1$ (KROSS) galaxies and their short gas depletion times, moderate amounts of stellar mass growth must have occured in galaxies since $z \approx 1$, that can be entirely accounted for by the gas already present in them at that epoch. Secondly, following depletion of the $z \approx 1$ gas reservoir, any further accretion of gas onto galaxies (and its subsequent conversion to stars) must be closely matched with similar levels of dark matter accretion (to keep the total mass-to-stellar mass ratio constant and equal to that of $z \approx 0$ galaxies). Depending on how quickly the star formation rate of galaxies decreases from $z \approx 1$, this may also support the postulate that star-forming galaxies have grown in a predominantly hierarchical fashion over the last ≈ 8 Gyrs (e.g. Cole et al., 2000).

Of course, the conclusions drawn here are based on “snapshots” of the TFR at only two epochs in the history of the Universe. We cannot rule out the possibility that the mass-to-light ratios of star-forming galaxies have not varied smoothly during the intervening period since $z \approx 1$. Given the stark changes that occur in the properties of galaxies over the same period, we can gain further insights by extending our carefully matched comparisons of the $z \approx 1$ and 0 TFRs to other intermediate redshifts. A program analagous to KROSS and SAMI is already underway, to observe a sample of galaxies at $z \approx 0.5$. It is discussed further in Chapter 5. Similarly, we could conduct an analogous analysis of galaxies at higher redshifts. Observations are underway to observe galaxies at $z \approx 1.5$ with KMOS.

Chapter 4

The Tully-Fisher Relation of COLD GASS Galaxies

4.1 Motivation

In Chapters 2 and 3 we presented the first direct comparison of the TFRs of star-forming galaxies at $z \approx 1$ and 0, constructed via the application of identical analysis methods and sample selections to integral field unit data exactly matched in quality at each epoch. The work presented in those chapters thus comprises the first measure of the evolution of the TFR since $z \approx 1$ that directly nullifies potentially different observational biases between the relations at $z \approx 1$ and 0. Whilst the conclusions drawn from those chapters have potentially important consequences for galaxy evolution theory, we must take steps to provide an independent measure of the TFR evolution over the same period in order to corroborate them. In this chapter we therefore look to alternatives to the use of Hα emission as a kinematic tracer in the previous chapters to provide a separate measure of the TFR evolution with redshift.

To facilitate a comparison of the TFRs at $z \approx 0$ and at higher redshifts ($z \gtrsim 1$), we must select a kinematic tracer that is viable at both epochs. We therefore require an emission line that at each epoch is emitted by star-forming galaxies and is easily detected using current technology, and that is sufficiently extended within a galaxy to probe the outer parts of its rotation curve. Aside from Hα emission, there are two (gas) emission lines that make good candidates in these respects, namely (HI) 21 cm emission from atomic gas in galaxies and carbon monoxide (CO) emission, that traces cold molecular gas in galaxies.

Whilst there is a large body of work on the TFR using HI observations (e.g. Tully & Fisher, 1977; Sprayberry et al., 1995; Bell & de Jong, 2001), there are several advantages to using observations of CO. First, atomic hydrogen in galaxies is currently only routinely detected in the local Universe. The Square Kilometre Array (SKA) precursors Australian Square Kilometre Array Pathfinder (ASKAP) and Karoo Array Telescope (MeerKat) can detect HI to moderate redshifts ($z \lesssim 0.4$; Meyer, 2009; Holwerda & Blyth, 2010; de Blok, 2011; Duffy et al., 2012), but the SKA itself will be required to routinely detect galaxies at $z > 1$ (Abdalla et al., 2015; Yahya et al., 2015). As discussed in § 1.3.1.1, multiple CO lines are however now regularly detected in the large majority of star-forming galaxies at $z \approx 1$–3 (e.g. Daddi et al., 2010; Magdis et al., 2012; Magnelli et al., 2012; Combes, 2013; Freundlich et al., 2013; Tacconi et al., 2010, 2013; Genzel et al., 2015), and in more extreme, star-bursting systems at redshifts as high as $z \approx 7$ (e.g. Walter et al., 2004; Riechers et al., 2008a,b, 2009; Wang et al., 2011; Wagg et al., 2014). CO thus allows to extend TFR studies probing the mass-to-light ratio and surface density of galaxies to the earliest precursors of today's galaxies.

Second, previous work has shown that the HI discs of galaxies, that are typically more extended spatially than the molecular gas, can also be kinematically unrelaxed, with e.g. large-scale warps (e.g. Verheijen, 2001). Molecular gas is generally more dynamically relaxed and suffers less from such problems. More importantly, the atomic hydrogen in early-type galaxies is often significantly disturbed, with much of the gas lying in tidal features or nearby dwarf galaxies (see e.g. Morganti et al., 2006; Serra et al., 2012), thus confusing low-resolution observations such as those obtained with single-dish telescopes. High-resolution interferometric observations are thus necessary to identify those early-type galaxies with a regular HI distribution appropriate to derive reliable TFRs (see e.g. den Heijer et al., 2015). On the other hand, Davis et al. (2011) clearly showed that CO single-dish observations easily yield robust and unbiased TFRs for early-type galaxies. CO observations thus offer the attractive possibility to derive TFRs more accurate than those currently available, and this across the entire Hubble sequence.

Our goal in this chapter is therefore to establish a benchmark CO TFR of local galaxies, as a pre-requisite to extend the relation to higher redshifts. There are clearly tracers other than CO that can be used at large redshifts. In addition to the Hα used in the previous chapters these are primarily other optical ionised gas emission lines such as [OII] and [OIII], and these should also be (and have been) pursued to provide independent probes of the evolution of the TFR (see e.g. Cresci et al., 2009; Gnerucci et al., 2011; Miller et al., 2011, 2012). However, it is known that ionised gas discs at $z \approx 1$–3 are turbulent (see e.g. Förster Schreiber et al., 2006b; Swinbank et al., 2012a), and great care must be taken when measuring and interpreting their rotational motions (e.g. Wisnioski et al., 2015; Stott et al., 2016, and Chapters 2 and 3). CO that traces the more dynamically-relaxed molecular gas avoids this particular problem.

In this chapter, we thus take a step toward establishing a local benchmark for the CO TFR, using the CO(1-0) line as a kinematic tracer. In future work our TFRs will be compared to those of a local sample (Torii et al., in prep.) and a sample of $z \lesssim 0.3$ galaxies (Topal et al., in prep.).

The sample, photometric data and kinematic data used in this chapter are described in § 4.2. TFRs are derived in § 4.4 (the rotation velocity measure adopted is defined in § 4.3.3 and extensively tested in § 4.3). The results are discussed in § 4.5. We summarise and conclude briefly in § 4.6.

4.2 Data

4.2.1 CO Velocity Widths

As discussed at length in § 4.3, we adopt as our TFR velocity measure the width of the integrated CO(1-0) line profile of galaxies from the CO Legacy Database for the *GALEX* Arecibo SDSS Survey (GASS; Catinella et al., 2010) (COLD GASS; Saintonge et al., 2011).

The GASS aimed to observe the neutral hydrogen content of a sample of ~ 1000 galaxies with the Arecibo 305 m telescope. More specifically, GASS galaxies were selected to have redshifts $0.025 < z < 0.05$, stellar masses $10^{10} < M_*/M_\odot < 10^{11.5}$ with a flat distribution in $\log(M_*/M_\odot)$, and positions within the overlap region of the Sloan Digitized Sky Survey (SDSS; York et al., 2000), Arecibo Legacy Fast ALFA Survey (ALFALFA; Giovanelli et al., 2005) and *GALEX* Medium Imaging Survey (MIS; Martin et al., 2005; Morrissey et al., 2005). No other selection criterion was applied. A follow-up survey (Catinella, in prep.) has extended the GASS sample to probe down to stellar masses of $10^9 M_\odot$. The sample selection and survey strategy are identical to those of the original GASS survey, but for the difference that the lower mass galaxies are selected in the redshift interval $0.01 < z < 0.02$.

The COLD GASS adds information about the molecular gas contents of a randomly-selected sample of 500 GASS galaxies over the full mass range $10^9 < M_*/M_\odot < 10^{11.5}$. Most galaxies ($\approx 80\%$) have angular diameters small enough to be observed with a single pointing of the Institut de Radioastronomie Millimétrique (IRAM) 30 m telescope. For larger galaxies, an extra pointing offset from the first was added. Fully reduced and baseline-subtracted integrated CO(1-0) spectra of all massive COLD GASS galaxies ($M_* > 10^{10} M_\odot$) are publicly available[1] (binned to 11.5 km s^{-1} channels), and spectra for the lower mass galaxies have been made available to us ahead of publication. Once combined with other multi-band observations, GASS and COLD GASS thus allow to measure the fraction of the galaxies' baryonic mass contained in atomic gas, molecular gas and stars.

Saintonge et al. define a "secure" detection in COLD GASS as one with a signal-to-noise ratio $S/N > 5$, where S/N is calculated as the ratio of the integrated line flux to its formal error. Considering the total data set available to us for this work, there are 260 securely detected galaxies. These form the basis of the current sample.

4.2.2 Near-infrared Luminosities

Many previous TFR studies have used K-band magnitudes to probe the bulk of the stellar mass in their sample galaxies. To that end, K_s-band magnitudes from the Two Micron All Sky Survey (2MASS; Skrutskie et al., 2006) were also considered here, but at the distances of the COLD GASS galaxies the depth of 2MASS is insufficient to accurately recover K_s-band magnitudes. Other deeper surveys are available, such as the UK Infrared Telescope Deep Sky Survey (UKIDSS; Lawrence et al., 2007), but these tend to have more limited

---

[1] http://www.mpa-garching.mpg.de/COLD_GASS/

sky coverage.

For this work, the *Wide-Field Infrared Survey Explorer* (*WISE*; Wright et al., 2010) Band 1 (≈ 3.4 μm) magnitude ($W1$) of each sample galaxy was thus adopted as a proxy for its total stellar mass. This quantity is available for 222 of the 260 secure COLD GASS CO detections. Specifically, the magnitude used was the *w1gmag* parameter from the All*WISE* Source Catalog[2]. This parameter is the $W1$ magnitude measured in an elliptical aperture, with a size, shape and orientation based on that reported in the 2MASS Extended Source Catalog (XSC[3]). To account for the larger *WISE* beam, the aperture is scaled-up accordingly. Those galaxies without an associated *w1gmag* value are excluded from this work.

It is unclear why 38 of the 260 galaxies securely detected do not have an associated *w1gmag* value. The 38 galaxies in question are present in the XSC, and the majority of them are also deemed to be extended sources by *WISE* and are present in the All*WISE* Source Catalog. However, the entries in the latter are not explicitly linked to the corresponding XSC objects despite their close proximity on the sky (typically $\sim 1''$). The 38 galaxies do each have a *WISE* Band 1 magnitude measured in a $13\farcs75$ radius aperture (≈ 23 kpc at $z \approx 0.03$, the typical redshift of the COLD GASS galaxies), *w1mag_4* from the All*WISE* Source Catalog. To ensure we do not bias our sample by excluding the 38 galaxies in question, we use the available *w1mag_4* values to conduct a Kolmogorov-Smirnov (K-S) two-sample test between the full 260 securely detected galaxies and the 222 galaxies that remain after the exclusion of the 38 galaxies mentioned. We define a null hypothesis that the *w1mag_4* values of the latter are drawn from the same continuous distribution as those of the former, rejecting the null hypothesis if the p-value $p < 0.05$. The test produced a p-value $p = 0.68$, so we cannot reject the null hypothesis. We therefore proceed with our analysis, confident that the exclusion of those 38 galaxies without an associated *w1gmag* value does not significantly bias the magnitude distribution of our remaining sample.

The bulk of the stellar mass is effectively probed at the wavelength of $W1$, but this band is not so far red as to significantly suffer from contamination due to dust emission. In

---

[2] http://wise2.ipac.caltech.edu/docs/release/allwise/

[3] http://irsa.ipac.caltech.edu/applications/2MASS/PubGalPS/

addition, Lagattuta et al. (2013) found that the $(K - W1)$ colours of a sample of 568 late-type galaxies drawn from the 2MASS Tully-Fisher all-sky galaxy catalog (Masters et al., 2008) are such that $(K - W1) \approx 0$ with a scatter of only ≈ 0.2 dex. They did find a weak trend towards bluer $(K - W1)$ colours at $W1 \geq 10.75$, but despite this it is clear that both the K and $W1$ bands, with similar wavelength ranges, are tracing the same stellar populations. It is thus acceptable to directly compare TFRs derived using either passband, at least in the regime where differences in depths between surveys is not an issue.

For each sample galaxy, the absolute *WISE* Band 1 magnitude (M_{W1}) was calculated as follows:

$$M_{\mathrm{W1}} = W1 - A_{3.4\mu\mathrm{m}} - \mu \ , \tag{4.1}$$

where $A_{3.4\mu\mathrm{m}}$ is the extinction in $W1$, calculated by first adopting the reddening value $E(B-V)$ from the dust maps of Schlafly & Finkbeiner (2011) taken from the NASA/IPAC Infrared Science Archive[4], and converting this to the corresponding $W1$-band extinction assuming

$$A_{3.4\mu\mathrm{m}} = R_{3.4\mu\mathrm{m}}\, E(B - V) \ , \tag{4.2}$$

where $R_{3.4\mu\mathrm{m}} = 0.18 \pm 0.1$ was adopted as measured in Yuan et al. (2013) using the stellar "standard pair" technique. The distance modulus μ is taken from the NASA/IPAC Extragalactic Database[5] (NED), and is derived from the galaxy's redshift adjusted for local deviations from the Hubble flow due to the Shapley Cluster, Virgo Cluster and Great Attractor.

Both a reddening and a distance modulus value were available for each of the 222 remaining galaxies.

4.2.3 Inclination Estimates

To account for projection effects, each sample galaxy's inclination i was calculated (following Equation 3.6) from the the observed ratio of the semi-minor to the semi-major axis of the galaxy q in SDSS r-band imaging, available for 217 of the 222 remaining sample

---

[4] http://irsa.ipac.caltech.edu/applications/DUST/

[5] http://ned.ipac.caltech.edu/

galaxies. Those galaxies without an associated q value are excluded from this work. The (intrinsic) axial ratio of an edge-on galaxy, q_0, is morphology dependent. We adopt the same prescription as Davis et al. (2011), whereby galaxies are divided into early types with $q_0 = 0.34$ and late types with $q_0 = 0.2$. See § 4.2.6 for a description of the morphological classifications used.

4.2.4 Stellar Masses

The stellar masses of our sample galaxies were taken from the Max Planck Institute for Astrophysics-Johns Hopkins University Data Release 7 (MPA-JHU DR7) derived data catalogue[6], and were determined using SDSS photometry via the spectral energy distribution (SED)-fitting method described by Salim et al. (2007b), assuming a Chabrier (2003) initial mass function (IMF). In this method, each galaxy's SED is compared to model SEDs from the library of Bruzual & Charlot (2003) to determine a stellar mass probability distribution. The stellar mass and its uncertainty are then taken as the median and half the difference between the 16th and 84th percentile of this distribution, respectively, and are available for 216 of the 217 remaining sample galaxies. The single galaxy without an associated stellar mass value is excluded from this work.

4.2.5 AGN Candidates

As the emission from an active galactic nucleus (AGN) can contaminate and occasionally far outweigh that of the stellar body of a galaxy, it is imperative to exclude from our sample galaxies hosting a substantial AGN. AGN-hosting galaxies would otherwise be systematically offset from the underlying TFR and would systematically bias our fits.

We used publicly available classifications from the *emissionLinesPort* table of the SDSS Data Release 10[7] to exclude AGN-candidates from our sample. Each SDSS galaxy was classified by a fit to its spectrum using adaptations of the Gas AND Absorption Line Fitting (GANDALF; Sarzi et al., 2006) and penalised PiXel Fitting (pPXF; Cappellari & Emsellem, 2004) routines to extract several emission lines. These were then used to place

---

[6] http://www.mpa-garching.mpg.de/SDSS/DR7/

[7] `http://skyserver.sdss.org/dr10`

each galaxy on a Baldwin, Phillips & Terlevich (BPT; Baldwin et al., 1981) diagram. Based on their position on the diagram, galaxies were divided into different categories that depend on the likelihood of the galaxy hosting an AGN. The classifications themselves are based on the work of Kauffmann et al. (2003), Kewley et al. (2001) and Schawinski et al. (2007). We thus excluded 9 galaxies classified as "Seyfert", further reducing our adopted sample to 207 galaxies.

4.2.6 Morphological Classes

Our COLD GASS sample was cross-referenced with the Galaxy Zoo 1 catalog (GZ1; see Lintott et al. 2008, 2011), providing crowd-sourced classifications of $\sim 600,000$ galaxies in the SDSS. Each galaxy is classified as either a spiral, an elliptical or "uncertain". Of our remaining sample of 207 galaxies drawn from COLD GASS, 143 are deemed to be spirals, 6 ellipticals and the remaining 58 are uncertain. For the purposes of this work, and in particular the inclination correction described in § 4.2.3, we equate those galaxies classified as spiral and uncertain to late-types, and those classified as elliptical to early-types.

We do not initially exclude any galaxy based on its GZ1 morphological classification. However, the exclusion (or inclusion) of those galaxies deemed elliptical or uncertain is discussed further in § 4.4.2, where we present the details of a more restricted sub-sample.

After applying all the criteria described in this section, we thus proceed with a final working sample of 207 COLD GASS galaxies.

4.3 Velocity Measure: W_{50}

4.3.1 Fitting Functions

As a characteristic velocity measure we adopt W_{50}, the width of the CO(1-0) integrated profile at 50% of its maximum, that should be roughly equal to twice the maximum rotation velocity of the galaxy V_{max}. In the presence of non-negligible noise, a fit to the profile is usually superior to a direct measurement of W_{50}, but the choice of the fitting function is not trivial and several different functions have been used in the past.

While it is expected that the characteristic velocity measure will vary depending on the function chosen, this is acceptable as long as different galaxy samples being compared are measured in the same manner. This is because the systematic effect introduced by any given function will cancel out when the difference between two (or more) samples is calculated. However, it is clearly preferable for the measured characteristic velocity to be independent of the signal-to-noise and amplitude-to-noise ratio (A/N) of the data, and the measurements should not be systematically biased as the width and/or shape of the profile vary. Despite previous work on the subject (e.g. Saintonge, 2007; Obreschkow et al., 2009a,b; Westmeier et al., 2014), as the signal-to-noise ratio of CO data is generally low (certainly lower than that of typical HI spectra of nearby galaxies; e.g Lavezzi & Dickey, 1998), we deemed it prudent to compare the results of several different fitting functions. Our goal is to ascertain which function is the most accurate and most importantly minimises potential biases as a function of A/N, inclination (apparent width) and rotation velocity (intrinsic width) (all related to the total S/N).

The functions compared include the standard single Gaussian,

$$f(v) = A\,\mathrm{e}^{\frac{-(v-v_0)^2}{2\sigma^2}} \quad , \tag{4.3}$$

where v is the velocity, $A > 0$ is the amplitude of the peak (maximum flux), v_0 is the velocity of the peak (and mean velocity; taken to be within ±500 km s^{-1} of the known systemic velocity), and $\sigma > 11.5$ km s^{-1} (the velocity bin width of the COLD GASS spectra) is the root mean square (rms) velocity (i.e. the velocity width) of the profile.

We also test a symmetric (with respect to the central velocity) Gaussian Double Peak function, composed of a parabolic function surrounded by two equidistant and identical (but mirrored) half-Gaussians forming the low and high velocity edges of the profile:

$$f(v) = \begin{cases} A_{\mathrm{G}} \times \mathrm{e}^{\frac{-[v-(v_0-w)]^2}{2\sigma^2}} & v < v_0 - w \\ A_{\mathrm{C}} + a\,(v-v_0)^2 & v_0 - w \le v \le v_0 + w \\ A_{\mathrm{G}} \times \mathrm{e}^{\frac{-[v-(v_0+w)]^2}{2\sigma^2}} & v > v_0 + w \end{cases} \quad , \tag{4.4}$$

where v_0 is the central (mean) velocity (again taken to be within ±500 km s^{-1} of the known systemic velocity), $w > 0$ is the half-width of the central parabola, $\sigma > 0$ km s^{-1} is the width of the profile edges, $A_\mathrm{G} > 0$ is the peak flux of the two half-Gaussians (centred at $v_0 \pm w$), $A_\mathrm{C} > 0$ is the flux at the central velocity, and $a = (A_\mathrm{G} - A_\mathrm{C}) \, / \, w^2$.

A variation of the Gaussian Double Peak function was also tested, the Exponential Double Peak function used by Crocker et al. (2012), where the two half-Gaussian edges are replaced by exponentials:

$$f(v) = \begin{cases} A_\mathrm{G} \times \mathrm{e}^{\frac{[v-(v_0-w)]}{\sigma}} & v < v_0 - w \\ A_\mathrm{C} + a\,(v - v_0)^2 & v_0 - w \le v \le v_0 + w \\ A_\mathrm{G} \times \mathrm{e}^{\frac{-[v-(v_0+w)]}{\sigma}} & v > v_0 + w \end{cases} , \tag{4.5}$$

where $A_\mathrm{G} > 0$ is the peak flux of the two exponentials, but all the parameters otherwise have the same meaning as for the Gaussian Double Peak function.

Finally, a fourth function was also tested, the generalised Busy Function adopted and discussed in detail by Westmeier et al. (2014). Briefly, it is the product of two error functions $\mathrm{erf}(x)$ and a polynomial. The resulting shape is similar to that of the double-peaked functions above, i.e. typically a peak (from the error functions) on either side of a central dip (from the polynomial). The generalised form is described by

$$\begin{aligned} B(v) = \tfrac{a}{4} \times \; & \{\mathrm{erf}\,[\,b_1(v - \gamma_1)\,] + 1\} \\ \times \; & \{\mathrm{erf}\,[\,b_2(\gamma_2 - v)\,] + 1\} \\ \times \; & (c\,|v - v_\mathrm{p}|^n + 1) \ , \end{aligned} \tag{4.6}$$

where $b_1 > 0$ and $b_2 > 0$ are respectively the slope of the left and right error function, whilst γ_1 and γ_2 describe their respective width. n, $c > 0$ and v_p are respectively the order, slope and offset of the polynomial. We adopted $n = 2$, yielding a parabola as for the double-peaked functions above. $a > 0$ determines the normalisation of the profile.

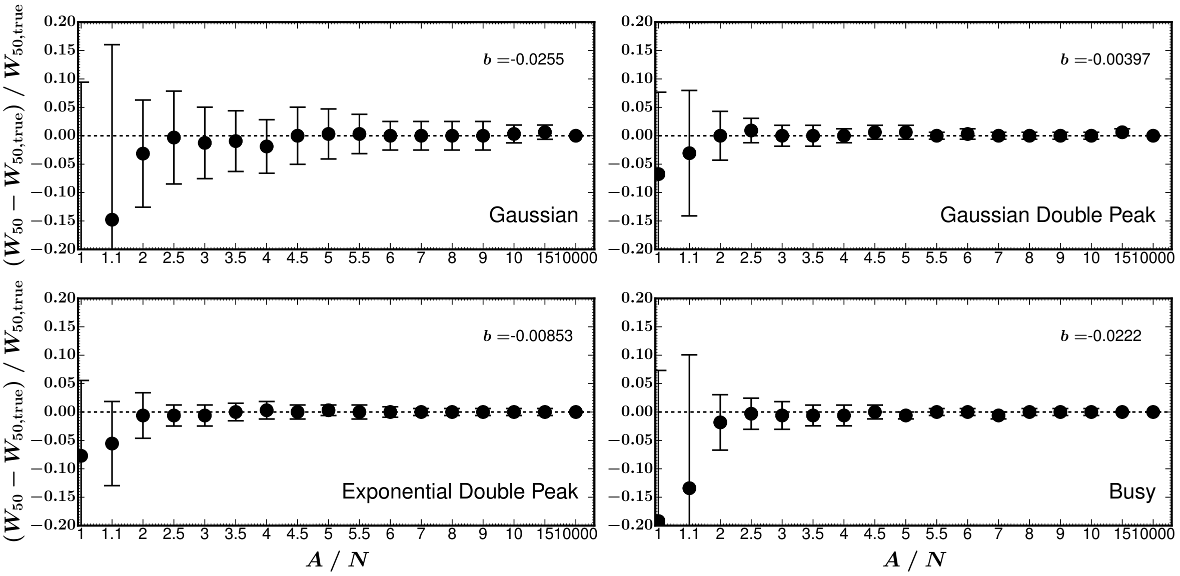

Figure 4.1: Fractional difference between W_{50} measured at $A/N = 10000$ ($W_{50,\mathrm{true}}$, effectively noiseless) and W_{50} measured for various values of A/N, this for an example case where the velocity $V_{\mathrm{c,flat}} = 210$ km s^{-1} and inclination $i = 70°$. The 4 panels show how consistent the measured W_{50} is for each of the four functions discussed in § 4.3.1 (i.e. Gaussian, Gaussian Double Peak, Exponential Double Peak, and Busy function). We quantify this with a bias measure b defined in § 4.3.2 and shown in the top-right corner of each panel.

4.3.2 Tests

To test which fitting function is most appropriate, a library of noiseless integrated spectra was generated using the KINematic Molecular Simulation (KinMS[8]) routine of Davis et al. (2013). Since the overall S/N is a function of both A/N and the profile width, while we are ultimately only interested in recovering the profile width for TFR studies, we have decided to probe the effects of these two parameters separately.

The shape of a galaxy's integrated CO emission profile is primarily dependent on the physical properties of the galaxy, and to a lesser extent on the nature of the telescope used to observe it. Broadly, the width of the profile depends on the galaxy's projected circular velocity, and therefore its dynamical mass (Casertano & Shostak, 1980), whilst the breadth of the flanks of the profile depends on the intrinsic turbulence of the gas. The integral of the profile is proportional to the galaxy's total molecular gas mass (e.g. Maloney & Black, 1988). The overall shape of the profile also depends on the distribution of the gas within the

---

[8] purl.org/KinMS

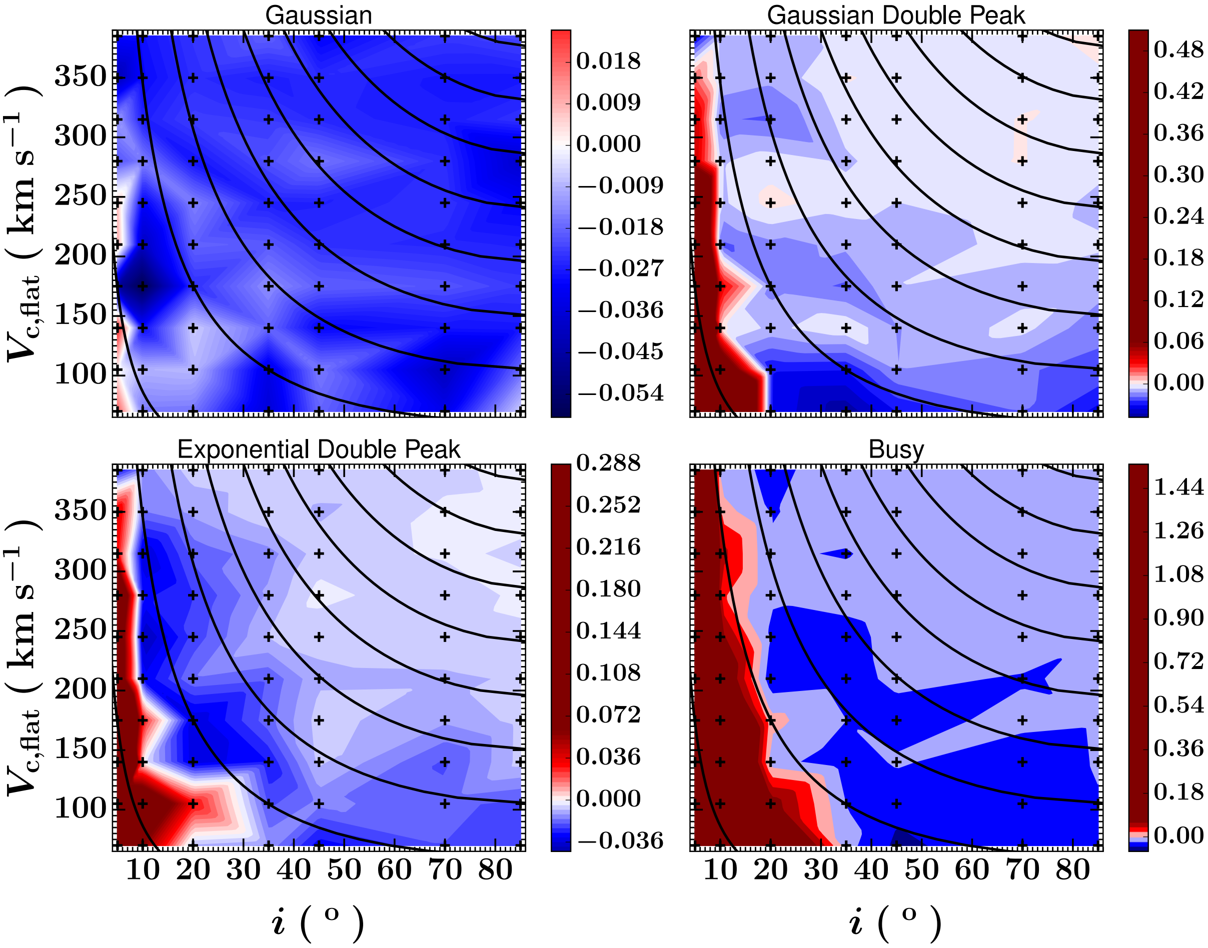

Figure 4.2: The bias b (as defined in the text) of the four analytical functions considered, as a function of the circular velocity $V_{\rm c,flat}$ and the inclination i. For each function, the common colour scale shows whether the fit is positively (red) or negatively (blue) biased. The data points (black crosses) indicate $V_{\rm c,flat} - i$ pairs where a measurement was made. Black lines show curves of constant $V_{\rm c,flat} \sin i$.

galaxy: the radial density profile will determine to what extent the CO emission samples the flat part of the galaxy's rotation curve - if the gas extends out to sufficient radii, the intrinsic profile will display a double-horned or boxy shape (e.g. Davis et al., 2011). Additionally, the central flux of the profile (and thus whether it is intrinsically double-horned or boxy) depends on the gas concentration within the disc (e.g. Wiklind et al., 1997; Lavezzi & Dickey, 1997, see § 4.4.2). Whether or not the *observed* profile appears Gaussian, boxy or double-horned also depends on the width of the velocity channels and the beam size of the telescope used to observe the galaxy; if the velocity channels are too broad or the beam size is smaller than the radial size of the galaxy, then the integrated emission profile may appear Gaussian despite being intrinsically boxy or double-horned (in the latter case it is not a true integrated profile).

Bearing all this in mind, the model spectra were created by assuming an edge-on exponential disc of molecular gas with a scalelength of $2''$, a realistic circular velocity curve that peaks at $3''$ and then remains flat, and a fixed molecular gas velocity dispersion of 12 km s^{-1}. A Gaussian single-dish telescope response with a $22''$ beam (full width at half maximum) was used to integrate the flux spatially, matching that of the IRAM 30 m telescope. This also ensures that our spectra contain essentially all the flux of the modeled discs, and the resulting spectra are intrinsically double-horned or boxy shaped.

Model integrated spectra with flat circular velocities $V_{\rm c,flat}$ ranging from 70 to 385 km s^{-1}, and with inclinations ranging from 5° to 85°, were generated and then binned to 11.5 km s^{-1} per channel to match the COLD GASS spectra. Each of the resulting spectra was then degraded by adding random Gaussian noise such that the desired A/N was reached, where the amplitude A is defined here as the peak of the spectrum before noise was added, and the noise N is defined as the root-mean-square (rms) of the spectrum in an area devoid of emission (thus equal to the dispersion of the Gaussian used to generate the noise).

For each input circular velocity $V_{\rm c,flat}$, inclination i and amplitude-to-noise ratio A/N, 150 realisations of the resulting model spectrum were generated. Each of these realisations was then fit with the four different functions described in § 4.3.1, and the width of the best fitting profile at 50% of the peak (W_{50}) was calculated. The fits were carried out using the

PYTHON package MPFIT[9] (Markwardt 2009; translated into PYTHON by Mark River and updated by Sergey Koposov), that employs a Levenberg-Marquardt minimisation algorithm. The adopted W_{50} and its uncertainty for each combination of $V_{\rm c,flat}$, i and A/N were then taken respectively as the median and median absolute deviation (with respect to the median itself) of the 150 associated measurements.

Figure 4.1 shows the fractional difference between the true width ($W_{\rm 50,true}$), defined as W_{50} measured at $A/N = 10,000$ (i.e. for an effectively noiseless spectrum), and that measured as a function of A/N, this for the case where $V_{\rm c,flat} = 210$ km s^{-1}, and $i = 70°$. We do not show the results for every combination of velocity and inclination that we tested, but rather select this case as an illustrative example. We do however summarise the results for each function tested in the four panels of Figure 4.2. This shows how self-consistent each of the four tested functions is as a function of $V_{\rm c,flat}$ and i, where self-consistency is taken here to mean both that the measured width is similar to its true value and that it does not vary systematically with decreasing A/N. This is judged by measuring the bias b, defined as the average fractional width difference over all A/N sampled. The bias for each function, and for each of the selected values of $V_{\rm c,flat}$ and i, is shown in the panels of Figure 4.2. It is clear that both Double Peak functions overestimate to varying degrees the line width (with respect to $W_{\rm 50,true}$) for low values of inclination ($i \lesssim 20°$), but are otherwise only slightly negatively biased. The Busy function displays the same trends, but is negatively biased to a greater degree than the Double Peak functions for high values of inclination ($i \gtrsim 20°$). The Gaussian function, however, is negatively biased in most cases, and to a greater degree than each of the three other functions.

Figure 4.3 attempts to distill further the information contained in Figure 4.2. It shows which function is most self-consistent as a function of $V_{\rm c,flat}$ and i, where self-consistency is again judged by the bias b. We found that the Gaussian Double Peak and Exponential Double Peak functions yield very similar results in terms of self-consistency, recovering the true width to a similar accuracy at a given circular velocity, inclination and amplitude-to-noise ratio. This is clear in the panels of Figure 4.2. Given the restricted velocity resolution of the COLD GASS spectra, and since the only real difference between the Gaussian Double

---

[9] https://code.google.com/p/astrolibpy/source/browse/mpfit/mpfit.py

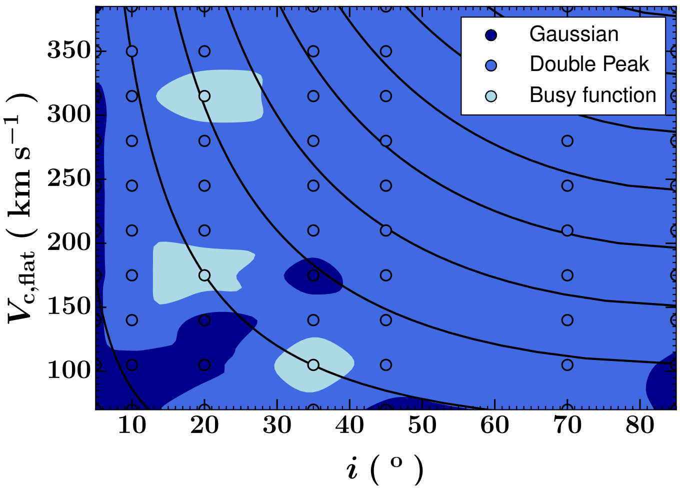

Figure 4.3: Self-consistency (as defined in the text) of the four analytical functions considered, as a function of the circular velocity $V_{\rm c,flat}$ and the inclination i. The colour coding shows which function is most self-consistent (dark blue: Gaussian function; blue: either of the Gaussian Double Peak or Exponential Double Peak function; light blue: Busy function). The data points (open circles) indicate $V_{\rm c,flat} - i$ pairs where a measurement was made. The underlying colour scale shows tri-tonal contours of the same measurements, for ease of interpretation. Black lines show curves of constant $V_{\rm c,flat} \sin i$. The Double Peak functions are the most self-consistent in the majority of the cases tested.

Peak and the Exponential Double Peak function is the shape of the edges, it was decided to group these two functions together when considering their self-consistency with respect to that of the Gaussian and Busy functions.

What is immediately obvious from Figure 4.3 is that the Busy function features very little in the plot; it was rarely the most self-consistent function. The main result is that the double-peaked functions are the most self-consistent in the majority of cases, be it the Gaussian Double Peak or the Exponential Double Peak function. The single Gaussian is the most self-consistent only at small inclinations (i.e. face-on discs) or small circular velocities. These two extremes are of course degenerate observationally, and this result is easily understood. Indeed, since any galaxy spectrum has a finite spectral resolution, the integrated velocity profile will appear Gaussian regardless of its intrinsic shape if the inclination or the circular velocity is small enough.

In addition to self-consistency, one should also consider how accurately each function recovers the circular velocity. For each of the four functions tested, Figure 4.4 thus shows the fractional difference between the true width ($W_{50,\rm true}$) and (twice) the projected circular

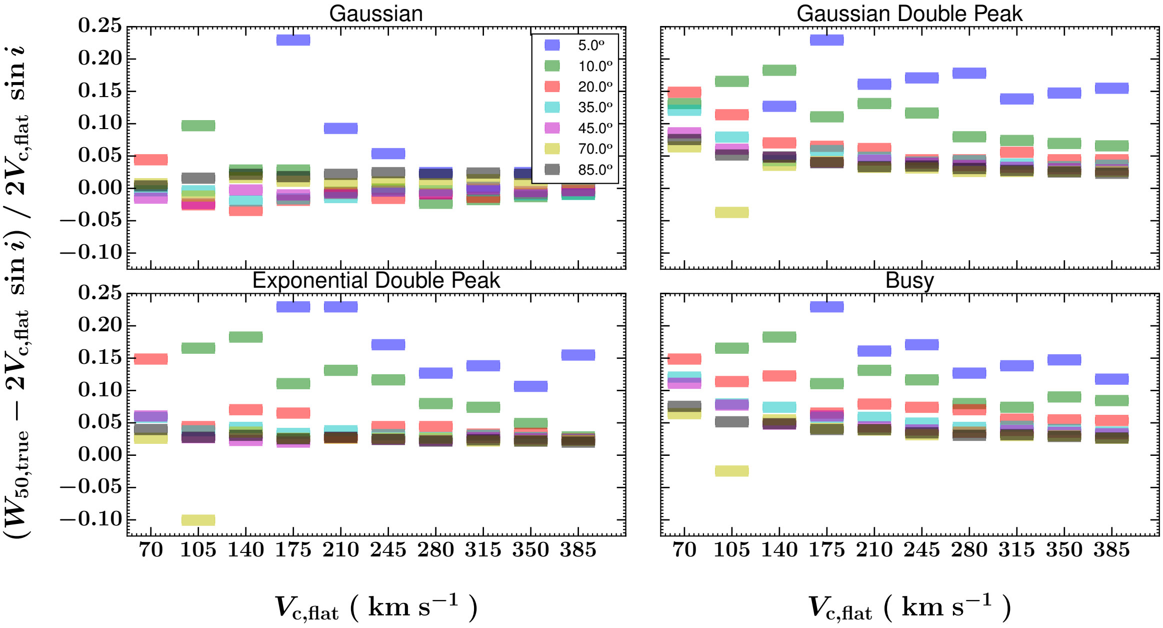

Figure 4.4: Fractional difference between the true width recovered ($W_{50,\rm true}$, W_{50} for $A/N = 10,000$) and twice the projected input circular velocity $2V_{\rm c,flat} \sin i$, this as a function of $V_{\rm c,flat}$ itself for different inclinations i. Each panel shows a different fitting function. In general, measurements of $W_{50,\rm true}$ are reasonably constant (as a function of $V_{\rm c,flat}$) for $i \geq 35°$ only.

velocity $2V_{\rm c,flat} \sin i$, this as a function of $V_{\rm c,flat}$ itself and for different values of the inclination i. In other words, Figure 4.4 summarises the position of the dashed black line, with respect to $2V_{\rm c,flat} \sin i$, in each of the panels of Figure 4.1 (but now for every velocity and inclination tested).

We recall here that a constant fractional offset is unimportant for TFR work, but that useful functions will minimise any systematic variation with circular velocity (and A/N). Figure 4.4 thus clearly shows that no function yields constant $W_{50,\rm true}$ measurements (as a function of $V_{\rm c,flat}$) at inclinations $i \leq 10°$, only the Gaussian Double Peak function does a reasonable job at $i = 20°$, and all functions are satisfactory at $i \geq 35°$.

Given that the cases in which the Gaussian function is most self-consistent cover only a small area in the parameter space of $V_{\rm c,flat}$ and i (see Fig. 4.3), and given that no function yields constant measurements at small i (Fig. 4.4), two conclusions must be drawn. First, galaxies observed at small inclinations ($i \leq 30°$) should be avoided. Second, the Gaussian Double Peak function is the most appropriate function with which to measure the CO(1-0) line widths of the COLD GASS galaxies (the Gaussian form of the profile's edge is also better justified physically than the exponential form). It should however be stressed that these conclusions are drawn here exclusively from simulated spectra with an intrinsic regular double-horned shape.

4.3.3 Measuring W_{50}

Given the conclusions drawn from § 4.3.2, the CO velocity width (W_{50}) of every sample galaxy was thus measured by fitting the Gaussian Double Peak function to its observed integrated CO(1-0) spectrum from COLD GASS, this using the Levenberg-Marquardt algorithm to minimise the reduced χ^2, given by

$$\chi^2_{\rm red} \equiv \left(\sum_i \frac{[F(v_i) - f(v_i)]^2}{\sigma^2_{\rm rms}} \right) / \ {\rm DOF} \ , \tag{4.7}$$

where $F(v_i)$ is the observed CO(1-0) spectrum flux density in velocity bin v_i, $f(v_i)$ is the model flux density in that same velocity bin from the Gaussian Double Peak function (i.e. the integral of the function across the bin divided by the bin width), $\sigma_{\rm rms}$ is the rms noise of the spectrum measured in a spectral range devoid of signal, DOF is the number of degrees of freedom associated with the fit, and the sum is taken over all velocity bins v_i of the spectrum. The best fits overlaid on the observed spectra are shown in Appendix C.2 for all galaxies in our final sub-sample (see § 4.4.2).

Despite the fact that the Gaussian Double Peak function proved to be the most robust function for fitting the CO profiles, this function reduces to a single Gaussian in the limit where the half-width of the central parabola $w \rightarrow 0$ (see Equation 4.4). As $w > 0$ was the only condition imposed on w during the Gaussian Double Peak function fitting process, there are cases where the best-fit value of w is less than the spectra's 11.5 km s^{-1} velocity bin width. In these cases, it is thus clear that a single Gaussian would be a more natural (and perhaps better) fit.

With this in mind, a strategy was adopted whereby each galaxy spectrum was fit with both the Gaussian Double Peak function and a standard Gaussian (see Equation 4.3). The value of $|1 - \chi^2_{\rm red}|$ for each function was then calculated and the two values compared. The fit with the smallest value was then adopted in each case.

One further caveat was necessary, since in some cases the best fit for the Gaussian Double Peak function resulted in the peak of the central quadratic A_{C} (i.e. the central flux) being significantly greater than the peak values of the flanking Gaussians A_{G}. In these cases the central quadratic has a convex rather than a concave or flat shape (as may be expected for respectively a double-horned or boxy-shaped profile). In these cases, specifically those for which $A_{\mathrm{C}} > (3/2)A_{\mathrm{G}}$, it was thus again deemed more appropriate to adopt the best-fit Gaussian rather than the Gaussian Double Peak function.

Finally, for each spectrum MPFIT was used to explore the parameter space to find the combination of parameters that best fit the data. The best fit that MPFIT returns can be sensitive to the user-supplied initial guesses as local minima in the χ^2 space can be mistaken for the global minimum by the fitting process. To reduce the chance of converging on a local minimum, and therefore not finding the true best-fit parameters, MPFIT was run several times for each spectrum, each time with a different set of initial guesses. The run with the smallest $|1-\chi^2_{\mathrm{red}}|$ value was then adopted as the best fit. The velocity width of the Gaussian Double Peak function at 50% of the peak, W_{50}, was then calculated in an analytical manner:

$$W_{50} = 2(w + \sigma\sqrt{2 \times \ln(2)}) \ . \tag{4.8}$$

The same applies to the pure Gaussian function with $w = 0$.

The velocity width uncertainty, ΔW_{50}, was then estimated by generating 150 realisations of the best-fit model, each with random Gaussian noise σ_{rms} added. Each realisation was fit as described above and ΔW_{50} taken as the standard deviation of the velocity width distribution.

4.4 COLD GASS Tully-Fisher Relations

4.4.1 Fitting the Tully-Fisher Relations

Both a forward and a reverse straight line fit was made to each of the resulting Tully-Fisher relations using a Levenberg-Marquardt minimisation technique, again with MPFIT. See

Table 4.1: Parameters of the $W1$-band Tully-Fisher relations.

Sample	Pivot	Fit	Slope	Intercept (mag)	Intrinsic Scatter (mag)	Total Scatter (mag)	Offset (mag)
Initial	2.49	Forward	-2.2 ± 0.3	-23.56 ± 0.07	0.92 ± 0.05	0.95 ± 0.02	-
		Reverse	-6.6 ± 0.7	-23.7 ± 0.1	1.5 ± 0.1	1.62 ± 0.01	-
		Bisector	-3.4 ± 0.3	-23.60 ± 0.01	-	-	-
		Fixed	-8.78	-23.8 ± 0.1	2.0 ± 0.1	2.18 ± 0.01	-0.8 ± 0.2
Sub-sample	2.58	Forward	-4.6 ± 0.4	-23.74 ± 0.07	0.59 ± 0.05	0.61 ± 0.01	-
		Reverse	-7.1 ± 0.6	-23.83 ± 0.09	0.73 ± 0.06	0.76 ± 0.01	-
		Bisector	-5.6 ± 0.3	-23.77 ± 0.01	-	-	-
		Fixed	-8.78	-23.9 ± 0.1	0.94 ± 0.08	0.96 ± 0.01	0.0 ± 0.1

Table 4.2: Parameters of the stellar mass Tully-Fisher relations.

Sample	Pivot	Fit	Slope	Intercept (dex)	Intrinsic Scatter (dex)	Total Scatter (dex)	Offset (dex)
Initial	2.49	Forward	1.0 ± 0.1	10.41 ± 0.03	0.44 ± 0.03	0.47 ± 0.01	-
		Reverse	3.3 ± 0.4	10.50 ± 0.06	0.77 ± 0.05	0.824 ± 0.004	-
		Bisector	1.7 ± 0.1	10.44 ± 0.01	-	-	-
		Fixed	3.05	10.49 ± 0.05	0.73 ± 0.05	0.765 ± 0.003	0.16 ± 0.06
Sub-sample	2.58	Forward	2.3 ± 0.2	10.48 ± 0.03	0.27 ± 0.02	0.287 ± 0.004	-
		Reverse	3.3 ± 0.3	10.51 ± 0.04	0.32 ± 0.03	0.344 ± 0.005	-
		Bisector	2.7 ± 0.2	10.49 ± 0.01	-	-	-
		Fixed	3.05	10.50 ± 0.03	0.30 ± 0.03	0.318 ± 0.003	-0.11 ± 0.04

§ 2.3.6 for definitions of the forward and reverse fit slope (m and M, respectively), intercept (b and B, respectively) calculated at a pivot point set to the median of the abscissa values, figures of merit ($\chi^2_{\rm for}$ and $\chi^2_{\rm rev}$, respectively), total scatter in the ordinate and abscissa ($\sigma^2_{\rm tot}$ and $\zeta^2_{\rm tot}$, respectively), and corresponding intrinsic scatter (respectively $\sigma_{\rm int}$ and $\zeta^2_{\rm int}$, and in each case determined as the value for which the reduced chi squared value of the fit is unity).

As stated in § 4.4.1, the reverse fit parameters can be directly compared to the forward fit parameters by defining the equivalent slope, intercept, intrinsic scatter and total scatter as $m^{'} \equiv 1/M$, $b^{'} \equiv -B/M$, $\sigma^{'}_{\rm int} \equiv M\zeta_{\rm int}$ and $\sigma^{'}_{\rm tot} \equiv M\zeta_{\rm tot}$, respectively (Williams et al., 2010).

4.4.2 Defining a Sub-sample

As described in § 4.2, an initial sample was drawn from the COLD GASS data that contains all galaxies with a secure CO(1-0) detection, *WISE* $W1$ photometry, an SDSS r-band axial ratio, a stellar mass via multi-band photometry, no AGN, and a GZ morphological classification for a total of 207 galaxies. The $W1$-band and stellar mass Tully-Fisher relations for this initial sample are shown in Figure 4.5(a) and 4.6(a), respectively, and the fit parameters are listed in Table 4.1 and 4.2, respectively. Clearly, for both the $W1$-band and stellar mass TFRs, the intrinsic and total scatters are very large for this initial sample.

There are several factors contributing to the observed scatter. Firstly, as shown in Figure 4.4, the measured velocity widths of nearly face-on galaxies are unreliable, in the sense that they do not accurately reproduce the intrinsic widths and their fractional errors are dependent on those widths. We thus removed from the initial sample galaxies with an inclination $i < 30°$, resulting in a sub-sample of 180 galaxies.

Secondly, one must gauge whether the CO extends to sufficiently large radii to sample the flat part of the galaxies' rotation curves. This is essential, as otherwise the measured velocity widths will not be representative of the total dynamical masses, introducing additional scatter in the relations. Although not necessary, empirical studies have shown that the kinematic tracer of galaxies with a boxy or double-horned integrated profile usually extends beyond the turn-over of the rotation curve (e.g. Davis et al., 2011). A Gaussian profile may

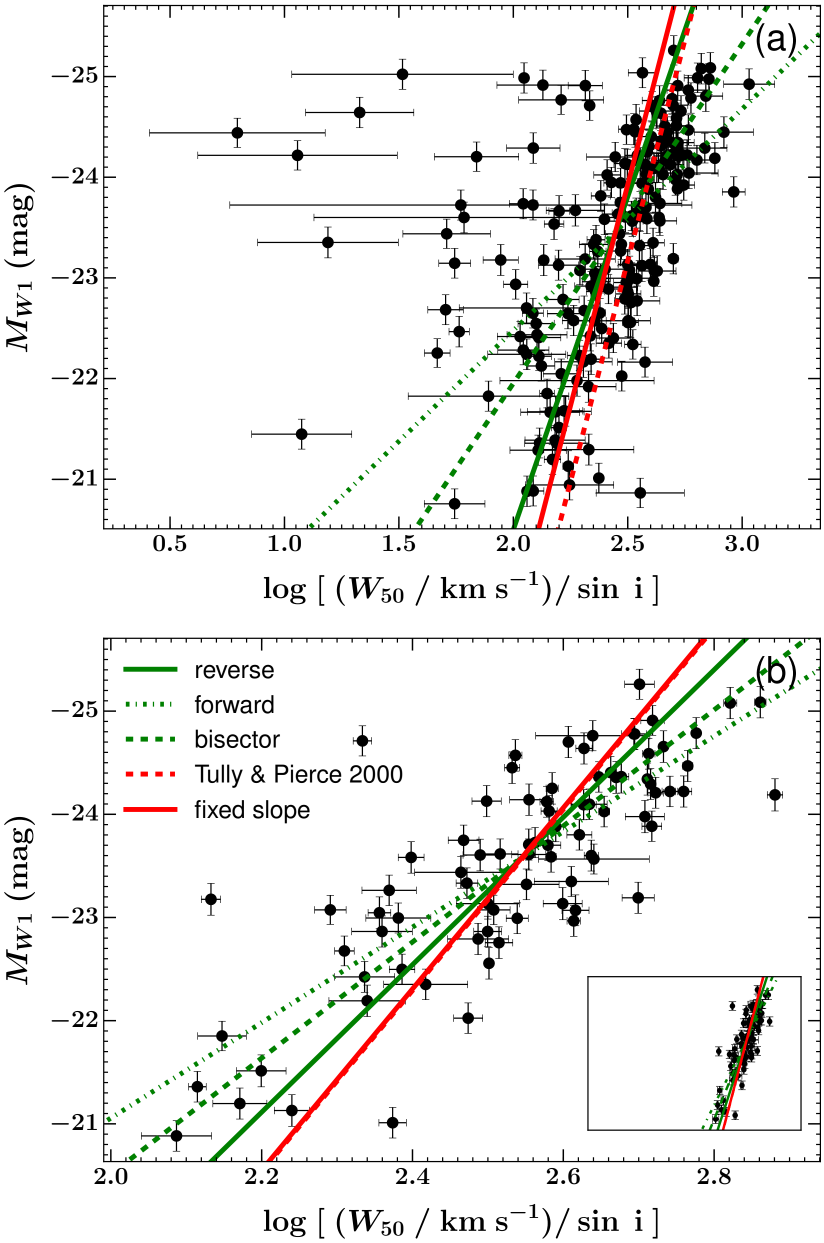

Figure 4.5: COLD GASS $W1$-band Tully-Fisher relations. (a) and (b) show the TFR for the initial COLD GASS sample and our final sub-sample, respectively. The x-axis is the width of the integrated CO(1-0) profile at 50% of the peak, corrected for the effect of inclination. The y-axis is the absolute *WISE* Band 1 magnitude $W1$ ($\approx$ 3.4 μm). The green dot-dashed, solid and dashed lines show the forward fit, reverse fit, and the bisector of the two, respectively. The dashed red line is the K-band TFR of Tully & Pierce (2000). The solid red line shows the best fit when the gradient is constrained to that of Tully & Pierce. To demonstrate the reduction in scatter between the initial and final sub-sample, the embedded panel in (b) shows the TFR for the final sub-sample but over the same axis ranges as (a).

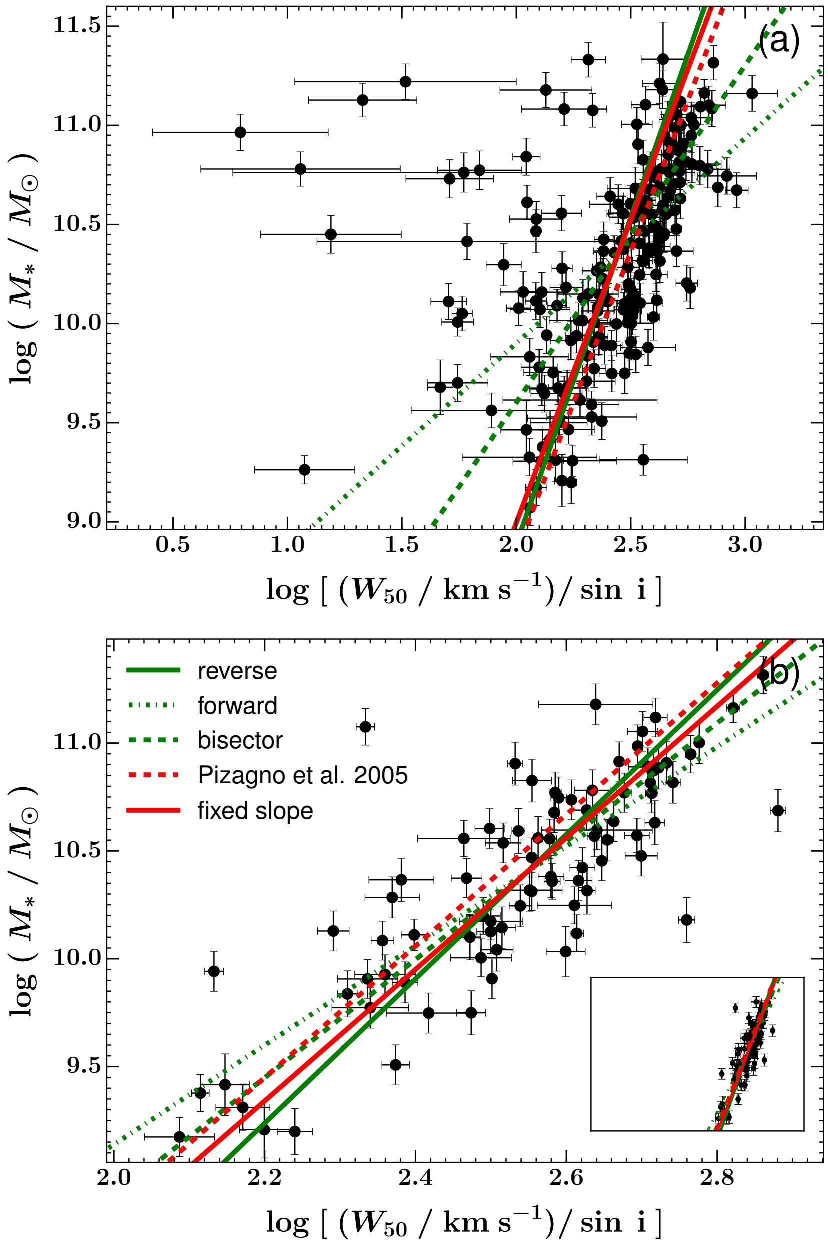

Figure 4.6: As Figure 4.5, but for the COLD GASS stellar mass Tully-Fisher relations. The dashed red line is the stellar mass TFR of Pizagno et al. (2005). The solid red line shows the best fit when the gradient is constrained to that of Pizagno et al.

imply that insufficient CO is present in the outer parts to robustly recover the flat part of the rotation curve, or that the rotation curve itself is not flat. Of course, a Gaussian profile can also arise, despite sufficient CO present in the outer parts of a galaxy, if there is a particularly high concentration of gas in the central regions of the galaxy (e.g. Wiklind et al., 1997; Lavezzi & Dickey, 1997), but this is a risk worth taking. Lastly, given the finite width of the velocity channels, rejecting profiles that do not appear boxy or double-horned may also exclude profiles that are intrinsically boxy or double-horned but simply have small line widths, an effect that would preferentially affect the low-mass end of the TFRs. However, this drawback is small compared to the benefits of significantly reduced scatter.

This approach is consistent with the understanding that the flat part of a galaxy's rotation curve is accurately recovered provided that the "flaring parameter" of the integrated profile (i.e. the ratio of the line width at 20% of the peak flux to that at 50%) is less than ≈ 1.2 (Lavezzi & Dickey, 1997, 1998). In other words, both methods select integrated profiles with steep edges. We therefore reduced our sample further by requiring that the integrated CO(1-0) profile of each galaxy be either boxy or double-horned. In practice, this amounts to excluding galaxies whose profile was best fit by a single Gaussian function rather than the Gaussian Double Peak function, resulting in a sub-sample of 94 galaxies.

Thirdly, we consider how well our line profile fits recover the true velocity widths at small amplitude-to-noise ratios A/N. As illustrated in Figure 4.1, $A/N \geq 1.5$ is generally required to recover the true velocity width to 10% or better. Given the limited size of the COLD GASS sample and the typical quality of the CO data, this threshold also ensures a final sub-sample with a sufficiently large number of galaxies for robust TFR fits. Applying this A/N cut results in a sub-sample of 88 galaxies.

Fourthly, to have confidence in the accuracy of the velocity widths derived from the profile fits, we remove those galaxies with a fractional uncertainty ΔW_{50} / $W_{50} > 20\%$. This further reduces our sub-sample to 84 galaxies.

Lastly, we consider the morphologies of our sample galaxies, as galaxies of different morphological types have different TFR zero-points (presumably due to different surface mass densities and mass-to-light ratios; see Eq. 1.1). In particular, there is a clear offset

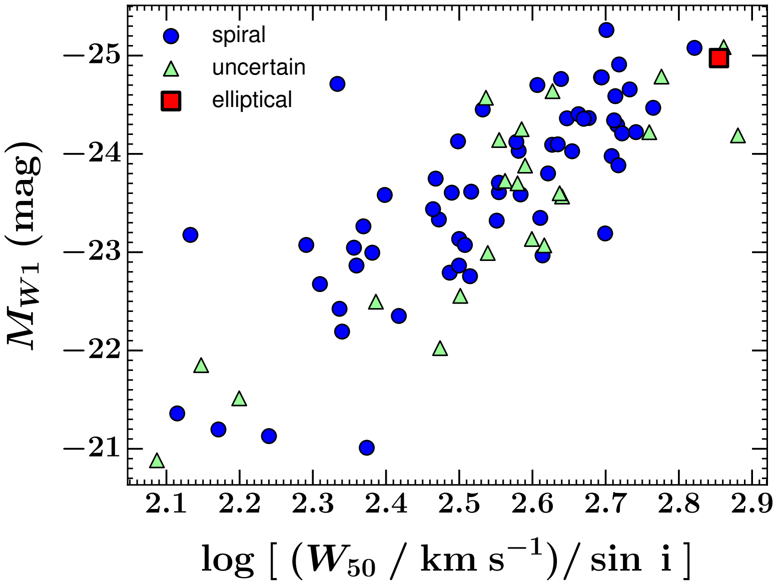

Figure 4.7: As Figure 4.5, but for an intermediate (although nearly final) COLD GASS sub-sample (as described in § 4.4.2). Error bars are omitted for clarity and the galaxies are identified by their GZ1 morphological type (see § 4.2.6): blue circles for spirals (late-types), red squares for ellipticals (early-types), and green triangles for uncertain types. It is clear that those galaxies deemed uncertain follow broadly the same relation as, and do not exhibit increased scatter in comparison to, those deemed spirals.

between early- and late-type galaxies (see e.g. Williams et al., 2010; Davis et al., 2011). In fact, the work of Davis et al. (2016) suggests that very massive early-type galaxies are again offset from the TFR of early-types of lower masses. There are also possible variations of the TFR slope among late-type galaxies (e.g. Lagattuta et al., 2013).

Figure 4.7 shows the TFR of our galaxy sub-sample after all the aforementioned cuts have been applied, and where all galaxies have been labeled according to their morphological type (see § 4.2.6). Error bars have been omitted for clarity. As there is only one early-type galaxy, it was removed from the sub-sample. As the galaxies of uncertain morphological type are essentially indistinguishable from the late-types, with a similar slope, zero-point and scatter, there is no reason to exclude them and we instead assimilate them to the late-type galaxies.

Overall, this thus leads to a final sub-sample comprising 83 late-type galaxies, that we use for both $W1$-band and stellar mass TFR fits. The resulting $W1$-band and stellar mass Tully-Fisher relations for this final sub-sample are shown in Figure 4.5(b) and 4.6(b), respectively, while the fit parameters are listed in Table 4.1 and 4.2, respectively. As desired, the observed scatters of our final sub-sample are significantly reduced compared to those of the initial sample, this for both the $W1$-band and stellar mass TFR.

4.4.3 The Tully-Fisher Relations

As described above, Figures 4.5 and 4.6 show the COLD GASS $W1$-band and stellar mass Tully-Fisher relation, respectively, for both the initial and final sub-samples, with the forward, reverse and bisector fits overlaid. Tables 4.1 and 4.2 list the corresponding fit parameters. The reverse fit parameters have been adjusted to be directly comparable to the forward fit parameters, as described in § 4.4.1.

A comparison relation is also displayed on each plot: for the $W1$-band TFR, the K-band relation of Tully & Pierce (2000), who used HI integrated profiles to measure the galaxy rotation velocities; for the stellar mass TFR, the stellar mass relation of Pizagno et al. (2005), who used long-slit observations of Hα emission to measure the ionised gas rotation. Based on the work of Madau & Dickinson (2014), we apply a small offset in $\log(M_*/M_\odot)$ of -0.034 dex to the latter, to convert from a Kroupa (Kroupa, 2001) to a Chabrier IMF. A fit to the COLD GASS data with the slope fixed to that of the comparison relation is also shown in each case, allowing to gauge any offset between the comparison and COLD GASS samples. We recall that with $(K - W1) \approx 0 \pm 0.2$ for late-type galaxies, a $W1$–K comparison is justified (Lagattuta et al., 2013).

As expected, the reverse fits are always much steeper than the forward fits, and indeed for both initial and final sub-samples and $W1$-band and stellar mass TFRs, the slopes of the reverse fits are much closer to those of the comparison samples.

It is well established that a significant bias in the slope is introduced by using a forward fit (e.g. Schechter, 1980; Teerikorpi, 1987; Sandage, 1988; Tully & Pierce, 2000; Tully & Courtois, 2012; Sorce et al., 2013), stemming from the selection criteria imposed on galaxy samples used in TFR studies. This bias is explained in detail by Willick (1994).

To understand why this approach is problematic, first consider the measured TFR of a complete (i.e. independent of any selection) sample of galaxies, with some Gaussian intrinsic scatter in magnitude (and indeed line width). For a given line width, a galaxy may be scattered either above or below the TFR if it is intrinsically brighter or dimmer than the corresponding mean magnitude for that line width (i.e. that predicted by the true, unbiased TFR). Now consider measuring the TFR for the same sample but for the common case where a limiting magnitude is imposed, such that galaxies dimmer than the limiting value are excluded from the analysis. At the faint end of the TFR, those galaxies that are intrinsically brighter than the mean will be preferentially included in the analysis, whilst those that are dimmer will be excluded. This acts to flatten the slope of the measured TFR, as at the small line width end the sample is biased brighter than the true underlying distribution. This bias is compounded by the fact that the uncertainties in the line width measurements are typically at least comparable (and often larger) than those in the luminosity measurements.

Since in this scenario there is no selection via line width, the reverse fit, which minimises the residuals in line width, avoids this bias. Willick (1994) points out that in practice some bias will still remain for the reverse fit when considering the TFR in a waveband other than that used to select the sample. This is particularly relevant to this work, since the GASS sample (and therefore COLD GASS) was not selected via a limiting $W1$ magnitude but was rather selected to be flat in $\log(M_*/M_\odot)$ above a minimum stellar mass value (see § 4.2.1). Nevertheless the bias in the reverse fit is much reduced compared to that of the forward fit. Willick et al. (1995), for example, find a reduction of a factor of 6 in the bias between the forward and reverse fit when examining the TFRs of several samples of spiral galaxies selected in the I and r bands. In light of this, the parameters in this work derived from a forward fit should be treated with a degree of caution.

As desired following the exclusion of potential sources of scatter (see § 4.4.2), for both the $W1$-band and the stellar mass TFR there is a much greater scatter in the initial sample than in the final sub-sample. In addition, the intrinsic and total scatters are always larger in the reverse fit than in the forward fit, reflecting the larger scatter in W_{50} than in M_{W1} and M_*.

4.5 Discussion

4.5.1 Slope

Treating the forward fits with suspicion, it is most sensible to compare the results of previous studies to the reverse fits only. The unconstrained reverse fit to the $W1$ TFR is shallower than the relation found by Tully & Pierce (2000) for both the initial and final sub-sample, even allowing for the uncertainties (although Tully & Pierce do not quote an uncertainty on their slope). However, the slope of both sub-sample's stellar mass TFR agrees with that of the Pizagno et al. (2005) TFR, after allowing for uncertainties (Pizagno et al. 2005 quote an uncertainty of ± 0.12 on their slope). The stellar masses are model dependent, however, so the significance of this result is uncertain, particularly given the comparatively shallower slope of the $W1$ relation.

Several factors could of course affect the slope of the COLD GASS TFRs, in particular a potential Malmquist bias and the fact that galaxies of various primarily late-type morphologies were amalgamated together. The former factor is likely to be most acute for the stellar mass TFRs, as the COLD GASS sample was stellar mass-selected, but it is unlikely to be important for the final sub-sample as our various selection criteria, particular the integrated profile shape criterion (see § 4.4.2), have largely washed out any abrupt stellar mass threshold. Of course the same criterion may also preferentially exclude those galaxies with small line widths. However, this effect is likely to be small in comparison to the Malmquist bias introduced via the GASS (and thus COLD GASS) selection function. The latter factor is undoubtedly present to some extent, but it is hard to quantify without better morphologies. Indeed, as our samples contain a variety of (mainly late-type) galaxy morphologies, and the slope of the TFR varies with galaxy type, the measured slopes are effectively averages of mutliple slopes for different galaxy morphologies.

Lastly, we must also consider whether the very use of CO as a kinematic tracer may bias the slope of the TFR, such that the resultant slope is shallower than that of the HI TFR of the same sample. Indeed, the line widths of Tully & Pierce (2000) are measured from HI observations, whereas the COLD GASS line widths are measured from CO(1-0). In Appendix C.1, for subsets of COLD GASS galaxies with both CO(1-0) and HI data, we compare the values of W_{50} as derived from the width of both the CO(1-0) and HI integrated profiles (as described in § 4.3.3). We find that the slope of the TFRs constructed using CO(1-0) are either comparable to or slightly shallower than those of the HI TFRs of the same galaxies. However, the slopes of both the CO(1-0) and HI TFRs agree within uncertainties. We may therefore cautiously attribute *some* of the difference in slope between the COLD GASS $W1$ TFR and the comparison relation to the use of CO(1-0) (rather than HI) as a kinematic tracer, but it should be stressed that, on the basis of the comparison in Appendix C.1, this is not likely to be the driving factor of the difference. Furthermore, as shown again in Appendix C.1, much is to be gained from using CO rather than HI, as it lead to much smaller intrinsic (and thus total) scatter for the sub-sample.

4.5.2 Inclinations

The uncertainties on the measured inclinations i contribute greatly to the uncertainties on the inclination-corrected velocity widths $W_{50}/\sin i$, particularly at small inclinations (and even with an $i > 30°$ threshold). The robustness of any constructed TFR is thus highly dependent on the accuracy of the inclination measurements. The scatter of the TFR is likely to increase with decreasing accuracy, with possibly a smaller systematic effect affecting the measured slope.

The axial ratio method used in this work is appropriate for the relatively shallow ground-based optical imaging used, but it is not particularly refined. First, it naively assumes that galaxies can be grouped into categories sharing a unique edge-on (intrinsic) axial ratio (here 0.2 and 0.34 for late types and early types, respectively). The morphologies of galaxies are in reality much more diverse, and the intrinsic axial ratio is likely to vary within any defined category. This is particularly relevant to our work, as the inclination measurements are ultimately dependent on the relatively crude GZ1 morphological classifications. Davis et al. (2011) in fact showed that the scatter in the TFR of a sample of early-type galaxies is reduced when one uses a measure of inclination derived from the intrinsically very flat dust features visible in high resolution (*Hubble Space Telescope*) imaging, rather than stellar light as used here. While the magnitude of the effect was certainly amplified by the use of early-type galaxies, it nevertheless illustrates the point.

Having said that, as our inclinations are based on rather shallow ground-based imaging, it may also be that they are systematically underestimated (the galaxies appearing rounder than they really should), leading to over-estimated inclination corrections to the velocity widths. As this effect is likely to be more acute in smaller, lower mass galaxies, however, it would lead to steeper rather than shallower TFRs.

4.5.3 Offset

We measure a small offset between the stellar mass TFR for both the initial and final sub-samples presented in this work and that of Pizagno et al. (2005) ($+0.16 \pm 0.06$ and -0.11 ± 0.04 dex, respectively). Considering the $W1$-band TFRs, we measure a large negative offset (-0.8 ± 0.2 mag) between the initial sample's TFR and that of Tully & Pierce (2000). However, this offset disappears when considering the (more reliable) $W1$-band TFR for the final sub-sample. Importantly, in all cases, the offset between the COLD GASS and the comparison sample TFR (at fixed slope) is much smaller than the intrinsic scatter. There is thus no evidence for any significant offset between the COLD GASS and comparison samples, as expected given the similar redshifts and morphologies of the samples' galaxies.

4.5.4 Scatter

The intrinsic and total scatters of the $W1$-band Tully-Fisher relation for our final sub-sample, for the forward unconstrained fit, were found to be 0.59 ± 0.05 and 0.61 ± 0.01 mag, respectively. These values are slightly larger than those of previous near-infrared TFR studies. Tully & Pierce (2000) found a K'-band total rms scatter of 0.44 mag for local spiral galaxies, whilst Verheijen (2001) found a 0.32 mag total scatter for the same passband. However, Pizagno et al. (2007) found an intrinsic scatter of 0.42–0.46 mag across the g, r, i and z bands.

Considering the stellar mass TFR of the final sub-sample, the intrinsic and total scatters of the forward unconstrained fit were found to be 0.27 ± 0.02 and 0.287 ± 0.004 dex, respectively. As with the $W1$-band relation, this is larger than previous TFR studies in the local universe. Bell & de Jong (2001) found a total scatter of just 0.13 dex, whilst Pizagno et al. (2005) similarly found an intrinsic scatter of 0.16 dex.

The reasons why we measure a slightly higher intrinsic scatter than previous studies are unclear. In Appendix C.1 we show that the use of line widths derived from CO(1-0) integrated profiles leads to increased scatter in the TFR, compared to the same TFR constructed using HI integrated profiles. However, this difference in scatter disappears when we apply the criteria used to select the sub-sample described in § 4.4.2. This implies that the increased scatter is due to the inclusion of CO(1-0) profiles that do not display a boxy or double-horned shape. Once these systems are removed, the intrinsic and total scatter of the CO(1-0) TFRs are actually less than those of the HI TFRs for the same galaxies.

As discussed above, the mix of several different late-type morphologies may affect the slope and scatter (through different mass surface densities Σ and mass-to-light ratios M/L), while our inclinations may be underestimated. While we have taken great care to estimate and propagate uncertainties on our measurements, it may also be that our observational errors are underestimated (leading to an overestimate of the intrinsic scatter). The uncertainties on the stellar masses and inclinations are particularly hard to reliably estimate.

4.5.5 Sample Selection

The selection criteria of GASS, and thus COLD GASS, present two potential problems when using galaxies drawn from these samples to build TFRs. The first, discussed at length above, is the problem of fitting a single TFR (slope and zero-point) to a sample of galaxies with differing morphologies. The second is that both the GASS and COLD GASS samples are chosen to be flat in $\log M_*$. This means that, compared to e.g. a volume- or flux-limited sample, galaxies of large masses will be over-represented. This could result in an inferred TFR with a shallower than expected slope, depending on how heavily weighted high-mass galaxies are in comparison to low-mass galaxies.

The sub-sample selection, as described in § 4.4.2, leads to a dramatic and significant reduction in the scatter of the TFRs. The main driver in this reduction is the exclusion of galaxies with profiles that do not appear boxy or double-horned. This ensures that we include in our analysis only those galaxies with sufficient CO in the outer parts to properly sample the flat parts of the rotation curve. This is at the expense of the possible rejection of profiles that are intrinsically boxy or double-horned but simply appear Gaussian due to their small line width and the finite width of the velocity channels. This cut by profile shape preferentially affects the low-mass end of the TFRs, and could therefore bias their resultant slopes. However, the effect is likely to be small (and opposite to the Malmquist bias) and the benefits of the significantly reduced scatter far outweigh the drawbacks.

4.6 Conclusions & Future Work

In an effort to firmly establish the CO TFR as a useful tool to probe the evolution of galaxies over cosmic time, we first tested the self-consistency and robustness of four functions appropriate to fit the integrated line profiles of galaxies, particularly in the low signal-to-noise ratio regime characteristic of molecular gas observations. The Gaussian Double Peak function was deemed to be the most self-consistent and to suffer the least from possible systematic biases as a function of the amplitude-over-noise ratio A/N, the galaxy inclination i and the intrinsic flat circular velocity $V_{\rm c,flat}$.

We then constructed the *WISE* $W1$-band and stellar mass TFRs relations of galaxies drawn from the COLD GASS sample, both for an initial sample of all galaxies with available data, and for a restricted sub-sample of galaxies with high quality measurements (thus decreasing the scatter). The rotation of the galaxies was determined by fitting the Gaussian Double Peak function to the integrated CO(1-0) line profile of each galaxy, and then measuring the width at 50% of the peak of the resultant fit (W_{50}). The $W1$ magnitudes were drawn directly from the *WISE* catalogue, and the stellar mass for each galaxy was determined via SED fitting of SDSS photometry.

The TFRs obtained from unconstrained forward fits have shallower slopes than those expected from previous studies. Considering only the more robust reverse fits, however, the best-fit TFRs for the final COLD GASS sub-sample are

$$M_{W1} = (-7.1 \pm 0.6)\left[\log\left(\frac{W_{50}/\sin i}{\rm km\ s^{-1}}\right) - 2.58\right] - 23.83 \pm 0.09 \tag{4.9}$$

and

$$\log(M_*/M_\odot) = (3.3 \pm 0.3)\left[\log\left(\frac{W_{50}/\sin i}{\mathrm{km\ s^{-1}}}\right) - 2.58\right] + 10.51 \pm 0.04\ . \tag{4.10}$$

The unconstrained reverse fit slope of the COLD GASS sub-sample $W1$-band TFR is still marginally shallower than that of Tully & Pierce (2000), but the slope of the stellar mass TFR agrees within the uncertainties with the relation of Pizagno et al. (2005). The intrinsic scatter (from forward fitting) is 0.59 ± 0.05 mag and 0.27 ± 0.02 dex for the $W1$-band and stellar mass sub-sample TFR, respectively.

Fixing the slopes to those of the relations from the comparison samples, small offsets are found with respect to the comparison samples, that are however less than the intrinsic scatters. The COLD GASS samples therefore agree with the comparison samples, although they have slightly larger scatters than expected. Possible causes of the increased scatters were discussed and include the method adopted to measure inclinations, and fitting a single TFR to samples of galaxies with various primarily late-type morphologies. Importantly, we showed that for a subset of COLD GASS galaxies in the final sub-sample with both CO(1-0) and HI data, the intrinsic and total scatters of the CO(1-0) TFRs were less than those of the same TFRs constructed using HI integrated profiles.

The COLD GASS initial sample and final sub-sample contain a number of galaxies comparable to those in previous CO TFR studies. Our work thus provides a robust local benchmark to be used for comparison with future CO work. In particular, Torii et al. (in prep.) will build a local reference sample based on observations of very nearby galaxies with the NANTEN2 telescope, and utilising identical fitting methods to ours. Topal et al. (in prep.) will compare the TFRs presented here with those measured using a sample of galaxies at $z \lesssim 0.3$, including luminous infrared galaxies (LIRGs) and galaxies from the Evolution of Gas in Normal Galaxies (EGNoG) survey.

With the dawn of ALMA (and the Northern Extended Millimeter Array[10]), it is now possible to relatively rapidly measure the CO emission of galaxies to large redshifts, when the first objects were forming and slowly settling into the discs we see today. In particular,

---

[10] http://iram-institute.org/EN/noema-project.php

significant samples of galaxies observed in CO are now being built to probe the epoch of peak global star formation activity ($1 \lesssim z \lesssim 3$), when turbulent gas-rich galaxies were building the bulk of their stellar mass. Our work therefore provide a robust reference point with which to compare future TFR studies of those objects and is a vital first step in providing a measure of the evolution of the TFR over the last ≈ 8 Gyr independent of that presented in Chapters 2 and 3.

Chapter 5

Conclusions

In this thesis we used the Tully-Fisher relation (TFR; Tully & Fisher, 1977), the correlation between a galaxy's luminosity and rotation velocity, as a tool to probe the evolution of the total-to-luminous matter ratio of star-forming galaxies since $z \approx 1$. In this chapter we summarise our key findings from each previous chapter. In § 5.1 we discuss future work that will build and expand upon that presented here.

In Chapter 2 we presented the stellar mass (M_*), and K-corrected K-band absolute magnitude (M_K) TFRs for sub-samples of the 585 galaxies spatially resolved in Hα emission by the K-band Multi-Object Spectrograph (KMOS; Sharples et al., 2013) Redshift One Spectroscopic Survey (KROSS; Stott et al., 2016). We modelled the line-of-sight velocity field of each of the KROSS galaxies (as traced by their Hα emission) with a simple arctangent function (Courteau, 1997) and extracted a rotation velocity, V_{80} at a radius equal to the major axis of an ellipse containing 80% of the total Hα flux. The large sample size of KROSS allowed us to select 210 galaxies with well measured rotation velocities, that we referred to as the *all* sub-sample. From those we extracted a further *disky* sub-sample of 56 galaxies that were rotationally supported, using the stringent criterion $V_{80}/\sigma > 3$, where σ is the flux-weighted average intrinsic velocity dispersion. We found an evolution of the M_* TFR zero-point of 0.41 ± 0.08 dex over the last ≈8 Gyr. However, we measured no evolution in the M_K TFR zero-point over the same period. Based on those measurements we concluded that (at fixed rotation velocity) the total mass-to-stellar mass ratio of disk-like galaxies has decreased by a factor of ≈ 0.6 since $z \approx 1$, whilst the K-band stellar mass-to-light ratio has increased by a factor ≈ 2.5 over the same period. We deduced that such changes would require a large (but plausible) amount of gas accretion on to galaxies over the last ≈ 8 Gyr, with its subsequent conversion to stars. Lastly, we reasoned that the ability of KROSS to differentiate, using integral field spectroscopy with KMOS, between those galaxies that were rotationally supported and those that were not explained why our findings were at odds with previous studies without the same capabilities.

Whilst the implications for galaxy evolution of the result presented in Chapter 2 are potentially important, the analysis of that chapter suffered from the fact that we could not compare TFRs constructed in a homogeneous manner at both epochs. Indeed, the relations at the two epochs differed in data quality, kinematic tracers, and the measures of galaxy parameters required for the TFR (i.e. rotation velocity, luminosity and stellar mass). Furthermore, as we relied on samples drawn from the literature to construct the $z \approx 0$ TFRs we were unable to match the sample selection of the relations between the two epochs. As a result, we could expect potentially different biases in the TFRs, confusing any measure of evolution between them. To address this, in Chapter 3 we presented a carefully matched comparison of the M_K and M_* TFRs at $z \approx 1$ and 0, using IFU observations of Hα emission from KROSS galaxies at $z \sim 1$ with KMOS and galaxies from the Sydney-Australian-Astronomical-Observatory Multi-object Integral-Field Spectrograph (SAMI; Croom et al., 2012) Galaxy Survey (e.g. Bryant et al., 2015) with the SAMI spectrograph.

We degraded the spatial and spectral resolution and sampling, and the Hα signal-to-noise of the original, high quality (HQ) SAMI observations to match those typical of KROSS, referring to the degraded data set as the low quality (LQ) SAMI data. We derived M_* and M_K for the HQ and LQ galaxies from fits to their corresponding spectral energy distributions (SEDs), truncating the LQ galaxies' SEDs to match the (restframe) wavelength range available for KROSS galaxies. After extracting and modelling (using the arctangent model of Chapter 2) the Hα velocity fields of the HQ and LQ data, a comparison between the two data sets revealed the LQ sample was biased against those galaxies that were more compact (or with more compact Hα emission) and slowly rotating. Despite this, the degrading process did not affect our ability to accurately recover key galaxy parameters. We found relations consistent with 1:1 with varying scatters between the measures of the rotation velocity at 1.3 times the effective radius r_e ($v_{2.2}$), the intrinsic velocity dispersion σ, M_K, and M_* calculated from the SAMI HQ and SAMI LQ data.

We constructed the SAMI HQ and LQ TFRs, first selecting sub-samples of galaxies from each data set based on the *all* and *disky* sub-sample selection criteria of Chapter 2. Due to the similarities between the criteria of the chapters, we retained the Chapter 2 nomenclature. Comparing the M_K and M_* TFRs of the *all* sub-samples for both data sets, somewhat surprisingly we found scatters along both axes of the LQ TFRs that were comparable to those of the corresponding HQ relations. For the *disky* sub-samples (from which we excluded galaxies with insufficient ratios of rotation velocity to intrinsic velocity dispersion, $v_{2.2}/\sigma < 3$), however, we found the scatters along both axes of the LQ M_K and M_* TFRs to be larger than those of the corresponding HQ relations, as one might expect. We explained the lower than expected scatters in the LQ TFRs (compared to the HQ relations) for the *all* sub-sample by considering that the *all* sub-sample of each data set includes more galaxies with low $v_{2.2}/\sigma$ (and thus $v_{2.2}$) than the *disky* sub-sample. Those galaxies disproportionately increase the TFRs scatters compared to galaxies with high $v_{2.2}/\sigma$. Since the LQ data was biased against such systems, the scatters in the LQ TFRs for the *all* sub-sample were reduced compared to those of the corresponding HQ relations. When those galaxies were entirely excluded from both data sets as for the *disky* sub-samples, the scatters of the TFRs then reflected the scatters in the velocity and luminosity (and mass) measures instead, that are larger for the LQ data than the HQ. Indeed, we found increased scatters of the LQ TFRs for the *disky* sub-sample compared to those of the corresponding HQ relations. The slopes and intercepts of the TFRs of the *all* and *disky* sub-samples were generally consistent between the HQ and LQ data sets.

Lastly, we compared the KROSS TFRs for the *all* and *disky* sub-samples to the corresponding SAMI LQ relations, the former constructed from improved best fit model velocity fields (with respect to Chapter 2), and measures of inclination and size derived from broad-band images (as opposed to the galaxies' Hα maps, as in Chapter 2). As in Chapter 2, we found shallower slopes for the M_K and M_* KROSS TFRs of the *all* sub-sample compared to the $z \approx 0$ relations, in this case the corresponding SAMI LQ TFRs. This discrepancy disappeared when considering the slopes of the TFRs for the *disky* sub-samples. We found the intrinsic scatters of the SAMI LQ TFRs for the *all* sub-sample to be smaller than or consistent with the corresponding KROSS relations. For the TFRs of the *disky* sub-samples, the intrinsic scatters of the KROSS relations were larger than those of the corresponding SAMI LQ relations in almost every case. Ignoring the offsets between the zero-points of the SAMI LQ and KROSS TFRs for the *all* sub-samples (that are affected by the inclusion of galaxies with insufficient ratios of rotation velocity to velocity dispersion, i.e. with $v_{2.2}/\sigma < 3$) in favour of those of the *disky* sub-samples, we found no evidence for any evolution in the M_K TFR zero-point for disk-like star-forming galaxies since $z \approx 1$. But we did measure an offset of 0.2 ± 0.2 dex between the stellar mass TFR zero-points of the same galaxies over the same period.

We concluded that at fixed rotation velocity the total mass-to-stellar mass ratio of disk-like star-forming galaxies has decreased by a factor of ≈ 0.4 since $z \approx 1$, whilst their K-band stellar mass-to-light ratio has increased by a factor of ≈ 1.6 over the same period. Whilst these changes can be entirely accounted for by the complete conversion into stars of the gas already present in (KROSS) galaxies at $z \approx 1$, we proposed a more likely scenario whereby the gas in those galaxies is converted to stars at a moderate rate with continued replenishment of the gas reservoir via accretion of external material. We also pointed out that, following the depletion of the initial $z \approx 1$ gas reservoir, any further baryonic accretion on to disk-like star-forming galaxies must be closely matched by the accretion of similar amounts of dark matter to keep the total mass-to-stellar mass ratio constant and equal to that of galaxies in the local Universe. Lastly we reasoned that, depending on how rapidly the $z \approx 1$ gas reservoir is depleted, our findings may also support the hypothesis that star-forming galaxies have grown in a principally hierarchical fashion over the last ≈ 8 Gyr.

In Chapters 2 and 3 we presented the first direct comparison of the TFRs at $z \approx 1$ and $z \approx 0$ using large samples of integral field unit (IFU) observations of galaxies at each epoch matched both in data quality and analysis methods. This allowed a straight forward comparison of the relations at each epoch, free of any difference in biases between them. Whilst this was a significant undertaking, to corroborate our results it is sensible also to pursue an alternative measure of the TFR evolution over the same period independent of the methods of those chapters. We must also make sure that our result is not biased by our choice of kinematic tracer (i.e. Hα emission).

In Chapter 4 we took the first step toward such an independent measure by constructing the TFR of $z \approx 0$ galaxies using integrated observations of their CO(1-0) emission. We presented the M_* and *Wide-Field Infrared Survey Explorer* (*WISE*; Wright et al., 2010) absolute Band 1 magnitude (M_{W1}) TFRs of subsets of galaxies from the CO Legacy Database for the *GALEX* Arecibo SDSS Survey (GASS; Catinella et al., 2010) (COLD GASS; Saintonge et al., 2011). We examined the benefits and drawbacks of several commonly used fitting functions in the context of measuring CO(1-0) line widths (and thus rotation velocities), favouring the Gaussian Double Peak function. We found the M_{W1} and M_* TFR, for a carefully selected sub-sample, to be

$$M_{W1} = (-7.1 \pm 0.6)\left[\log\left(\frac{W_{50}/\sin i}{\text{km s}^{-1}}\right) - 2.58\right] - 23.83 \pm 0.09\ , \tag{5.1}$$

and

$$\log(M_*/M_\odot) = (3.3 \pm 0.3)\left[\log\left(\frac{W_{50}/\sin i}{\text{km s}^{-1}}\right) - 2.58\right] + 10.51 \pm 0.04\ , \tag{5.2}$$

respectively, where W_{50} is the width of a galaxy's CO(1-0) integrated profile at 50% of its maximum and the inclination i was derived from the galaxy axial ratio measured on the SDSS r-band image. We found no evidence for any significant offset between the TFRs of COLD GASS galaxies and those of comparison samples of similar redshifts and morphologies. The slope of the COLD GASS M_* TFR agreed with the relation of Pizagno et al. (2005). However, we measured a comparatively shallower slope for the COLD GASS M_{W1} TFR as compared to the relation of Tully & Pierce (2000). We attributed this to the fact that the COLD GASS sample comprises galaxies of various (late-type) morphologies. Nevertheless, the work presented in that chapter provides a robust reference point with which to compare future CO TFR studies at higher redshifts, the numbers of which we expect to increase dramatically with the recent dawn of the Atacama Large Millimeter/submillimeter Array (ALMA).

5.1 Future Work

In this thesis we have taken significant steps in charting the evolution of the TFR across almost half the age of the Universe. In this section we detail future work that will build upon and extend that presented in the previous chapters.

5.1.1 $z \approx 0.5$ and $z \approx 1.5$ TFRs with KMOS

It is clear from the work of Chapters 2 and 3 that IFU surveys have opened new windows on the nature of galaxies at $z \approx 1$ (e.g. KROSS) and in the local Universe (e.g. SAMI). The results presented there showed that (at fixed rotation velocity) disk-like star-forming galaxies have undergone significant changes to their total mass-to-stellar mass and K-band stellar mass-to-light ratios since $z \approx 1$, implying moderate stellar mass growth over the last ≈ 8 Gyr. It is still unclear which processes drove these changes, at which point since $z \approx 1$ they occured or how they can be reconciled with the findings of previous studies that show that the co-moving star formation rate density in the Universe has dramatically declined from its peak at $z \approx$ 1–3 to the present day (e.g. Lilly et al., 1996; Madau et al., 1996; Hopkins & Beacom, 2006).

With the KMOS-Cluster Lensing And Supernova survey with *Hubble* (CLASH; Postman et al., 2012) (K-CLASH) survey, we will bridge the gap in redshift and understanding by using KMOS to study the spatially resolved gas kinematics and chemistry of galaxies in the field and in clusters at $z \approx 0.5$. K-CLASH (of which the author of this thesis is a co-principal investigator) is a University of Oxford KMOS guaranteed time observations (GTO) programme that, among other objectives, aims to compose a statistically large and representative sample of field galaxies at $z \approx 0.5$ for direct comparison with similar studies at high redshift (e.g. KROSS) and in the local Universe (e.g. SAMI). K-CLASH observations (which are already underway) are conducted in a manner entirely analogous to those of KROSS, targeting Hα and [NII] doublet ([NII]6548 and [NII]6583) emission in galaxies with KMOS. As such they facilitate the simple extension of the carefully matched comparisons of the $z \approx 1$ and $z \approx 0$ TFRs presented in Chapter 2 to star-forming galaxies at $z \approx 0.5$.

Similarly, with access to deep KMOS observations of Hα emission from star-forming galaxies at $z \approx 1.5$ currently being conducted as part of a Durham University KMOS GTO programme, we may also extend our TFR comparisons to include galaxies at even further look-back times than KROSS.

Combining these data with those already analysed in Chapters 2 and 3 will provide a comprehensive measure of the evolution of the TFR, and thus the relative amounts of baryonic and dark matter in galaxies, over half the age of the Universe.

5.1.2 $z \gtrsim 1$ TFR with ALMA

With the dawn of ALMA it is now possible to construct the TFR at the peak epoch of global star formation in the Universe ($z \approx 1$–3) using spectral line emission from CO as a tracer of galaxy kinematics. Using archival observations of $z \gtrsim 1$ galaxies, we can extend the work presented in Chapter 4 to study the CO TFR at higher redshifts than previously possible. Conducting a careful comparison between $z \gtrsim 1$ CO TFRs and the TFRs of COLD GASS galaxies presented in Chapter 4 will provide an independent test for any evolution of the mass-to-light ratios of galaxies over the last ≈ 8 Gyr.

Appendix A

Additional Plots for Chapter 2

A.1 Asymmetric Rotation Curves

The dynamical modelling of KROSS velocity maps is described in Section §2.3.1 and in further detail in Stott et al. (2016). Here we test the effect on the TFR scatter of those galaxies for which the Hα emission extends up to or beyond r_{80} on only one side of the rotation curve i.e. asymmetrical rotation curves. Figure A.1 shows that the exclusion of such systems in favour of only those with symmetrical (i.e. with Hα emission extending up to or beyond r_{80} on both sides) rotation curves does not significantly reduce the scatter in the TFR for sub-sample *all* ($\sigma_{\text{int}} = 0.36 \pm 0.04$ for galaxies with symmetric rotation curves versus $\sigma_{\text{int}} = 0.40 \pm 0.04$ for those with asymmetric rotation curves). We therefore only exclude from our analysis those galaxies for which the maximum radial extend of the Hα emission is less than r_{80} on *both* sides of the rotation curve.

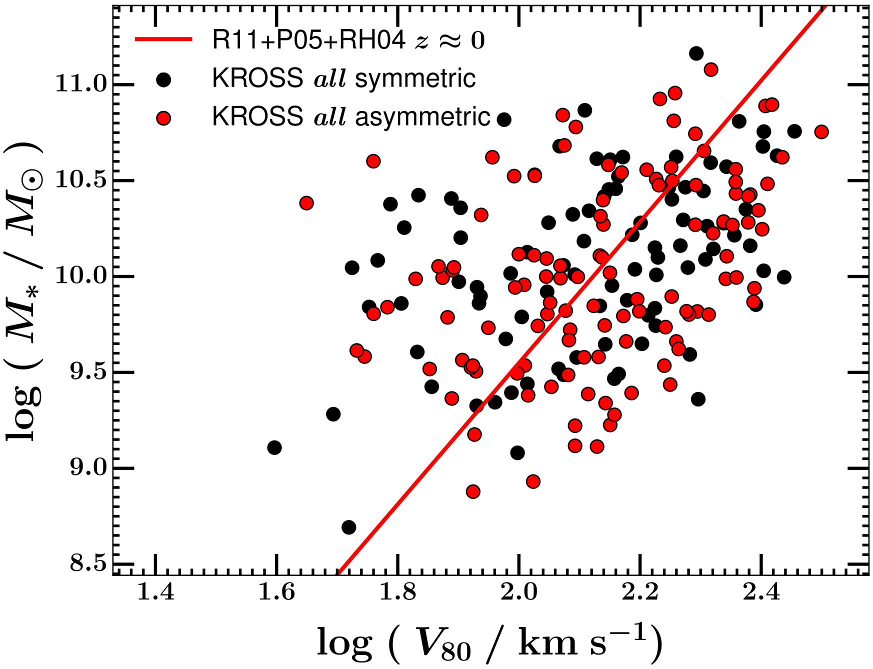

Figure A.1: The TFR for those galaxies in sub-sample *all* (as described in Section § 2.3.5). Error bars are omitted for clarity. The points are coloured according to whether they represent galaxies with either a symmetric or asymmetric rotation curve. There is no significant reduction in scatter between those galaxies with symmetric or asymmetric rotation curves. We therefore include both groups of galaxies in our analysis.

A.2 Disky Galaxies

Figure A.2 shows the best fitting model velocity fields (see §2.3.1) for the KROSS *disky* sub-sample (see §2.3.5). For each galaxy the observed ("DATA") and best fitting model ("MODEL") velocity fields are displayed alongside the residual ("RESIDUAL") between the two. Also included is the associated integrated Hα flux map ("Hα"), and the extracted rotation curve from the inclination corrected observed and model velocity fields. See Figure 2.1 for a full description.

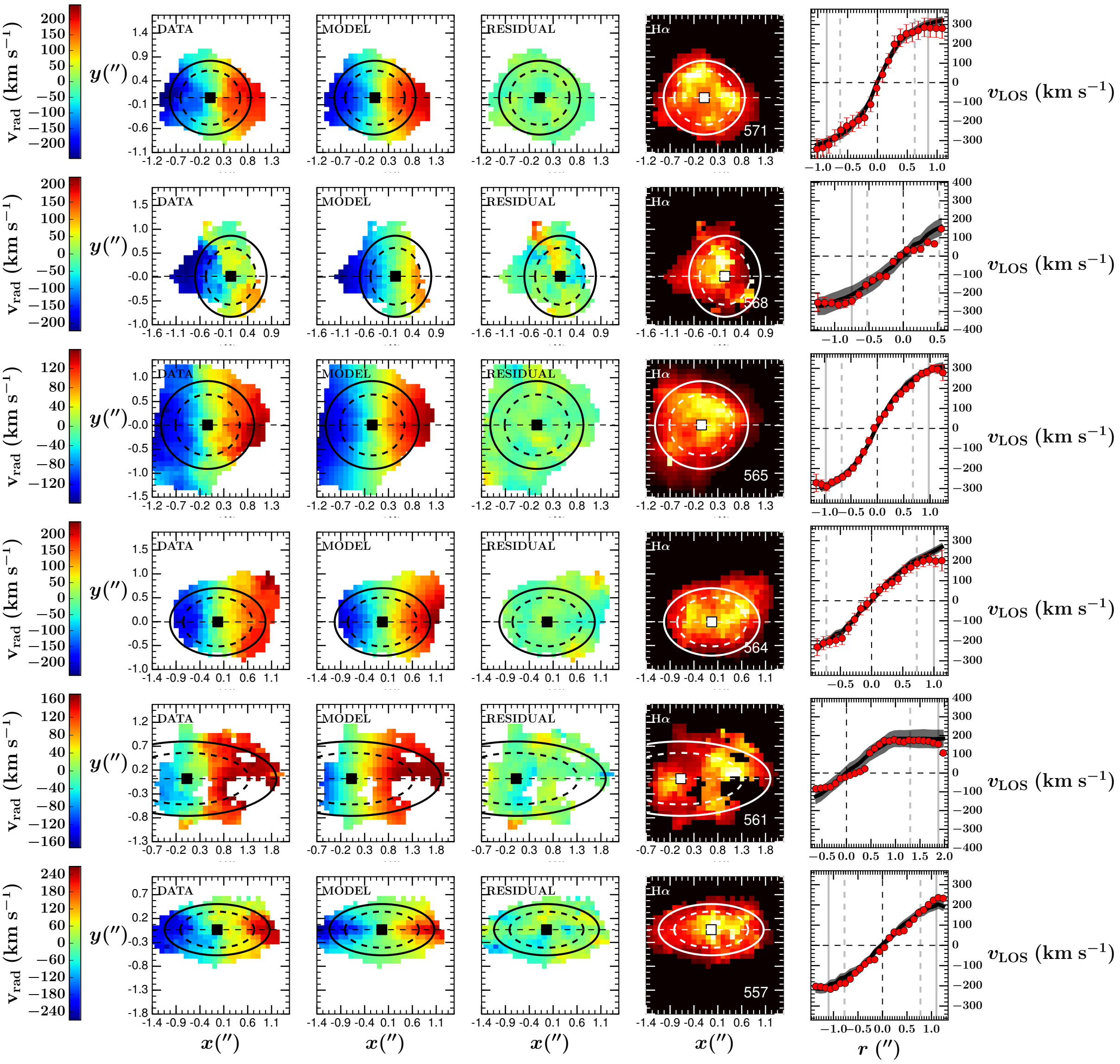

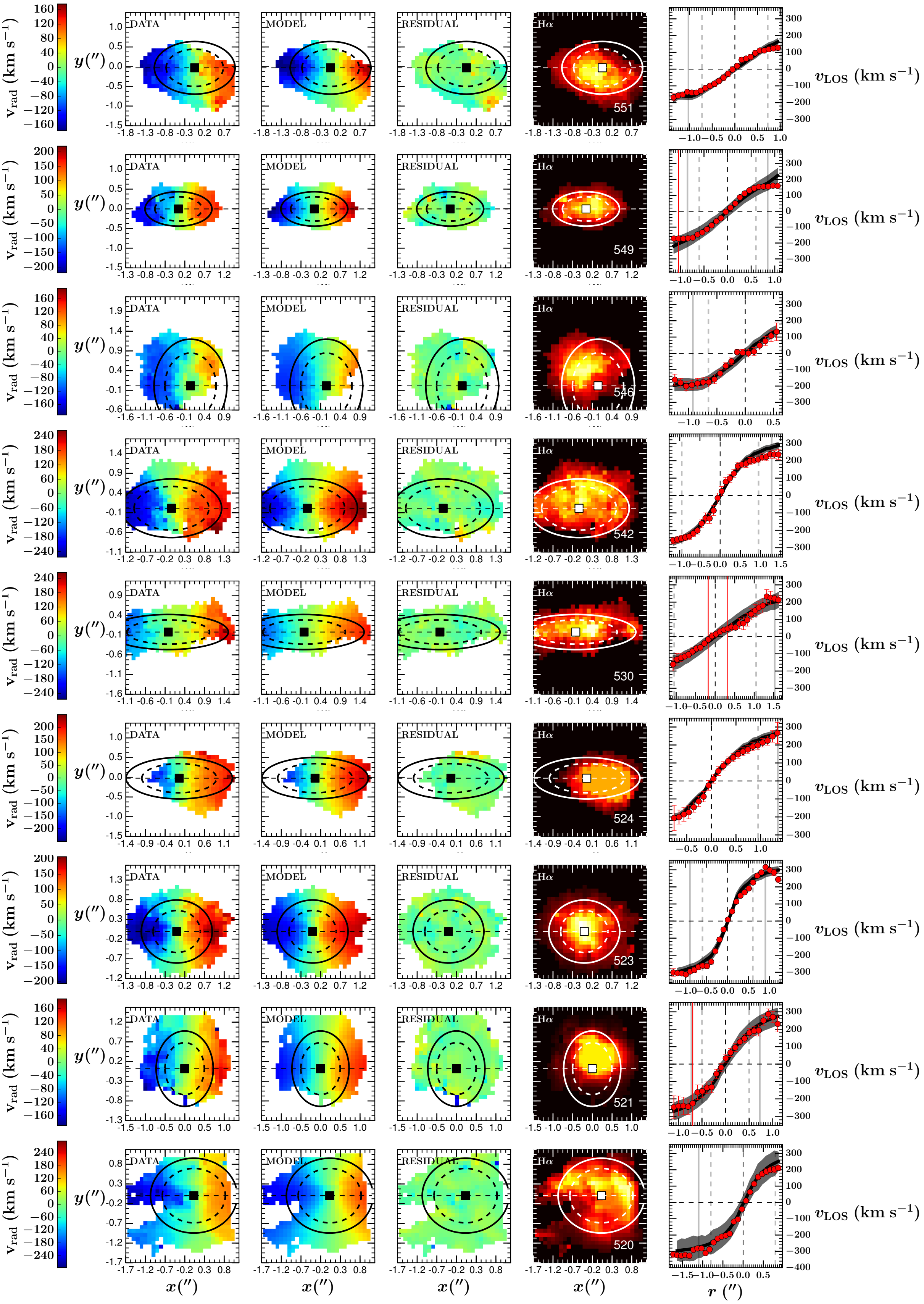
$v_{\rm rad}$ (km s^{-1})
$y('')$
DATA
MODEL
RESIDUAL
Hα
551
549
546
542
530
524
523
521
520
$v_{\rm LOS}$ (km s^{-1})
$x('')$
r $('')$

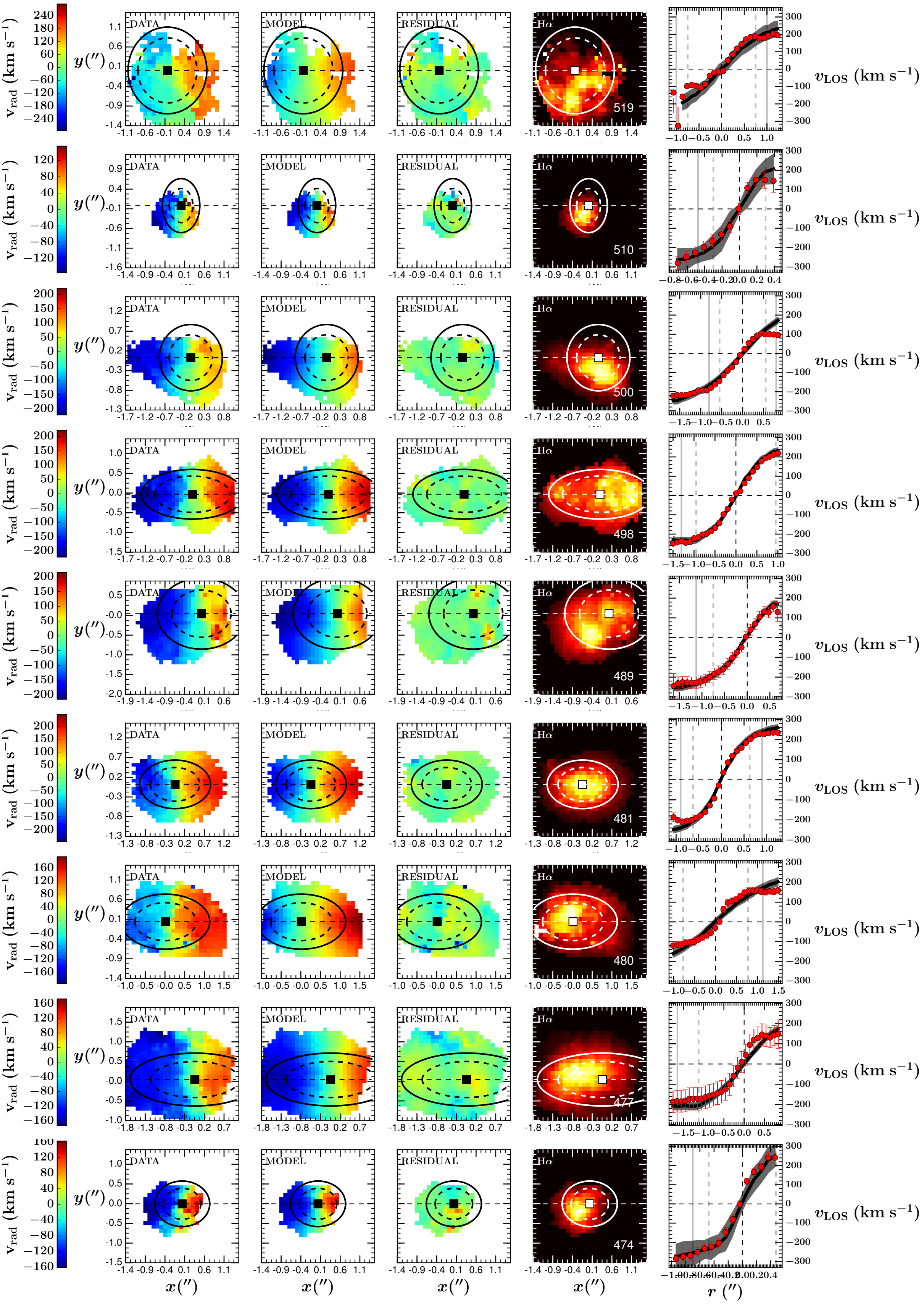
DATA
MODEL
RESIDUAL
Hα
519
510
500
498
489
481
480
477
474
$\mathrm{v_{rad}}$ (km s^{-1})
$y('')$
$x('')$
r $('')$
v_{LOS} (km s^{-1})

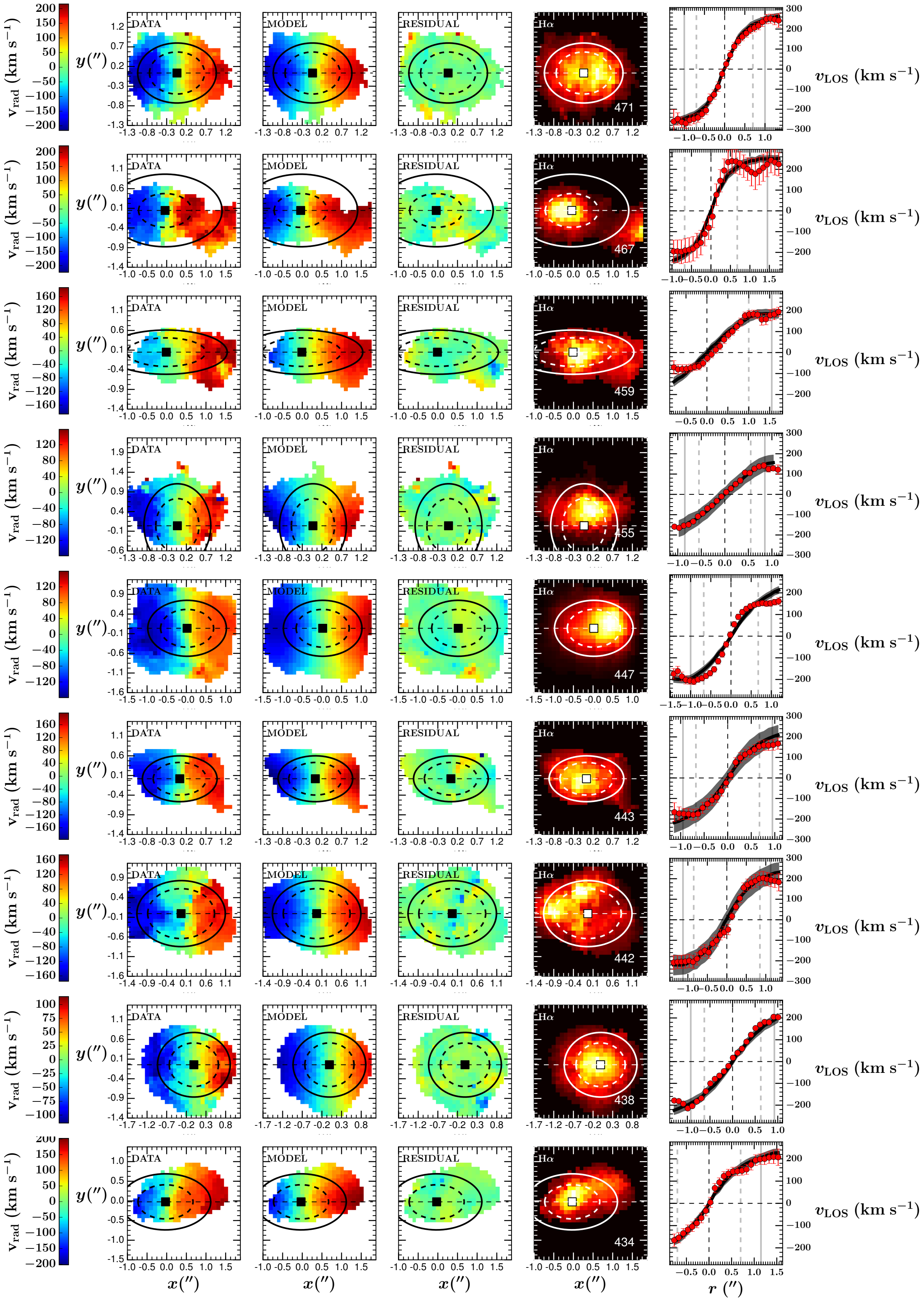

$\mathrm{v_{rad}}$ (km s^{-1})
$y('')$
DATA
MODEL
RESIDUAL
Hα
$v_{\rm LOS}$ (km s^{-1})
471
467
459
455
447
443
442
438
434
$x('')$
r ($''$)

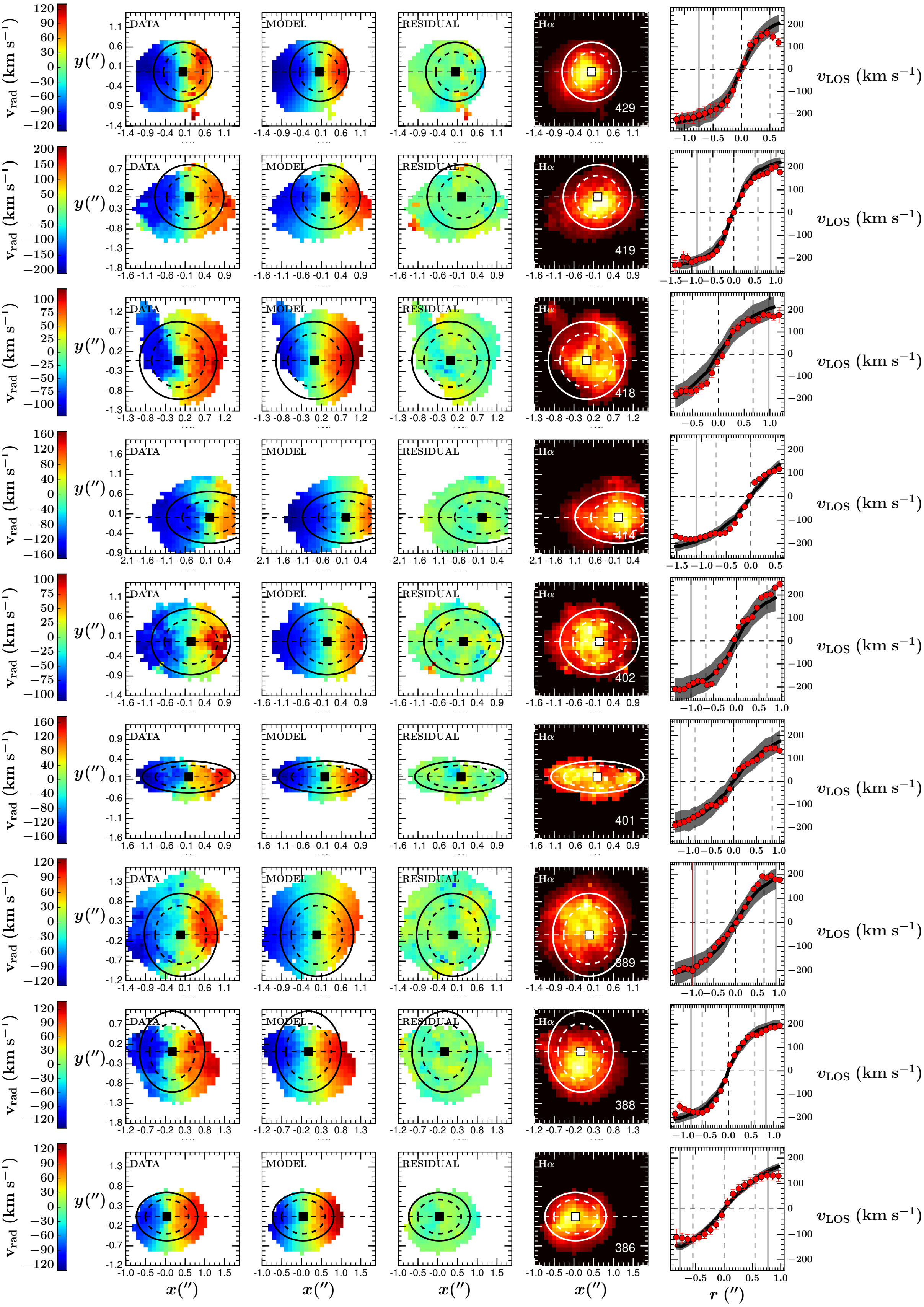
DATA
MODEL
RESIDUAL
Hα
429
419
418
414
402
401
389
388
386
$v_{\rm rad}$ (km s^{-1})
$y('')$
$x('')$
$v_{\rm LOS}$ (km s^{-1})
r ($''$)

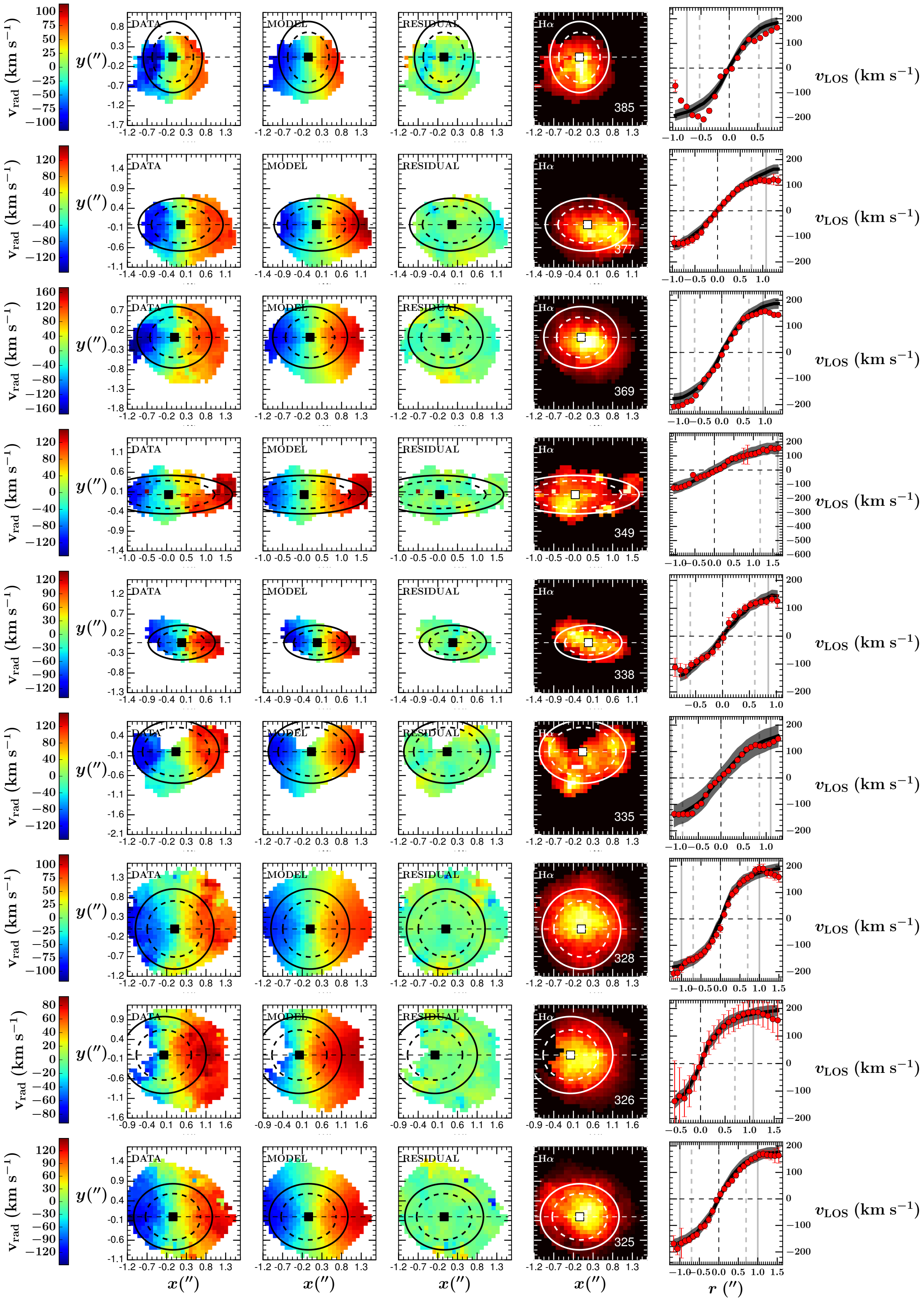
DATA
MODEL
RESIDUAL
Hα
385
377
369
349
338
335
328
326
325
$\mathrm{v_{rad}}$ (km s^{-1})
$y('')$
$x('')$
r ('')
v_{LOS} (km s^{-1})

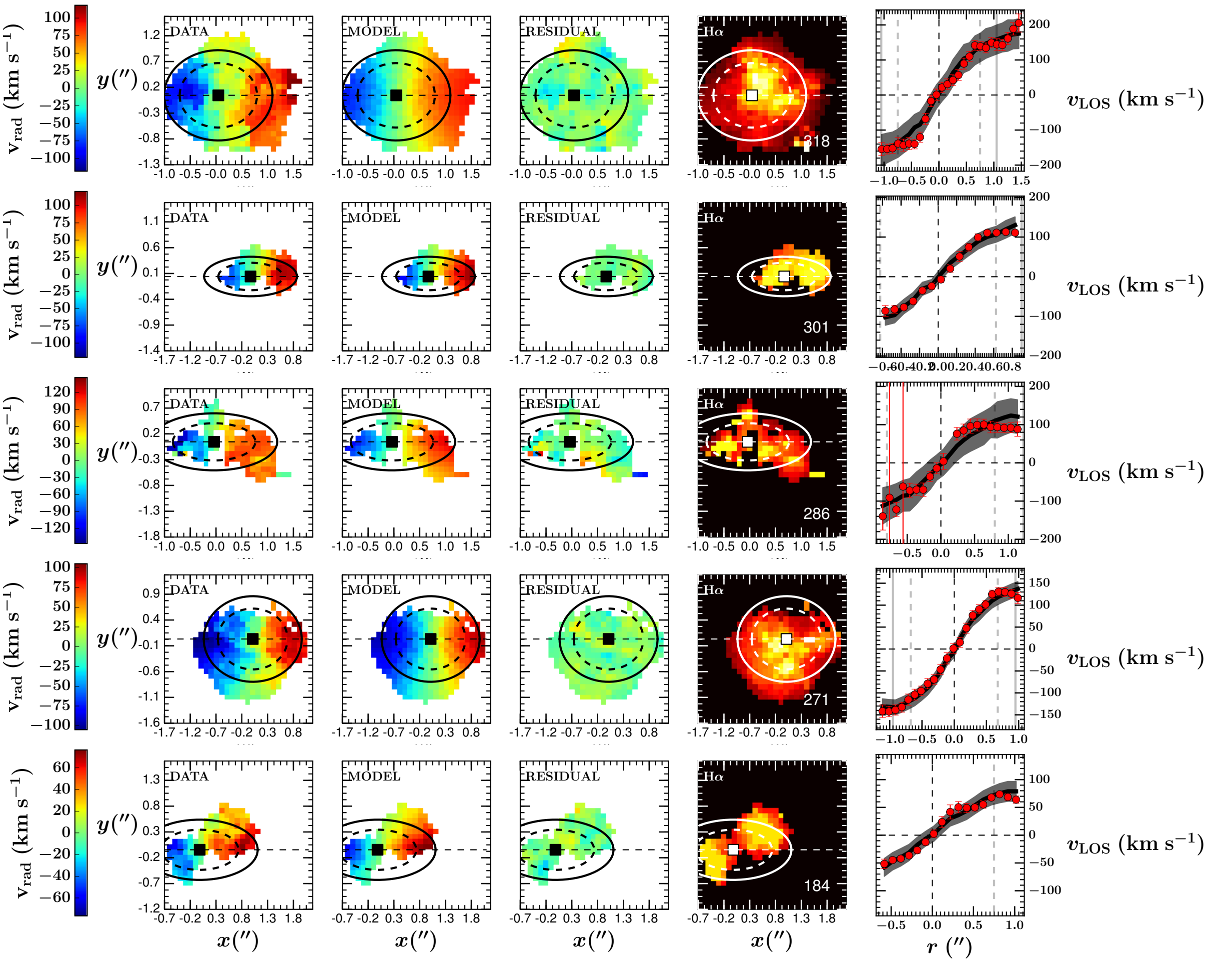

Figure A.2: The best fitting model velocity fields (see §2.3.1) for the KROSS *disky* sub-sample (see §2.3.5). See Figure 2.1 for a full description. For a minority of galaxies a small number of points in the observed rotation curve (as represented by the red points in the far right panel for each plot) have very large ($\gtrsim 200$ km s^{-1}) error bars. In these cases the velocity axis range does not include the full extent of the error bars but rather is restricted to better present the majority of the data.

Appendix B

Additional Plots for Chapter 3

Figures B.1, B.2 and B.3 show the observed and best fit model velocity fields for respectively the SAMI HQ (see § 3.2.3.3), SAMI LQ (see § 3.3.2.1) and KROSS (see § 3.4.1) *disky* subsample as defined in § 3.4.3. For each galaxy we also include the Hα flux map, along with the residual between the observed and best fit velocity field. Lastly we include rotation curves extracted from the observed and best fit velocity fields, respectively. See Figure 3.1 for a more detailed description of the plots.

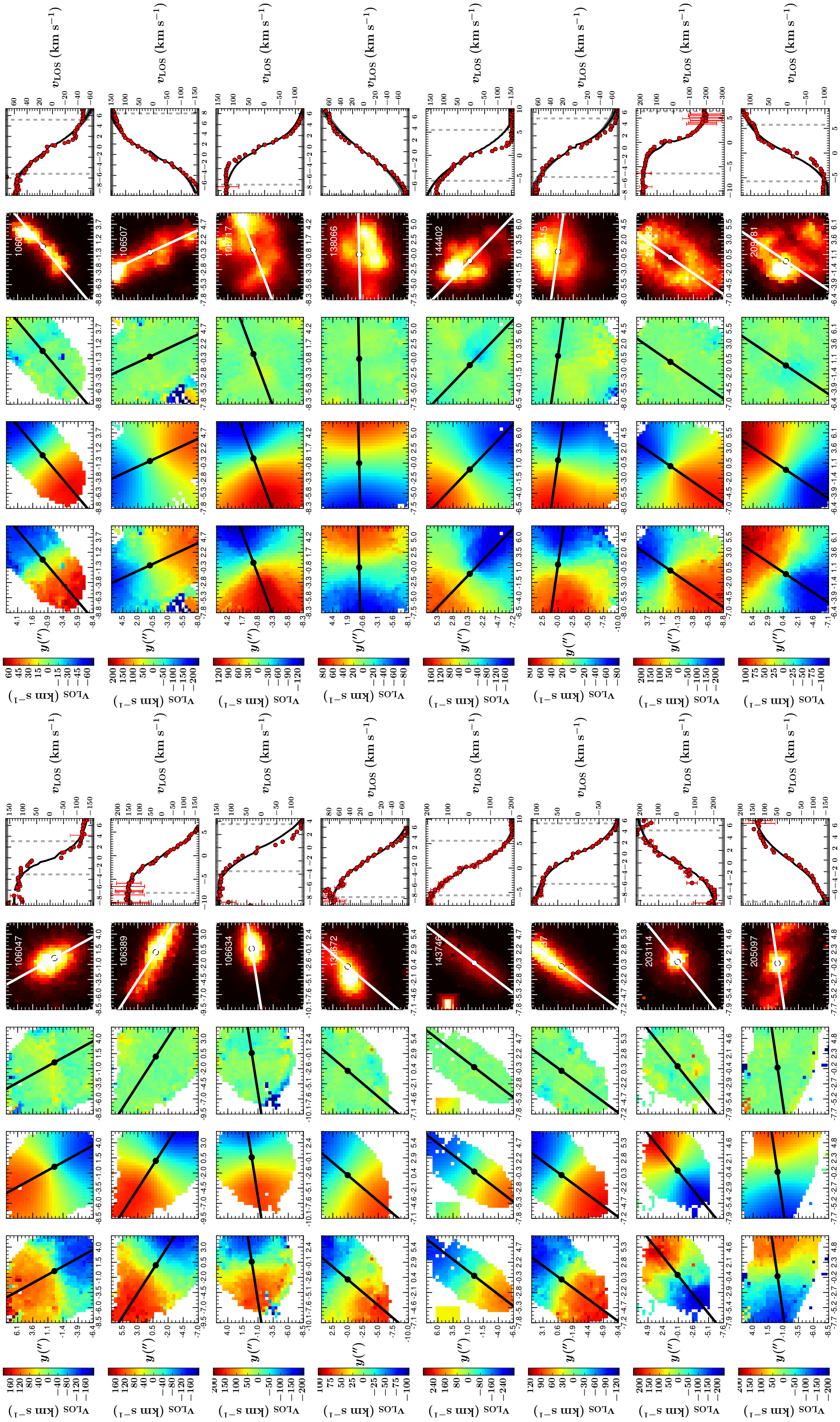
vLOS (km s⁻¹)
y('')
x('')
r ('')
106047
106389
106634
203114
205097
106507
138066
144402

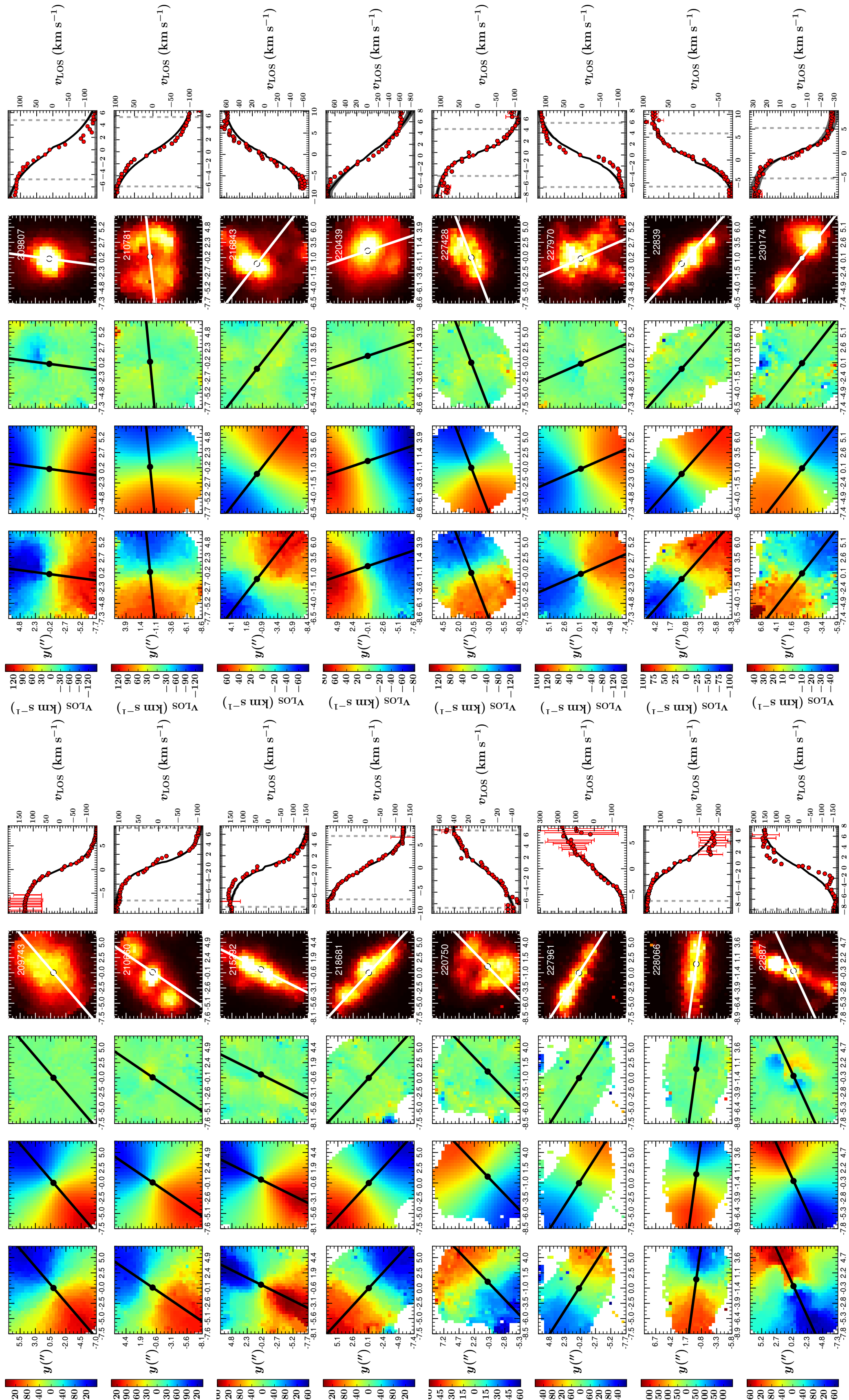
209807
210781
216843
220439
227428
227970
230174
209743
218681
220750
227961
228066
vLOS (km s−1)
x (″)
y (″)
r (″)

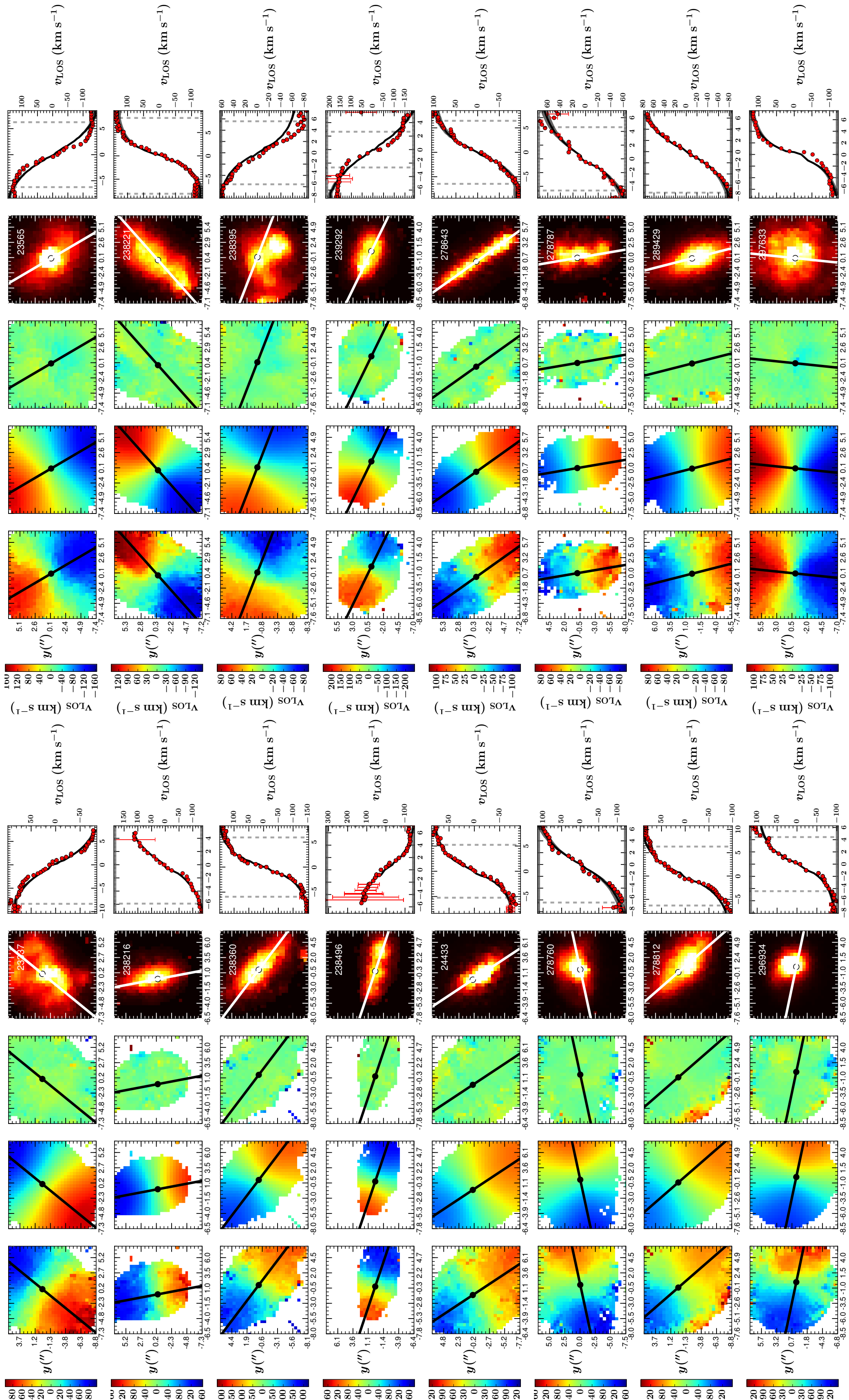
23565
238221
238395
239292
278643
278787
289429
297633
23737
238216
238360
238496
24433
278760
278812
296934
$v_{\rm LOS}$ (km s^{-1})
$y('')$
$x('')$
r ('')

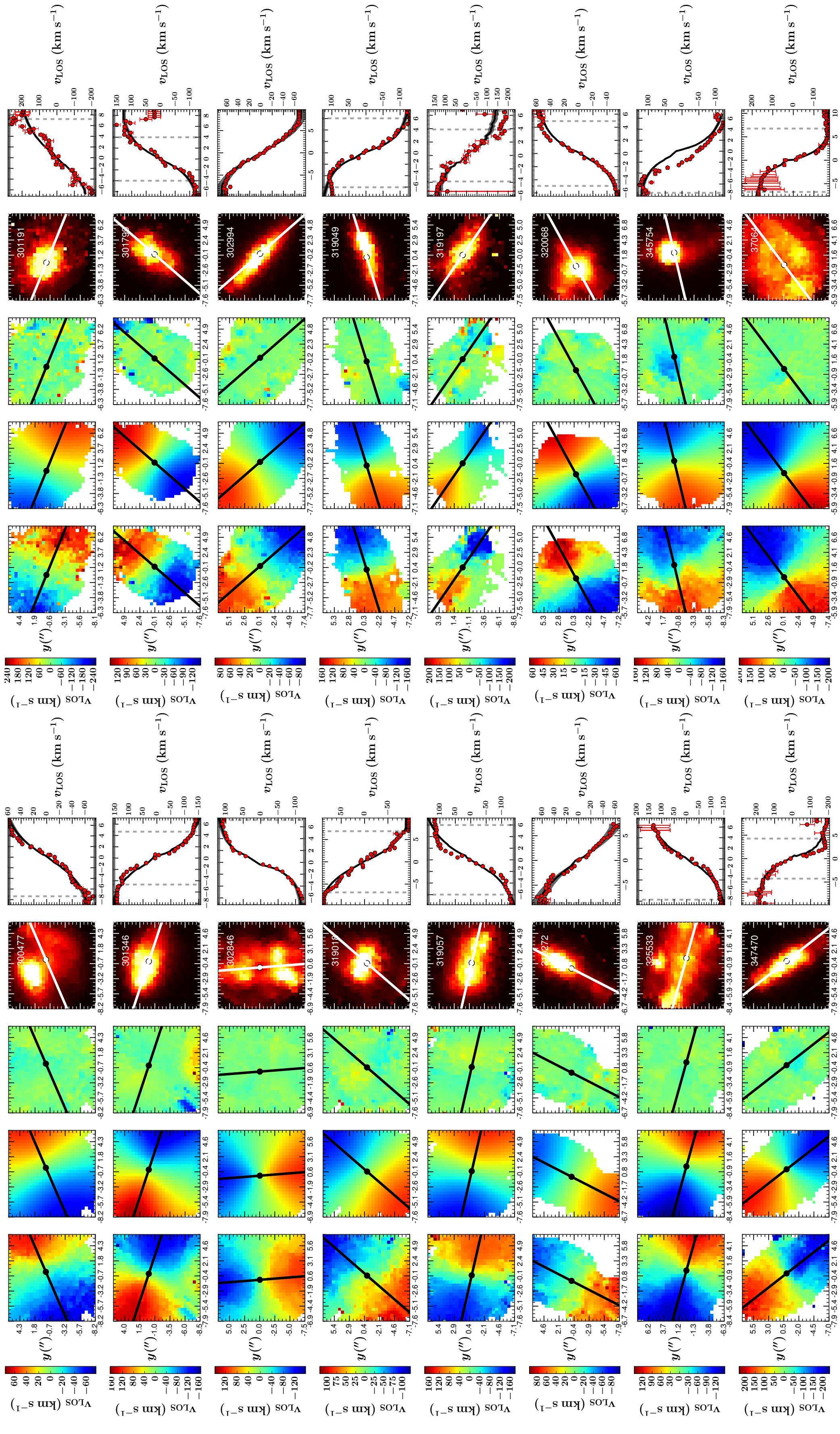
301191
302994
319049
319197
320068
345754
300477
301346
302846
319057
325533
347470
$v_{\rm LOS}$ (km s^{-1})
$y('')$
$x('')$
$r('')$

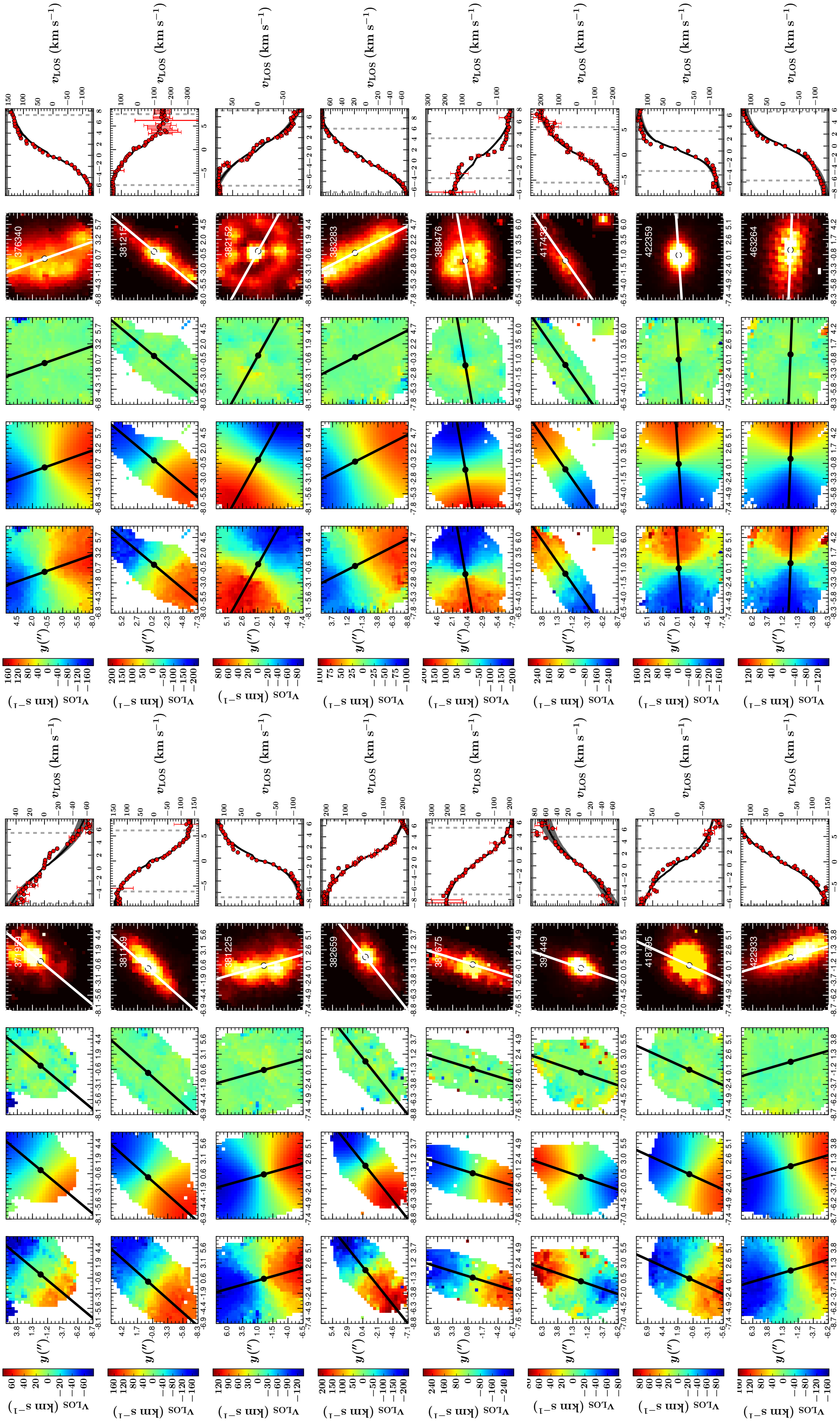
376340
381215
382152
383283
388476
422359
463264
381225
382659
397449
422933
$v_{\rm LOS}$ (km s^{-1})
$y('')$
$x('')$
$r('')$

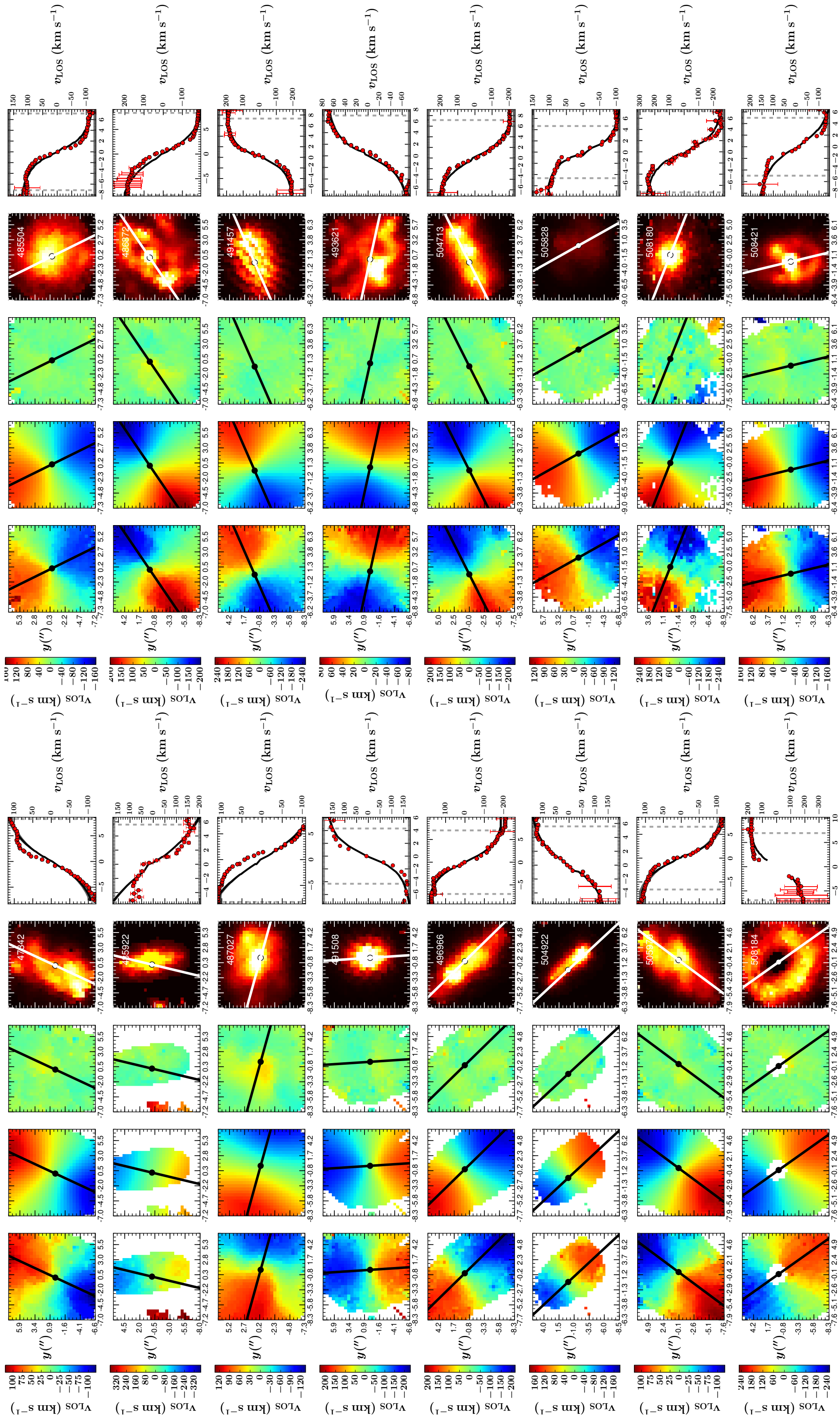
485504
486372
491457
493621
504713
505828
508180
508421
485922
487027
491508
496966
504922
508184
$v_{\rm LOS}$ (km s^{-1})
r ($''$)
x ($''$)
y ($''$)

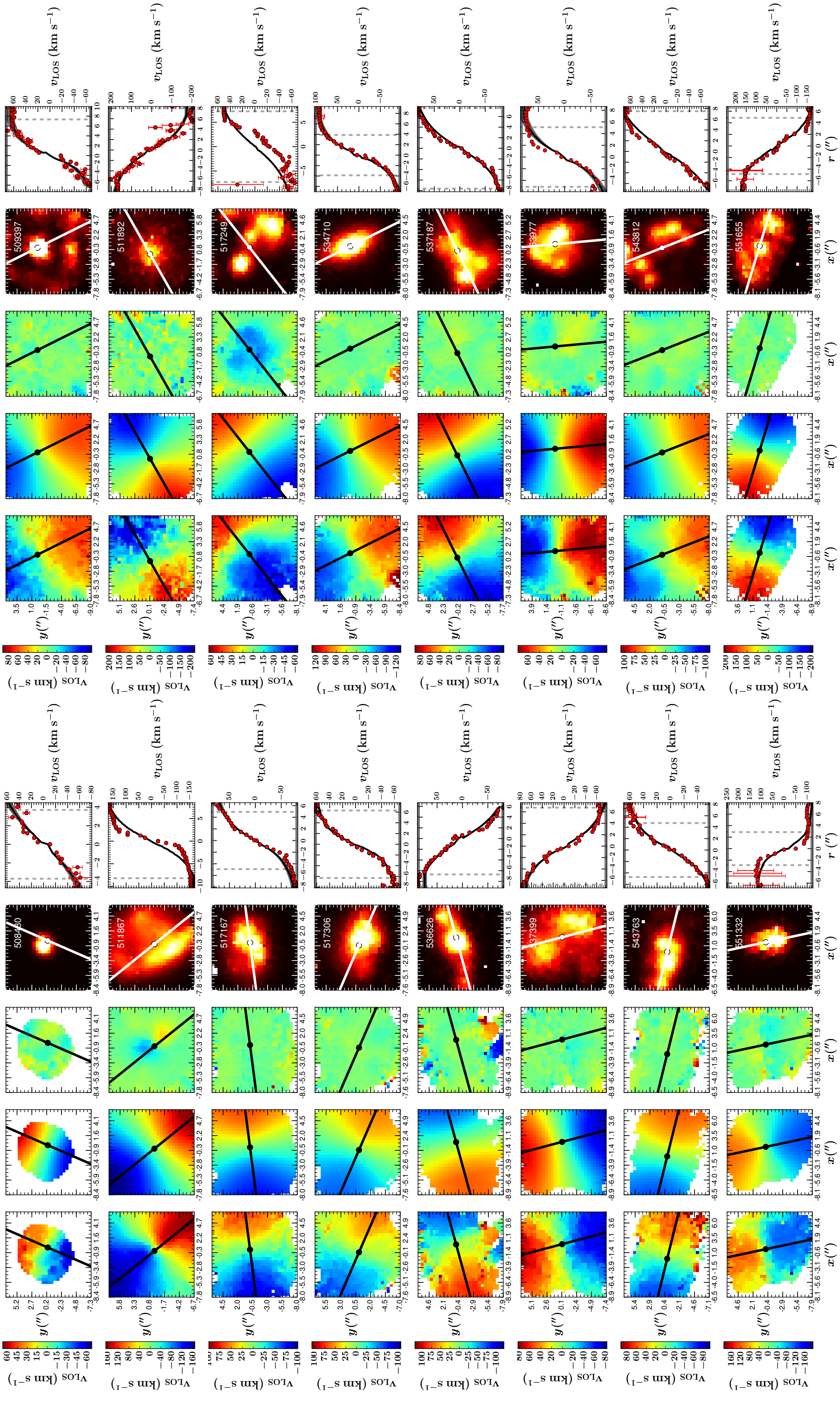
509397
511892
517249
534710
537187
53977
543812
551655
511867
517167
517306
536626
37399
543763
551332
$v_{\rm LOS}$ (km s^{-1})
$y('')$
$x('')$
$r('')$

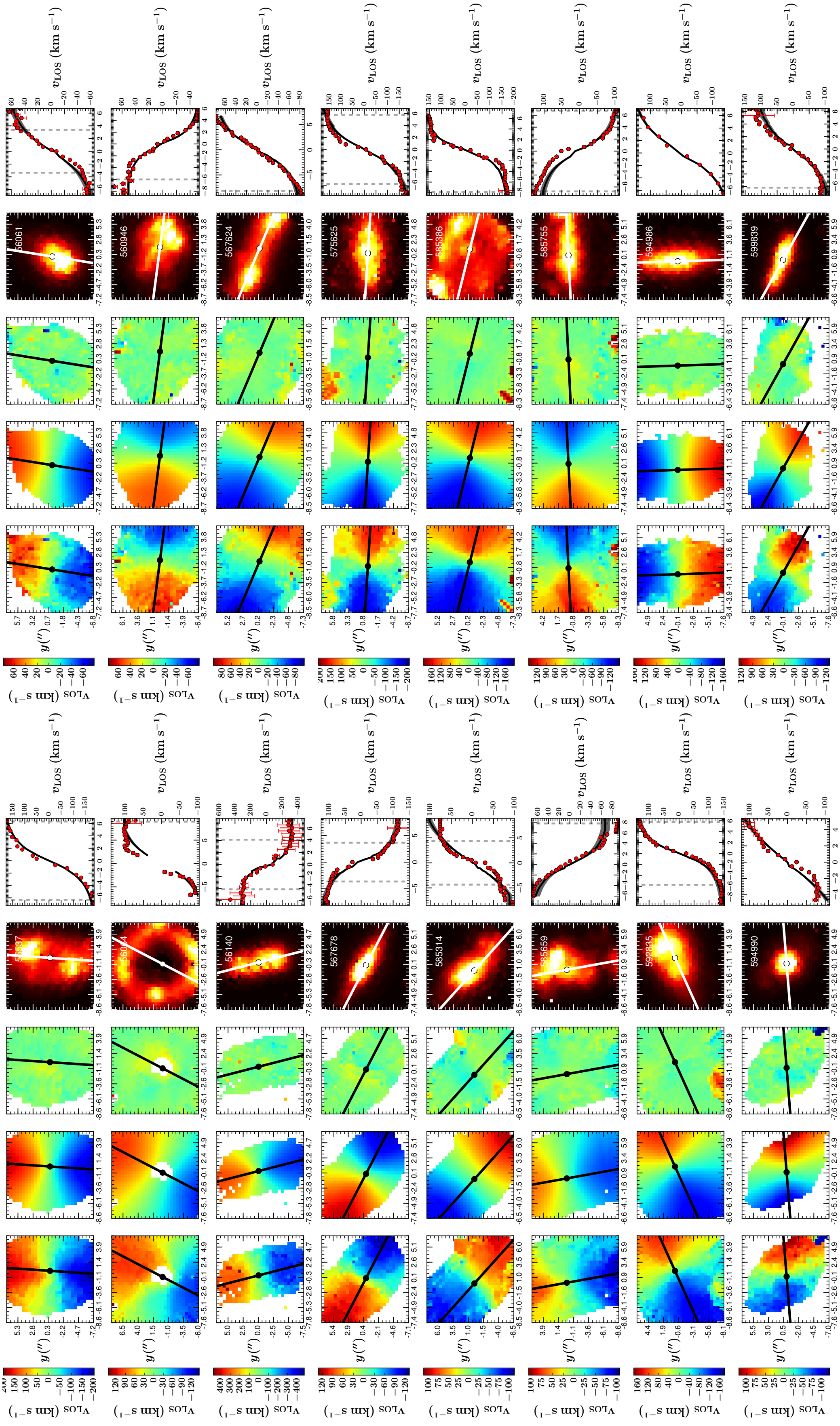
55537
56140
567678
585314
585659
592835
594990
56061
560946
567624
575625
585386
585755
594986
599839
$v_{\rm LOS}$ (km s^{-1})
$y('')$
$x('')$
$r('')$

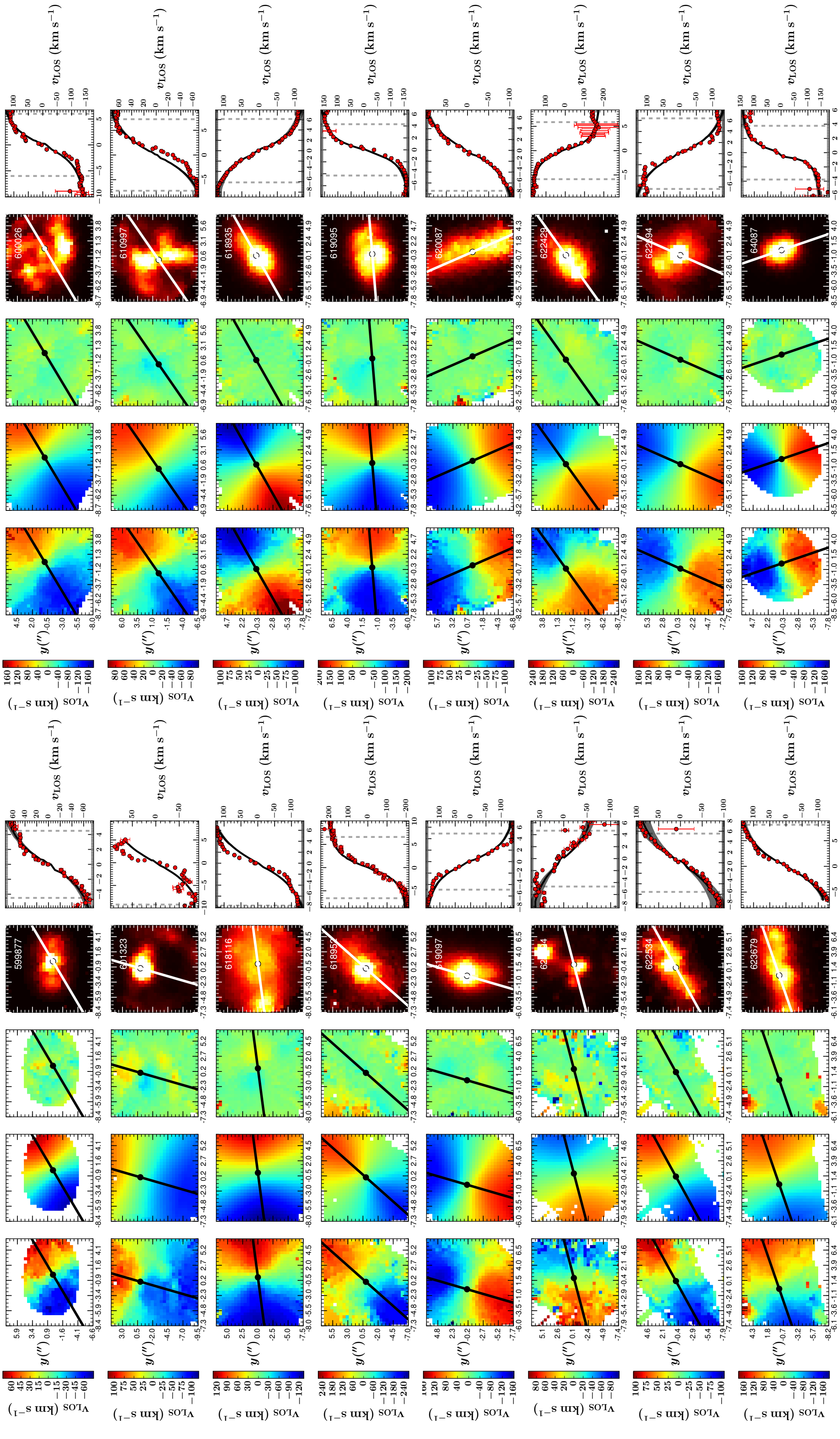
600026
610997
618935
619095
620087
622429
64087
599877
618116
622534
623679
$v_{\rm LOS}$ (km s^{-1})
y ($''$)
x ($''$)
r ($''$)

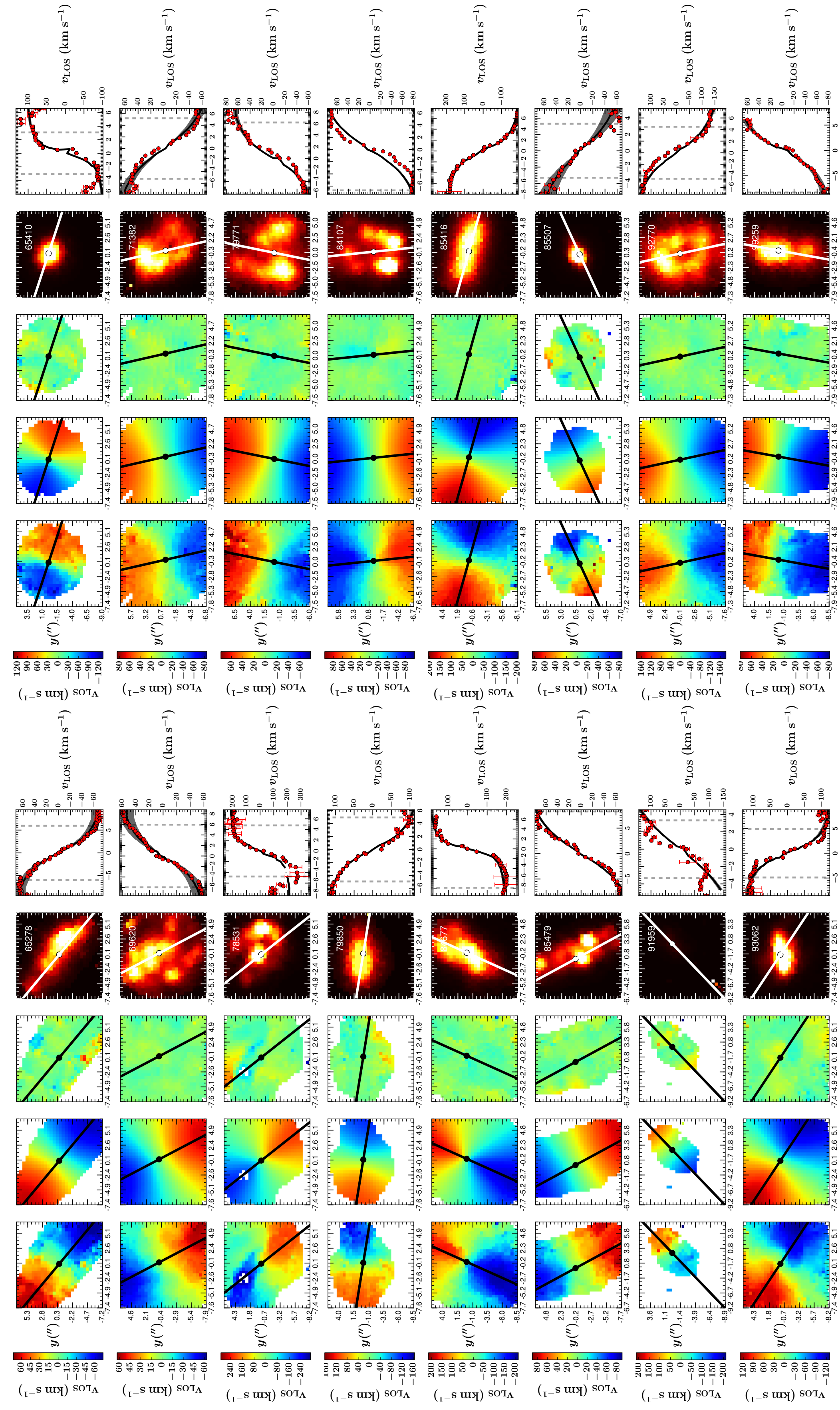
65410
71382
3771
84107
85416
85507
92770
9259
65278
69620
78531
79850
77
85479
91959
93062
$v_{\rm LOS}$ (km s^{-1})
$y('')$
$x('')$
$r('')$

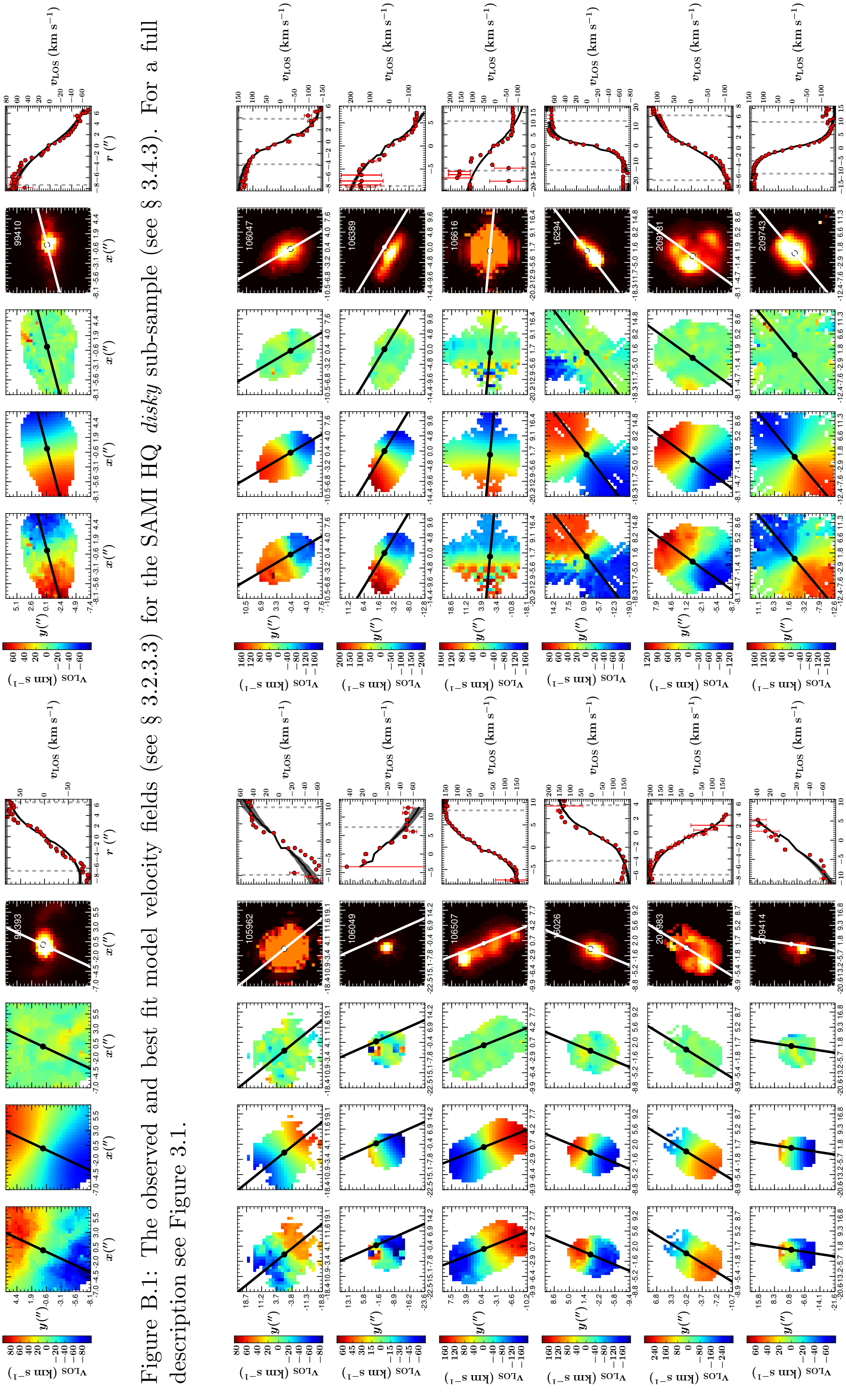

Figure B.1: The observed and best fit model velocity fields (see § 3.2.3.3) for the SAMI HQ *disky* sub-sample (see § 3.4.3). For a full description see Figure 3.1.

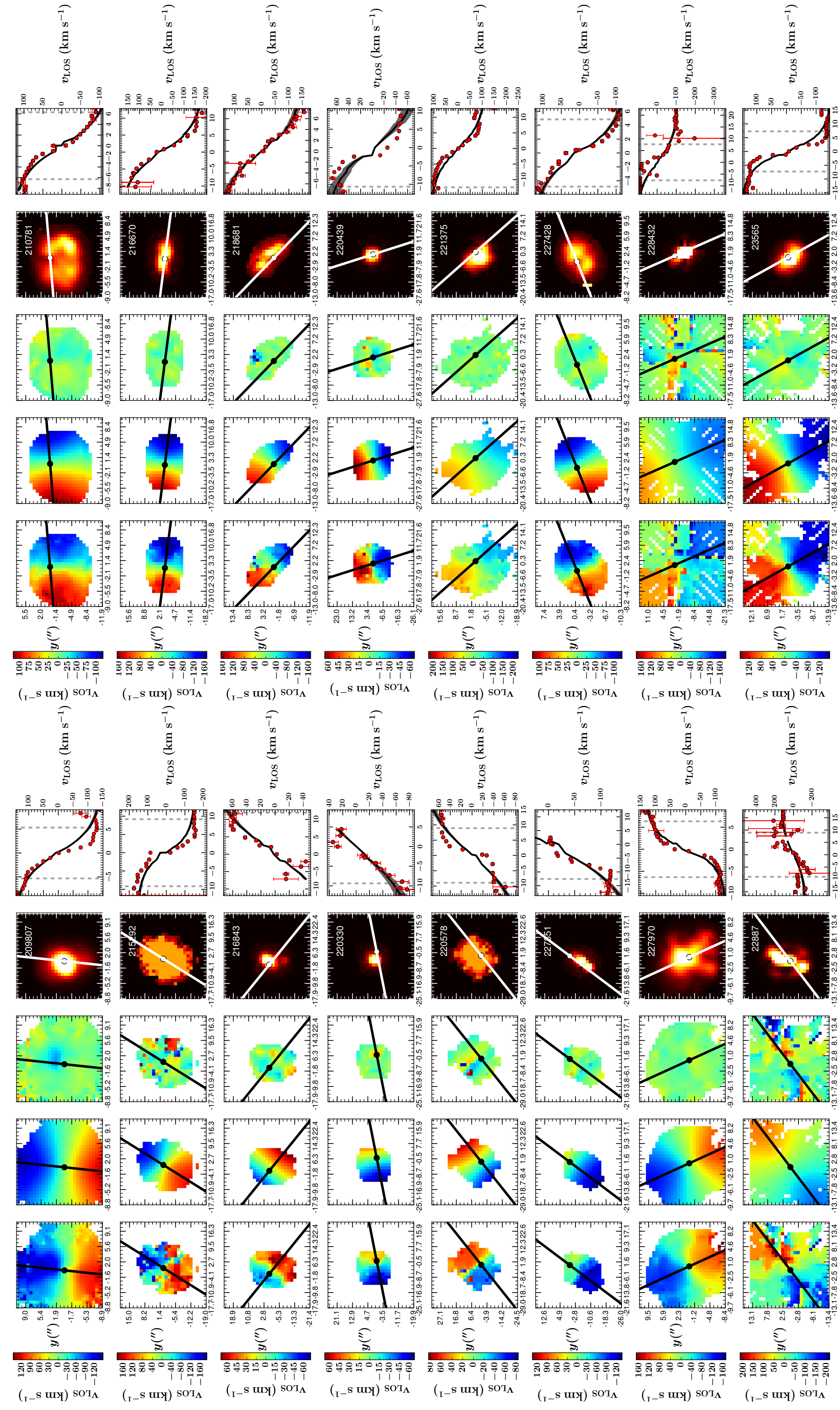

210781
216670
218681
220439
221375
227428
228432
23565
209807
215292
216843
220330
220578
227351
227970
22887
$v_{\rm LOS}$ (km s^{-1})
$y('')$
$x('')$
$r('')$

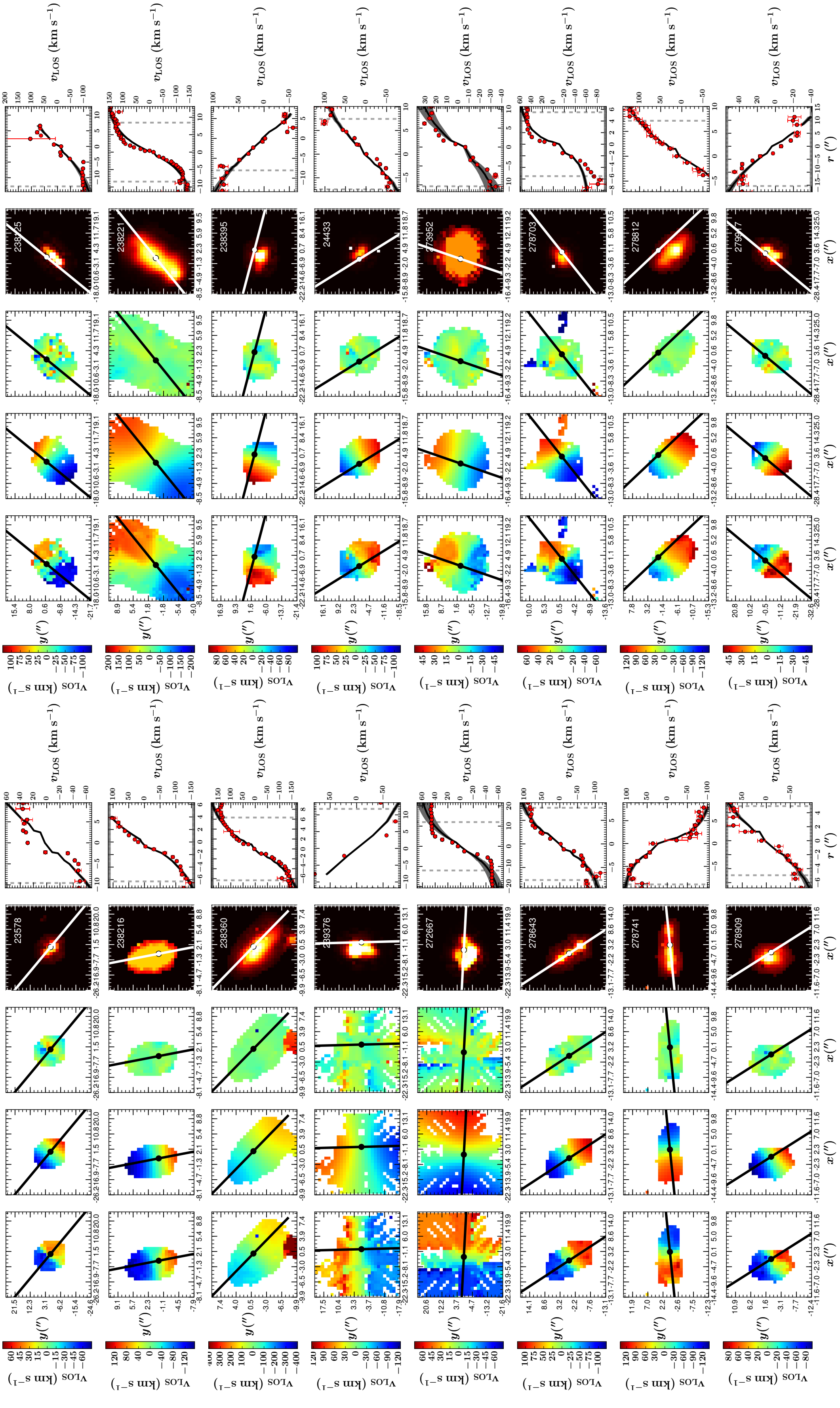
23578
238216
238360
239376
272667
278643
278741
278909
238221
238395
24433
273952
278703
278812
$v_{\rm LOS}$ (km s^{-1})
$y('')$
$x('')$
r $('')$

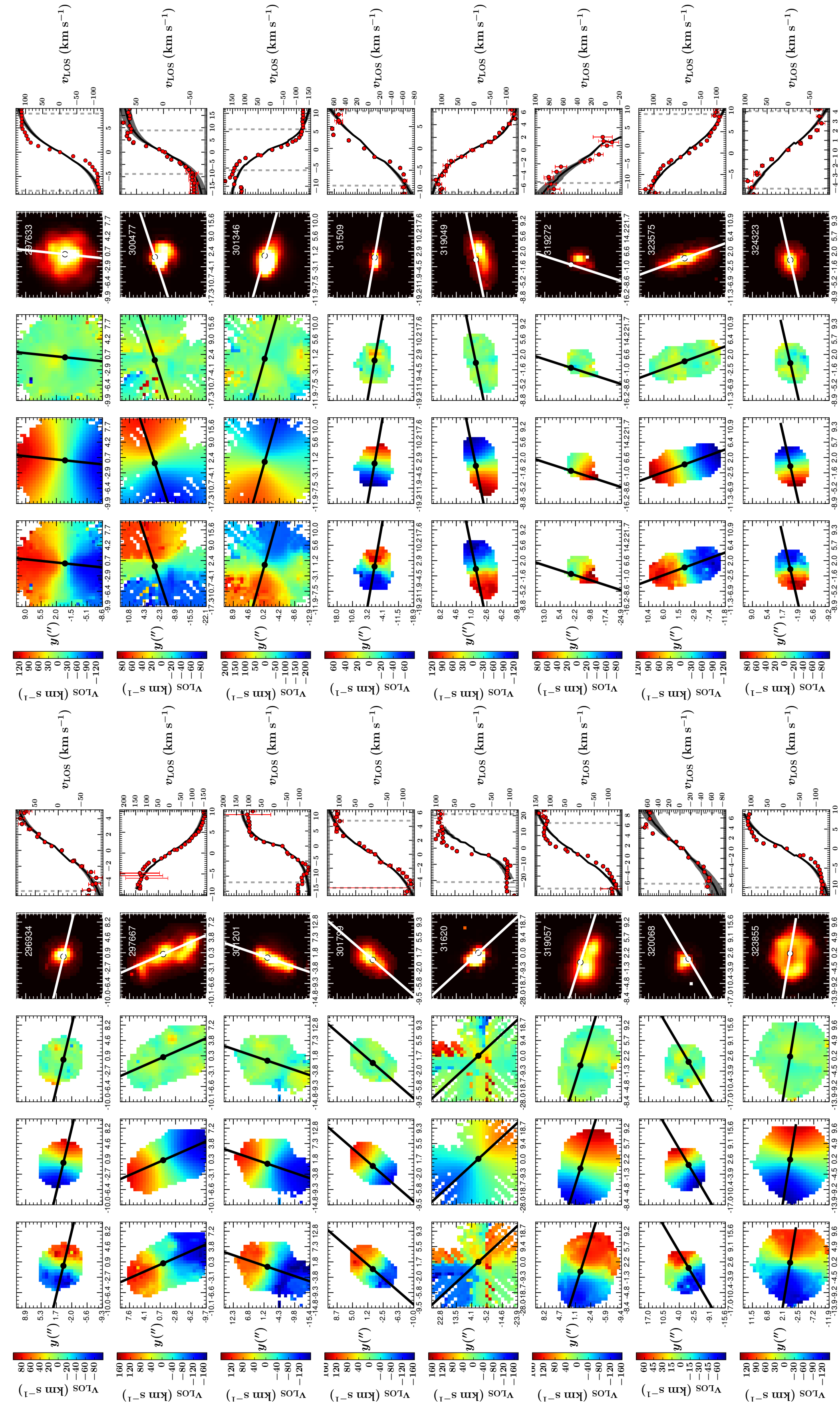
297633
300477
301346
31509
319049
319272
323575
324323
296934
297667
301201
31620
319057
320068
323855
$v_{\rm LOS}$ (km s^{-1})
$y('')$
$x('')$
$r('')$

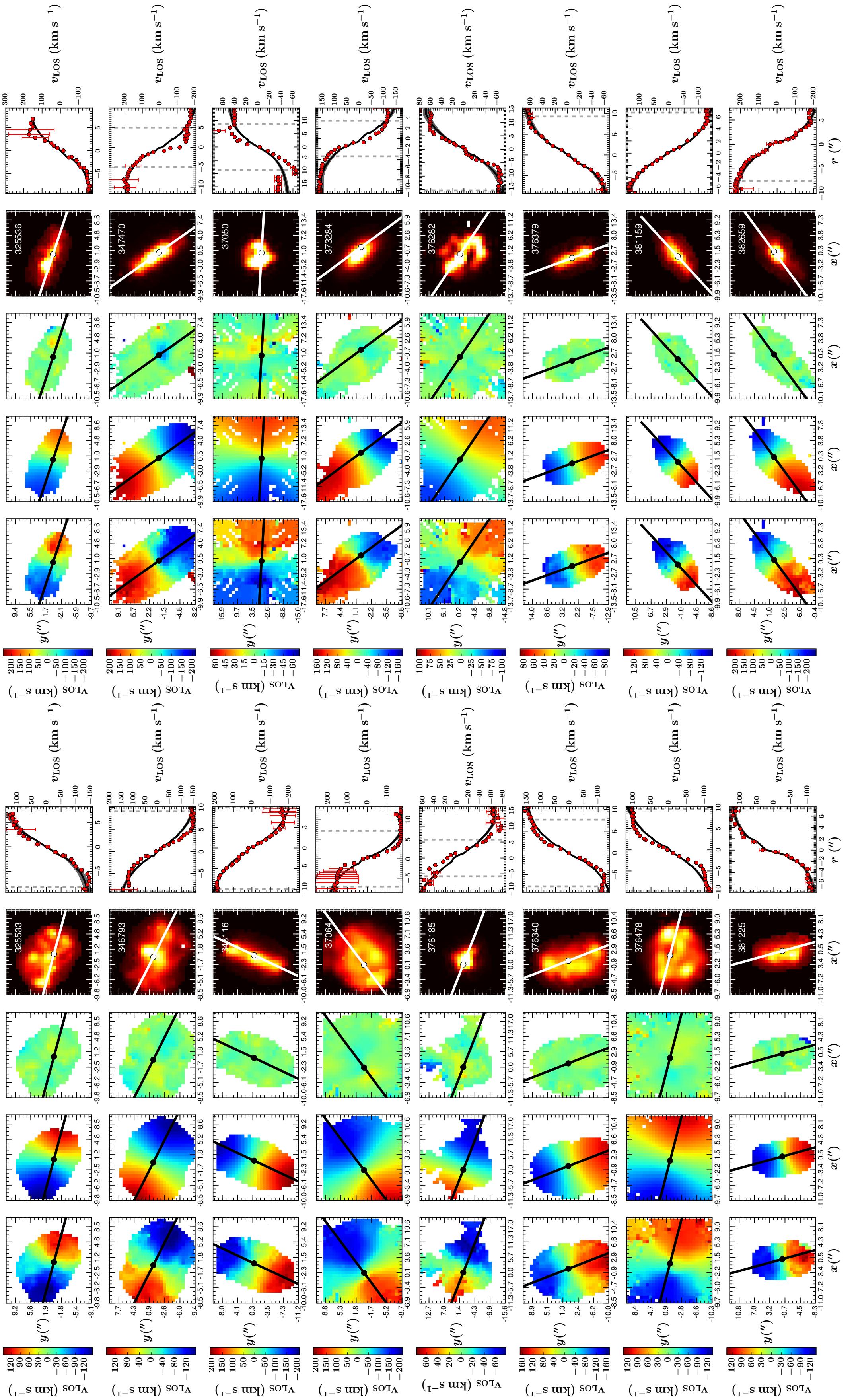
325536
347470
37050
373284
376282
376379
381159
382659
325533
346793
376185
376340
376478
381225
$v_{\rm LOS}$ (km s^{-1})
V$_{\rm LOS}$ (km s^{-1})
$y('')$
$x('')$
$r('')$

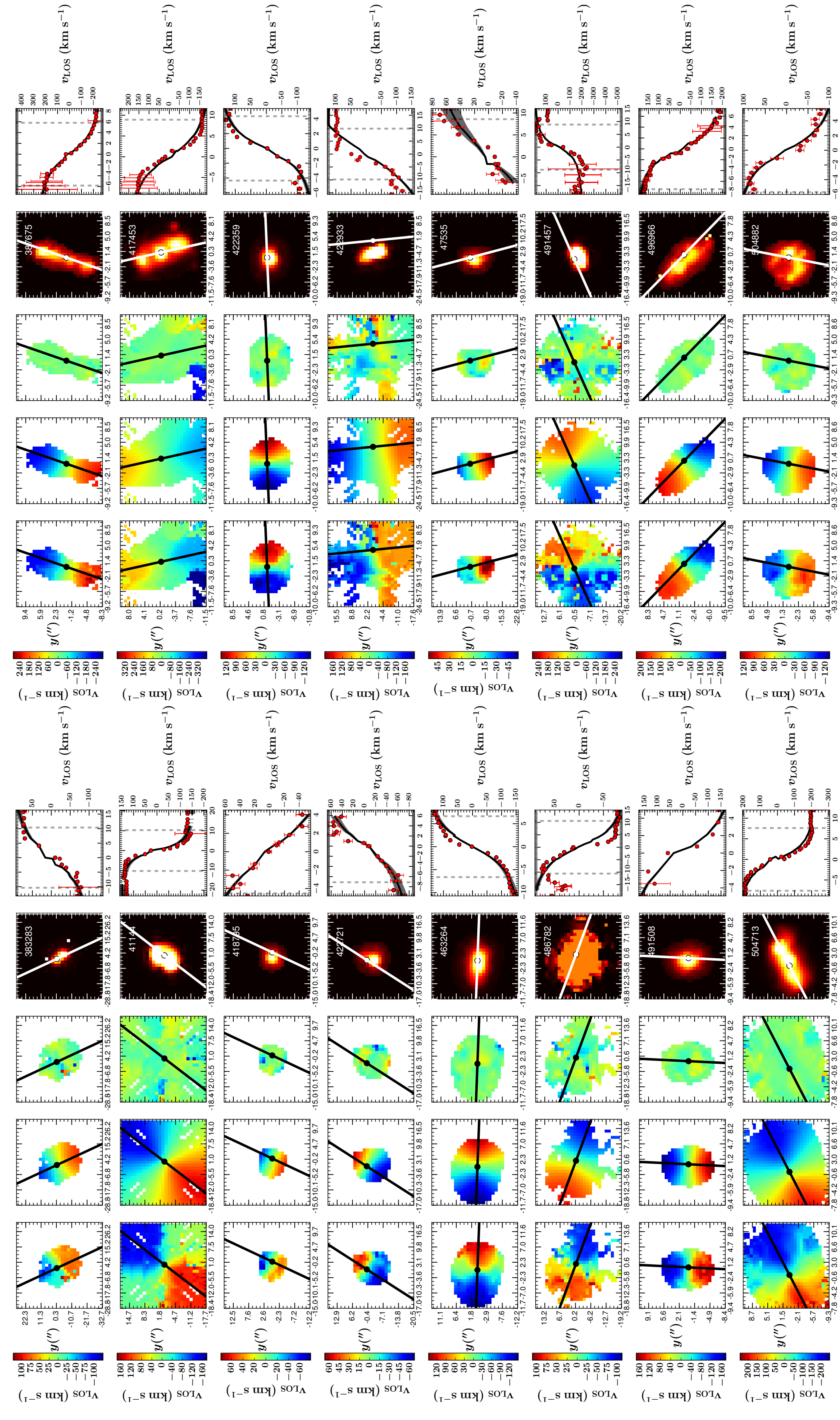

387675
417453
422359
422933
47535
491457
496966
504882
383283
463264
486782
504713
$v_{\rm LOS}$ (km s^{-1})
$y('')$
$x('')$
$r('')$

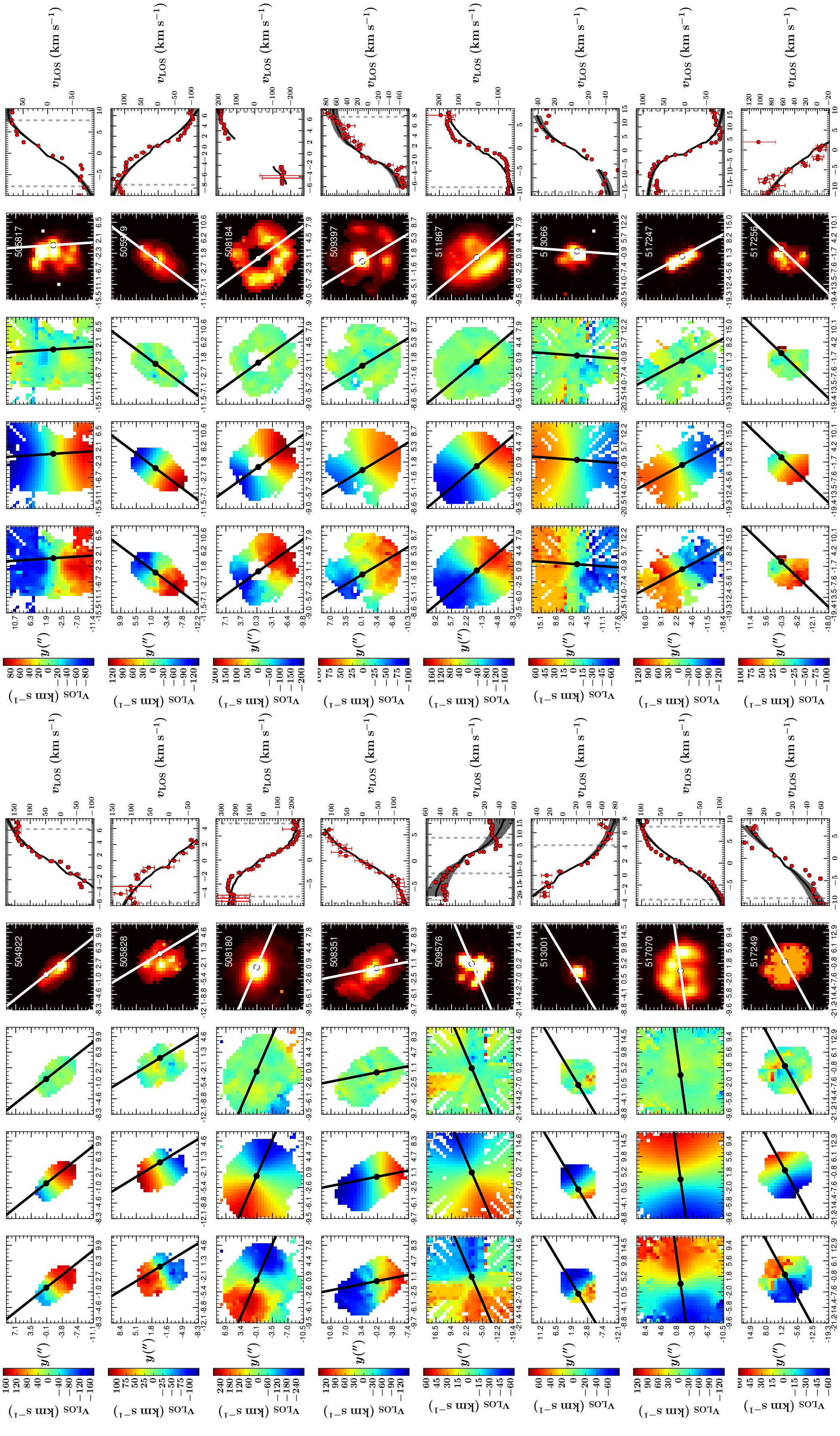
504922
505828
508180
508351
509576
513001
517070
517249
505817
508184
509397
511867
517247
517256
$v_{\rm LOS}$ (km s^{-1})
y ('')
x ('')
r ('')

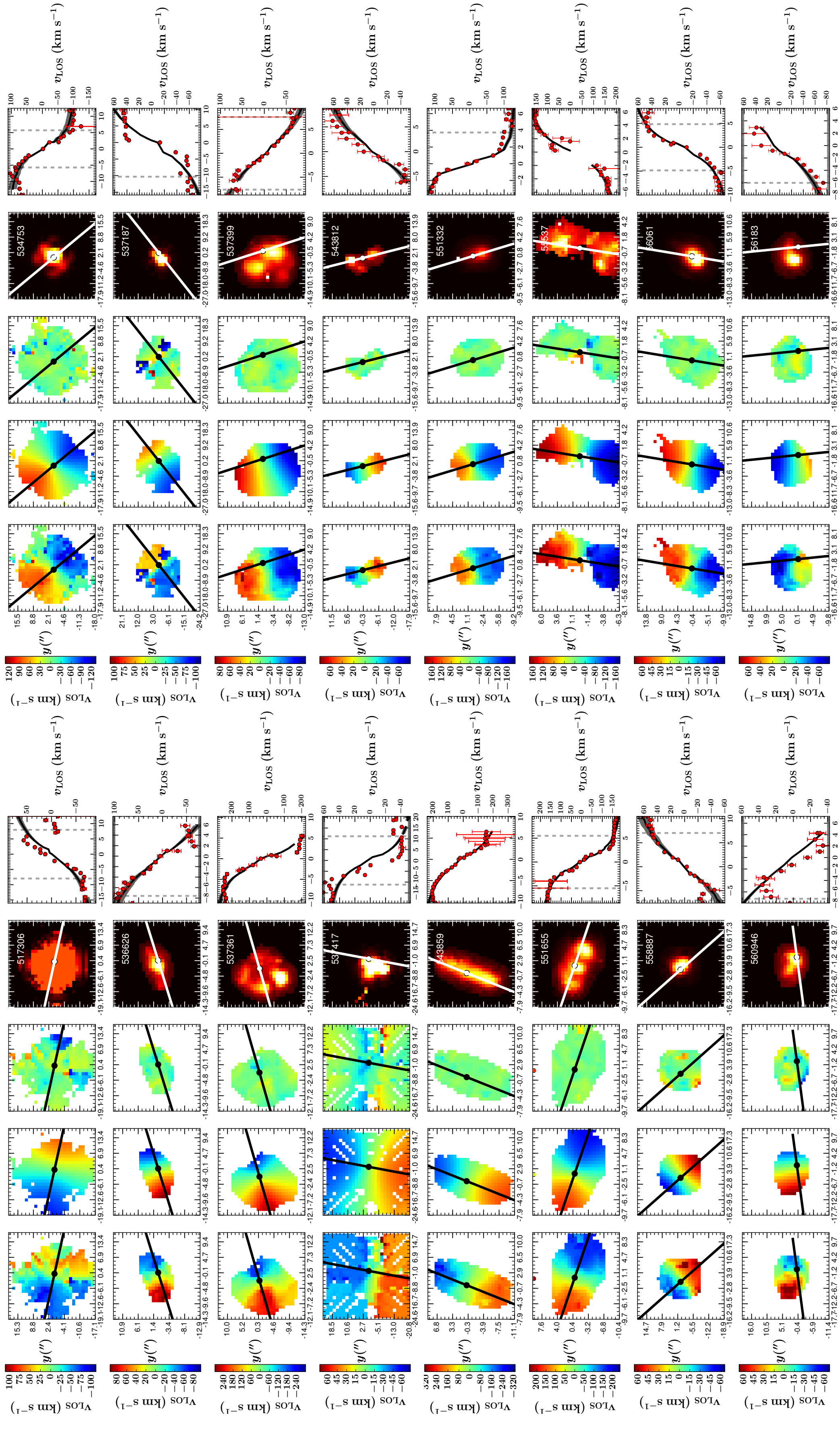
534753
537187
537399
543812
551332
517306
536626
537361
560946
551655
558887
56183
$v_{\rm LOS}$ (km s^{-1})
$y('')$
$x('')$
r ('')

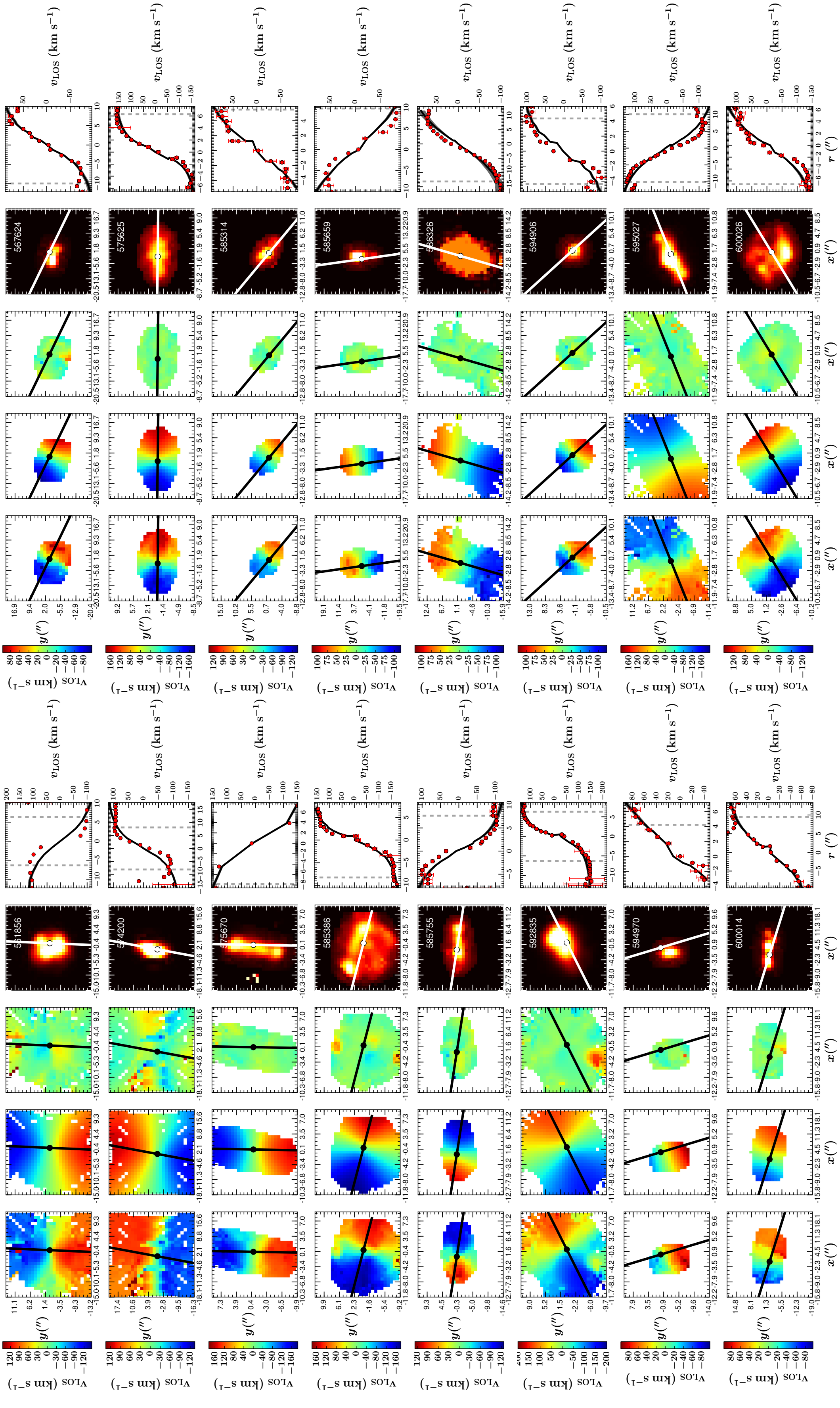
567624
575625
585314
585659
586326
594906
595027
600026
561856
574200
575670
585386
585755
592835
594970
600014
$v_{\rm LOS}$ (km s^{-1})
$y ('')$
$x ('')$
$r ('')$

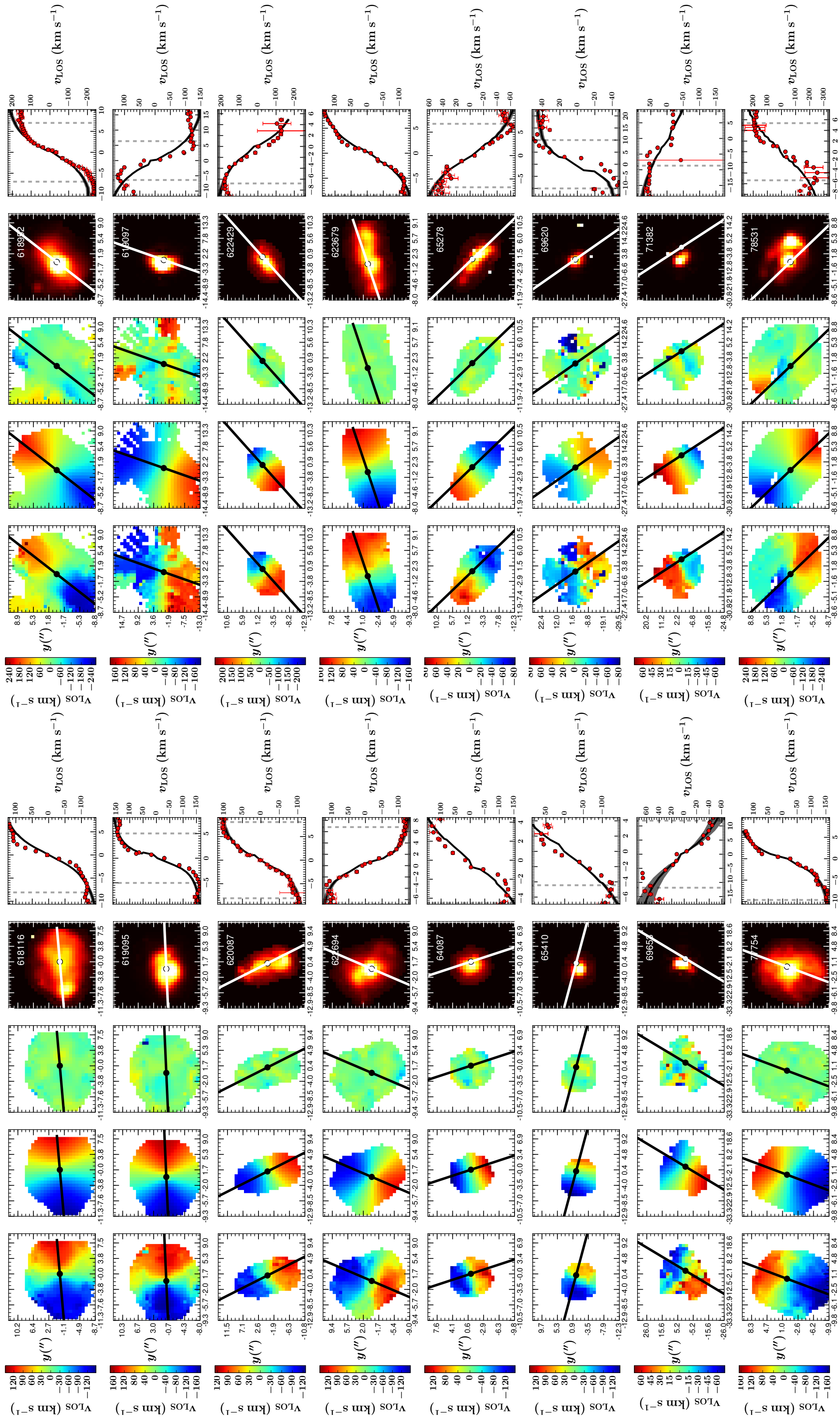
618116
619095
620087
64087
65410
618922
622429
623679
65278
69620
71382
78531
$v_{\rm LOS}$ (km s^{-1})
$y('')$
$x('')$
$r\ ('')$

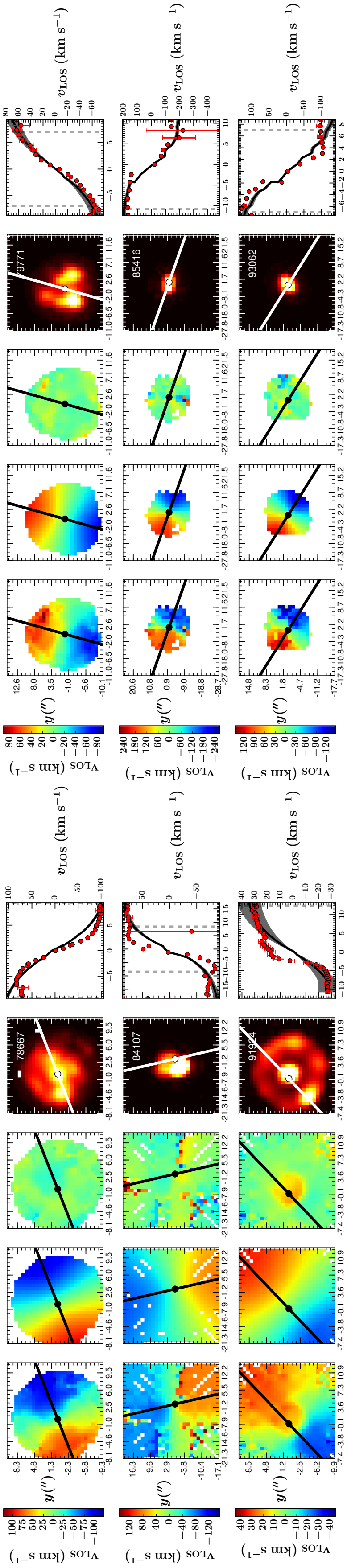

Figure B.2: The observed and best fit model velocity fields (see § 3.3.2.1) for the SAMI LQ *disky* sub-sample (see § 3.4.3). For a full description see Figure 3.1.

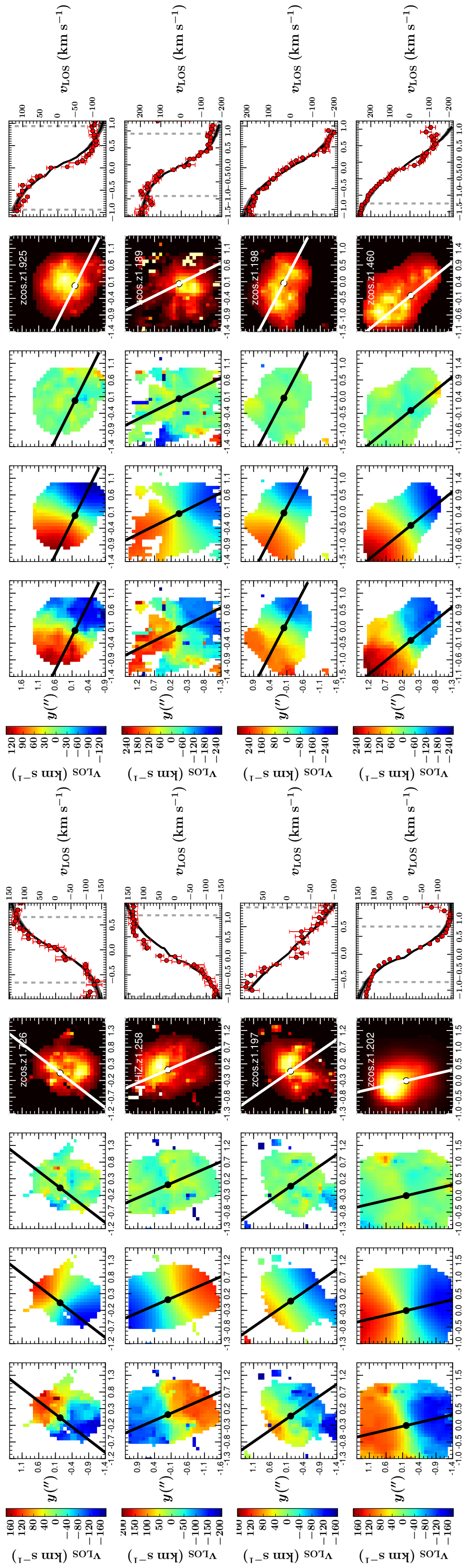

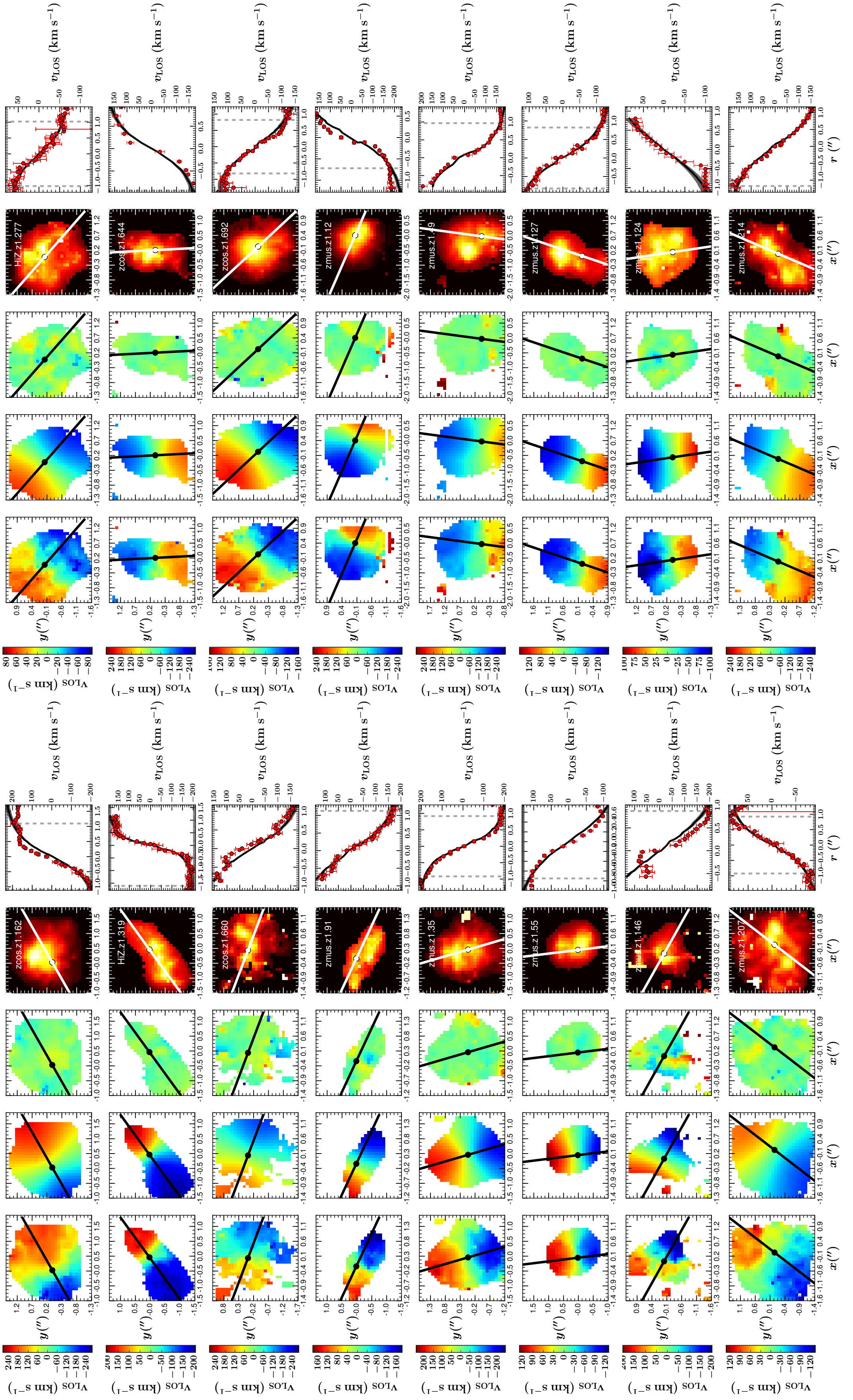
zcos.z1.162
HiZ.z1.319
zcos.z1.660
zmus.z1.91
zmus.z1.35
zmus.z1.55
zmus.z1.146
zmus.z1.207
HiZ.z1.277
zcos.z1.644
zcos.z1.692
zmus.z1.12
zmus.z1.127
zmus.z1.124
zmus.z1.214
$v_{\rm LOS}$ (km s^{-1})
$y('')$
$x('')$
$r('')$

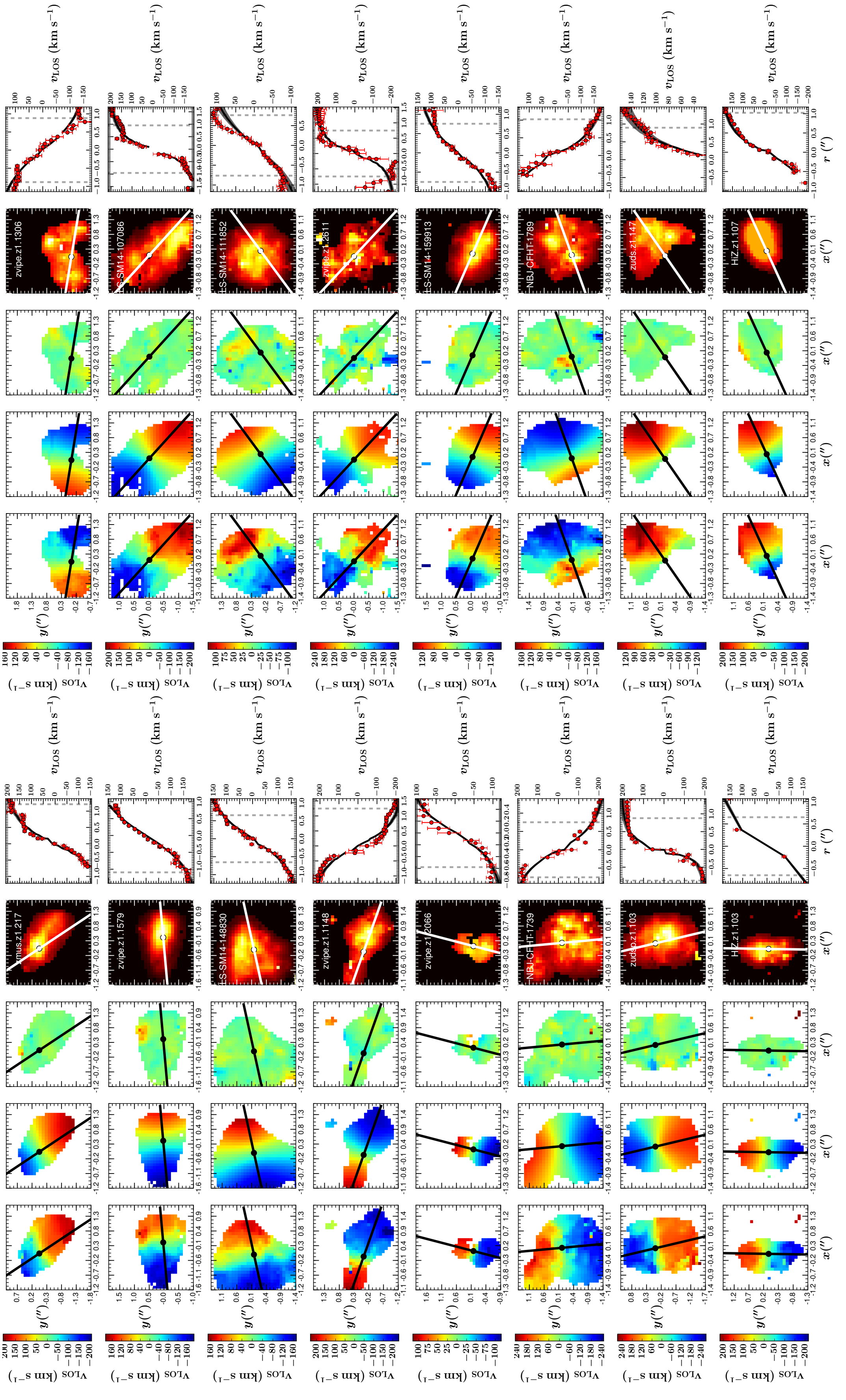
zvipe.z1.1306
-SM14-107086
LS-SM14-111852
zvipe.z1.2811
LS-SM14-159913
NBJ-CFHT-1789
zuds.z1.147
HiZ.z1.107
cmus.z1.217
zvipe.z1.1579
LS-SM14-148830
zvipe.z1.1148
zvipe.z1.2066
NBJ-CFHT-1739
zudsp.z1.103
HiZ.z1.103
$v_{\rm LOS}$ (km s^{-1})
y (″)
x (″)
r (″)

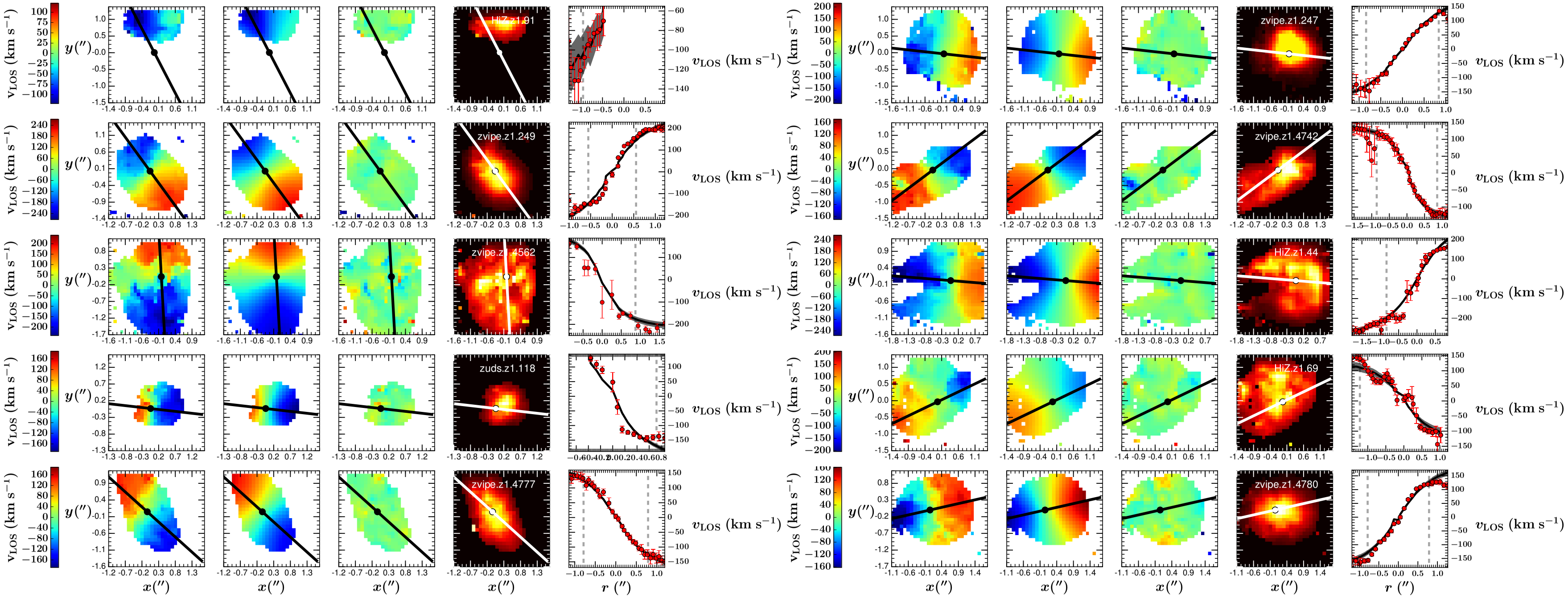

Figure B.3: The observed and best fit model velocity fields (see § 3.4.1) for the revised KROSS *disky* sub-sample (see § 3.4.3). For a full description see Figure 3.1.

Appendix C

Additional Plots for Chapter 4

C.1 Comparison with HI

In § 4.1 we discussed the relative advantages of constructing the TFR using CO(1-0) as a dynamical tracer rather than HI, the use of the latter being well established. In this section we compare the values of W_{50} derived from COLD GASS CO(1-0) integrated profiles to those derived from GASS HI integrated profiles of the same galaxies. We measure the latter by fitting the Double Peak Gaussian function to the HI spectra in the same manner as described in § 4.3.3.

The majority of the GASS HI galaxy spectra were obtained with the Arecibo 305 m telescope (see § 4.2.1 for more detail). The spectra are available as part of the GASS data releases[1] (Catinella et al., 2010, 2012, 2013). However, as described in Catinella et al. (2010), GASS galaxies were not re-observed with Arecibo if a suitable HI detection was already available from the ALFALFA survey or the Cornell HI archive (Haynes et al., 2011). As such, the comparison conducted in this section draws on HI W_{50} values measured from spectra from all three sources. We denote all measurements of the width of a galaxy's HI integrated profile at 50% of its maximum as $W_{50,\mathrm{HI}}$. For clarity, in this section only, we denote the CO(1-0) W_{50} values described in § 4.3.3 as $W_{50,\mathrm{CO}}$.

Of the 207 COLD GASS galaxies in the initial sample defined in § 4.2, 155 originate from the COLD GASS DR3, with the remaining 52 from the low mass extension of COLD GASS.

---

[1] http://wwwmpa.mpa-garching.mpg.de/GASS/data.php

HI spectra for galaxies in the COLD GASS low mass extension are not publicly available, so we exclude these galaxies from our comparison. Of the remaining 155 galaxies, 140 have a corresponding HI spectrum that is publicly available. We detect a signal (i.e. $A/N > 1$) in 136 of these (76 observed directly by GASS, 38 from ALFALFA and 22 from the Cornell archive). As all 136 of these spectra obey the selection criteria of the initial sample as defined in § 4.2, we include them all in our comparison. Of the 83 COLD GASS galaxies comprising the sub-sample defined in § 4.4.2, we exclude 17 galaxies that originate from the COLD GASS low mass extension (for the reason discussed). The remaining 66 galaxies originate from the COLD GASS DR3. 59 of these have a corresponding HI spectrum that is publicly available. To maintain consistency in our comparison, we apply the same selection criteria to the derived HI line widths as those used to define the sub-sample in § 4.4.2. To this end we exclude two galaxies with $A/N < 1.5$, leaving 57 spectra (30 from GASS, 16 from ALFALFA and 11 from the Cornell archive).

We compare the values of $W_{50,\mathrm{CO}}$ and $W_{50,\mathrm{HI}}$ for both the initial sample and sub-sample in Figure C.1. This shows that, for both the sample and sub-sample, the two measures of line width generally correlate well with one another. However, the scatter around the 1:1 line is much larger for the initial sample than for the sub-sample. The increased scatter in the initial sample is a consequence of the inclusion of galaxies with CO(1-0) integrated profiles that do not display a double-horned or boxy shape, i.e. profiles for which we cannot be sure the CO sufficiently probes the outer parts of the galaxy's rotation curve (see § 4.4.2). Considering only the sub-sample, the two measures of line width are in good agreement ($[W_{50,\mathrm{HI}} - W_{50,\mathrm{CO}}]_{\mathrm{M}} = 8 \pm 45$ km s^{-1}, where the uncertainty is the median absolute deviation with respect to the median itself).

The HI velocity widths are typically larger than the CO velocity widths at lowest values of $W_{50,\mathrm{CO}}$, as is apparent from the free fit (solid red) line in panel (b) of Figure C.1. Conversely, for the highest values of $W_{50,\mathrm{CO}}$, $W_{50,\mathrm{HI}}$ tends to be smaller. This trend is weaker but still present in the sub-sample, as is shown by the free fit (solid blue) line in panel (c) of Figure C.1.

To investigate whether this bias translates into a significant difference between TFRs constructed using CO(1-0) line widths and HI line widths, we plot in Figure C.2 both the

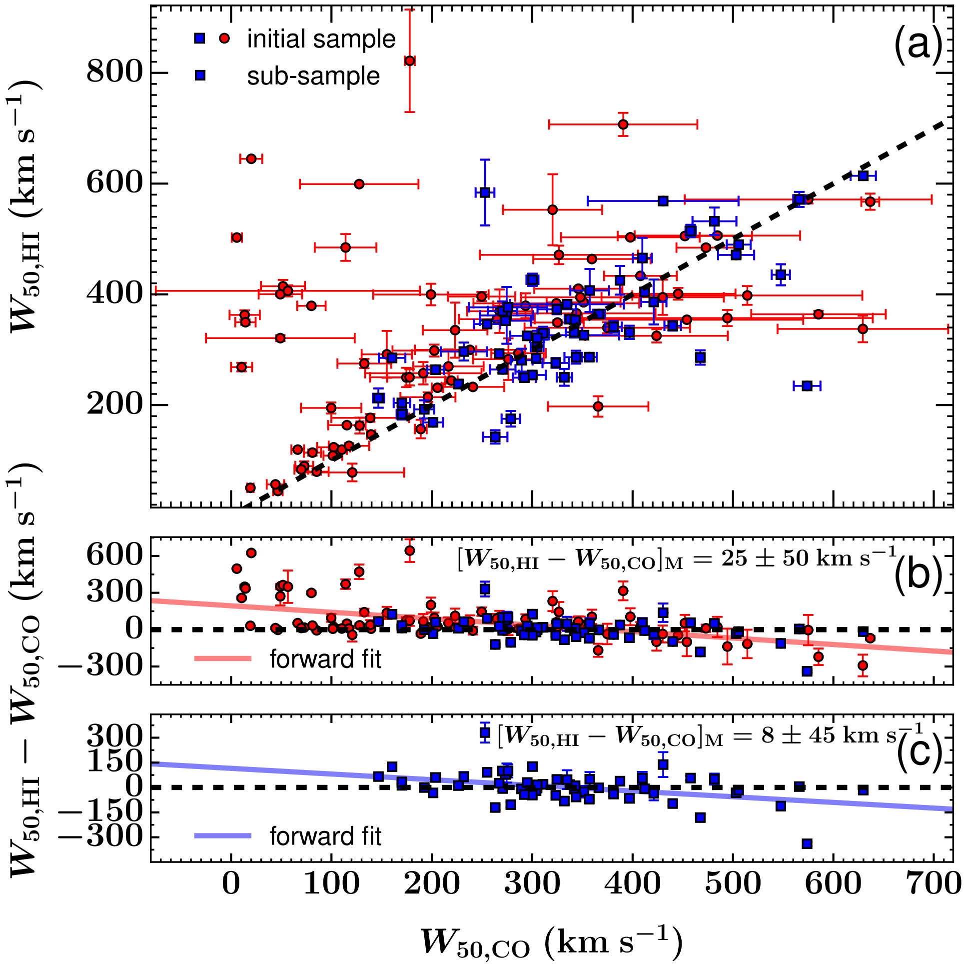

Figure C.1: Comparison between $W_{50,\mathrm{CO}}$ and $W_{50,\mathrm{HI}}$ for galaxies in the initial sample (see § 4.2; red circles and blue squares), and the final sub-sample (see § 4.4.2; blue squares) that have a corresponding HI detection in GASS. (a) Correlation between the two measures of line width for both the initial sample and sub-sample. The dashed black line represents the 1:1 relation. (b) and (c) Line width difference $W_{50,\mathrm{HI}} - W_{50,\mathrm{CO}}$ for the initial sample and sub-sample, respectively. The red solid line ($W_{50,\mathrm{HI}} - W_{50,\mathrm{CO}} = (-0.53 \pm 0.07)[W_{50,\mathrm{CO}} - 277.4] + 48 \pm 10$) and blue solid line ($W_{50,\mathrm{HI}} - W_{50,\mathrm{CO}} = (-0.3 \pm 0.1)[W_{50,\mathrm{CO}} - 323.5] + 5 \pm 11$) represent a free forward fit to the data points in respectively (b) and (c). The median difference is displayed in the top right of both (b) and (c), along with its uncertainty (the median absolute deviation from the median itself). $W_{50,\mathrm{CO}}$ and $W_{50,\mathrm{HI}}$ differ much less for galaxies in the final sub-sample than for galaxies only included in the initial sample.

$W1$-band and the stellar mass TFR of both the initial sample and the final sub-sample, this using both $W_{50,\mathrm{CO}}$ and $W_{50,\mathrm{HI}}$ values. For consistency, we only consider here galaxies with both CO and HI data. This allows to directly compare how the use of either measure of line width affects the relations. The corresponding TFR fit parameters are listed in Table C.1. For reasons discussed in § 4.4.3, the reverse fit is preferred to the conventional forward fit (see § 4.4.1 for a description of both). In addition, it is more informative here to examine how the scatter in the velocity width changes when considering either $W_{50,\mathrm{CO}}$ or $W_{50,\mathrm{HI}}$ than the scatter in the $W1$ magnitudes or stellar masses. For both these reasons, we examine only the reverse fits to the TFRs, as shown in Figure C.2.

Whilst in all cases the slopes of both the $W_{50,\mathrm{CO}}$ and $W_{50,\mathrm{HI}}$ TFRs agree within uncertainties, the slopes of both HI TFRs of the sub-sample are steeper than those of the CO(1-0) TFRs for the same galaxies. The intercepts agree within the uncertainties for all the TFRs of the sub-sample. However, the intercepts of both the stellar mass and $W1$ CO(1-0) TFRs of the initial sample are offset to higher values along the ordinate compared to those of the corresponding HI relations. For both the stellar mass and $W1$-band TFRs of the initial sample, the total and intrinsic scatter of the $W_{50,\mathrm{HI}}$ relations are significantly less than those of the $W_{50,\mathrm{CO}}$ relations. Conversely, considering the TFRs of the sub-sample, the total and intrinsic scatter of the CO relations are significantly smaller. It is clear then that TFRs constructed using CO and HI line widths are comparable in terms of slope and intercept, but differ in terms of intrinsic and total scatter. Considering the HI TFRs (both the $W1$-band and stellar mass relations), there is only a small reduction in the intrinsic and total scatter between the initial sample and the final sub-sample. The reduction in scatter for the CO TFRs is much greater - primarily as a result of excluding from the sub-sample those galaxies with CO(1-0) integrated profiles that do not display a boxy or double-horned shape (see § 4.4.2 and § 4.5.5). We therefore conclude that, assuming the selection criteria of the sub-sample are applied, the CO and HI line widths, and thus the resultant TFRs, are comparable, but that the scatter is greatly reduced by using CO.

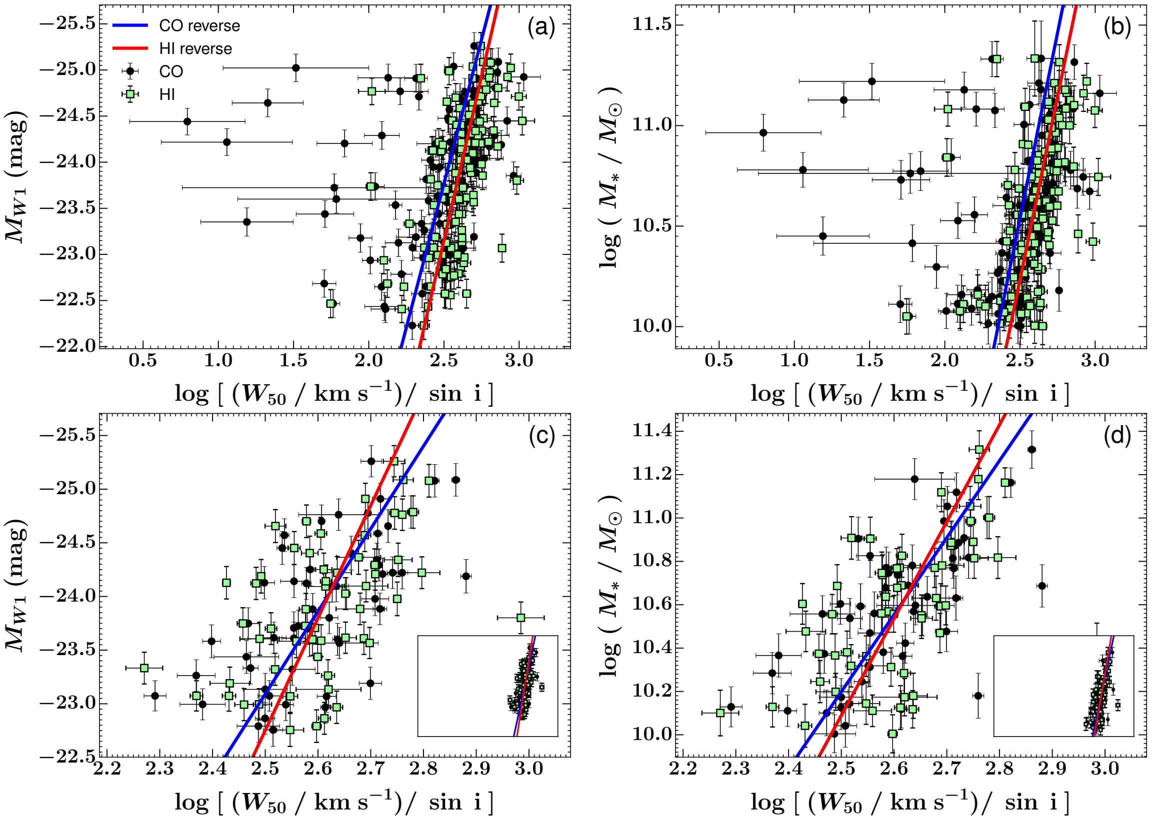

Figure C.2: Comparison of the $W1$-band and stellar mass Tully-Fisher relations using W_{50} values derived from COLD GASS CO(1-0) integrated profiles ($W_{50,\mathrm{CO}}$, black points) and GASS HI integrated profiles ($W_{50,\mathrm{HI}}$, pale green points), this for the same galaxies with both CO and HI data. (a) and (c) show the absolute $W1$-band TFR of those galaxies from respectively the initial COLD GASS sample and our final sub-sample. The x-axis is the width of the integrated profile (CO(1-0) or HI) at 50% of the peak, corrected for the effect of inclination. For (a) and (c), the y-axis is the absolute *WISE* Band 1 magnitude $W1$ (≈ 3.4 μm). The solid blue line show the reverse fit to the CO(1-0) data points. The reverse fit to the HI data points is shown as the solid red line. To demonstrate the reduction in scatter between the initial sample and final sub-sample, the embedded panel in (c) shows the TFR for the final sub-sample but over the same axis ranges as (a). (b) and (d) are as (a) and (c), but for the stellar mass TFRs.

Table C.1: Reverse fit parameters of the $W1$-band and stellar mass Tully-Fisher relations presented in Figure C.2. The pivot value is 2.6 for all relations (see § 4.4.1).

TFR	Tracer	Sample	Slope	Intercept (dex)	Intrinsic Scatter (dex)	Total Scatter (dex)
M_*	CO	Inital	4 ± 2	10.9 ± 0.2	0.93 ± 0.09	0.985 ± 0.007
		Sub-sample	3.6 ± 0.6	10.55 ± 0.04	0.28 ± 0.03	0.310 ± 0.007
	H I	Initial	3.6 ± 0.6	10.60 ± 0.05	0.56 ± 0.04	0.580 ± 0.005
		Sub-sample	4.5 ± 0.9	10.53 ± 0.06	0.43 ± 0.05	0.445 ± 0.009
				(mag)	(mag)	(mag)
M_{W1}	CO	Inital	−6 ± 1	−24.4 ± 0.2	1.6 ± 0.1	1.61 ± 0.01
		Sub-sample	−8 ± 1	−23.9 ± 0.1	0.68 ± 0.07	0.69 ± 0.01
	H I	Initial	−7 ± 1	−23.9 ± 0.1	1.07 ± 0.07	1.104 ± 0.009
		Sub-sample	−10 ± 3	−23.8 ± 0.2	1.1 ± 0.1	1.09 ± 0.02

C.2 Galaxy Spectra

Figure C.3 shows the Gaussian Double Peak function fits to each of the COLD GASS galaxy spectra in our final sub-sample, as described in § 4.3.3 and § 4.4.2. The data are plotted in blue and the best fit function in green. The solid red line indicates the best fit central velocity (v_0), whilst the dashed red lines show the width at 50% of the peak (W_{50}).

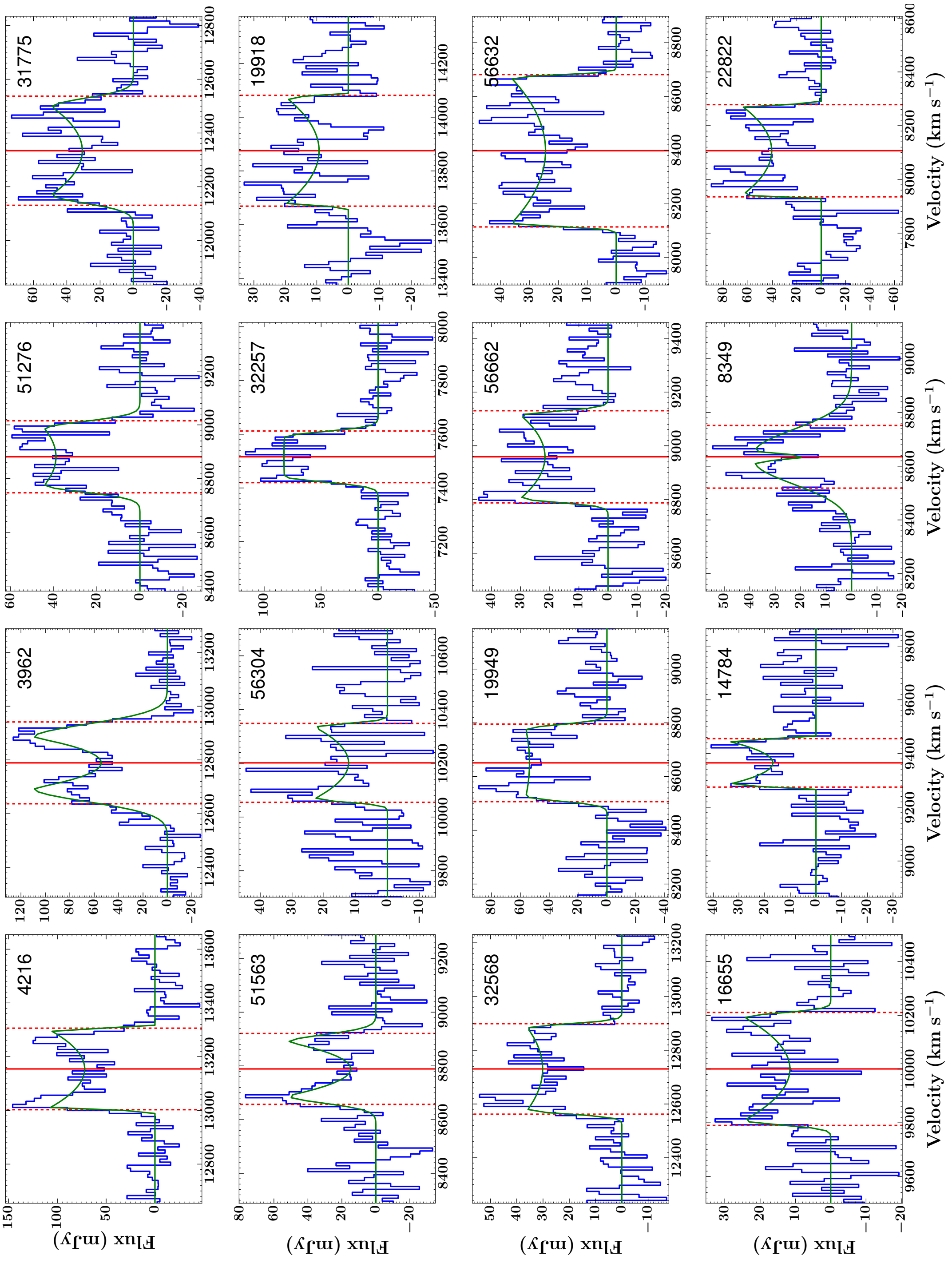
4216
3962
51276
31775
51563
56304
32257
19918
32568
19949
56662
56632
16655
14784
8349
22822
Flux (mJy)
Flux (mJy)
Flux (mJy)
Flux (mJy)
Velocity (km s^{-1})
Velocity (km s^{-1})
Velocity (km s^{-1})
Velocity (km s^{-1})

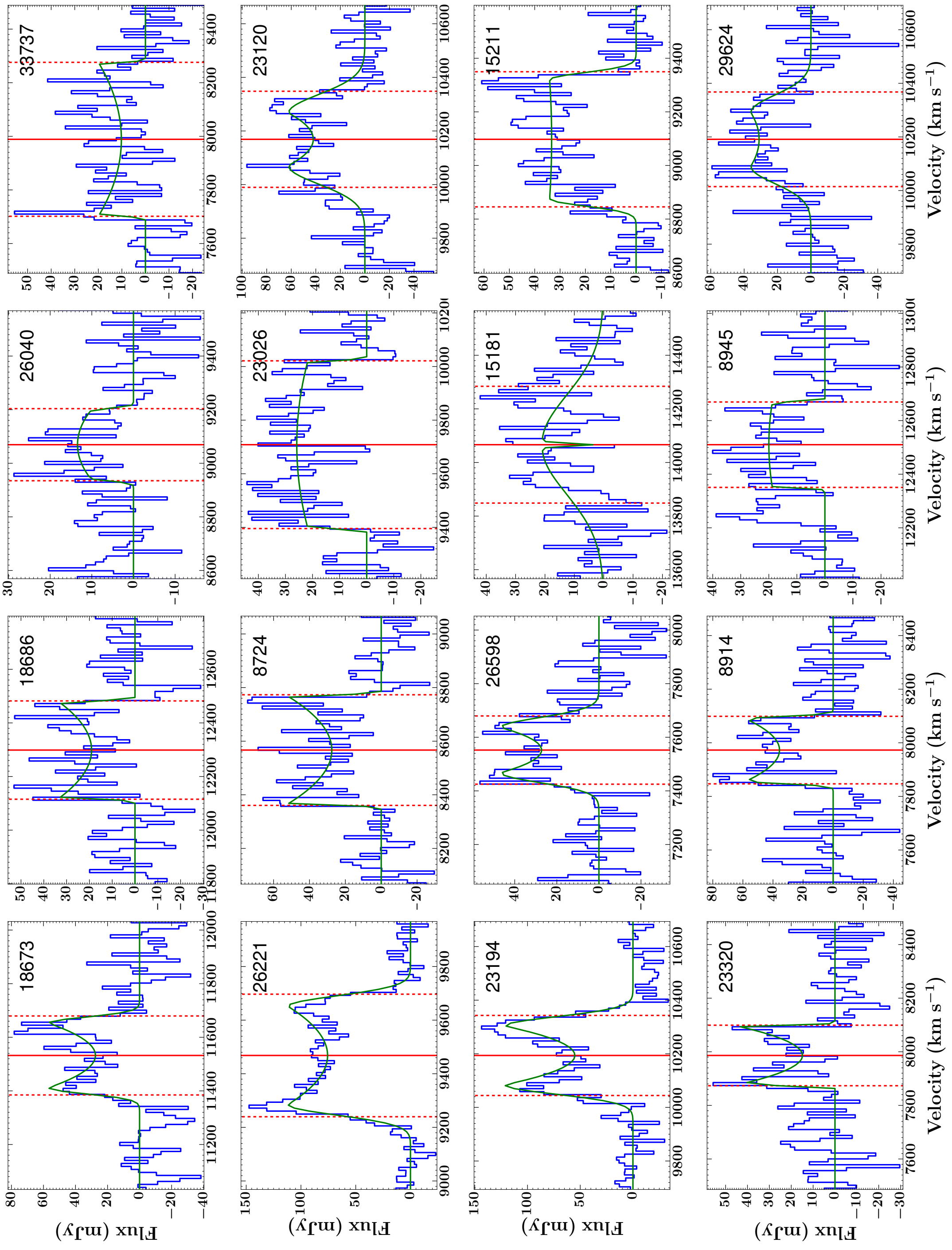
18673
18686
26040
33737
26221
8724
23026
23120
23194
26598
15181
15211
23320
8914
8945
29624
Flux (mJy)
Velocity (km s^{-1})

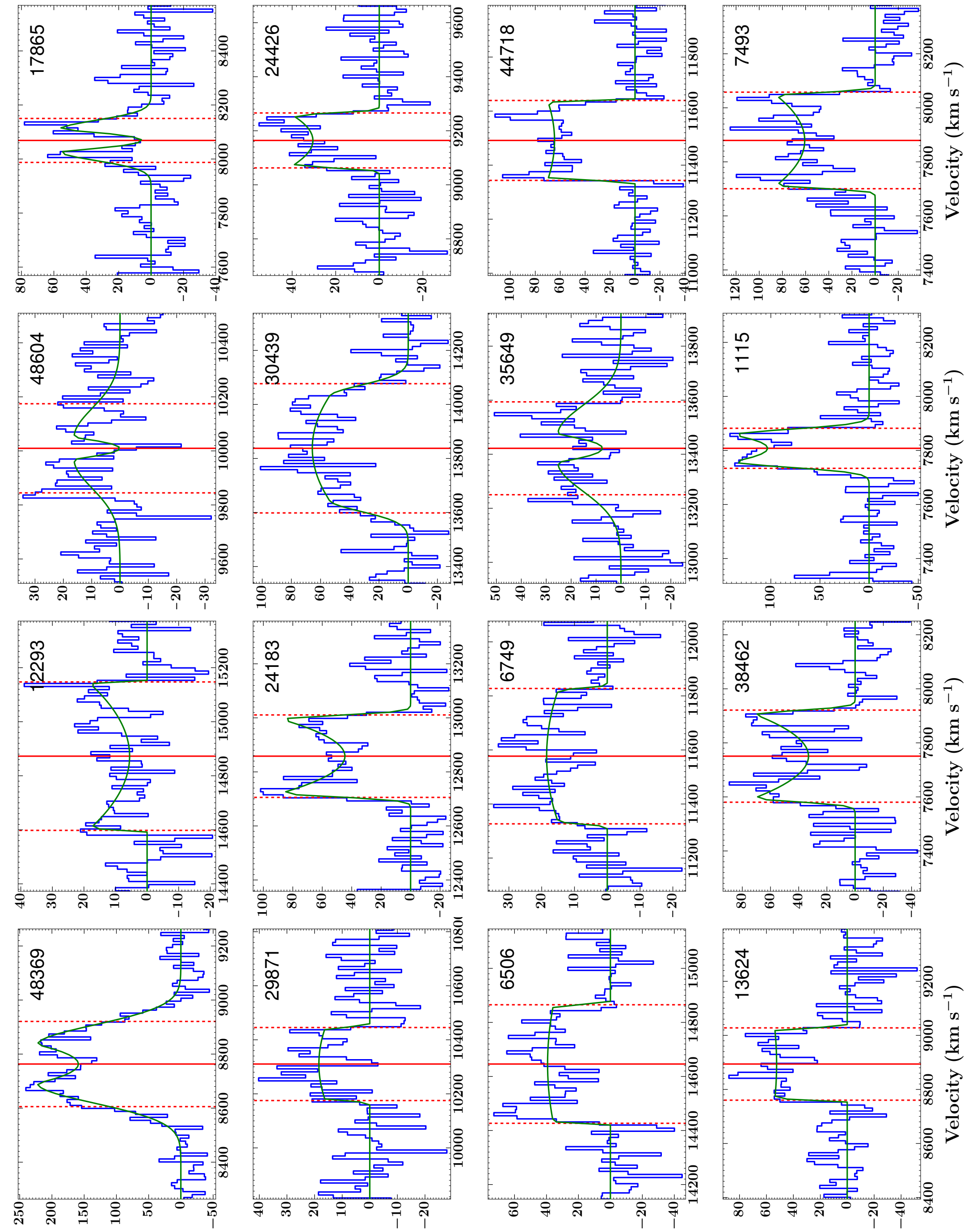
48369
12293
48604
17865
29871
24183
30439
24426
6506
6749
35649
44718
13624
38462
1115
7493
Flux (mJy)
Flux (mJy)
Flux (mJy)
Flux (mJy)
Velocity (km s^{-1})
Velocity (km s^{-1})
Velocity (km s^{-1})
Velocity (km s^{-1})

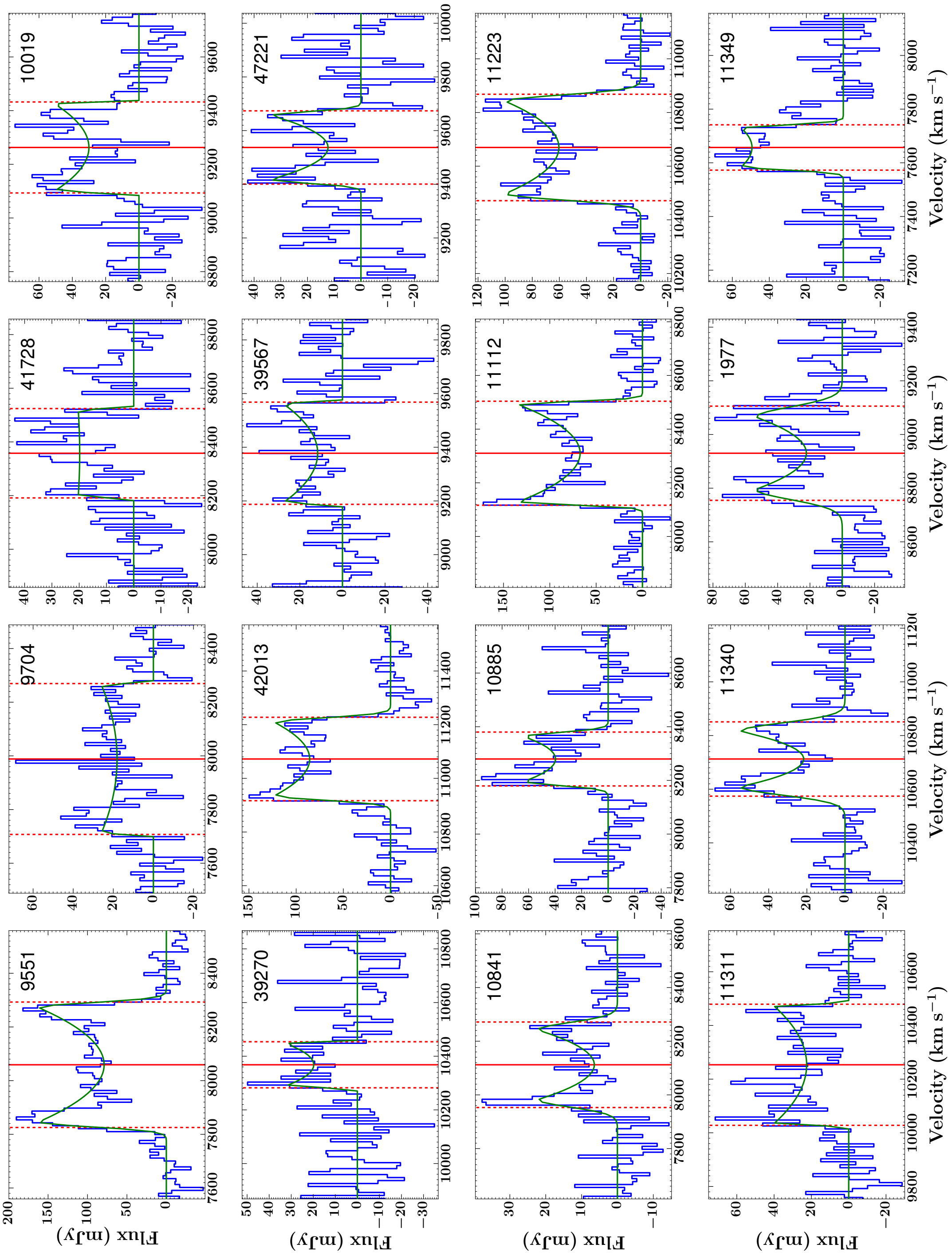
9551
9704
41728
10019
39270
42013
39567
47221
10841
10885
11112
11223
11311
11340
1977
11349
Flux (mJy)
Velocity (km s^{-1})

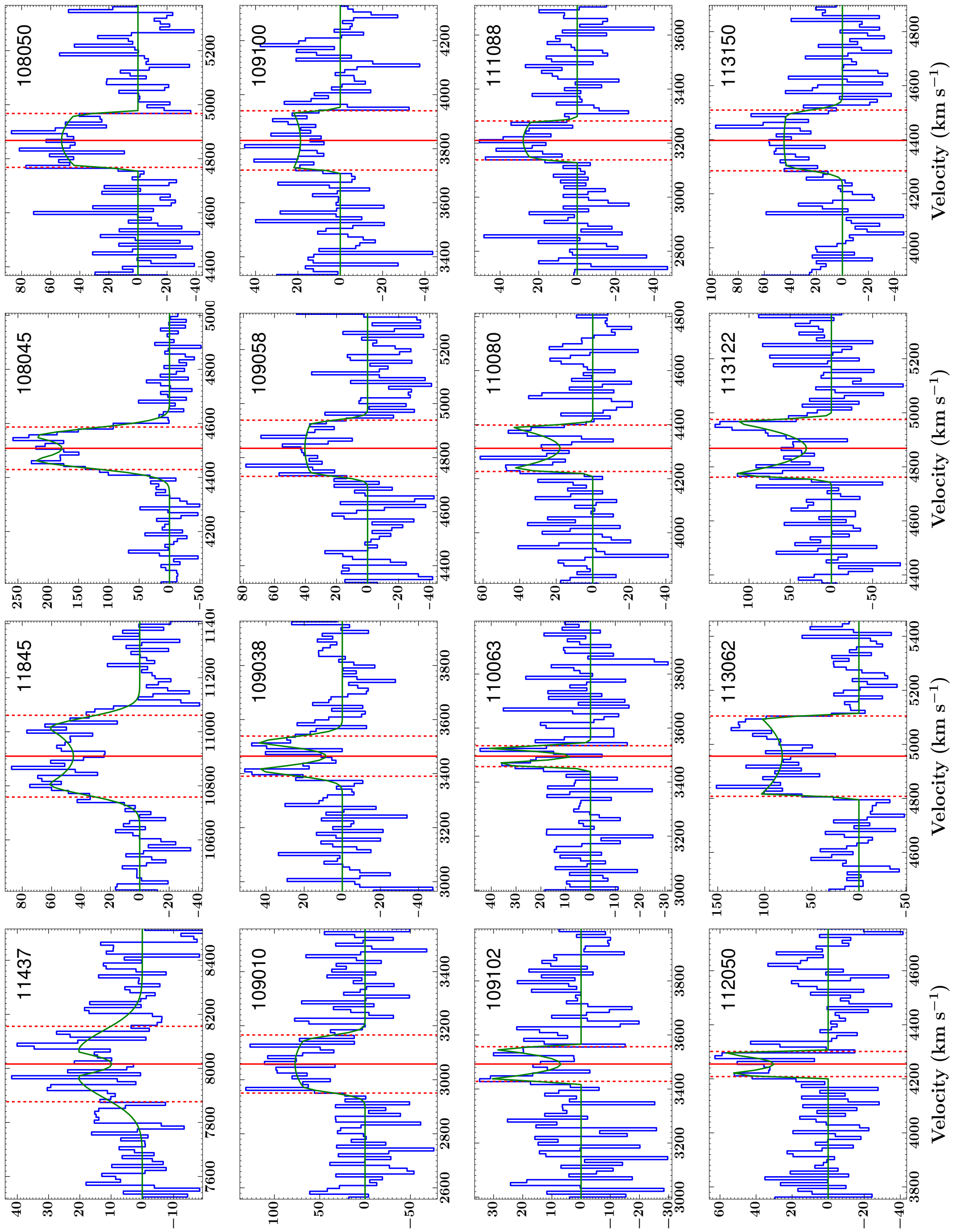
11437
11845
108045
108050
109010
109038
109058
109100
109102
110063
110080
111088
112050
113062
113122
113150
Flux (mJy)
Velocity (km s^{-1})

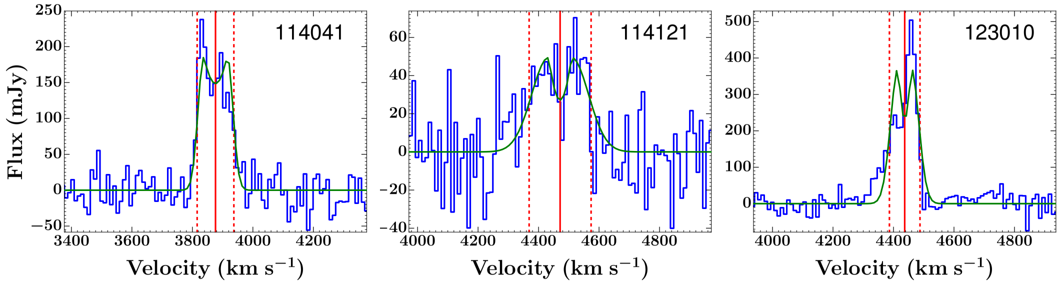

Figure C.3: The Gaussian Double Peak function fits to each of the COLD GASS galaxy spectra in our final sub-sample, as described in § 4.3.3 and § 4.4.2. The data are plotted in blue and the best fit function in green. The solid red line indicates the best fit central velocity (v_0), whilst the dashed red lines show the width at 50% of the peak (W_{50}). The COLD GASS ID is displayed in the top right of each panel.

Bibliography

Aaronson, M., 1983. The Tully-Fisher relation and its application to the distance scale. *Highlights of Astronomy*, **6**, 269–282.

Abazajian, K., Adelman-McCarthy, J. K., Agüeros, M. A., Allam, S. S., Anderson, S. F. et al., 2003. The First Data Release of the Sloan Digital Sky Survey. *AJ*, **126**, 2081–2086.

Abdalla, F. B., Bull, P., Camera, S., Benoit-Lévy, A., Joachimi, B., Kirk, D., Kloeckner, H. R., Maartens, R., Raccanelli, A., Santos, M. G. & Zhao, G. B., 2015. Cosmology from HI galaxy surveys with the SKA. *Advancing Astrophysics with the Square Kilometre Array (AASKA14)*, 17.

Abraham, R. G., 1999. Quantifying Morphological Evolution from Low to High Redshifts. *Astrophysics & Space Science*, **269**, 323–338.

al Rahman Al Sufi, A., 1965. *Book of Pictures of the (Fixed) Stars, MS. Marsh 144*. Bodleian Libraries, University of Oxford.

Allen, J. T., Croom, S. M., Konstantopoulos, I. S., Bryant, J. J., Sharp, R. et al., 2015. The SAMI Galaxy Survey: Early Data Release. *MNRAS*, **446**, 1567–1583.

Aragón-Salamanca, A., Alonso-Herrero, A., Gallego, J., García-Dabó, C. E., Pérez-González, P. G., Zamorano, J. & Gil de Paz, A., 2003. Star Formation Rate Estimators: [OII]3727 vs Hα for Local Star-forming Galaxies. In E. Perez, R. M. Gonzalez Delgado & G. Tenorio-Tagle, eds., *Star Formation Through Time*, vol. 297 of *Astronomical Society of the Pacific Conference Series*, 191.

ARNOUTS, S., CRISTIANI, S., MOSCARDINI, L., MATARRESE, S., LUCCHIN, F., FONTANA, A. & GIALLONGO, E., 1999. Measuring and modelling the redshift evolution of clustering: the Hubble Deep Field North. *MNRAS*, **310**, 540–556.

ARNOUTS, S., WALCHER, C. J., LE FÈVRE, O., ZAMORANI, G., ILBERT, O. ET AL., 2007. The SWIRE-VVDS-CFHTLS surveys: stellar mass assembly over the last 10 Gyr. Evidence for a major build up of the red sequence between z = 2 and z = 1. *A&A*, **476**, 137–150.

BACON, R., COPIN, Y., MONNET, G., MILLER, B. W., ALLINGTON-SMITH, J. R., BUREAU, M., CAROLLO, C. M., DAVIES, R. L., EMSELLEM, E., KUNTSCHNER, H., PELETIER, R. F., VEROLME, E. K. & DE ZEEUW, P. T., 2001. The SAURON project - I. The panoramic integral-field spectrograph. *MNRAS*, **326**, 23–35.

BALDRY, I. K., BALOGH, M. L., BOWER, R. G., GLAZEBROOK, K., NICHOL, R. C., BAMFORD, S. P. & BUDAVARI, T., 2006. Galaxy bimodality versus stellar mass and environment. *MNRAS*, **373**, 469–483.

BALDRY, I. K., GLAZEBROOK, K., BRINKMANN, J., IVEZIĆ, Ž., LUPTON, R. H., NICHOL, R. C. & SZALAY, A. S., 2004. Quantifying the Bimodal Color-Magnitude Distribution of Galaxies. *ApJ*, **600**, 681–694.

BALDWIN, J. A., PHILLIPS, M. M. & TERLEVICH, R., 1981. Classification parameters for the emission-line spectra of extragalactic objects. *PASP*, **93**, 5–19.

BARNES, J. E. & HERNQUIST, L. E., 1991. Fueling starburst galaxies with gas-rich mergers. *ApJ*, **370**, L65–L68.

BECKWITH, S. V. W., STIAVELLI, M., KOEKEMOER, A. M., CALDWELL, J. A. R., FERGUSON, H. C., HOOK, R., LUCAS, R. A., BERGERON, L. E., CORBIN, M., JOGEE, S., PANAGIA, N., ROBBERTO, M., ROYLE, P., SOMERVILLE, R. S. & SOSEY, M., 2006. The Hubble Ultra Deep Field. *AJ*, **132**, 1729–1755.

BELL, E. F. & DE JONG, R. S., 2001. Stellar Mass-to-Light Ratios and the Tully-Fisher Relation. *ApJ*, **550**, 212–229.

Bell, E. F., McIntosh, D. H., Katz, N. & Weinberg, M. D., 2003. The Optical and Near-Infrared Properties of Galaxies. I. Luminosity and Stellar Mass Functions. *ApJS*, **149**, 289–312.

Bell, E. F., Wolf, C., Meisenheimer, K., Rix, H.-W., Borch, A., Dye, S., Kleinheinrich, M., Wisotzki, L. & McIntosh, D. H., 2004. Nearly 5000 Distant Early-Type Galaxies in COMBO-17: A Red Sequence and Its Evolution since z˜1. *ApJ*, **608**, 752–767.

Bernardi, M., Roche, N., Shankar, F. & Sheth, R. K., 2011. Evidence of major dry mergers at Mstar greater than 2 times 10 11 MSun from curvature in early-type galaxy scaling relations? *MNRAS*, **412**, L6–L10.

Bertin, E. & Arnouts, S., 1996. SExtractor: Software for source extraction. *A&AS*, **117**, 393–404.

Birnboim, Y. & Dekel, A., 2003. Virial shocks in galactic haloes? *MNRAS*, **345**, 349–364.

Bland-Hawthorn, J., Bryant, J., Robertson, G., Gillingham, P., O'Byrne, J., Cecil, G., Haynes, R., Croom, S., Ellis, S., Maack, M., Skovgaard, P. & Noordegraaf, D., 2011. Hexabundles: imaging fiber arrays for low-light astronomical applications. *Optics Express*, **19**, 2649.

Bois, M., Emsellem, E., Bournaud, F., Alatalo, K., Blitz, L. et al., 2011. The ATLAS^{3D} project - VI. Simulations of binary galaxy mergers and the link with fast rotators, slow rotators and kinematically distinct cores. *MNRAS*, **416**, 1654–1679.

Bolzonella, M., Miralles, J.-M. & Pelló, R., 2000. Photometric redshifts based on standard SED fitting procedures. *A&A*, **363**, 476–492.

Bonnet, H., Conzelmann, R., Delabre, B., Donaldson, R., Fedrigo, E., Hubin, N. N., Kissler-Patig, M., Lizon, J.-L., Paufique, J., Rossi, S., Stroebele, S. & Tordo, S., 2004. First light of SINFONI AO-module at VLT. In D. Bonaccini Calia,

B. L. Ellerbroek & R. Ragazzoni, eds., *Advancements in Adaptive Optics*, vol. 5490 of *Society of Photo-Optical Instrumentation Engineers (SPIE) Conference Series*, 130–138.

Booth, R. S., de Blok, W. J. G., Jonas, J. L. & Fanaroff, B., 2009. MeerKAT Key Project Science, Specifications, and Proposals. *ArXiv e-prints*.

Bottinelli, L., Gouguenheim, L., Paturel, G. & de Vaucouleurs, G., 1980. The 21 centimeter line width as an extragalactic distance indicator. *ApJ*, **242**, L153–L156.

Bottinelli, L., Gouguenheim, L. & Teerikorpi, P., 1988. The value of H(0) from the infrared Tully-Fisher relation. *A&A*, **196**, 17–25.

Brammer, G. B., van Dokkum, P. G., Franx, M., Fumagalli, M., Patel, S. et al., 2012. 3D-HST: A Wide-field Grism Spectroscopic Survey with the Hubble Space Telescope. *ApJS*, **200**, 13.

Bridge, C. R., Appleton, P. N., Conselice, C. J., Choi, P. I., Armus, L., Fadda, D., Laine, S., Marleau, F. R., Carlberg, R. G., Helou, G. & Yan, L., 2007. The Role of Galaxy Interactions and Mergers in Star Formation at z¡=1.3: Mid-Infrared Properties in the Spitzer First Look Survey. *ApJ*, **659**, 931–940.

Bruzual, G. & Charlot, S., 2003. Stellar population synthesis at the resolution of 2003. *MNRAS*, **344**, 1000–1028.

Bryant, J. J., Bland-Hawthorn, J., Fogarty, L. M. R., Lawrence, J. S. & Croom, S. M., 2014. Focal ratio degradation in lightly fused hexabundles. *MNRAS*, **438**, 869–877.

Bryant, J. J., Owers, M. S., Robotham, A. S. G., Croom, S. M., Driver, S. P. et al., 2015. The SAMI Galaxy Survey: instrument specification and target selection. *MNRAS*, **447**, 2857–2879.

Buitrago, F., Trujillo, I., Conselice, C. J. & Häussler, B., 2013. Early-type galaxies have been the predominant morphological class for massive galaxies since only z $\sim$ 1. *MNRAS*, **428**, 1460–1478.

Bundy, K., Bershady, M. A., Law, D. R., Yan, R., Drory, N. et al., 2015. Overview of the SDSS-IV MaNGA Survey: Mapping nearby Galaxies at Apache Point Observatory. *ApJ*, **798**, 7.

Bureau, M., Mould, J. R. & Staveley-Smith, L., 1996. A New I-Band Tully-Fisher Relation for the Fornax Cluster: Implication for the Fornax Distance and Local Supercluster Velocity Field. *ApJ*, **463**, 60.

Cappellari, M. & Emsellem, E., 2004. Parametric Recovery of Line-of-Sight Velocity Distributions from Absorption-Line Spectra of Galaxies via Penalized Likelihood. *PASP*, **116**, 138–147.

Cappellari, M., Emsellem, E., Krajnović, D., McDermid, R. M., Scott, N. et al., 2011a. The ATLAS^{3D} project - I. A volume-limited sample of 260 nearby early-type galaxies: science goals and selection criteria. *MNRAS*, **413**, 813–836.

Cappellari, M., Emsellem, E., Krajnović, D., McDermid, R. M., Serra, P. et al., 2011b. The ATLAS^{3D} project - VII. A new look at the morphology of nearby galaxies: the kinematic morphology-density relation. *MNRAS*, **416**, 1680–1696.

Cardamone, C. N., van Dokkum, P. G., Urry, C. M., Taniguchi, Y., Gawiser, E., Brammer, G., Taylor, E., Damen, M., Treister, E., Cobb, B. E., Bond, N., Schawinski, K., Lira, P., Murayama, T., Saito, T. & Sumikawa, K., 2010. The Multiwavelength Survey by Yale-Chile (MUSYC): Deep Medium-band Optical Imaging and High-quality 32-band Photometric Redshifts in the ECDF-S. *ApJS*, **189**, 270–285.

Casertano, S. & van Gorkom, J. H., 1991. Declining rotation curves - The end of a conspiracy? *AJ*, **101**, 1231–1241.

Casertano, S. P. R. & Shostak, G. S., 1980. On galaxy masses determined from H I profiles. *A&A*, **81**, 371–374.

Catinella, B., Haynes, M. P. & Giovanelli, R., 2005. Rotational Widths for Use in the Tully-Fisher Relation. I. Long-Slit Spectroscopic Data. *AJ*, **130**, 1037–1048.

CATINELLA, B., SCHIMINOVICH, D., CORTESE, L., FABELLO, S., HUMMELS, C. B., MORAN, S. M., LEMONIAS, J. J., COOPER, A. P., WU, R., HECKMAN, T. M. & WANG, J., 2013. The GALEX Arecibo SDSS Survey - VIII. Final data release. The effect of group environment on the gas content of massive galaxies. *MNRAS*, **436**, 34–70.

CATINELLA, B., SCHIMINOVICH, D., KAUFFMANN, G., FABELLO, S., HUMMELS, C., LEMONIAS, J., MORAN, S. M., WU, R., COOPER, A. & WANG, J., 2012. The GALEX Arecibo SDSS Survey. VI. Second data release and updated gas fraction scaling relations. *A&A*, **544**, A65.

CATINELLA, B., SCHIMINOVICH, D., KAUFFMANN, G., FABELLO, S., WANG, J. ET AL., 2010. The GALEX Arecibo SDSS Survey - I. Gas fraction scaling relations of massive galaxies and first data release. *MNRAS*, **403**, 683–708.

CHABRIER, G., 2003. Galactic Stellar and Substellar Initial Mass Function. *PASP*, **115**, 763–795.

CHARBONNEAU, P., 1995. Genetic Algorithms in Astronomy and Astrophysics. *ApJS*, **101**, 309.

CICONE, C., MAIOLINO, R., STURM, E., GRACIÁ-CARPIO, J., FERUGLIO, C., NERI, R., AALTO, S., DAVIES, R., FIORE, F., FISCHER, J., GARCÍA-BURILLO, S., GONZÁLEZ-ALFONSO, E., HAILEY-DUNSHEATH, S., PICONCELLI, E. & VEILLEUX, S., 2014. Massive molecular outflows and evidence for AGN feedback from CO observations. *A&A*, **562**, A21.

CIRASUOLO, M., MCLURE, R. J., DUNLOP, J. S., ALMAINI, O., FOUCAUD, S., SMAIL, I., SEKIGUCHI, K., SIMPSON, C., EALES, S., DYE, S., WATSON, M. G., PAGE, M. J. & HIRST, P., 2007. The evolution of the near-infrared galaxy luminosity function and colour bimodality up to z ˜= 2 from the UKIDSS Ultra Deep Survey Early Data Release. *MNRAS*, **380**, 585–595.

COLE, S. & KAISER, N., 1989. Biased clustering in the cold dark matter cosmogony. *MNRAS*, **237**, 1127–1146.

Cole, S., Lacey, C. G., Baugh, C. M. & Frenk, C. S., 2000. Hierarchical galaxy formation. *MNRAS*, **319**, 168–204.

Combes, F., 2013. Molecular Gas in High Redshift Galaxies. In R. Kawabe, N. Kuno & S. Yamamoto, eds., *New Trends in Radio Astronomy in the ALMA Era: The 30th Anniversary of Nobeyama Radio Observatory*, vol. 476 of *Astronomical Society of the Pacific Conference Series*, 23.

Conselice, C. J., Blackburne, J. A. & Papovich, C., 2005a. The Luminosity, Stellar Mass, and Number Density Evolution of Field Galaxies of Known Morphology from z = 0.5 to 3. *ApJ*, **620**, 564–583.

Conselice, C. J., Bluck, A. F. L., Buitrago, F., Bauer, A. E., Grützbauch, R. et al., 2011. The Hubble Space Telescope GOODS NICMOS Survey: overview and the evolution of massive galaxies at 1.5< z< 3. *MNRAS*, **413**, 80–100.

Conselice, C. J., Bundy, K., Ellis, R. S., Brichmann, J., Vogt, N. P. & Phillips, A. C., 2005b. Evolution of the Near-Infrared Tully-Fisher Relation: Constraints on the Relationship between the Stellar and Total Masses of Disk Galaxies since z˜1. *ApJ*, **628**, 160–168.

Conselice, C. J., Bundy, K., U, V., Eisenhardt, P., Lotz, J. & Newman, J., 2008. The faint and extremely red K-band-selected galaxy population in the DEEP2/Palomar fields. *MNRAS*, **383**, 1366–1384.

Contini, T., Garilli, B., Le Fèvre, O., Kissler-Patig, M., Amram, P., Epinat, B., Moultaka, J., Paioro, L., Queyrel, J., Tasca, L., Tresse, L., Vergani, D., López-Sanjuan, C. & Perez-Montero, E., 2012. MASSIV: Mass Assemby Survey with SINFONI in VVDS. I. Survey description and global properties of the 0.9 < z < 1.8 galaxy sample. *A&A*, **539**, A91.

Courteau, S., 1997. Optical Rotation Curves and Linewidths for Tully-Fisher Applications. *AJ*, **114**, 2402.

COURTEAU, S. & RIX, H.-W., 1997. Maximal Disks and the Tully-Fisher Relation. In *American Astronomical Society Meeting Abstracts*, vol. 29 of *Bulletin of the American Astronomical Society*, 1332.

CRAIN, R. A., SCHAYE, J., BOWER, R. G., FURLONG, M., SCHALLER, M., THEUNS, T., DALLA VECCHIA, C., FRENK, C. S., MCCARTHY, I. G., HELLY, J. C., JENKINS, A., ROSAS-GUEVARA, Y. M., WHITE, S. D. M. & TRAYFORD, J. W., 2015. The EAGLE simulations of galaxy formation: calibration of subgrid physics and model variations. *MNRAS*, **450**, 1937–1961.

CRESCI, G., HICKS, E. K. S., GENZEL, R., SCHREIBER, N. M. F., DAVIES, R. ET AL., 2009. The SINS Survey: Modeling the Dynamics of z ~ 2 Galaxies and the High-z Tully-Fisher Relation. *ApJ*, **697**, 115–132.

CROCKER, A., KRIPS, M., BUREAU, M., YOUNG, L. M., DAVIS, T. A. ET AL., 2012. The ATLAS^{3D} project - XI. Dense molecular gas properties of CO-luminous early-type galaxies. *MNRAS*, **421**, 1298–1314.

CROOM, S. M., LAWRENCE, J. S., BLAND-HAWTHORN, J., BRYANT, J. J., FOGARTY, L. ET AL., 2012. The Sydney-AAO Multi-object Integral field spectrograph. *MNRAS*, **421**, 872–893.

DADDI, E., ELBAZ, D., WALTER, F., BOURNAUD, F., SALMI, F., CARILLI, C., DANNERBAUER, H., DICKINSON, M., MONACO, P. & RIECHERS, D., 2010. Different Star Formation Laws for Disks Versus Starbursts at Low and High Redshifts. *ApJ*, **714**, L118–L122.

DAVIES, R. I., AGUDO BERBEL, A., WIEZORREK, E., CIRASUOLO, M., FÖRSTER SCHREIBER, N. M., JUNG, Y., MUSCHIELOK, B., OTT, T., RAMSAY, S., SCHLICHTER, J., SHARPLES, R. & WEGNER, M., 2013. The Software Package for Astronomical Reductions with KMOS: SPARK. *A&A*, **558**, A56.

Davis, T. A., Alatalo, K., Bureau, M., Cappellari, M., Scott, N. et al., 2013. The ATLAS^{3D} Project - XIV. The extent and kinematics of the molecular gas in early-type galaxies. *MNRAS*, **429**, 534–555.

Davis, T. A., Bureau, M., Young, L. M., Alatalo, K., Blitz, L. et al., 2011. The ATLAS^{3D} project - V. The CO Tully-Fisher relation of early-type galaxies. *MNRAS*, **414**, 968–984.

Davis, T. A., Greene, J., Ma, C.-P., Pandya, V., Blakeslee, J. P., McConnell, N. & Thomas, J., 2016. The MASSIVE survey - III. Molecular gas and a broken Tully-Fisher relation in the most massive early-type galaxies. *MNRAS*, **455**, 214–226.

de Blok, W. J. G., 2011. The MeerKAT Karoo Array Telescope and its HI Emission Line Surveys. In C. Carignan, F. Combes & K. C. Freeman, eds., *IAU Symposium*, vol. 277 of *IAU Symposium*, 96–99.

de Vaucouleurs, G., 1953. On the distribution of mass and luminosity in elliptical galaxies. *MNRAS*, **113**, 134.

de Zeeuw, P. T., Bureau, M., Emsellem, E., Bacon, R., Carollo, C. M., Copin, Y., Davies, R. L., Kuntschner, H., Miller, B. W., Monnet, G., Peletier, R. F. & Verolme, E. K., 2002. The SAURON project - II. Sample and early results. *MNRAS*, **329**, 513–530.

Dekel, A. & Birnboim, Y., 2006. Galaxy bimodality due to cold flows and shock heating. *MNRAS*, **368**, 2–20.

Dekel, A., Birnboim, Y., Engel, G., Freundlich, J., Goerdt, T., Mumcuoglu, M., Neistein, E., Pichon, C., Teyssier, R. & Zinger, E., 2009a. Cold streams in early massive hot haloes as the main mode of galaxy formation. *Nature*, **457**, 451–454.

Dekel, A., Sari, R. & Ceverino, D., 2009b. Formation of Massive Galaxies at High Redshift: Cold Streams, Clumpy Disks, and Compact Spheroids. *ApJ*, **703**, 785–801.

den Heijer, M., Oosterloo, T. A., Serra, P., Józsa, G. I. G., Kerp, J., Morganti, R., Cappellari, M., Davis, T. A., Duc, P.-A., Emsellem, E., Krajnović, D., McDermid, R. M., Naab, T., Weijmans, A.-M. & de Zeeuw, P. T., 2015. The H I Tully-Fisher relation of early-type galaxies. *A&A*, **581**, A98.

Dewdney, P. E., Hall, P. J., Schilizzi, R. T. & Lazio, T. J. L. W., 2009. The Square Kilometre Array. *IEEE Proceedings*, **97**, 1482–1496.

Di Teodoro, E. M., Fraternali, F. & Miller, S. H., 2016. Flat rotation curves and a non-evolving Tully-Fisher relation from KMOS galaxies at z˜1. *ArXiv e-prints*.

Dickey, J. M. & Kazes, I., 1992. The Tully-Fisher relation for the CO line. *ApJ*, **393**, 530–543.

Dickinson, M., 1998. Color-Selected High Redshift Galaxies and the HDF. In M. Livio, S. M. Fall & P. Madau, eds., *The Hubble Deep Field*, 219.

Dickinson, M., Giavalisco, M. & GOODS Team, 2003. The Great Observatories Origins Deep Survey. In R. Bender & A. Renzini, eds., *The Mass of Galaxies at Low and High Redshift*, 324.

Driver, S. P., Hill, D. T., Kelvin, L. S., Robotham, A. S. G., Liske, J. et al., 2011. Galaxy and Mass Assembly (GAMA): survey diagnostics and core data release. *MNRAS*, **413**, 971–995.

Driver, S. P., Wright, A. H., Andrews, S. K., Davies, L. J., Kafle, P. R. et al., 2016. Galaxy And Mass Assembly (GAMA): Panchromatic Data Release (far-UV-far-IR) and the low-z energy budget. *MNRAS*, **455**, 3911–3942.

Drory, N., Bender, R., Feulner, G., Hopp, U., Maraston, C., Snigula, J. & Hill, G. J., 2004. The Munich Near-Infrared Cluster Survey (MUNICS). VI. The Stellar Masses of K-Band-selected Field Galaxies to z˜1.2. *ApJ*, **608**, 742–751.

Dubois, Y., Devriendt, J., Slyz, A. & Teyssier, R., 2012. Self-regulated growth of supermassive black holes by a dual jet-heating active galactic nucleus feedback mechanism: methods, tests and implications for cosmological simulations. *MNRAS*, **420**, 2662–2683.

Duffy, A. R., Meyer, M. J., Staveley-Smith, L., Bernyk, M., Croton, D. J., Koribalski, B. S., Gerstmann, D. & Westerlund, S., 2012. Predictions for ASKAP neutral hydrogen surveys. *MNRAS*, **426**, 3385–3402.

Dutton, A. A., van den Bosch, F. C. & Dekel, A., 2010. On the origin of the galaxy star-formation-rate sequence: evolution and scatter. *MNRAS*, **405**, 1690–1710.

Dutton, A. A., van den Bosch, F. C., Faber, S. M., Simard, L., Kassin, S. A., Koo, D. C., Bundy, K., Huang, J., Weiner, B. J., Cooper, M. C., Newman, J. A., Mozena, M. & Koekemoer, A. M., 2011. On the evolution of the velocity-mass-size relations of disc-dominated galaxies over the past 10 billion years. *MNRAS*, **410**, 1660–1676.

Edge, A., Sutherland, W., Kuijken, K., Driver, S., McMahon, R., Eales, S. & Emerson, J. P., 2013. The VISTA Kilo-degree Infrared Galaxy (VIKING) Survey: Bridging the Gap between Low and High Redshift. *The Messenger*, **154**, 32–34.

Efstathiou, G., 2000. A model of supernova feedback in galaxy formation. *MNRAS*, **317**, 697–719.

Eisenhauer, F., Abuter, R., Bickert, K., Biancat-Marchet, F., Bonnet, H. et al., 2003. SINFONI - Integral field spectroscopy at 50 milli-arcsecond resolution with the ESO VLT. In M. Iye & A. F. M. Moorwood, eds., *Instrument Design and Performance for Optical/Infrared Ground-based Telescopes*, vol. 4841 of *Proc. SPIE*, 1548–1561.

Eisenstein, D. J. & Loeb, A., 1996. Can the Tully-Fisher Relation Be the Result of Initial Conditions? *ApJ*, **459**, 432.

Ekholm, T., Lanoix, P., Teerikorpi, P., Fouqué, P. & Paturel, G., 2000. Investigations of the Local Supercluster velocity field. III. Tracing the backside infall with distance moduli from the direct Tully-Fisher relation. *A&A*, **355**, 835–847.

Elbaz, D., Daddi, E., Le Borgne, D., Dickinson, M., Alexander, D. M., Chary, R.-R., Starck, J.-L., Brandt, W. N., Kitzbichler, M., MacDonald, E., Nonino, M., Popesso, P., Stern, D. & Vanzella, E., 2007. The reversal of the star formation-density relation in the distant universe. *A&A*, **468**, 33–48.

Elmegreen, B. G., Bournaud, F. & Elmegreen, D. M., 2008. Bulge Formation by the Coalescence of Giant Clumps in Primordial Disk Galaxies. *ApJ*, **688**, 67–77.

Emsellem, E., Cappellari, M., Krajnović, D., van de Ven, G., Bacon, R., Bureau, M., Davies, R. L., de Zeeuw, P. T., Falcón-Barroso, J., Kuntschner, H., McDermid, R. M., Peletier, R. F., Sarzi, M. & van den Bosch, R. C. E., 2008. Fast and slow rotators: the build-up of the red sequence. In M. Bureau, E. Athanassoula & B. Barbuy, eds., *Formation and Evolution of Galaxy Bulges*, vol. 245 of *IAU Symposium*, 11–14.

Epinat, B., Tasca, L., Amram, P., Contini, T., Le Fèvre, O., Queyrel, J., Vergani, D., Garilli, B., Kissler-Patig, M., Moultaka, J., Paioro, L., Tresse, L., Bournaud, F., López-Sanjuan, C. & Perret, V., 2012. MASSIV: Mass Assembly Survey with SINFONI in VVDS. II. Kinematics and close environment classification. *A&A*, **539**, A92.

Faber, S. M., Willmer, C. N. A., Wolf, C., Koo, D. C., Weiner, B. J. et al., 2007. Galaxy Luminosity Functions to z˜1 from DEEP2 and COMBO-17: Implications for Red Galaxy Formation. *ApJ*, **665**, 265–294.

Fazio, G. G., Hora, J. L., Allen, L. E., Ashby, M. L. N., Barmby, P. et al., 2004. The Infrared Array Camera (IRAC) for the Spitzer Space Telescope. *ApJS*, **154**, 10–17.

Flores, H., Hammer, F., Puech, M., Amram, P. & Balkowski, C., 2006. 3D spectroscopy with VLT/GIRAFFE. I. The true Tully Fisher relationship at z $\sim$ 0.6. *A&A*, **455**, 107–118.

Forbes, J. C., Krumholz, M. R., Burkert, A. & Dekel, A., 2014. Balance among gravitational instability, star formation and accretion determines the structure and evolution of disc galaxies. *MNRAS*, **438**, 1552–1576.

Foreman-Mackey, D., Hogg, D. W., Lang, D. & Goodman, J., 2013. emcee: The MCMC Hammer. *PASP*, **125**, 306–312.

Förster Schreiber, N. M., Genzel, R., Bouché, N., Cresci, G., Davies, R. et al., 2009. The SINS Survey: SINFONI Integral Field Spectroscopy of z ˜ 2 Star-forming Galaxies. *ApJ*, **706**, 1364–1428.

Förster Schreiber, N. M., Genzel, R., Eisenhauer, F., Lehnert, M. D., Tacconi, J. J. et al., 2006a. The SINS Survey: Rotation Curves and Dynamical Evolution of Distant Galaxies with SINFONI. *The Messenger*, **125**.

Förster Schreiber, N. M., Genzel, R., Lehnert, M. D., Bouché, N., Verma, A., Erb, D. K., Shapley, A. E., Steidel, C. C., Davies, R., Lutz, D., Nesvadba, N., Tacconi, L. J., Eisenhauer, F., Abuter, R., Gilbert, A., Gillessen, S. & Sternberg, A., 2006b. SINFONI Integral Field Spectroscopy of z ˜ 2 UV-selected Galaxies: Rotation Curves and Dynamical Evolution. *ApJ*, **645**, 1062–1075.

Fouque, P., Bottinelli, L., Gouguenheim, L. & Paturel, G., 1990. The extragalactic distance scale. II - The unbiased distance to the Virgo Cluster from the B-band Tully-Fisher relation. *ApJ*, **349**, 1–21.

Freedman, W. L. & Turner, M. S., 2003. Colloquium: Measuring and understanding the universe. *Reviews of Modern Physics*, **75**, 1433–1447.

Freeman, K. C., 1970. On the Disks of Spiral and S0 Galaxies. *ApJ*, **160**, 811.

Freundlich, J., Combes, F., Tacconi, L. J., Cooper, M. C., Genzel, R. et al., 2013. Towards a resolved Kennicutt-Schmidt law at high redshift. *A&A*, **553**, A130.

Gawiser, E. & MUSYC Collaboration, 2003. MUSYC: A Deep Square-degree UBVRIzJHK Survey of the Formation and Evolution of Galaxies and Their Central Black Holes. In *American Astronomical Society Meeting Abstracts*, vol. 35 of *Bulletin of the American Astronomical Society*, 1249.

Genzel, R., Burkert, A., Bouché, N., Cresci, G., Förster Schreiber, N. M. et al., 2008. From Rings to Bulges: Evidence for Rapid Secular Galaxy Evolution at z ˜ 2 from Integral Field Spectroscopy in the SINS Survey. *ApJ*, **687**, 59–77.

Genzel, R., Newman, S., Jones, T., Förster Schreiber, N. M., Shapiro, K. et al., 2011. The Sins Survey of z ˜ 2 Galaxy Kinematics: Properties of the Giant Star-forming Clumps. *ApJ*, **733**, 101.

Genzel, R., Tacconi, L. J., Eisenhauer, F., Förster Schreiber, N. M., Cimatti, A. et al., 2006. The rapid formation of a large rotating disk galaxy three billion years after the Big Bang. *Nature*, **442**, 786–789.

Genzel, R., Tacconi, L. J., Lutz, D., Saintonge, A., Berta, S. et al., 2015. Combined CO and Dust Scaling Relations of Depletion Time and Molecular Gas Fractions with Cosmic Time, Specific Star-formation Rate, and Stellar Mass. *ApJ*, **800**, 20.

Ginsburg, A. & Mirocha, J., 2011. PySpecKit: Python Spectroscopic Toolkit. Astrophysics Source Code Library.

Giovanelli, R., Haynes, M. P., da Costa, L. N., Freudling, W., Salzer, J. J. & Wegner, G., 1997. The Tully-Fisher Relation and H_0. *ApJ*, **477**, L1–L4.

Giovanelli, R., Haynes, M. P., Kent, B. R., Perillat, P., Saintonge, A. et al., 2005. The Arecibo Legacy Fast ALFA Survey. I. Science Goals, Survey Design, and Strategy. *AJ*, **130**, 2598–2612.

Gnedin, O. Y., Weinberg, D. H., Pizagno, J., Prada, F. & Rix, H.-W., 2007. Dark Matter Halos of Disk Galaxies: Constraints from the Tully-Fisher Relation. *ApJ*, **671**, 1115–1134.

Gnerucci, A., Marconi, A., Cresci, G., Maiolino, R., Mannucci, F., Calura, F., Cimatti, A., Cocchia, F., Grazian, A., Matteucci, F., Nagao, T., Pozzetti, L. & Troncoso, P., 2011. Dynamical properties of AMAZE and LSD galaxies from gas kinematics and the Tully-Fisher relation at z ˜ 3. *A&A*, **528**, A88.

Gwyn, S. D. J., 2011. The CFHT Legacy Survey: stacked images and catalogs. *ArXiv e-prints*.

Haehnelt, M. G., Natarajan, P. & Rees, M. J., 1998. High-redshift galaxies, their active nuclei and central black holes. *MNRAS*, **300**, 817–827.

Hambly, N. C., Collins, R. S., Cross, N. J. G., Mann, R. G., Read, M. A., Sutorius, E. T. W., Bond, I., Bryant, J., Emerson, J. P., Lawrence, A., Rimoldini, L., Stewart, J. M., Williams, P. M., Adamson, A., Hirst, P., Dye, S. & Warren, S. J., 2008. The WFCAM Science Archive. *MNRAS*, **384**, 637–662.

Harrison, C. M., Alexander, D. M., Mullaney, J. R. & Swinbank, A. M., 2014. Kiloparsec-scale outflows are prevalent among luminous AGN: outflows and feedback in the context of the overall AGN population. *MNRAS*, **441**, 3306–3347.

Haynes, M. P., Giovanelli, R., Martin, A. M., Hess, K. M., Saintonge, A. et al., 2011. The Arecibo Legacy Fast ALFA Survey: The α.40 H I Source Catalog, Its Characteristics and Their Impact on the Derivation of the H I Mass Function. *AJ*, **142**, 170.

Hernquist, L., 1989. Tidal triggering of starbursts and nuclear activity in galaxies. *Nature*, **340**, 687–691.

Hinshaw, G., Larson, D., Komatsu, E., Spergel, D. N., Bennett, C. L. et al., 2013. Nine-year Wilkinson Microwave Anisotropy Probe (WMAP) Observations: Cosmological Parameter Results. *ApJS*, **208**, 19.

Holwerda, B. & Blyth, S., 2010. Trumpeting the Vuvuzela: The deepest HI observations with MeerKAT. In *ISKAF2010 Science Meeting*, 68.

Hopkins, A. M. & Beacom, J. F., 2006. On the Normalization of the Cosmic Star Formation History. *ApJ*, **651**, 142–154.

Hopkins, P. F., Quataert, E. & Murray, N., 2012. Stellar feedback in galaxies and the origin of galaxy-scale winds. *MNRAS*, **421**, 3522–3537.

HUBBLE, E. P., 1925. Cepheids in Spiral Nebulae. *Popular Astronomy*, **33**.

HUBBLE, E. P., 1926. Extragalactic nebulae. *ApJ*, **64**.

HUBBLE, E. P., 1936. *Realm of the Nebulae.*

ILBERT, O., ARNOUTS, S., MCCRACKEN, H. J., BOLZONELLA, M., BERTIN, E. ET AL., 2006. Accurate photometric redshifts for the CFHT legacy survey calibrated using the VIMOS VLT deep survey. *A&A*, **457**, 841–856.

JAMES, P. A., BRETHERTON, C. F. & KNAPEN, J. H., 2009. The Hα galaxy survey. VII. The spatial distribution of star formation within disks and bulges. *A&A*, **501**, 207–220.

JOHNSTON, S., TAYLOR, R., BAILES, M., BARTEL, N., BAUGH, C. ET AL., 2008. Science with ASKAP. The Australian square-kilometre-array pathfinder. *Experimental Astronomy*, **22**, 151–273.

JOSEPH, R. D., MEIKLE, W. P. S., ROBERTSON, N. A. & WRIGHT, G. S., 1984. Recent star formation in interacting galaxies. I - Evidence from JHKL photometry. *MNRAS*, **209**, 111–122.

KARIM, A., SCHINNERER, E., MARTÍNEZ-SANSIGRE, A., SARGENT, M. T., VAN DER WEL, A., RIX, H.-W., ILBERT, O., SMOLČIĆ, V., CARILLI, C., PANNELLA, M., KOEKEMOER, A. M., BELL, E. F. & SALVATO, M., 2011. The Star Formation History of Mass-selected Galaxies in the COSMOS Field. *ApJ*, **730**, 61.

KASSIN, S. A., WEINER, B. J., FABER, S. M., KOO, D. C. & LOTZ, J. M., 2007a. The Stellar Mass Tully-Fisher Relation to z=1.2. In J. Afonso, H. C. Ferguson, B. Mobasher & R. Norris, eds., *Deepest Astronomical Surveys*, vol. 380 of *Astronomical Society of the Pacific Conference Series*, 477.

KASSIN, S. A., WEINER, B. J., FABER, S. M., KOO, D. C., LOTZ, J. M., DIEMAND, J., HARKER, J. J., BUNDY, K., METEVIER, A. J., PHILLIPS, A. C., COOPER, M. C., CROTON, D. J., KONIDARIS, N., NOESKE, K. G. & WILLMER, C. N. A., 2007b. The Stellar Mass Tully-Fisher Relation to z = 1.2 from AEGIS. *ApJ*, **660**, L35–L38.

Katz, N., Keres, D., Dave, R. & Weinberg, D. H., 2003. How Do Galaxies Get Their Gas? In J. L. Rosenberg & M. E. Putman, eds., *The IGM/Galaxy Connection. The Distribution of Baryons at z=0*, vol. 281 of *Astrophysics and Space Science Library*, 185.

Kauffmann, G., Heckman, T. M., Tremonti, C., Brinchmann, J., Charlot, S., White, S. D. M., Ridgway, S. E., Brinkmann, J., Fukugita, M., Hall, P. B., Ivezić, Ž., Richards, G. T. & Schneider, D. P., 2003. The host galaxies of active galactic nuclei. *MNRAS*, **346**, 1055–1077.

Kawata, D. & Mulchaey, J. S., 2008. Strangulation in Galaxy Groups. *ApJ*, **672**, L103.

Kennicutt, Jr., R. C., 1983. The rate of star formation in normal disk galaxies. *ApJ*, **272**, 54–67.

Kennicutt, Jr., R. C., 1998. Star Formation in Galaxies Along the Hubble Sequence. *ARA&A*, **36**, 189–232.

Kent, S. M., 1986. Dark matter in spiral galaxies. I - Galaxies with optical rotation curves. *AJ*, **91**, 1301–1327.

Kereš, D., Katz, N., Fardal, M., Davé, R. & Weinberg, D. H., 2009. Galaxies in a simulated ΛCDM Universe - I. Cold mode and hot cores. *MNRAS*, **395**, 160–179.

Kereš, D., Katz, N., Weinberg, D. H. & Davé, R., 2005. How do galaxies get their gas? *MNRAS*, **363**, 2–28.

Kewley, L. J., Dopita, M. A., Sutherland, R. S., Heisler, C. A. & Trevena, J., 2001. Theoretical Modeling of Starburst Galaxies. *ApJ*, **556**, 121–140.

Khochfar, S., Emsellem, E., Serra, P., Bois, M., Alatalo, K. et al., 2011. The ATLAS^{3D} project - VIII. Modelling the formation and evolution of fast and slow rotator early-type galaxies within ΛCDM. *MNRAS*, **417**, 845–862.

Kim, J.-W., Edge, A. C., Wake, D. A. & Stott, J. P., 2011. Clustering properties of high-redshift red galaxies in SA22 from the UKIDSS Deep eXtragalactic Survey. *MNRAS*, **410**, 241–256.

Krajnović, D., Cappellari, M., de Zeeuw, P. T. & Copin, Y., 2006. Kinemetry: a generalization of photometry to the higher moments of the line-of-sight velocity distribution. *MNRAS*, **366**, 787–802.

Kroupa, P., 2001. On the variation of the initial mass function. *MNRAS*, **322**, 231–246.

Lagattuta, D. J., Mould, J. R., Staveley-Smith, L., Hong, T., Springob, C. M., Masters, K. L., Koribalski, B. S. & Jones, D. H., 2013. WISE TF: A Mid-infrared, 3.4 μm Extension of the Tully-Fisher Relation Using WISE Photometry. *ApJ*, **771**, 88.

Lavezzi, T. E. & Dickey, J. M., 1997. Recovering Galaxy Rotation Speeds from Irregular Emission Profiles. *AJ*, **114**, 2437.

Lavezzi, T. E. & Dickey, J. M., 1998. The Interchangeability of CO and H I in the Tully-Fisher Relation. *AJ*, **116**, 2672–2681.

Lavezzi, T. E. & Dickey, J. M., 1999. ^{12}CO(1-0) Line Widths as Tully-Fisher Observables. In C. L. Carilli, S. J. E. Radford, K. M. Menten & G. I. Langston, eds., *Highly Redshifted Radio Lines*, vol. 156 of *Astronomical Society of the Pacific Conference Series*, 80.

Lawrence, A., Warren, S. J., Almaini, O., Edge, A. C., Hambly, N. C. et al., 2007. The UKIRT Infrared Deep Sky Survey (UKIDSS). *MNRAS*, **379**, 1599–1617.

Lilly, S. J., Le Fevre, O., Hammer, F. & Crampton, D., 1996. The Canada-France Redshift Survey: The Luminosity Density and Star Formation History of the Universe to Z approximately 1. *ApJ*, **460**, L1.

Lin, C. C. & Shu, F. H., 1964. On the Spiral Structure of Disk Galaxies. *ApJ*, **140**, 646.

Lintott, C., Schawinski, K., Bamford, S., Slosar, A., Land, K., Thomas, D., Edmondson, E., Masters, K., Nichol, R. C., Raddick, M. J., Szalay, A., Andreescu, D., Murray, P. & Vandenberg, J., 2011. Galaxy Zoo 1: data release of morphological classifications for nearly 900 000 galaxies. *MNRAS*, **410**, 166–178.

Lintott, C. J., Schawinski, K., Slosar, A., Land, K., Bamford, S., Thomas, D., Raddick, M. J., Nichol, R. C., Szalay, A., Andreescu, D., Murray, P. & Vandenberg, J., 2008. Galaxy Zoo: morphologies derived from visual inspection of galaxies from the Sloan Digital Sky Survey. *MNRAS*, **389**, 1179–1189.

Lonsdale, C. J., Farrah, D. & Smith, H. E., 2006. *Ultraluminous Infrared Galaxies*, 285.

Madau, P. & Dickinson, M., 2014. Cosmic Star-Formation History. *ARA&A*, **52**, 415–486.

Madau, P., Ferguson, H. C., Dickinson, M. E., Giavalisco, M., Steidel, C. C. & Fruchter, A., 1996. High-redshift galaxies in the Hubble Deep Field: colour selection and star formation history to z˜4. *MNRAS*, **283**, 1388–1404.

Madau, P., Pozzetti, L. & Dickinson, M., 1998. The Star Formation History of Field Galaxies. *ApJ*, **498**, 106–116.

Magdis, G. E., Daddi, E., Sargent, M., Elbaz, D., Gobat, R., Dannerbauer, H., Feruglio, C., Tan, Q., Rigopoulou, D., Charmandaris, V., Dickinson, M., Reddy, N. & Aussel, H., 2012. The Molecular Gas Content of $z = 3$ Lyman Break Galaxies: Evidence of a Non-evolving Gas Fraction in Main-sequence Galaxies at $z > 2$. *ApJ*, **758**, L9.

Magnelli, B., Saintonge, A., Lutz, D., Tacconi, L. J., Berta, S. et al., 2012. Dust temperature and CO $\rightarrow$ H_2 conversion factor variations in the SFR-M_* plane. *A&A*, **548**, A22.

Maier, C., Kuchner, U., Ziegler, B. L., Verdugo, M., Balestra, I., Girardi, M., Mercurio, A., Rosati, P., Fritz, A., Grillo, C., Nonino, M. & Sartoris, B., 2016. CLASH-VLT: Strangulation of cluster galaxies in MACS J0416.1-2403 as seen from their chemical enrichment. *A&A*, **590**, A108.

Maiolino, R., Nagao, T., Grazian, A., Cocchia, F., Marconi, A., Mannucci, F., Cimatti, A., Pipino, A., Fontana, A., Granato, G. L., Matteucci, F., Pentericci, L., Risaliti, G., Salvati, M. & Silva, L., 2008a. The Mass-Metallicity Relation at z>3. In J. G. Funes & E. M. Corsini, eds., *Formation and Evolution of Galaxy Disks*, vol. 396 of *Astronomical Society of the Pacific Conference Series*, 409.

Maiolino, R., Nagao, T., Grazian, A., Cocchia, F., Marconi, A. et al., 2008b. AMAZE. I. The evolution of the mass-metallicity relation at z $>$ 3. *A&A*, **488**, 463–479.

Maloney, P. & Black, J. H., 1988. I(CO)/N(H2) conversions and molecular gas abundances in spiral and irregular galaxies. *ApJ*, **325**, 389–401.

Mannucci, F., Cresci, G., Maiolino, R., Marconi, A., Pastorini, G., Pozzetti, L., Gnerucci, A., Risaliti, G., Schneider, R., Lehnert, M. & Salvati, M., 2009. LSD: Lyman-break galaxies Stellar populations and Dynamics - I. Mass, metallicity and gas at z ˜ 3.1. *MNRAS*, **398**, 1915–1931.

Mannucci, F. & Maiolino, R., 2008. LSD and AMAZE: the mass-metallicity relation at z $>$ 3. In L. K. Hunt, S. C. Madden & R. Schneider, eds., *Low-Metallicity Star Formation: From the First Stars to Dwarf Galaxies*, vol. 255 of *IAU Symposium*, 106–110.

Markwardt, C. B., 2009. Non-linear Least-squares Fitting in IDL with MPFIT. In D. A. Bohlender, D. Durand & P. Dowler, eds., *Astronomical Data Analysis Software and Systems XVIII*, vol. 411 of *Astronomical Society of the Pacific Conference Series*, 251.

Martig, M., Bournaud, F., Teyssier, R. & Dekel, A., 2009. Morphological Quenching of Star Formation: Making Early-Type Galaxies Red. *ApJ*, **707**, 250–267.

Martin, D. C., Fanson, J., Schiminovich, D., Morrissey, P., Friedman, P. G. et al., 2005. The Galaxy Evolution Explorer: A Space Ultraviolet Survey Mission. *ApJ*, **619**, L1–L6.

Martin, D. C., Wyder, T. K., Schiminovich, D., Barlow, T. A., Forster, K. et al., 2007. The UV-Optical Galaxy Color-Magnitude Diagram. III. Constraints on Evolution from the Blue to the Red Sequence. *ApJS*, **173**, 342–356.

Masters, K. L., Springob, C. M. & Huchra, J. P., 2008. 2MTF. I. The Tully-Fisher Relation in the Two Micron All Sky Survey J, H, and K Bands. *AJ*, **135**, 1738–1748.

Mathewson, D. S., Ford, V. L. & Buchhorn, M., 1992. A southern sky survey of the peculiar velocities of 1355 spiral galaxies. *ApJS*, **81**, 413–659.

McAlpine, S., Helly, J. C., Schaller, M., Trayford, J. W., Qu, Y. et al., 2015. The EAGLE simulations of galaxy formation: public release of halo and galaxy catalogues. *ArXiv e-prints*.

McGaugh, S. S., 2012. The Baryonic Tully-Fisher Relation of Gas-rich Galaxies as a Test of ΛCDM and MOND. *AJ*, **143**, 40.

McGaugh, S. S., Schombert, J. M., Bothun, G. D. & de Blok, W. J. G., 2000. The Baryonic Tully-Fisher Relation. *ApJ*, **533**, L99–L102.

Mendez, A. J., Coil, A. L., Lotz, J., Salim, S., Moustakas, J. & Simard, L., 2011. AEGIS: The Morphologies of Green Galaxies at $0.4 < z < 1.2$. *ApJ*, **736**, 110.

Meyer, M., 2009. Exploring the HI Universe with ASKAP. In *Panoramic Radio Astronomy: Wide-field 1-2 GHz Research on Galaxy Evolution*, 15.

Meyer, M. J., Zwaan, M. A., Webster, R. L., Schneider, S. & Staveley-Smith, L., 2008. Tully-Fisher relations from an HI-selected sample. *MNRAS*, **391**, 1712–1728.

Miller, S. H., Bundy, K., Sullivan, M., Ellis, R. S. & Treu, T., 2011. The Assembly History of Disk Galaxies. I. The Tully-Fisher Relation to z ˜= 1.3 from Deep Exposures with DEIMOS. *ApJ*, **741**, 115.

Miller, S. H., Ellis, R. S., Sullivan, M., Bundy, K., Newman, A. B. & Treu, T., 2012. The Assembly History of Disk Galaxies. II. Probing the Emerging Tully-Fisher Relation during 1 ¡ z ¡ 1.7. *ApJ*, **753**, 74.

Morganti, R., de Zeeuw, P. T., Oosterloo, T. A., McDermid, R. M., Krajnović, D., Cappellari, M., Kenn, F., Weijmans, A. & Sarzi, M., 2006. Neutral hydrogen in nearby elliptical and lenticular galaxies: the continuing formation of early-type galaxies. *MNRAS*, **371**, 157–169.

Morrissey, P., Schiminovich, D., Barlow, T. A., Martin, D. C., Blakkolb, B. et al., 2005. The On-Orbit Performance of the Galaxy Evolution Explorer. *ApJ*, **619**, L7–L10.

Muzzin, A., Marchesini, D., Stefanon, M., Franx, M., Milvang-Jensen, B., Dunlop, J. S., Fynbo, J. P. U., Brammer, G., Labbé, I. & van Dokkum, P., 2013. A Public K_s -selected Catalog in the COSMOS/ULTRAVISTA Field: Photometry, Photometric Redshifts, and Stellar Population Parameters. *ApJS*, **206**, 8.

Naab, T., Oser, L., Emsellem, E., Cappellari, M., Krajnović, D. et al., 2014. The ATLAS^{3D} project - XXV. Two-dimensional kinematic analysis of simulated galaxies and the cosmological origin of fast and slow rotators. *MNRAS*, **444**, 3357–3387.

Navarro, J. F., Frenk, C. S. & White, S. D. M., 1997. A Universal Density Profile from Hierarchical Clustering. *ApJ*, **490**, 493–508.

Nelson, E. J., van Dokkum, P. G., Brammer, G., Förster Schreiber, N., Franx, M., Fumagalli, M., Patel, S., Rix, H.-W., Skelton, R. E., Bezanson, R., Da Cunha, E., Kriek, M., Labbe, I., Lundgren, B., Quadri, R. & Schmidt, K. B., 2012. Spatially Resolved Hα Maps and Sizes of 57 Strongly Star-forming Galaxies at z ˜ 1 from 3D-HST: Evidence for Rapid Inside-out Assembly of Disk Galaxies. *ApJ*, **747**, L28.

Noguchi, M., 1999. Early Evolution of Disk Galaxies: Formation of Bulges in Clumpy Young Galactic Disks. *ApJ*, **514**, 77–95.

Obreschkow, D., Croton, D., De Lucia, G., Khochfar, S. & Rawlings, S., 2009a. Simulation of the Cosmic Evolution of Atomic and Molecular Hydrogen in Galaxies. *ApJ*, **698**, 1467–1484.

Obreschkow, D., Klöckner, H.-R., Heywood, I., Levrier, F. & Rawlings, S., 2009b. A Virtual Sky with Extragalactic H I and CO Lines for the Square Kilometre Array and the Atacama Large Millimeter/Submillimeter Array. *ApJ*, **703**, 1890–1903.

Oke, J. B., Cohen, J. G., Carr, M., Cromer, J., Dingizian, A., Harris, F. H., Labrecque, S., Lucinio, R., Schaal, W., Epps, H. & Miller, J., 1995. The Keck Low-Resolution Imaging Spectrometer. *PASP*, **107**, 375.

Papovich, C., Finkelstein, S. L., Ferguson, H. C., Lotz, J. M. & Giavalisco, M., 2011. The rising star formation histories of distant galaxies and implications for gas accretion with time. *MNRAS*, **412**, 1123–1136.

Parry, I. R., Mackay, C. D., Johnson, R. A., McMahon, R. G., Dean, A., Ramaprakash, A. N., King, D. L., Pritchard, J. M., Medlen, S. R., Sabbey, C. S., Ellis, R. S. & Aragon-Salamanca, A., 2000. CIRPASS: a NIR integral field and multi-object spectrograph. In M. Iye & A. F. Moorwood, eds., *Optical and IR Telescope Instrumentation and Detectors*, vol. 4008 of *Society of Photo-Optical Instrumentation Engineers (SPIE) Conference Series*, 1193–1202.

Pasquini, L., Avila, G., Blecha, A., Cacciari, C., Cayatte, V. et al., 2002. Installation and commissioning of FLAMES, the VLT Multifibre Facility. *The Messenger*, **110**, 1–9.

Peng, Y., Maiolino, R. & Cochrane, R., 2015. Strangulation as the primary mechanism for shutting down star formation in galaxies. *Nature*, **521**, 192–195.

Pérez-González, P. G., Rieke, G. H., Villar, V., Barro, G., Blaylock, M., Egami, E., Gallego, J., Gil de Paz, A., Pascual, S., Zamorano, J. & Donley, J. L., 2008. The Stellar Mass Assembly of Galaxies from z = 0 to z = 4: Analysis of a Sample Selected in the Rest-Frame Near-Infrared with Spitzer. *ApJ*, **675**, 234–261.

Pilbratt, G. L., Riedinger, J. R., Passvogel, T., Crone, G., Doyle, D., Gageur, U., Heras, A. M., Jewell, C., Metcalfe, L., Ott, S. & Schmidt, M., 2010. Herschel Space Observatory. An ESA facility for far-infrared and submillimetre astronomy. *A&A*, **518**, L1.

Pizagno, J., Prada, F., Weinberg, D. H., Rix, H.-W., Harbeck, D., Grebel, E. K., Bell, E. F., Brinkmann, J., Holtzman, J. & West, A., 2005. Dark Matter and Stellar Mass in the Luminous Regions of Disk Galaxies. *ApJ*, **633**, 844–856.

Pizagno, J., Prada, F., Weinberg, D. H., Rix, H.-W., Pogge, R. W., Grebel, E. K., Harbeck, D., Blanton, M., Brinkmann, J. & Gunn, J. E., 2007. The Tully-Fisher Relation and its Residuals for a Broadly Selected Sample of Galaxies. *AJ*, **134**, 945–972.

Postman, M., Coe, D., Benítez, N., Bradley, L., Broadhurst, T. et al., 2012. The Cluster Lensing and Supernova Survey with Hubble: An Overview. *ApJS*, **199**, 25.

Puech, M., Flores, H., Hammer, F., Yang, Y., Neichel, B. et al., 2008. IMAGES. III. The evolution of the near-infrared Tully-Fisher relation over the last 6 Gyr. *A&A*, **484**, 173–187.

Puget, P., Stadler, E., Doyon, R., Gigan, P., Thibault, S. et al., 2004. WIRCam: the infrared wide-field camera for the Canada-France-Hawaii Telescope. In A. F. M. Moorwood & M. Iye, eds., *Ground-based Instrumentation for Astronomy*, vol. 5492 of *Proc. SPIE*, 978–987.

Reyes, R., Mandelbaum, R., Gunn, J. E., Pizagno, J. & Lackner, C. N., 2011. Calibrated Tully-Fisher relations for improved estimates of disc rotation velocities. *MNRAS*, **417**, 2347–2386.

Rhee, M.-H., 2004. Mass-to-Light Ratio and the Tully-Fisher Relation. *Journal of Korean Astronomical Society*, **37**, 91–117.

Rhee, M.-H. & Broeils, A. H., 2005. HI Linewidths, Rotation Velocities and the Tully-Fisher Relation. *Journal of Astronomy and Space Sciences*, **22**.

Riechers, D. A., Walter, F., Bertoldi, F., Carilli, C. L., Aravena, M., Neri, R., Cox, P., Weiss, A. & Menten, K. M., 2009. Imaging Atomic and Highly Excited

Molecular Gas in a z = 6.42 Quasar Host Galaxy: Copious Fuel for an Eddington-limited Starburst at the End of Cosmic Reionization. *ApJ*, **703**, 1338–1345.

Riechers, D. A., Walter, F., Brewer, B. J., Carilli, C. L., Lewis, G. F., Bertoldi, F. & Cox, P., 2008a. A Molecular Einstein Ring at z = 4.12: Imaging the Dynamics of a Quasar Host Galaxy Through a Cosmic Lens. *ApJ*, **686**, 851–858.

Riechers, D. A., Walter, F., Carilli, C. L., Bertoldi, F. & Momjian, E., 2008b. Formation of a Quasar Host Galaxy through a Wet Merger 1.4 Billion Years after the Big Bang. *ApJ*, **686**, L9–L12.

Saintonge, A., 2007. The Arecibo Legacy Fast ALFA Survey. IV. Strategies for Signal Identification and Survey Catalog Reliability. *AJ*, **133**, 2087–2096.

Saintonge, A., Kauffmann, G., Kramer, C., Tacconi, L. J., Buchbender, C. et al., 2011. COLD GASS, an IRAM legacy survey of molecular gas in massive galaxies - I. Relations between H_2, H I, stellar content and structural properties. *MNRAS*, **415**, 32–60.

Saintonge, A. & Spekkens, K., 2011. Disk Galaxy Scaling Relations in the SFI++: Intrinsic Scatter and Applications. *ApJ*, **726**, 77.

Sakai, S., Mould, J. R., Hughes, S. M. G., Huchra, J. P., Macri, L. M. et al., 2000. The Hubble Space Telescope Key Project on the Extragalactic Distance Scale. XXIV. The Calibration of Tully-Fisher Relations and the Value of the Hubble Constant. *ApJ*, **529**, 698–722.

Salim, S., Rich, R. M., Charlot, S., Brinchmann, J., Johnson, B. D. et al., 2007a. UV Star Formation Rates in the Local Universe. *ApJS*, **173**, 267–292.

Salim, S., Rich, R. M., Charlot, S., Brinchmann, J., Johnson, B. D. et al., 2007b. UV Star Formation Rates in the Local Universe. *ApJS*, **173**, 267–292.

Salpeter, E. E., 1955. The Luminosity Function and Stellar Evolution. *ApJ*, **121**, 161.

Sánchez, S. F., Kennicutt, R. C., Gil de Paz, A., van de Ven, G., Vílchez, J. M. et al., 2012. CALIFA, the Calar Alto Legacy Integral Field Area survey. I. Survey presentation. *A&A*, **538**, A8.

Sánchez Almeida, J., Elmegreen, B. G., Muñoz-Tuñón, C. & Elmegreen, D. M., 2014. Star formation sustained by gas accretion. *A&A Rev.*, **22**, 71.

Sancisi, R., Fraternali, F., Oosterloo, T. & van der Hulst, T., 2008. Cold gas accretion in galaxies. *A&A Rev.*, **15**, 189–223.

Sandage, A., 1988. A case for H0 = 42 and Omega(0) = 1 using luminous spiral galaxies and the cosmological time scale test. *ApJ*, **331**, 583–604.

Sandage, A. & Tammann, G. A., 1976. Steps toward the Hubble constant. VII - Distances to NGC 2403, M101, and the Virgo cluster using 21 centimeter line widths compared with optical methods: The global value of H sub 0. *ApJ*, **210**, 7–24.

Sarzi, M., Falcón-Barroso, J., Davies, R. L., Bacon, R., Bureau, M., Cappellari, M., de Zeeuw, P. T., Emsellem, E., Fathi, K., Krajnović, D., Kuntschner, H., McDermid, R. M. & Peletier, R. F., 2006. The SAURON project - V. Integral-field emission-line kinematics of 48 elliptical and lenticular galaxies. *MNRAS*, **366**, 1151–1200.

Schawinski, K., Thomas, D., Sarzi, M., Maraston, C., Kaviraj, S., Joo, S.-J., Yi, S. K. & Silk, J., 2007. Observational evidence for AGN feedback in early-type galaxies. *MNRAS*, **382**, 1415–1431.

Schaye, J., Crain, R. A., Bower, R. G., Furlong, M., Schaller, M. et al., 2015. The EAGLE project: simulating the evolution and assembly of galaxies and their environments. *MNRAS*, **446**, 521–554.

Schechter, P. L., 1980. Mass-to-light ratios for elliptical galaxies. *AJ*, **85**, 801–811.

Schlafly, E. F. & Finkbeiner, D. P., 2011. Measuring Reddening with Sloan Digital Sky Survey Stellar Spectra and Recalibrating SFD. *ApJ*, **737**, 103.

SCOVILLE, N., 2007. The Cosmic Evolution Survey: COSMOS. In A. J. Baker, J. Glenn, A. I. Harris, J. G. Mangum & M. S. Yun, eds., *From Z-Machines to ALMA: (Sub)Millimeter Spectroscopy of Galaxies*, vol. 375 of *Astronomical Society of the Pacific Conference Series*, 166.

SELLWOOD, J. A. & CARLBERG, R. G., 1984. Spiral instabilities provoked by accretion and star formation. *ApJ*, **282**, 61–74.

SERRA, P., OOSTERLOO, T., MORGANTI, R., ALATALO, K., BLITZ, L. ET AL., 2012. The ATLAS^{3D} project - XIII. Mass and morphology of H I in early-type galaxies as a function of environment. *MNRAS*, **422**, 1835–1862.

SÉRSIC, J. L., 1963. Influence of the atmospheric and instrumental dispersion on the brightness distribution in a galaxy. *Boletin de la Asociacion Argentina de Astronomia La Plata Argentina*, **6**, 41.

SHAPIRO, K. L., GENZEL, R., FÖRSTER SCHREIBER, N. M., TACCONI, L. J., BOUCHÉ, N. ET AL., 2008. Kinemetry of SINS High-Redshift Star-Forming Galaxies: Distinguishing Rotating Disks from Major Mergers. *ApJ*, **682**, 231–251.

SHARP, R., ALLEN, J. T., FOGARTY, L. M. R., CROOM, S. M., CORTESE, L. ET AL., 2015. The SAMI Galaxy Survey: cubism and covariance, putting round pegs into square holes. *MNRAS*, **446**, 1551–1566.

SHARPLES, R., BENDER, R., AGUDO BERBEL, A., BEZAWADA, N., CASTILLO, R. ET AL., 2013. First Light for the KMOS Multi-Object Integral-Field Spectrometer. *The Messenger*, **151**, 21–23.

SHEN, S., MO, H. J., WHITE, S. D. M., BLANTON, M. R., KAUFFMANN, G., VOGES, W., BRINKMANN, J. & CSABAI, I., 2003. The size distribution of galaxies in the Sloan Digital Sky Survey. *MNRAS*, **343**, 978–994.

SILK, J. & REES, M. J., 1998. Quasars and galaxy formation. *A&A*, **331**, L1–L4.

SIMPSON, J. M., SWINBANK, A. M., SMAIL, I., ALEXANDER, D. M., BRANDT, W. N. ET AL., 2014. An ALMA Survey of Submillimeter Galaxies in the Extended Chandra

Deep Field South: The Redshift Distribution and Evolution of Submillimeter Galaxies. *ApJ*, **788**, 125.

Skrutskie, M. F., Cutri, R. M., Stiening, R., Weinberg, M. D., Schneider, S. et al., 2006. The Two Micron All Sky Survey (2MASS). *AJ*, **131**, 1163–1183.

Smethurst, R. J., Lintott, C. J., Simmons, B. D., Schawinski, K., Marshall, P. J., Bamford, S., Fortson, L., Kaviraj, S., Masters, K. L., Melvin, T., Nichol, R. C., Skibba, R. A. & Willett, K. W., 2015. Galaxy Zoo: evidence for diverse star formation histories through the green valley. *MNRAS*, **450**, 435–453.

Smith, J. K., Bunker, A. J., Vogt, N. P., Abraham, R. G., Aragón-Salamanca, A., Bower, R. G., Parry, I. R., Sharp, R. S. & Swinbank, A. M., 2004. Hα kinematics of a z˜ 1 disc galaxy from near-infrared integral field spectroscopy. *MNRAS*, **354**, L19–L23.

Sobral, D., Best, P. N., Smail, I., Mobasher, B., Stott, J. & Nisbet, D., 2014. The stellar mass function of star-forming galaxies and the mass-dependent SFR function since z = 2.23 from HiZELS. *MNRAS*, **437**, 3516–3528.

Sobral, D., Matthee, J., Best, P. N., Smail, I., Khostovan, A. A., Milvang-Jensen, B., Kim, J.-W., Stott, J., Calhau, J., Nayyeri, H. & Mobasher, B., 2015. CF-HiZELS, an $\tilde{1}0$ deg^2 emission-line survey with spectroscopic follow-up: Hα, [O III] + Hβ and [O II] luminosity functions at z = 0.8, 1.4 and 2.2. *MNRAS*, **451**, 2303–2323.

Sobral, D., Swinbank, A. M., Stott, J. P., Matthee, J., Bower, R. G., Smail, I., Best, P., Geach, J. E. & Sharples, R. M., 2013. The Dynamics of z = 0.8 Hα-selected Star-forming Galaxies from KMOS/CF-HiZELS. *ApJ*, **779**, 139.

Sofue, Y. & Rubin, V., 2001. Rotation Curves of Spiral Galaxies. *ARA&A*, **39**, 137–174.

Sorce, J. G., Courtois, H. M., Tully, R. B., Seibert, M., Scowcroft, V., Freedman, W. L., Madore, B. F., Persson, S. E., Monson, A. & Rigby, J., 2013. Calibration of the Mid-infrared Tully-Fisher Relation. *ApJ*, **765**, 94.

SPEAGLE, J. S., STEINHARDT, C. L., CAPAK, P. L. & SILVERMAN, J. D., 2014. A Highly Consistent Framework for the Evolution of the Star-Forming "Main Sequence" from z ˜ 0-6. *ApJS*, **214**, 15.

SPRAYBERRY, D., BERNSTEIN, G. M., IMPEY, C. D. & BOTHUN, G. D., 1995. The mass-to-light ratios of low surface brightness spiral galaxies: Clues from the Tully-Fisher relation. *ApJ*, **438**, 72–82.

SPRINGOB, C. M., HAYNES, M. P., GIOVANELLI, R. & KENT, B. R., 2005. A Digital Archive of H I 21 Centimeter Line Spectra of Optically Targeted Galaxies. *ApJS*, **160**, 149–162.

STARK, D. V., MCGAUGH, S. S. & SWATERS, R. A., 2009. A First Attempt to Calibrate the Baryonic Tully-Fisher Relation with Gas-Dominated Galaxies. *AJ*, **138**, 392–401.

STEINMETZ, M. & NAVARRO, J. F., 1999. The Cosmological Origin of the Tully-Fisher Relation. *ApJ*, **513**, 555–560.

STOTT, J. P., SOBRAL, D., SWINBANK, A. M., SMAIL, I., BOWER, R., BEST, P. N., SHARPLES, R. M., GEACH, J. E. & MATTHEE, J., 2014. A relationship between specific star formation rate and metallicity gradient within z $\sim$ 1 galaxies from KMOS-HiZELS. *MNRAS*, **443**, 2695–2704.

STOTT, J. P., SWINBANK, A. M., JOHNSON, H. L., TILEY, A., MAGDIS, G., BOWER, R., BUNKER, A. J., BUREAU, M., HARRISON, C. M., JARVIS, M. J., SHARPLES, R., SMAIL, I., SOBRAL, D., BEST, P. & CIRASUOLO, M., 2016. The KMOS Redshift One Spectroscopic Survey (KROSS): dynamical properties, gas and dark matter fractions of typical z $\sim$ 1 star-forming galaxies. *MNRAS*, **457**, 1888–1904.

STOUGHTON, C., LUPTON, R. H., BERNARDI, M., BLANTON, M. R., BURLES, S. ET AL., 2002. Sloan Digital Sky Survey: Early Data Release. *AJ*, **123**, 485–548.

STRATEVA, I., IVEZIĆ, Ž., KNAPP, G. R., NARAYANAN, V. K., STRAUSS, M. A. ET AL., 2001. Color Separation of Galaxy Types in the Sloan Digital Sky Survey Imaging Data. *AJ*, **122**, 1861–1874.

Strickland, D. K., Heckman, T. M., Colbert, E. J. M., Hoopes, C. G. & Weaver, K. A., 2004. A High Spatial Resolution X-Ray and Hα Study of Hot Gas in the Halos of Star-forming Disk Galaxies. II. Quantifying Supernova Feedback. *ApJ*, **606**, 829–852.

Sutherland, W., Emerson, J., Dalton, G., Atad-Ettedgui, E., Beard, S. et al., 2015. The Visible and Infrared Survey Telescope for Astronomy (VISTA): Design, technical overview, and performance. *A&A*, **575**, A25.

Swinbank, A. M., Smail, I., Sobral, D., Theuns, T., Best, P. N. & Geach, J. E., 2012a. The Properties of the Star-forming Interstellar Medium at z = 0.8-2.2 from HiZELS: Star Formation and Clump Scaling Laws in Gas-rich, Turbulent Disks. *ApJ*, **760**, 130.

Swinbank, A. M., Sobral, D., Smail, I., Geach, J. E., Best, P. N., McCarthy, I. G., Crain, R. A. & Theuns, T., 2012b. The properties of the star-forming interstellar medium at z = 0.84-2.23 from HiZELS: mapping the internal dynamics and metallicity gradients in high-redshift disc galaxies. *MNRAS*, **426**, 935–950.

Tacconi, L. J., Genzel, R., Neri, R., Cox, P., Cooper, M. C. et al., 2010. High molecular gas fractions in normal massive star-forming galaxies in the young Universe. *Nature*, **463**, 781–784.

Tacconi, L. J., Neri, R., Genzel, R., Combes, F., Bolatto, A. et al., 2013. Phibss: Molecular Gas Content and Scaling Relations in z ˜ 1-3 Massive, Main-sequence Star-forming Galaxies. *ApJ*, **768**, 74.

Teerikorpi, P., 1987. Cluster population incompleteness bias and distances from the Tully-Fisher relation - Theory and numerical examples. *A&A*, **173**, 39–42.

Teyssier, R., Chapon, D. & Bournaud, F., 2010. The Driving Mechanism of Starbursts in Galaxy Mergers. *ApJ*, **720**, L149–L154.

Toomre, A., 1964. On the gravitational stability of a disk of stars. *ApJ*, **139**, 1217–1238.

Tully, R. B. & Courtois, H. M., 2012. Cosmicflows-2: I-band Luminosity-H I Linewidth Calibration. *ApJ*, **749**, 78.

TULLY, R. B. & FISHER, J. R., 1977. A new method of determining distances to galaxies. *A&A*, **54**, 661–673.

TULLY, R. B. & PIERCE, M. J., 2000. Distances to Galaxies from the Correlation between Luminosities and Line Widths. III. Cluster Template and Global Measurement of H_0. *ApJ*, **533**, 744–780.

TURNER, J. L., BECK, S. C., BENFORD, D. J., CONSIGLIO, S. M., HO, P. T. P., KOVÁCS, A., MEIER, D. S. & ZHAO, J.-H., 2015. Highly efficient star formation in NGC 5253 possibly from stream-fed accretion. *Nature*, **519**, 331–333.

TUTUI, Y., SOFUE, Y., HONMA, M., ICHIKAWA, T. & WAKAMATSU, K.-I., 2001. Hubble Constant at Intermediate Redshift Using the CO-Line Tully-Fisher Relation. *PASJ*, **53**, 701–712.

VAN DEN BOSCH, F. C., 2000. Semianalytical Models for the Formation of Disk Galaxies. I. Constraints from the Tully-Fisher Relation. *ApJ*, **530**, 177–192.

VAN DOKKUM, P. G., BRAMMER, G., FUMAGALLI, M., NELSON, E., FRANX, M. ET AL., 2011. First Results from the 3D-HST Survey: The Striking Diversity of Massive Galaxies at $z > 1$. *ApJ*, **743**, L15.

VERHEIJEN, M. A. W., 2001. The Ursa Major Cluster of Galaxies. V. H I Rotation Curve Shapes and the Tully-Fisher Relations. *ApJ*, **563**, 694–715.

WAGG, J., CARILLI, C. L., ARAVENA, M., COX, P., LENTATI, L., MAIOLINO, R., MCMAHON, R. G., RIECHERS, D., WALTER, F., ANDREANI, P., HILLS, R. & WOLFE, A., 2014. Karl G. Jansky Very Large Array Observations of Cold Dust and Molecular Gas in Starbursting Quasar Host Galaxies at z ˜ 4.5. *ApJ*, **783**, 71.

WALTER, F., CARILLI, C., BERTOLDI, F., MENTEN, K., COX, P., LO, K. Y., FAN, X. & STRAUSS, M. A., 2004. Resolved Molecular Gas in a Quasar Host Galaxy at Redshift $z=6.42$. *ApJ*, **615**, L17–L20.

WANG, B. & SILK, J., 1994. Gravitational instability and disk star formation. *ApJ*, **427**, 759–769.

WANG, R., WAGG, J., CARILLI, C. L., NERI, R., WALTER, F., OMONT, A., RIECHERS, D. A., BERTOLDI, F., MENTEN, K. M., COX, P., STRAUSS, M. A., FAN, X. & JIANG, L., 2011. Far-infrared and Molecular CO Emission from the Host Galaxies of Faint Quasars at z ~ 6. *AJ*, **142**, 101.

WESTMEIER, T., JUREK, R., OBRESCHKOW, D., KORIBALSKI, B. S. & STAVELEY-SMITH, L., 2014. The busy function: a new analytic function for describing the integrated 21-cm spectral profile of galaxies. *MNRAS*, **438**, 1176–1190.

WIKLIND, T., COMBES, F., HENKEL, C. & WYROWSKI, F., 1997. Molecular gas in the elliptical galaxy NGC 759. Interferometric CO observations. *A&A*, **323**, 727–738.

WILLIAMS, M. J., BUREAU, M. & CAPPELLARI, M., 2010. The Tully-Fisher relations of early-type spiral and S0 galaxies. *MNRAS*, **409**, 1330–1346.

WILLIAMS, R. J., QUADRI, R. F., FRANX, M., VAN DOKKUM, P. & LABBÉ, I., 2009. Detection of Quiescent Galaxies in a Bicolor Sequence from Z = 0-2. *ApJ*, **691**, 1879–1895.

WILLICK, J. A., 1994. Statistical bias in distance and peculiar velocity estimation. 1: The 'calibration' problem. *ApJS*, **92**, 1–31.

WILLICK, J. A., COURTEAU, S., FABER, S. M., BURSTEIN, D. & DEKEL, A., 1995. Homogeneous Velocity-Distance Data for Peculiar Velocity Analysis. I. Calibration of Cluster Samples. *ApJ*, **446**, 12.

WILLICK, J. A., STRAUSS, M. A., DEKEL, A. & KOLATT, T., 1997. Maximum Likelihood Comparisons of Tully-Fisher and Redshift Data: Constraints on Ω and Biasing. *ApJ*, **486**, 629–664.

WISNIOSKI, E., FÖRSTER SCHREIBER, N. M., WUYTS, S., WUYTS, E., BANDARA, K. ET AL., 2015. The KMOS^{3D} Survey: Design, First Results, and the Evolution of Galaxy Kinematics from 0.7 <= z <= 2.7. *ApJ*, **799**, 209.

WOOTTEN, A. & THOMPSON, A. R., 2009. The Atacama Large Millimeter/Submillimeter Array. *IEEE Proceedings*, **97**, 1463–1471.

Wright, A. H., Robotham, A. S. G., Bourne, N., Driver, S. P., Dunne, L. et al., 2016. Galaxy And Mass Assembly: accurate panchromatic photometry from optical priors using LAMBDAR. *MNRAS*, **460**, 765–801.

Wright, E. L., Eisenhardt, P. R. M., Mainzer, A. K., Ressler, M. E., Cutri, R. M. et al., 2010. The Wide-field Infrared Survey Explorer (WISE): Mission Description and Initial On-orbit Performance. *AJ*, **140**, 1868–1881.

Yahya, S., Bull, P., Santos, M. G., Silva, M., Maartens, R., Okouma, P. & Bassett, B., 2015. Cosmological performance of SKA H I galaxy surveys. *MNRAS*, **450**, 2251–2260.

Yang, X., Mo, H. J. & van den Bosch, F. C., 2003. Constraining galaxy formation and cosmology with the conditional luminosity function of galaxies. *MNRAS*, **339**, 1057–1080.

York, D. G., Adelman, J., Anderson, Jr., J. E., Anderson, S. F., Annis, J. et al., 2000. The Sloan Digital Sky Survey: Technical Summary. *AJ*, **120**, 1579–1587.

Yuan, H. B., Liu, X. W. & Xiang, M. S., 2013. Empirical extinction coefficients for the GALEX, SDSS, 2MASS and WISE passbands. *MNRAS*, **430**, 2188–2199.

Zahid, H. J., Dima, G. I., Kewley, L. J., Erb, D. K. & Davé, R., 2012. A Census of Oxygen in Star-forming Galaxies: An Empirical Model Linking Metallicities, Star Formation Rates, and Outflows. *ApJ*, **757**, 54.